Faculty of Art, Design and the Built Environment

Ulster University at Jordanstown

Belfast School of Architecture and the Built Environment

Laboratory study of the tyre / grooved runway Marshall asphalt surface interface

by:

Jason Darragh Ferguson

BSc (Hons), DPP, GMICE, MIAT, ISMARTI, AFHEA

Thesis submitted for the degree of

Doctor of Philosophy

August 2022

TABLE OF CONTENTS

List of Figures

LIST OF TABLES

ACKNOWLEDGEMENTS

The author wishes to express his sincere thanks to Dr David Woodward and Dr Phillip Millar for the opportunities and experiences afforded to him during his research.

The author wishes to express thanks to Mr Ian Martin for his humour, knowledge and honesty throughout the research journey. His friendship is greatly appreciated.

The author wishes to express his appreciation to his partner- Ryan who had to endure the frustrations along the way.

Finally, the author wishes to express his thanks to his parents for their curiosity in my research.

ABSTRACT

This thesis focuses on a laboratory investigation of the tyre / grooved runway surface interface. A critical review of available literature identified significant knowledge gaps. Most literature relates to the tyre/road surface interface with relatively little considering grooved runway asphalt. There is little literature related to laboratory-based investigation identifying the need for new laboratory methods.

For example, no method is specified to assess the wear characteristics of grooved Marshall Asphalt (GMA) to predict its in-service performance. Performance is based on the initial skid resistance value and does consider the evolution of skid resistance and other interface characteristics during the runways life span. A new test method was developed using the Road Test Machine to subject asphalt test specimens to low-speed, high-stress conditions to simulate wear, enabling the performance of the GMA to be assessed. It was found that grooving contributes positively to skid resistance; however, there is a balance between optimum skid resistance and asphalt degradation as all dimensions considered wore differently depending on rib width/groove spacing ratio.

Photogrammetry generated a total of 88 3D models of the test surfaces. This enabled analysis of volumetric data to explain the evolution of the British Pendulum Value of the grooved surfaces as they were trafficked. The Volume of Material in the Peaks was found to relate to the micro-texture surface of the aggregate. A Step Height analysis assessed how groove and rib dimensions evolved. The width of the asphalt rib does not change when subjected to simulated trafficking; however, the height of the rib decreases. This decrease will reduce the water evacuation capability of the grooved surface. This method integrated into a runway monitoring plan would strengthen the asset maintenance plan of the runway.

Significant ambiguity was found in the current EN 13036 test method for determining skid resistance of grooved surfaces. Published research utilising the British Pendulum Tester for grooved surfaces has consistently omitted reference to an important adaptation to the method. New research within this thesis has significantly contributed to the knowledge of the interface between the British Pendulum Tester and a grooved surface. This work identified the pendulum slider bounces across the grooved surface and that pendulum values are based on 57% less contact when not measured according to the adaption within the method.

Based on this work, it will be recommended that the existing method be revised to eliminate the ambiguity and provide clarity to the method. The adaption to the method in this work led to a novel approach to trafficking GMA at an alternative angle to that typically adapted in practice. This simple approach demonstrated favourable pendulum data, with GMA sawn at an angle of 6 degrees to the direction of trafficking, offering higher pendulum value longevity than that typically used in practice (0 degrees).

Rubber accumulation of the runway surface is detrimental to the friction of the surface, particularly during wet conditions. The thesis found that information relating to the theory of rubber deposition on runway surfaces is limited. Rubber is deposited on the runway surface when an aircraft lands on the runway surface due to the impact temperature generated at the tyre pavement interface when the tyre makes contact with the runway surface. A scaled experiment simulated within the constraints of a laboratory environment the process of a landing aircraft tyre touching down on the runway surface. The investigation generated 396 temperature data sets.

Whilst not a direct comparison, the method is similar to what happens in reality. The experiment explored how parameters such as surface texture, aircraft speed and tyre load contribute to impact temperature. It was found that landing speed contributes greatest to impact temperature during landing conditions.

The data applies to aviation industry scenarios, and the new test methods developed have the potential to offer insight into the performance of grooved surfaces.

LIST OF ABBREVIATIONS

µm	Micrometer
3D	Three Dimensional
AFC	Abbott Firestone Curve
AMBR	Areal Material Bearing Ratio
ANOVA	Analysis of the Variance
AOI	Area of Interest
AP1	Aluminium Plate 1
ASTM	American Society for Testing and Materials now known as ASTM International
BPT	British Pendulum Tester
CAA	Civil Aviation Authority
CFME	Continuous Friction Measurement Equipment
CRP	Close Range Photogrammetry
DFT	Dynamic Friction Tester
DMRB	Design Manual for Roads and Bridges
DSMM	Digital Surf MountainsMaps
EASL	Equivalent Axle Single Load
FAA	Federal Aviation Administration
FAP	Friction After Polishing
FPA	Focal Plain Array
GMA	Grooved Marshall Asphalt
GN	Grip Number
GP	Glass Plate

HRA	Hot Rolled Asphalt
IA	Interface Angle
ICAO	International Civil Aviation Organization
km/h	Kilometers per hour
kN	Kilo Newtons
Ms	Millisecond
PSI	Pounds per Square Inch
PTV	Pendulum Test Value
RA	Rotation Angle
Rpm	Revolutions per minute
RTM	Road Testing Machine
SARPs	Standards and Recommended Practices
SCRIM	Sideway-force Coefficient Routine Investigation Machine
SIM	Stress in Motion
SLR	Single Lens Reflex
SMA	Stone Mastic Asphalt
UK	United Kingdom
ULTRA	Ulster Tyre Road Assimilator
UTRSI	Ulster Tyre Road Surface Interface
Vmc	Volume of material in the core
Vmp	Volume of material in the peaks
Vvc	Volume of voids in the core
Vvv	Volume of voids in the valleys
SV	SCRIM Value

SC	SCRIM Co-efficient

GLOSSARY

Areal	Areal relates to a defined area or Area of Interest (AOI)
Occlusion	The obstruction / prevention of light penetrating the full depth of a surface
Penetration Drainage	Aggregate micro-texture penetrating the thin water film present on a wet pavement
Idealised Surface	A surface with limited surface texture

NOTE ON ACCESS TO CONTENTS

"I hereby declare that with effect from the date on which the thesis is deposited in the Research Office of the University of Ulster, the thesis shall remain confidential with access or copying prohibited. Following expiry of this period I permit

1. the Librarian of the University to allow the thesis to be copied in whole or in part without reference to me on the understanding that such authority applies to the provision of single copies made for study purposes or for inclusion within the stock of another library.
2. the thesis to be made available through the Ulster Institutional Repository and/or EThOS under the terms of the Ulster eTheses Deposit Agreement which I have signed.

IT IS A CONDITION OF USE OF THIS THESIS THAT ANYONE WHO CONSULTS IT MUST RECOGNISE THAT THE COPYRIGHT RESTS WITH THE UNIVERSITY AND THEN SUBSEQUENTLY TO THE AUTHOR ON THE EXPIRY OF THIS PERIOD AND THAT NO QUOTATION FROM THE THESIS AND NO INFORMATION DERIVED FROM IT MAY BE PUBLISHED UNLESS THE SOURCE IS PROPERLY ACKNOWLEDGED."

CHAPTER 1.

INTRODUCTION

1.1 Introduction

This thesis considers the tyre/runway surface interface. This chapter states the background and justification behind the research project. The title of the thesis is defined, and the research questions and objectives are stated. The organisation of the thesis is stated with a synopsis of each chapter.

1.2 Background

The operational safety of a runway is one of the most important considerations for an airport operator. The in-service skid resistance of the runway is derived from the macro and microscale characteristics of the asphalt. Both texture scales serve different functions, but as a collective, the combined effect of both, contribute to skid resistance.

The International Civil Aviation Organization (ICAO) is an organisation that sets the aviation standard practices worldwide. ICAO promotes the safe and orderly development of international civil aviation throughout the world. It sets standards and regulations necessary for, among other things, aviation safety.

Each member state and aviation organisation works collaboratively to develop their International Standards and Recommended Practices within ICAO (SARPs). This structure aims to adopt a harmonised approach globally with differences based on the implementation at a national level. Within the United Kingdom (UK), the Civil Aviation Authority (CAA) is responsible for aviation-related activities. This is the national regulatory body in the UK, and it implements the ICAO SARPs in national legislation.

The Aerodrome Design Manual Part 1- Runways, 2020, sets out guidance material on the geometric design of runways and associated aerodrome elements, namely, runway shoulders, runway strips, runway end safety areas, clearways and stop ways. Chapter 5 covers the physical characteristics of the runway, particularly subsection 5.1.22 – 5.1.25 deals with pavement surface texture. Further guidance on surface texture is provided in Part 3 – Pavements.

Part 3 – deals with friction concerning surface drainage, stating that for friction to be adequately achieved, three engineering design measures must be satisfied;

- Surface drainage (surface slope);
- Tyre surface interface drainage (macrotexture); and
- Penetration drainage (microtexture)

Surface drainage of the runway serves to minimise water depth on the surface of the pavement. This is provided through an adequately sloped surface through both longitudinal and transverse directions. Surface texture treatment is a practice used to facilitate improved tyre pavement interaction under wet conditions. It is not, however, used as a substitute for an inadequate runway slope. Interface drainage is regarded as the drainage under a moving tyre. The purpose is two fold;

- To reduce residual bulk surface water from intruding into the forward area of the interface
- To drain intruding water to the outside of the interface.

The objective is to achieve high water dispersion rates under a moving tyre. Interface drainage is speed-related. It is influenced by tyre speed. In this context, surface macrotexture becomes important in the higher speed ranges. In terms of the operational speed of an aircraft, be it landing or taking off, it is within the higher speed ranges that adequate friction is critical to the stopping distance and directional control capability of the aircraft.

In the context of interface drainage, it is worth noting the comparison of road surface texture/road vehicle tyres - runway surface texture/aircraft tyres. The pavement of a road surface is generally of a lower texture (closed textured surface) than a runway surface. Therefore adequate drainage at the interface of a road tyre with a 'smoother' road texture is maintained by the patterned vehicle tyre tread, which contributes significantly to the drainage capability at the tyre interface. Aircraft tyres cannot be manufactured with similar tread characteristics and therefore have a series of circumferentially grooved treads, contributing much less to interface drainage. Therefore it is the role of the runway to provide adequate interface drainage through sufficient runway texture characteristics to maintain adequate wet weather friction.

Conventional flexible runways constructed with specifications similar to a road surface utilised a close textured asphalt material. This material demonstrated a notable decrease in wet friction at high aircraft speeds and increased aquaplaning at small water film thicknesses. Therefore, surface treatment in the form of grooving (perpendicular to the runway centreline) is used to improve wet weather frictional characteristics. Even with modern runways, the contribution of grooving to wet weather skid resistances has been recognised so much that grooving is specified for new runways. Figure 1.0 demonstrates how grooving inhibits the tyre's flexibility, sealing the path of water escape, therefore reducing the likelihood of aquaplaning to a manageable level. Natural interfacial drainage

facilitated through asphalt macrotexture is somewhat slow due to the complex arrangement of aggregate. Grooving whilst improving interfacial drainage enhances the efficiency of bulk water drainage as it provides a shorter drainage path for the removal of water.

Figure 1.0. Tyre interfacing grooved pavement (Zuzelo, 2014).

The one action that separates the activity of an aircraft utilising an asphalt pavement and a vehicle utilising an asphalt pavement is that when an aircraft lands. At the moment of touchdown, the runway experiences a sudden impact force as it starts to interact with the tyre configuration of the aircraft. The total weight of the landing aircraft is then transferred to the runway surface, and the aircraft continues to lose speed assisted by controlled braking.

During landing, the aircraft tyre is stationary with respect to the horizontal landing speed of the aircraft. Upon touchdown, the aircraft tyres are required to match the speed of the aircraft almost instantly. At the moment of touchdown, the runway experiences a sudden impact force as it starts to interact with the tyre configuration of the aircraft. The total weight of the landing aircraft is then transferred to the runway surface as it continues to lose speed assisted by controlled braking. During landing, the touchdown zone of the runway experiences a rapid transition of tyre/surface interface conditions. At the initial moment of touchdown, heat is generated as the tyres interact with the runway surface, absorbing the initial loading from the aircraft. During this initial period of contact, rubber from the aircraft tyre vaporises, releasing a puff of smoke. The runway surface can only provide limited friction with the aircraft at this period. Slip occurs as the tyres continue to interact with the runway surface, with slip distance dependent on surface parameters of the runway. Skid-marks are formed as a consequence of rubber becoming detached by abrasion between the slipping tyres and the runway surface (Alroqi et al., 2016).

Figure 1.1. Aircraft tyres upon touchdown (Groot, 2019).

Research developments in the area of asphalt grooving has suggested grooving modifications contribute positively to skid resistance and grooving longevity, including greater resistance to rubber contamination. Whilst such modifications have been suggested, grooving contractor ROADGRIP (2020) is sceptical of modifications citing there is not enough data to draw a firm conclusion.

1.3 Justification

Research (Daiutolo, 2013) relating to grooved pavements suggests a lack of understanding between the tyre and grooved pavement interface. Available research has concluded from analysis based on the initial skid resistance value of grooved pavements. It has not considered the variability of skid-resistance due to trafficking and the contribution of grooving, which further influences the interface condition.

Pressure at the tyre interface has been investigated previously through pinned strain gauges; developments in technology - XSENSOR Pressure Pad utilised at Ulster University have shown how interface pressure changes for trafficking. Such changes for grooved surfaces has not been quantified or reported previously and is a contribution to knowledge therefore.

Developments in the area of grooving have considered the geometry of the groove, limited studies have shown trapezoidal grooving offers benefits over standard square groove; however, there is a lack of research considering the contribution of grooving dimensions, their influence on interface conditions and how such dimensions perform with trafficking.

Published data has omitted reference to an important method within the British Standard for measuring grooved pavements. Such a consistent omission in research publications suggests that BS EN 13036 - Road and airfield surface characteristics - Test methods have not been considered in their entirety. Available research in this context could be misleading.

Research has reported that landing aircraft tyres generate smoke at the interface due to rubber vaporising; this is due to tyre slippage at the interface as the stationary tyre is expected to match the horizontal landing speed of the aircraft instantly. This has led to investigations relating to the pre-spin up of the tyre before touchdown, which would reduce/eliminate slippage at the tyre interface during touchdown. Research has omitted to investigate the external mechanisms such as tyre speed, tyre loading, and surface texture, contributing to the interface interaction.

The found information suggests further work is required to provide an understanding of the;

- friction measurement of grooved runway surfaces
- performance of the grooved runway surface when subjected to trafficking
- effect of trafficking on the grooved surface skid resistance
- interface between the tyre and the grooved runway surface
- influence of aircraft parameters on tyre impact temperature

1.4 Research questions, aim and objectives

The research questions are:

1. Can the durability of Grooved Marshall Asphalt (GMA) be predicted?
2. Can the friction tyre/runway surface interface be better understood?
3. Can evolution of the tyre/surface interface be modelled in laboratory experiments in three dimensions?
4. What is the potential impact of the research presented in this thesis to the design and maintenance of grooved runways?
5. What are the limitations of the research presented in this thesis and the implications for further work?

The aim of this thesis is to critically evaluate the laboratory performance of 'the tyre/runway surface interface'.

The objectives are:

- Critical review of literature to establish gaps in knowledge
- Design suitable test methods to address knowledge gaps
- Analyse the experimental outputs of test methods in respect of the friction tyre/runway surface interface
- Evaluate the significance of specific parameters to the tyre/runway surface interface such as interface pressure and groove parameters.
- Evaluate the skid resistance performance of different groove dimensions.
- Evaluate the contribution of 3D modelling to the friction tyre/runway surface interface
- Draw conclusions and make recommendations for further research.

1.5 Organisation of the thesis

The organisation of the thesis is covered across thirteen chapters as follows:

- **Chapter 1 Introduction**

  Details the background and justification to the research presented. It presents the thesis aim, research questions and objectives.

- **Chapter 2 Literature review**

  Reviews existing literature on subjects that are of significance to this research. Presents a critical review to distinguish the knowledge gaps used as the basis for the research presented in this thesis.

- **Chapter 3 Research methods**

  Presents the research methods implemented in this thesis in order to meet the objectives and address the research questions stated.

- **Chapter 4 Test Surfaces**

  Considers different combinations of grooving dimensions; rib width, groove width and groove depth from a theoretical approach.

- **Chapter 5 Investigation of the ASTM friction tyre / idealised surface interface using pressure mapping**

  The interface pressure between a smooth test tyre and idealised aluminium test surface are considered. The distribution and severity of interface pressure due to differing groove dimensions is considered.

- **Chapter 6 Evolution of the ASTM friction tyre / grooved Marshall asphalt interface due to simulated wear using pressure mapping**

  The interface pressure between a smooth test tyre and Grooved Marshall Asphalt test specimens are considered. The change in interface pressure and distribution due to simulated trafficking is considered.

- **Chapter 7 Evolution of grooved Marshall asphalt skid resistance**

  The influence of grooving on skid resistance is considered using Grooved Marshall Asphalt of differing groove dimensions. Both standard and non-standard methods are considered. A metrological height parameter is considered to explain the change in skid resistance.

- **Chapter 8 Evolution of Grooved Marshall asphalt areal parameters**

  This chapter investigates the evolution of areal surface texture parameters for eight Marshall Asphalt test surfaces.

- **Chapter 9 Investigating the grooved surface interface with British Pendulum Skid Resistance Tester (BPSRT).**

This chapter investigates the interface between the British Skid Resistance pendulum tester and grooved test specimens using the paint removal technique.

- **Chapter 10 Laboratory Investigation of Aircraft Impact Temperature**

  This chapter investigates tyre impact temperature. A small, scale laboratory experiment simulated a landing tyre making contact with a moving surface. The influence of speed, load, tyre off set and surface texture on tyre impact temperature was reported.

- **Chapter 11 Discussion**

  This chapter discusses the findings from the previous chapters and how they relate to the set objectives. It presents the impact of the research.

- **Chapter 12 Conclusion**

  Addresses the research questions through the overall conclusions presented fro m the research.

- **Chapter 13 Future recommendations**

  This chapter presents recommendations for further research.

1.6 Limitations

The research presented is derived from laboratory experiments. The outputs require validation by in service measurements which is beyond the scope of this thesis. Potential types of measurements are included in Recommendations for Further Research.

1.7 PhD Research Process

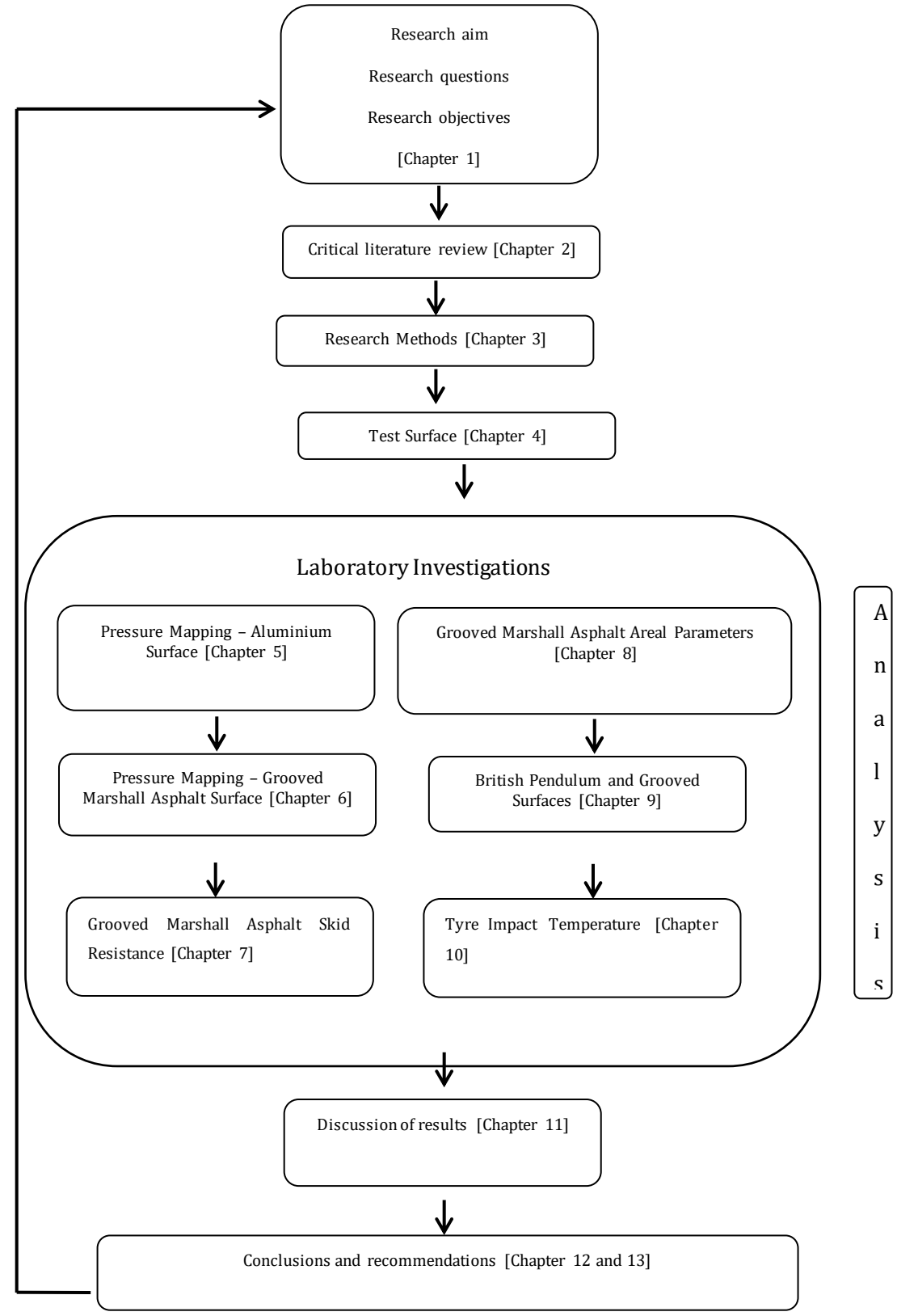

Figure 1.2. PhD research process.

CHAPTER 2.

LITERATURE REVIEW

2.1 Introduction

This chapter considers literature relating to the investigation undertaken in this research. The review focuses on factors relating to tyre pavement interaction. The chapter concludes with a critical review from which knowledge gaps are identified, and findings presented.

2.2 Runway Pavement

The International Civil Aviation Organisation (ICAO), 2017 defines a runway as a

'rectangular area on a land aerodrome prepared for the landing and take-off of aircraft'.

Runway pavements are constructed with either concrete (rigid pavement) or asphalt (flexible pavement), depending on design parameters and the local ground conditions. Flexible asphalt pavements are frequently used as runway pavements (White,2018) therefore this thesis will focus on flexible pavements.

Marshall Asphalt (MA) is a type of asphalt concrete designed to achieve specific design parameters. Due to the controlled environment in which MA is manufactured, its material properties are consistent and therefore it provides the necessary functional characteristics for airfield pavement applications; good rideability, good frictional characteristics, durable hard-wearing surface and high strength (MOD, 2009). In the United Kingdom (UK), various asphalt mixes are used in highway applications. Hot Rolled Asphalt (HRA) is a standard asphalt mix where aggregate chippings are rolled into the mix after it has been laid. HRA would be unsuitable for runway pavements because the aggregate chippings are likely to be '*plucked*' from the surface or spall and create a hazard with ingestion into jet engines.

There is no fundamental difference between a runway and a highway with principles of design applied to both; however, both differ with their use, notably, tyre load repetitions, tyre pressures and traffic patterns.

Highway pavements are subjected to a greater frequency of loading than runway pavements. Loading from vehicles is designed based on Equivalent Axle Single Load (EASL) (Pavement Interactive, 2020). All vehicle types in the pavement design life are converted to a single standard axle load, whereas airfield pavement design account for the aircraft's maximum gross weight. Small aircraft tyres pressure is similar to vehicular tyre pressure. However, larger aircraft increases tyre loading substantially therefore increased tyre pressure, as shown in Figure 2.0.

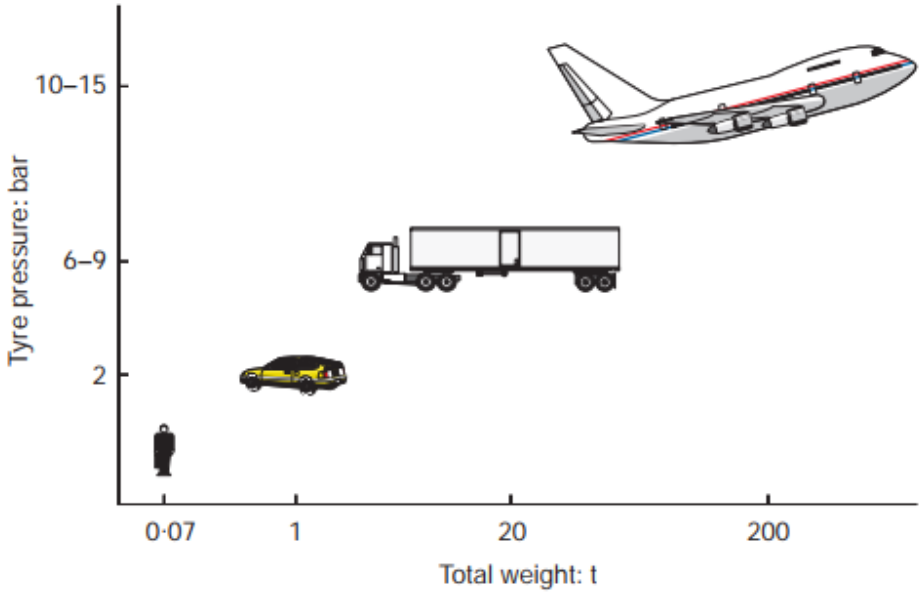

Figure 2.0. Weight Vs Tyre Pressure (Hameed, 2022)

Traffic patterns for highways move in channels where the outer shoulders of the pavement experience trafficking only, whereas runway traffic patterns can differ depending on the undercarriage wheel configuration.

2.3 Runway Layout

The configuration of an airfield layout is often dependent on the availability of land coupled with land constraints and specific environmental considerations; therefore, the runway layout is specific to local operational constraints and can be considered airport specific.

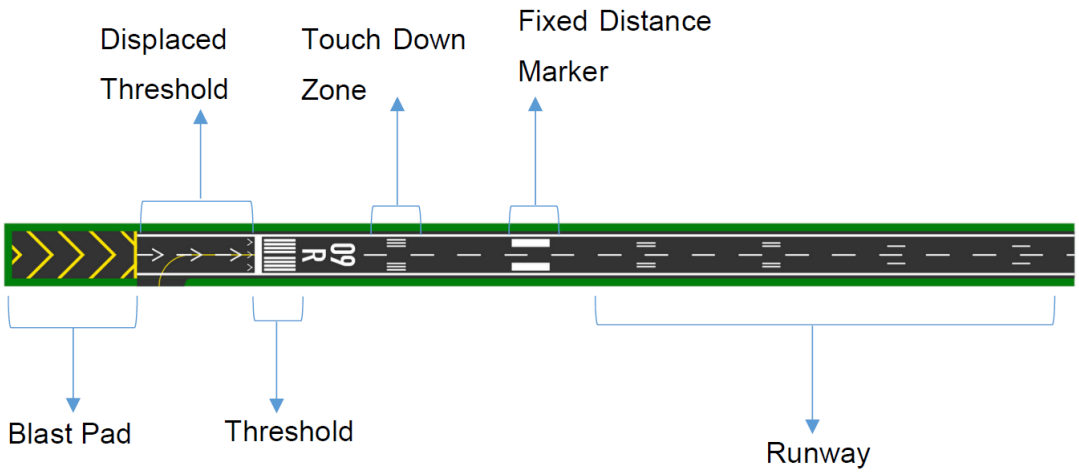

Figure 2.1. Typical Runway Layout (Safi, 2016).

As seen in Figure 2.1, a typical runway layout can be considered in 6 sections as noted above. Each section serves a different purpose and may or may not be constructed differently from the main runway section.

A blast pad may be placed at either end of the runway with the sole purpose of acting as an emergency extension to the main runway to provide additional length in the event of rejected take off. The threshold/displaced threshold follows the blast pad. The threshold denotes the beginning of the runway where the aircraft aligns with the centre markings before take off. A displaced threshold is a longer length of a threshold. These are used when there is an encroachment (such as residential housing or farm buildings) affecting the normal 3 degree landing position of the aircraft therefore effectively increasing the length of the runway. Thresholds are not used for landing. Following the threshold is the TouchDown Zone; this is the area where the pilot visually aims to touchdown during landing. The main runway section itself is located after the touchdown zone. The main runway section is used for take-off and landing and is painted with a series of fixed distance markers enabling pilots to judge distance.

Not considered above is the runway clear way and taxi exits. A clear way is an area at the end of the runway beyond the paved surface free from obstructions and controlled by the airport operator. Taxi exits and high-speed exits are areas intercepting the main runway, which enable aircraft to leave the main runway section where the aircraft has slowed down sufficiently for taxing to the airport gate.

2.4 Marshall Asphalt

Marshall asphalt is the most frequent asphalt surfacing material used for airfield applications White, 2018. The Ministry of Defence (United Kingdom) describe Marshall Asphalt as an asphalt Concrete designed to achieve specified stability, flow, voids and density characteristics. Marshall Asphalt, by nature, is designed to be a dense material. During its conception in the 1930s/ 1940, 's Invented by Bruce Marshall, his focus was to provide a material with an optimum asphalt content which will provide maximum strength within the mix with minimum deformation from applied loading.

Its use for airfield applications dates back to world war two, when its structural performance was recognised and adopted as the standard airfield pavement to address poor performance exhibited by existing asphalt pavements under increasing aircraft wheel loads.

The Marshall method assesses the asphalt design mix's strength and flexibility. Strength is assessed by the mix stability. Stability refers to the maximum load carried by a compacted test specimen at a standard test temperature of 60°C. The temperature of 60°C is considered the point at which an asphalt pavement is at its weakest. Flexibility refers to the 'plastic flow value' or amount of deformation of the test specimen. Flow is measured by the change in diameter of the test specimen on the same axis at which the loading is applied. This measurement is compared prior to loading and at maximum loading.

By omission, the description of Marshall Asphalt set out by the Ministry of Defence focuses on specific mechanical and, by consequence, structural performance characteristics, not surface performance characteristics such as wear. There is no method specified within the design to assess the surface performance of the mix. Therefore, there is scope for further optimisation within the Marshall method by consideration of the surface performance.

2.5 Pavement Friction

In the context of an asphalt surface, pavement friction is the interaction between the tyre and pavement surface. It is influenced by the pavement characteristics with particular regard to pavement texture. Therefore, friction between the tyre and pavement is not a single property of either it is instead a product of both, which is interdependent on both.

2.6 Friction

Friction is defined as the resistance to motion during sliding or rolling conditions experienced when a body moves tangentially over another with which it is in contact (Grosch, 1974). Friction (also commonly known as skid resistance in the world of asphalt) is characterised using the dimensionless friction co-efficient, μ. This is calculated based on the ratio of the tangential force (F) at the contact interface; between the tyre rubber and the horizontal surface to the perpendicular force or vertical load (FW) (Normal load) (Hall et al., 2009) and is given by:

$$\mu = \frac{F}{Fw}$$

Hall et al., (2009) consider pavement friction to be the force that resists the relative motion between a vehicle tyre and a pavement surface. For automobiles, friction is described as rolling friction due to the tangential nature of the interaction. The forces involved in rolling friction are illustrated in Figure 2.2.

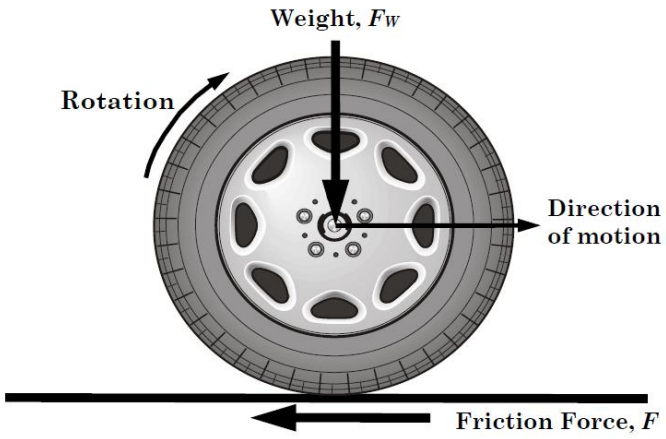

Figure 2.2. Frictional forces contributing to rolling friction (Hall et al., 2009).

Figure 2.2 illustrates the resistive forces acting on a vehicular tyre as it passes over the pavement. The tangential force required to initiate motion from inertia is called static frictional force, and the force required to maintain this motion is known as kinetic frictional force. Therefore, for an automobile on a level plane, the coefficient of static friction is either greater than or equal to the coefficient of kinetic friction. Therefore, the tyre cannot move until there is an input force (Grosch, 1974). Figure 2.3 illustrates the movement of an object in the static and kinetic friction regions.

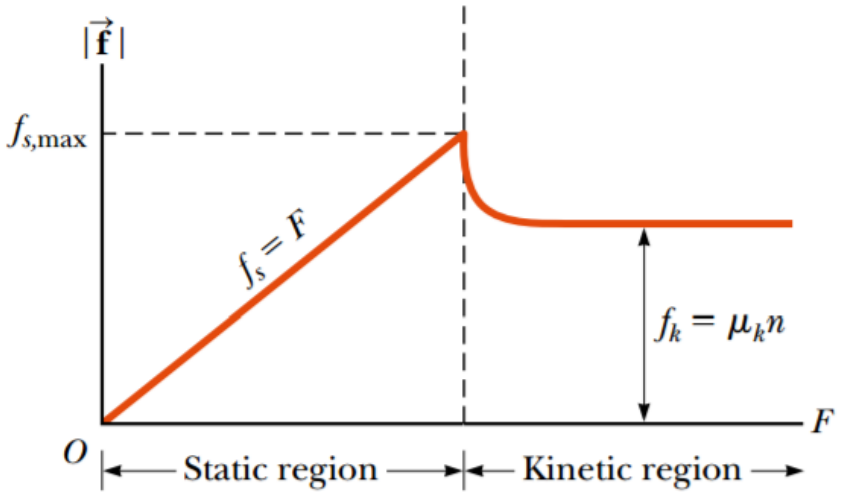

Figure 2.3. Static and Kinetic friction associated with a moving an object (Serway and Vuille, 2012).

As seen in Figure 2.3, for an object moving over a surface such as a tyre, the input force is linearly counteracted by the resistive force of the pavement as illustrated in the static region; force of static friction (f_s)= Horizontal Force (F).

The resistive force can only provide a limited amount of resistance to counteract, and therefore $f_{s,max}$, , illustrates the maximum available resistance. After this point, slippage occurs, and the object moves from Static to Kinetic friction.

When in motion, the frictional force is less than that of $f_{s,max}$ .In Figure 2.3, the kinetic region illustrates an object moving at a constant acceleration. The magnitude of the coefficient of static friction (f_k) = coefficient of kinetic friction (μ_K) multiplied by the magnitude of the normal force (n) exerted by one surface on the other (Serway and Vuille, 2012).

2.6.1 Longitudinal Friction

Friction acting through the tyre when in motion can be considered longitudinal and lateral. Longitudinal friction acts along the direction of tyre motion. Lateral friction refers to forces that act at right angles to the direction of movement of the tyre. These forces only occur when the tyre is in motion.

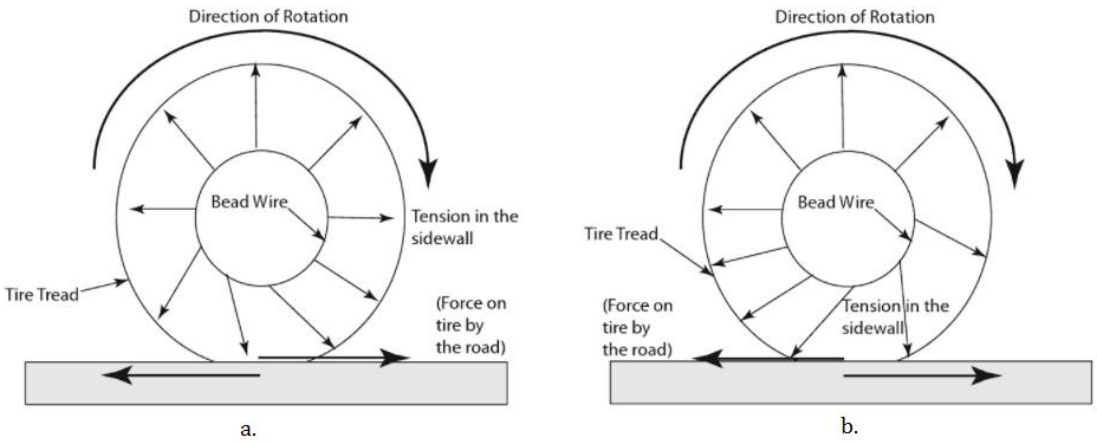

Figure 2.4. Longitudinal forces on a tyre under acceleration (a) and braking (b) (Edmonson, 2011)

Figure 2.4 illustrates the tensional forces in the tyre that arise due to longitudinal friction. For the tyre to overcome inertia, the forces have to be sufficient to exceed the initial static friction at the tyre/surface interface. At the trailing edge of the tyre contact patch, tension in the tyre results in the trailing edge being pulled upwards; this causes the rubber to stretch and eventually slip. On the leading edge, the opposite effect occurs; the tyre is pulled downwards, forcing it into the pavement. At this point, the leading edge of the tyre does not slip and remains in instantaneous contact with the pavement.

Interaction on a molecular level can be characterised using the analogy of spring and dampener. On a molecular level, the process of adhesion takes precedent in the tyre. As the tyre passes over the pavement surface, the molecular interaction can be summarised in three stages.

1. At the leading edge, an adhesive bond is formed.
2. As the tyre continues to move, the band is stretched, the plastic properties of the rubber facilitate resistance to deformation, which creates resistance to motion, therefore, opposing slippage.
3. As the tyre continues to move, the ability to resist deformation becomes too great, and the bond is broken.

Figure 2.5 illustrates the three stages described.

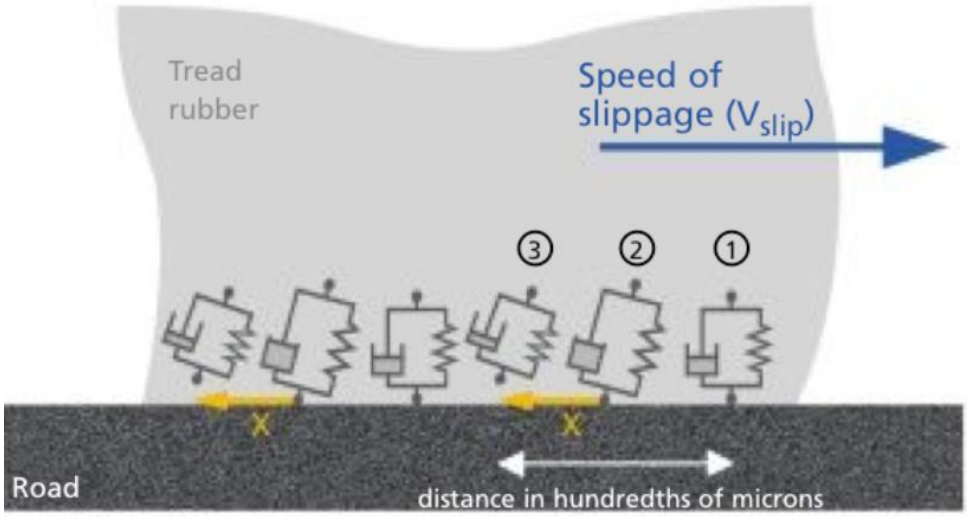

Figure 2.5. Molecular adhesion mechanism of grip generation at road-tyre interface (Michelin, 2001).

The analogy of spring and dampener illustrates the viscoelastic properties of the tyre. Whilst it has been appreciated that forces are acting through the tyre, this is subsequently transferred through the tyre contact patch to the pavement. Therefore, loading conditions are transferred from the vehicle through the tyre to the pavement.

According to Newton's third law of motion, every action has an equal and opposite reaction. Therefore, the pavement will have an equal force acting on the interface of the contact patch. This introduces the concept of rolling resistance and rolling friction.

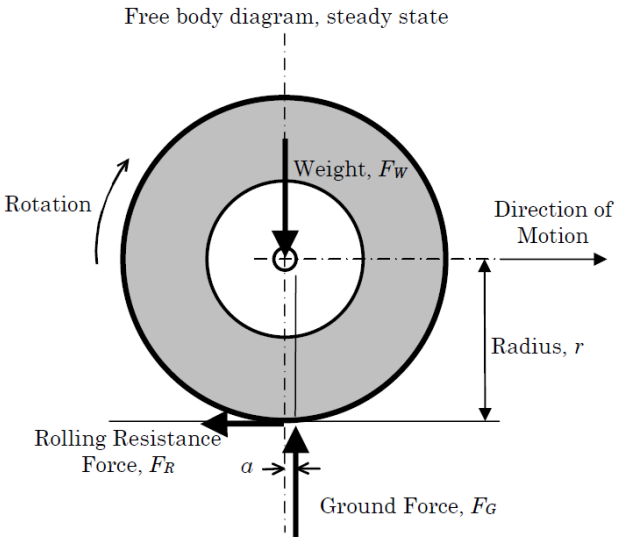

Figure 2.6. Vehicle Tyre Schematic of rolling resistance of a tyre rolling at a constant speed (Hall et al., 2009)

Figure 2.6 illustrates the ground force acting through the tyre's contact patch when it is in motion. The ground force acts through the centre of pressure of the contact patch resulting in a displacement α. The displacement creates a moment that must be overcome for the tyre to rotate. This force is known as the rolling resistance.

2.6.2 Rolling Resistance

When a tyre is moving, the energy input, speed, has to be more significant to keep the tyre rolling; thus, α is a function of speed, and this increases with speed. Both the tyre and the pavement contribute to rolling resistance; therefore, rolling resistance is a function of;

- Pavement Characteristics; texture, condition, surface contaminants.
- Tyre Characteristics; bulk properties, tread design, material properties.

Tyre rolling resistance increases for increased tyre loading, speed, reduced inflation pressure, all of which contribute to high hysteresis losses through increased tyre deformation (Ghosh et al., 2003). In tyres, Bridgestone considers rolling resistance to be caused by hysteresis. As the tyre rotates, it continuously deforms under the loading from the vehicle; this loss of energy dissipates as heat. It, therefore, is attributed to the viscoelastic properties of the rubber. In a free-rolling tyre, Clark and Dodge (1979) consider tyre rolling loss to be wholly attributed by hysteresis so much that other influencing factors such as ground friction can be considered negligible.

In perspective, a steel wheel will run a further distance than that of a rubber wheel under similar conditions. Rolling resistance could be considered relative to the amount of energy lost when the tyre goes through cyclic pressuring. Cyclic pressure is illustrated in Figure 2.7. The transition from A to B and then B to A on the curve illustrates the process of loading and unloading the tyre.

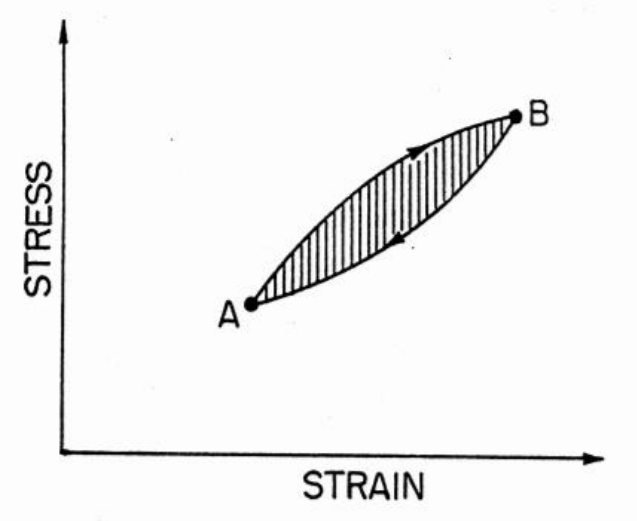

Figure 2.7. Pressure – Strain curve of loss experienced by rubber tyres (Clarke and Dodge, 1979).

Hall et al. (2009) consider that hysteresis relates to the amount of energy lost as a tyre moves over a road surface and deforms due to its interaction with the macrotexture. Hysteresis is characterised whereby energy loss (in the form of heat); in the case of a rubber tyre, deformation, to be greater than energy recovery. Considering this, a harder tyre would deform less and therefore reduce the rolling resistance, and a softer tyre would deform

more and therefore increase rolling resistance. Ejsmont et al. (2018) note rolling resistance to be influenced by tyre temperature, with Harsh et al. (2019) noting that tyre tread temperature significantly affects tyre stiffness, it is, therefore, reasonable to consider hysteresis to be predominantly temperature sensitive.

As hysteric energy is lost as heat at lower ambient temperatures, rolling resistance will be much greater than that at higher temperatures. Therefore, as the tyre reaches equilibrium temperature, the effects of hysteresis will be much less. Considering this, data presented by Clark and Dodge (1979) and Redrouthu (2014) illustrate the influence of speed on rolling resistance to be somewhat conflicting. As speed directly influences the tyre/surface interaction (higher speed, more interactions and tyre deformation), it would be expected that this directly influences tyre temperature and therefore reduce rolling resistance.

However, data presented by Clark and Dodge (1979) shows that when comparing rolling resistance vs speed, for speed greater than 50mph, rolling resistance increases for all tyres considered in the study. Data presented by Redrouthu (2014) supports a similar view; however, the speed at which rolling resistance increased was greater than 62mph. Both speeds are similar, although, given the date of publication, improvement in technology could account for the slight difference in speed. Therefore, the influence of hysteresis below 62mph is independent of speed. Nevertheless, as previously detailed, at higher speeds, there is a greater force required to displace the moment as presented in Figure 2.6.

2.6.3 Lateral Friction

Lateral friction forces act through the tyre when the tyre is performing a manoeuvre, or the tyre is forced to compensate for the pavement's geometry. Lateral forces are more prevalent in cars than aircraft tyres as aircraft do not perform the same range of manoeuvres, and aircraft tyre tread is simple and the runway geometry consistent.

As a vehicle manoeuvres, the lateral force makes the vehicle follow a curved path; with the addition of speed, the radius of curvature of the vehicle increases resulting in a greater friction demand; as the pavement can only provide limited friction, sideways slip may occur. Introducing braking and manoeuvring simultaneously leads to greater demand on the available friction, i.e., the pavement can only provide a limited amount of friction and is, therefore, not infinite. The available friction is shared across both mechanisms, therefore, decreasing the amount of available friction. Figure 2.8 illustrates lateral forces acting on the tyre.

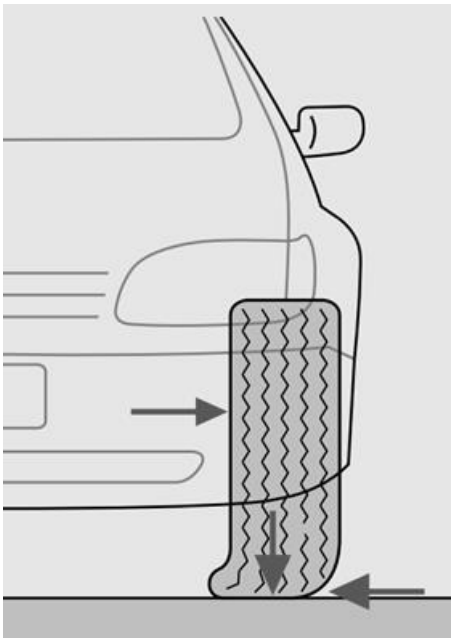

Figure 2.8. Lateral force acting on vehicle tyre (Kost, 2014).

In lateral and longitudinal friction, when operating at the limits of the tyre grip, the relationship is one that where one force increases, the other must decrease by the proportional amount. Therefore, slippage will occur where the sum of the available friction components is exceeded (Hall et al., 2009).

2.7 Surface Texture

Various characteristics affect the available skid resistance of asphalt pavements; surface characteristics, environmental conditions, vehicle and tyre characteristics, and Vehicle operation. However, this review will only consider the surface characteristics with a particular focus on surface texture.

Asphalt surface texture is characterised according to the size of its wavelength (Miller et al.,2012). These properties influence the tyre/surface interaction within the interface of the tyre contact patch. There are generally three surface texture wavelengths that contribute to pavement friction, but the third contributes more to the general ride quality.

- Micro texture – Less than -0.5mm wavelength
- Macro texture – 0.5-50mm wavelength
- Mega texture – 50mm to 500mm wavelength (ISO,2022)

Each texture contributes to skid resistance differently but works simultaneously to contribute to the available friction.

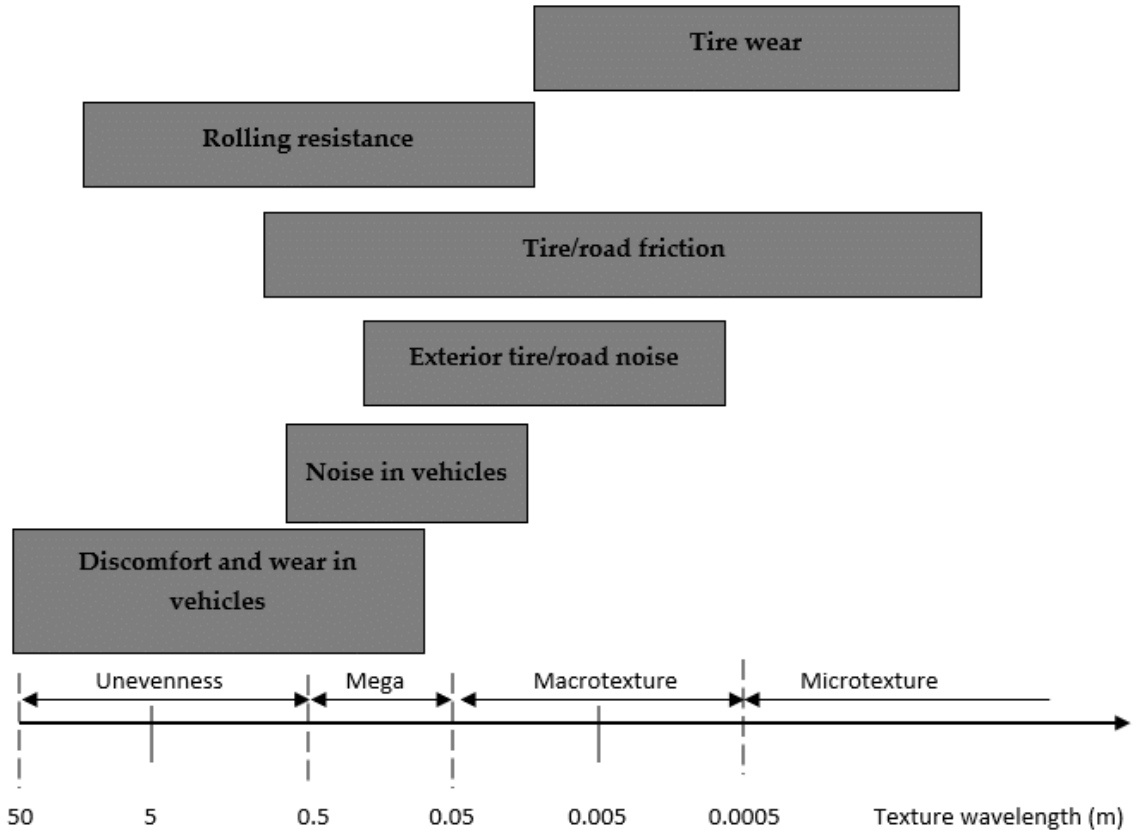

Figure 2.9 Tyre Pavement interactions at different asphalt texture wavelengths (Copetti and Sangiorgi, 2021).

2.7.1 Micro Texture

Microtexture refers to the roughness of the surface of the aggregate particles (fine-scale texture). In an asphalt product, the mastic; fines and bitumen, in a mixture is the primary contributor to wet skid resistance at low speeds Friel (2013). During wet weather conditions, the roughness of the microtexture facilitates tyre pavement interaction as it penetrates the semi-permanent film of water, sustaining contact and therefore improve wet weather skid resistance. Figure 2.10 illustrates both micro and macrotexture.

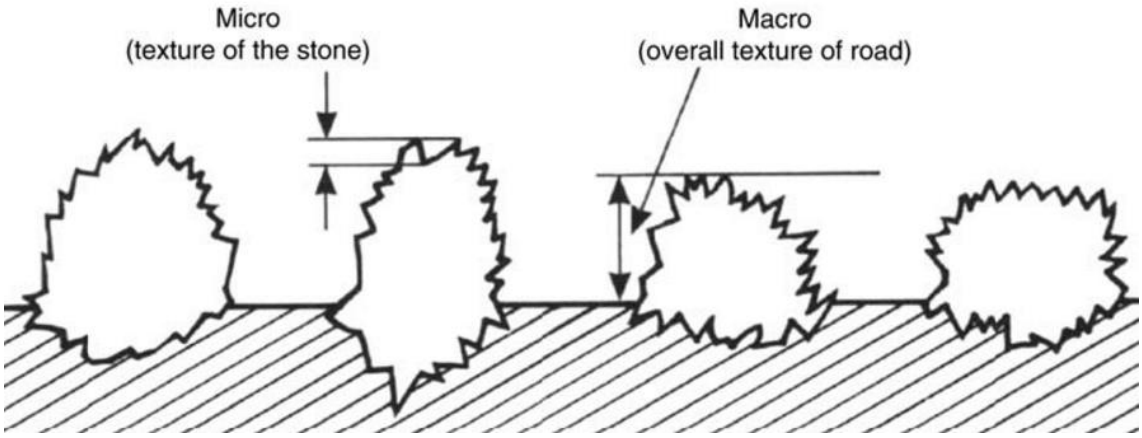

Figure 2.10. Micro & Macro texture. (Sahhaf and Rahmi, 2014).

2.7.2 Macro Texture

Macrotexture refers to the larger irregularities in the road surface (coarse-scale texture). These larger irregularities are associated with voids between stone particles. Macrotexture is responsible for facilitating the removal of water during wet conditions. It provides a means of drainage from the contact interface of the tyre through aggregate spacing (Ferguson, 2017). The physical deformation of the tyre generates the frictional mechanism associated with macrotexture at the contact interface. At higher speed conditions, the significance of macrotexture is critical (Friel, 2013).

2.7.3 Positive & Negative Texture

Macrotexture occurs in two forms; positive and negative texture, as a result of asphalt mix design. Figure 2.11 illustrates the difference between positive and negative textures. Positive texture refers to aggregate particles protruding from the road surface. Such texture contributes to pavement drainage by providing a path for water to disperse. This would be typical in Hot Rolled Asphalt and Asphalt Concrete.

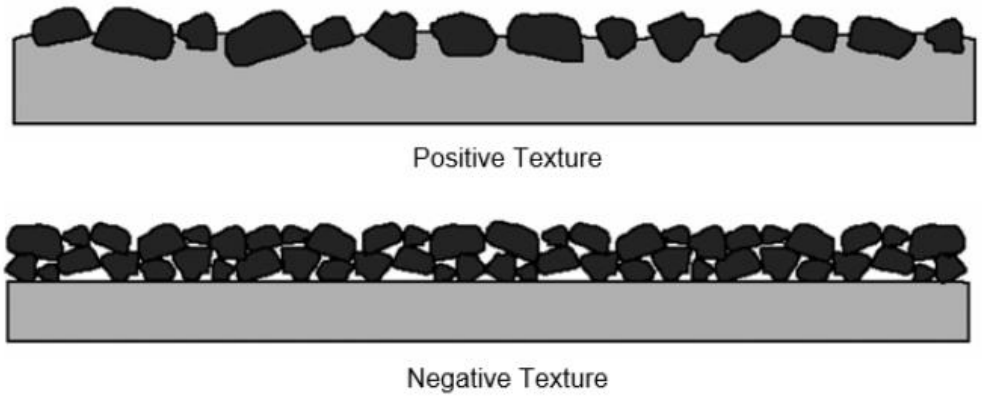

Figure 2.11. Positive and Negative Texture (DMRB, 2006).

Negative texture refers to a dense, flat, compacted surface where the drainage network lies below the tyre plane. The negative texture is characterised by aggregate to aggregate contact, which develops deflections from a plane downwards to the valley like furrows (Viera et al., 2019). Such texture is common in thin asphalt surfacings and Stone Mastic Asphalt (SMA).

2.7.4 Mega Texture

Megatexture is a component of the surface profile of flexible pavement. Low mega texture reduces the demands on the vehicle's suspension, especially during braking and steering; it also reduces water ponding (BLASTRAC 2012). Unless a consistent surface characteristic, the presence of mega texture illustrate pavement distress such as potholes (McQuaid, 2015). Poor mega texture can occur due to surface deformation such as rutting and can have a knock-on effect such as water ponding and therefore increase the risk of aquaplaning.

2.7.5 Asphalt Grooving

The purpose of grooving is somewhat misconstrued. Grooving is not used for surface drainage or to provide friction. It is suggested that grooving does contribute to surface drainage and friction. Grooving removes bulk water from the surface. Zuzelo (2014) claims that worn aircraft tyres experience better braking on grooved pavements than newly treaded tyres on non-grooved pavements in the presence of water.

2.7.6 Grooving Geometry

The Federal Aviation Administration (FAA) (FAA, 1997) specifies Standard Square grooving as illustrated in Figure 2.12 to be 6mm x 6mm x 38mm centre to centre spacing.

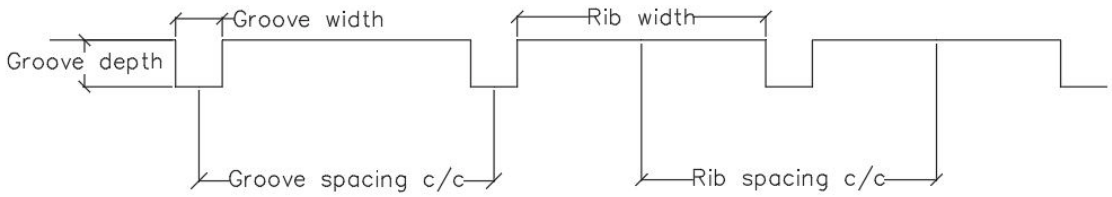

Figure 2.12. Definition of Grooving Parameters.

There is no published research which considers the performance of grooving dimensions. The original research pertaining to the FAA justification for recommending 6mm x 6mm x 38mm centre to centre spacing is unavailable.

Chu and Fwa (2019) evaluated the effect of different grooving parameter dimensions on skid resistance for non-trafficked dense-graded asphalt, Portland cement concrete and an idealised aluminium plate surface. It is not possible to make a direct comparison in terms of skid resistance due to different material properties considered; however, the study found that grooving contributes positively to skid resistance, and the measured PTV values had increased with an increase between groove width and centre-centre spacing.

The study also found that gap width and gap depth had a weak correlation with measured PTV. While the study reported the findings of different grooving parameter dimensions, correlations were drawn by comparing the PTV against the parameters noted in Figure 2.11. It could be argued that drawing direct correlations based on different material properties is somewhat inappropriate due to the different texture properties exhibited by different materials.

Grooving has developed since its introduction; however, the conservative nature of the aviation industry constrains/delays such developments. Trapezoidal grooving has proven to offer increased benefits to standard grooving, including similar friction co-efficient, reduced tyre wear, reduced rubber build-up and increased pavement life Patterson (, 2012); Pasindu and Fwa (2015). Whilst trapezoidal grooving has proven to offer increased benefits,

it could be argued that considering the dimensions only, trapezoidal has a greater cross-sectional area than square grooving, and therefore the greater dimensions will provide better water dissipation on the surface, matching the cross-sectional area of both geometries may offer greater contrast.

The data is somewhat limited, and trapezoidal grooving has not been in service long enough to determine its whole life service benefits; however, studies have proved favourable. Asphalt Grooving Contractors such as ROADGRIP (2020) consider the 'jury to be out' as to whether trapezoidal grooving is any better for safety over time, citing there is not enough data at this stage to draw a firm conclusion. Both geometries provide comparable levels of skid resistance; however, it is the longer-term service performance that has distinguished both.

There is limited literature available on how a tyre interfaces a grooved surface. Therefore, there is little known about the performance of grooving.

2.7.7 Anisotropic Texture

Anisotropic texture is not a new form of texture; its existence stems back about 40+ years. This texture exhibits periodic properties such as grooves which details a consistent texture characteristic (BS ISO 13473-2:2002). Anisotropic texture is not limited to transverse or longitudinal grooves, but these are common methods of providing anisotropic texture, such as those sawn laterally into an asphalt pavement or formed by grinding a concrete pavement. Examples are illustrated in Figure 2.13.

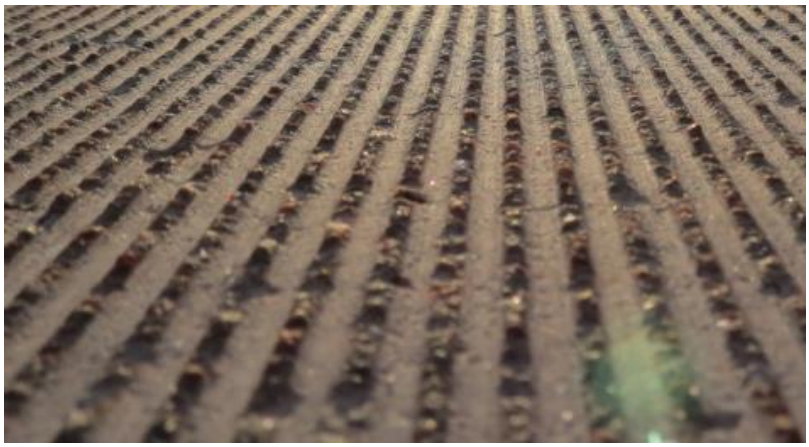

(a) Concrete Otto Alte Teigeler (OAT) Grinding. (Otto Alte Teigeler ,2017)

(b) Marshall Asphalt Grooving .(Aviation Pros,2011)

Figure 2.13. Examples of artificial texture.

From its introduction, the benefits of grooving have been widely researched. It is generally appreciated in literature by Wu et al. (2002), Ju et al. (2013) and Zuzelo (2014) that grooving facilitates tyre pavement interaction during wet weather conditions. As grooves lie beneath the tyre, the tyre cannot seal the path of water escape, and the grooves reduce the likelihood of aquaplaning to a manageable level.

2.7.8 Texture Vs Tyre Interface Review

The importance of texture at the tyre pavement interface is well-rehearsed in literature by Woodward et al. (2014a), Woodward et al. (2014b), and Ejsmont et al. (2017). The phenomenon affects vehicle stability and therefore contributes to the safety of pavements. Vaiana et al., (2012) considers the mechanism of interaction at the interface in three parts;

- Friction,
- Adhesion,
- Hysteresis

Friction, adhesion, and hysteresis have been considered above, however not in consideration of pavement texture. Pavement texture can be considered a variable surface as it is subject to change under trafficking and environmental effects. Texture degradation in the form of aggregate polishing, for example, affects the interface interaction, which affects the available friction.

At the molecular level, polishing affects adhesion at the tyre interface. Adhesion is dominant at lower speed conditions until critical slip occurs. It is, therefore, reasonable to suggest that polishing will affect the level of critical slip, which would reduce the level at which slip occurs; this would be prominent during wet weather conditions when microtexture is critical.

At the macro level, texture contributes to the hysteric function at the tyre interface as the tyre repeatedly envelopes the aggregate surface. At this point, texture influences the transfer of tangential forces to horizontal forces which oppose slippage. Polishing effectively reduces the texture height reducing the scale of tyre deformation at the interface, therefore, reducing friction due to hysteric loss.

Based on the information considered, is reasonable to conclude that friction is not a property derived from a single mechanism nor a property of the tyre and pavement surface individually (O'Hare, 2017) but a property that is interdependent on the interaction derived at the tyre pavement interface as well as how a vehicle is controlled.

2.8 Measurement of Friction

Friction measurement devices generally comprise two categories; laboratory devices and field measurement devices. Each measurement device operates on different principles, and therefore, their frictional data cannot be directly compared.

2.8.1 Laboratory Devices

Laboratory devices are also known as portable devices due to their size and convenience. The most common being The British Pendulum Tester (BPT). The ease of use is well known; however, research has shown that the BPT exhibits erratic behaviour for coarse-textured surfaces. This is further affected by aggregate gap width or the number of gaps that surface texture exhibits (Fwa et al., 2003, Liu et al., 2004). Laboratory devices typically measure friction at low speeds. Mataei et al. (2016) consider such devices to be influenced by the microtexture of the aggregate.

Measurement of Grooved surfaces under BS EN 13036 states that on '*surfaces bearing a regular pattern such as grooved asphalt, tests should be made with the slider operating at an angle of approximately 80° to the grooves*'.

There is no clarification as to the measurement of 80°, and this would be open to interpretation. Two possible scenarios are illustrated as follows.

1. The slider is rotated 80° from the normal – the difficulty with this interpretation is that the BPT is measuring friction longitudinally to the grooves and therefore is unrealistic as to the interaction between the tyre and the grooved surface. Figure 2.14 demonstrates a schematic of the standard interaction of the pendulum for this scenario.

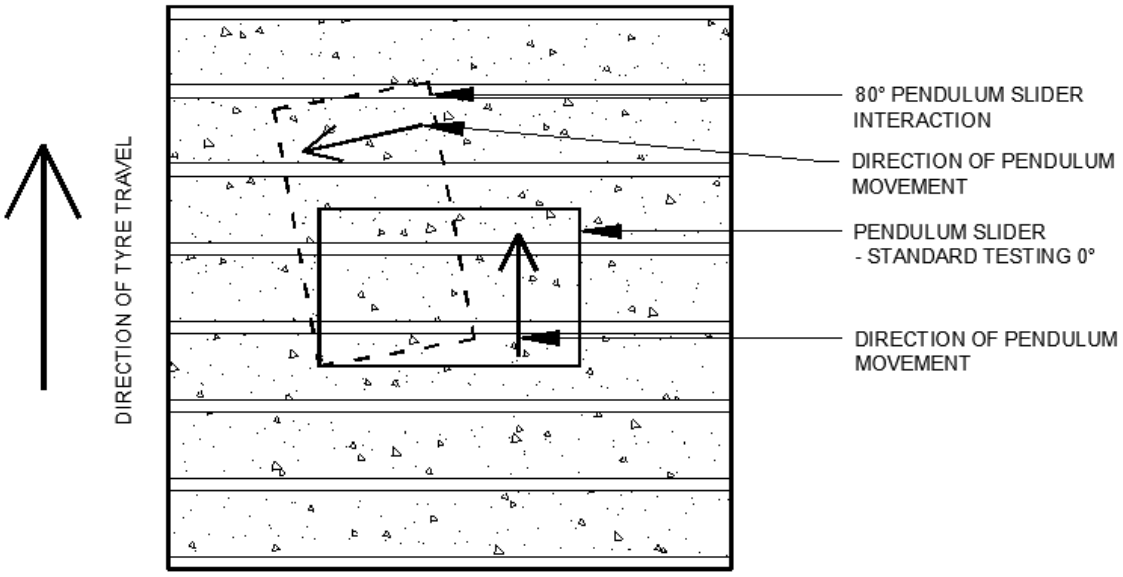

Figure 2.14. British Pendulum slider schematic standard testing for scenario 1 for interaction on a grooved test specimen.

2. The tyre interacts with the grooved surface laterally ~ 90° to the direction of travel; therefore, 80° could be interpreted as a 10° offset, as illustrated in Figure 2.15.

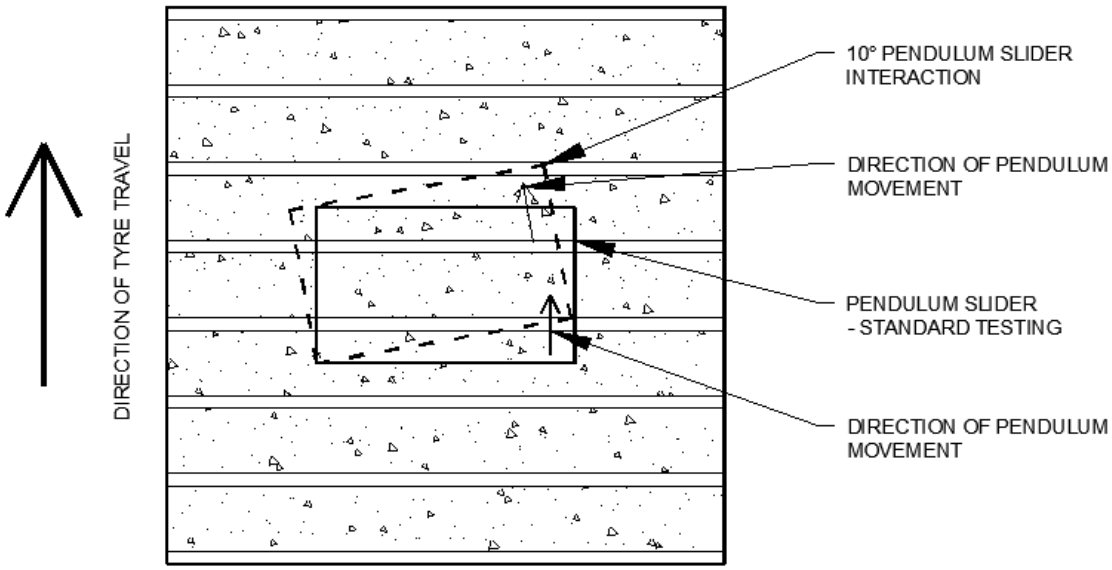

Figure 2.15. BS EN 13036 British Pendulum slider schematic standard testing Vs interpretation 2 interaction on a grooved test specimen.

It is reasonable to suggest scenario two interpretation more realistic as the change of angle when the pendulum interfaces the grooved surface mitigate the influence of the sawn grooves. It has been observed that the Standard BS EN 13036 for The British Pendulum Test has not been considered in its entirety. Lee et al. (2005), Pancer and Karcaca (2016) utilising the British pendulum for grooved surfaces have consistently omitted any reference to the pendulum interacting at 80° due to the presence of grooving.

Other portable devices include the Dynamic Friction Tester (DFT). This device differs from the BPT in that three rubber pads on a disc rotate horizontally at a lateral speed of between 20 to 80 km/hr under a constant load. Both devices operate on similar principles in that they measure a loss of kinetic energy due to the interaction between the rubber pads and the aggregate surface. Similar to the BPT, the DFT exhibits erratic behaviour when measuring coarse surface texture. Fwa and Liu (2019) consider the DFT to be unable to measure the skid resistance of a grooved pavement due to the parallel nature of the grooves and the potential for the rubber sliders to be damaged, striking the wall of the grooves.

In recent times the introduction of the Wehner Schulze Friction after Polishing (FAP) machine has attempted to evaluate the friction performance in a laboratory to predict the performance of skid resistance over the service life of an in situ pavement (Kellermann-Kinner and Gudrun, 2018). Whilst it is not yet portable, a mobile version exists mounted on a truck vehicle. Friel and Woodward (2016) found that for Hot Rolled Asphalt, the interface measured using the FAP machine is not comparable to real life, where greater amounts of tyre drape occur at the interface.

Whilst laboratory devices have their limitations; they help evaluate the durability of skid resistance against polishing (Chu and Fwa, 2019). There is a re-occurring theme of laboratory friction measuring devices exhibiting limitations for coarse texture surfaces. The application of measuring skid resistance of Grooved Surfaces with the British Pendulum requires further clarification. The method of altering the interface angles warrants further investigation.

2.8.2 Site Measurement

On-site measurement devices, usually Continuous Friction Measurement Equipment (CFME), operate on the principle of a locked or fixed slip device that slides on the pavement surface. A controlled flow of water is applied to the road surface immediately in front of the test tyre for these devices. As the vehicle moves forward, the test tyre slides on the wet surface, and the force generated converted to a wet skid resistance value (WDM Limited, 2020).

In the UK, the wet skid resistance of highways is monitored using the Sideway-force Coefficient Routine Investigation Machine (SCRIM machine) and the data presented as a SCRIM Value (SV). The test tyre is mounted at an angle of 20° to the direction of travel. The tyre is a smooth pneumatic tyre of standard hardness and freely rotates under a known load. This measurement is calculated to be average for each continuous 5, 10, 20m section (WDM Limited, 2020). The SCRIM device is the only specified device to measure the skid resistance of trunk roads in the UK.

The skid resistance of airfield pavements is measured using a device with a fixed slip of 15%-17%, the Grip Tester being the most common. The Grip tester is a trailer attached to a vehicle that measures continuously and dynamically the longitudinal skid resistance coefficient of the pavement expressed as a Grip Number (GN) (British Standard, 2000).

Figure 2.16. Findlay Irvine GripTester (Findlay Irvine, 2020)

CAP 683 document published by the Civil Aviation Authority specifies the assessment of runway surface friction characteristics. The document provides guidance to Aerodrome Operators undertaking runway surface friction assessments by describing the key elements of the procedure (Civil Aviation Authority,2010). For a grip tester the document states the minimum friction level to be 0.55. When the surface friction falls below this the aerodrome operator has a duty to report pavement "may be slippery when wet“ to pilots until such times when maintenance improves the frictional values.

It is impossible to directly compare data collected from different measurement devices as measurements are collected according to diverse principles. De Solminihac et al. (2008) found that skid resistance measurements usually exhibit high variability. Dunford (2010) suggests that variability results from different operating practices, including exact test lines on the pavement surface. Dunford (2010) recommends the conversion factor of GN to SC as SC = 0.89 * GN.

In different ways, all measure the force developed on a rubber tyre or slider passing over a wetted road surface and derive a value related to the coefficient of friction and the state of polish of the road surface (DMRB, 2015).

2.9 Runway friction values

Asi (2007) evaluated the skid resistance of different Marshall Asphalt (MA) mixes using the British Pendulum. The average measured skid resistance for MA was in the region of 87 PTV. The addition of slag by 30% increased the average skid resistance to 99. By admission Asi, (2007) conceded that the test specimens were not subjected to simulated trafficking and, therefore, skid numbers are probably unusually high. Despite this, it would not be uncommon for the skid resistance to increase as trafficking wears the excess surface bitumen exposing the microtexture surface, influencing early life skid resistance.

Chu and Fwa, (2019) performed a similar analysis of grooved specimens. Similar to Asi (2007), test specimens were not subjected to simulated trafficking. The study found that grooving increased skid resistance from 87 PTV to 90/94 for non-standard grooving dimensions of 5mm x 4mm x 30mm centre to centre spacing and 10mm x 8mm x 55mm centre to centre spacing, respectively.

Patterson (2012) noted that skid resistance values measured using a Dynatest 6850 Slip Friction Tester for ungrooved asphalt deteriorated significantly with water exposure. The grooved sections for both standard and trapezoidal-shaped maintained consistent frictional values throughout water exposure. Patterson (2012) found that frictional values range as shown in Table 2.0.

Table 2.0. Patterson, (2012) Friction Findings.

	Surface Texture		
Surface Conditions	Ungrooved	Standard Square	Trapezoidal
Dry Surface	0.82~0.94	0.71	0.8
Wet Surface (Light Rain)	0.78~0.91	0.68	0.73
Wet Surface (5mins After Heavy Rain)	0.62~0.91	0.65	0.69
Wet Surface (10mins After Heavy Rain)	0.7~0.91	0.71	0.71

*NOTE the distance for each section differed, Ungrooved = 1500ft, Standard Grooving = 250ft, Trapezoidal = 250ft, friction readings were averaged at 250ft interval.

Patterson (2012) noted that the frictional values noted in Table 2.0 for both groove shapes were comparable, making it almost impossible to distinguish between both based on the frictional values. Data presented by Zuzelo (2014) also suggest comparable frictional values.

Woodward et al. (2016) considered the wear of the frictional characteristic of SMA due to simulated trafficking. The data generally showed that the early life skid resistance declined up to 800 wheel passes. Post 800 wheel passes, skid resistance increased up to approximately 8000 wheel passes, where it continued to decline up to 100,000 wheel passes.

2.10 Tyre Performance

Tyres by design are expected to perform distinct functions depending on their use; however, generally, they all perform the following functions;

- Support the weight of the vehicle
- Provide grip for braking and acceleration
- Maintain steering and directional control
- Act as a shock absorber from irregularities in the road surface (BRIDGESTONE,2021)

There is two type of tyre architecture classified as Radial or Bias tyre due to their material configuration. Figure 2.17 illustrates both tyre profiles. Change from Cross-ply tyres to Radial tyres was brought about due to a tyre burst on the Concorde aircraft piercing the fuel and subsequently causing the aircraft to crash (Lewis, 2010).

Figure 2.17. Radial vs Bias Ply Tyre configuration (Srirangam, 2015)

Both material configurations are designed for different uses and therefore provide specific performance characteristics. Radial tyres consist of cables radiating around the circumference of the tyre crown with material ply forming a belt around the tyre; this enables the sidewalls and the crown of the tyre to function as two independent features of the tyre (Michelin, 2015). The radial architecture enables the sidewalls to be flexible; the footprint of the radial tyre is not as long as the bias tyre. However, the greater width of the crown facilitates grip, offering greater grip at angles when cornering. Figure 2.18 details the contact patch for both tyre architectures.

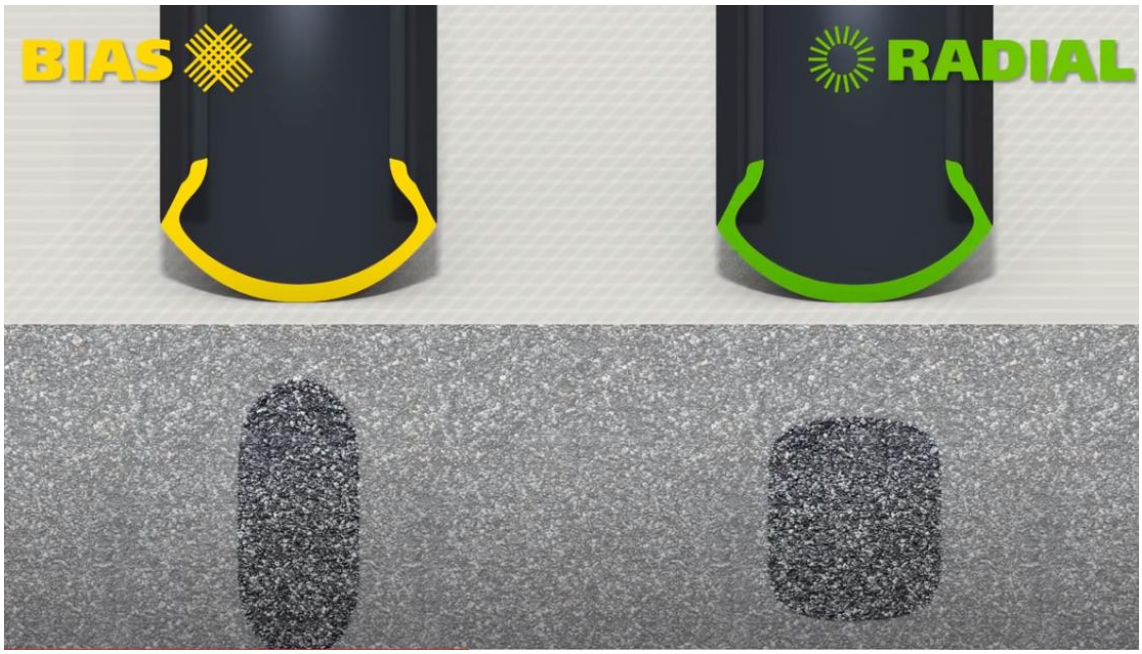

Figure 2.18. Bias Vs Radial tyre contact patch (Michelin, 2015).

Bias tyres consist of diagonally orientated cables of ply laminated diagonally across each other; this makes the tyre less flexible, and the thick cross lamination makes the tyre more sensitive to overheating.

Both the tyre crown and side walls are of the same manufacture; therefore, they each show similar mechanical characteristics. The rigid structure of the bias carcass enables the bias tyre to withstand heavier loads; however, the stiffness transmits the irregularities through the vehicle structure. The flexibility of the radial structure facilitates comfort by cushioning the effect of irregularities of the pavement surface. The consequence of design can affect the performance of tyres as seen in the bias tyres where at high speed, the profile of the tyre

becomes deformed and therefore influences the vehicle stability whereas radial tyres remain stable.

The architecture influences the contact interface pressure, and radial structure facilitates an even distribution of tyre load; therefore, the tyre wears evenly, whereas bias tyre contact pressure is concentrated centrally within the circumferential axis of the tyre; therefore, the tyre is prone to the greatest wear at the crown centre. Figure 2.19 illustrates contact pressure for each tyre architecture.

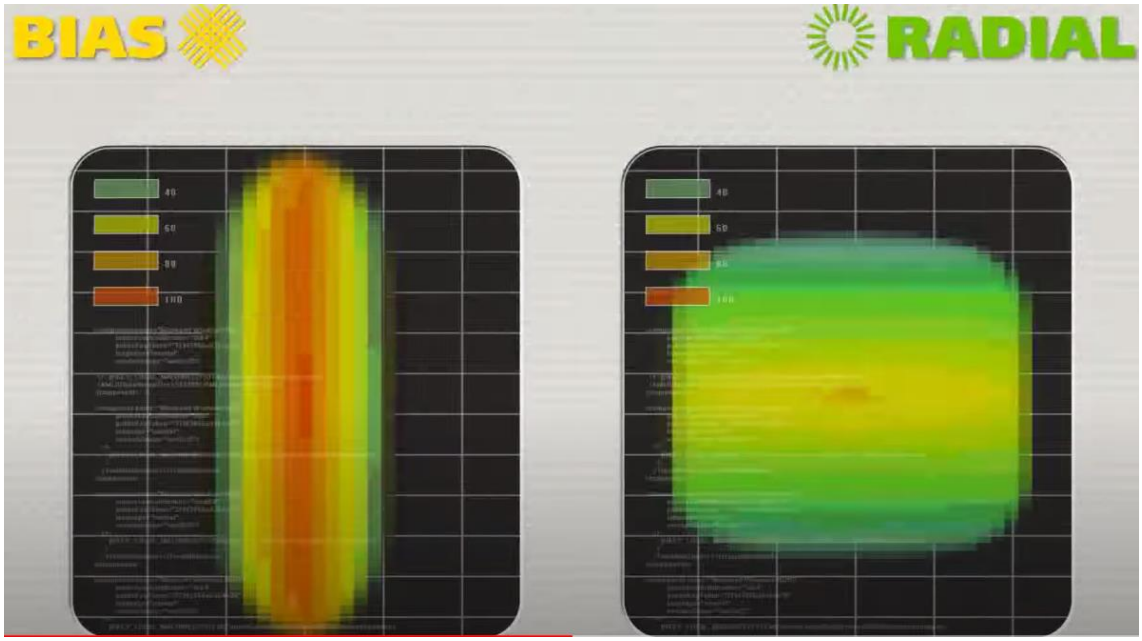

Figure 2.19. Tyre Contact Pressure for Bias and Radial tyres (Michelin, 2015).

Based on the tyre configuration Bias tyres are suitable for;

- Vehicles travelling at moderate speeds with small to medium size engines
- Vehicle with flexible chassis
- Heavy or heavily loaded bikes

Radial structure suitable for:

- Powerful performance vehicles with rigid chassis
- Sporting vehicle

In aviation radial tyres are typical for that used on aircraft. The GripTester utilises an ASTM 1844 friction measuring tyre which is of bias construction.

2.10.1 Tyre Contact Patch

An aircraft or a vehicle interacts with a pavement surface through its contact patch. The tyre transfers its loading to the pavement and subsequently through the base layers. The contact patch is complex due to various factors which influence its interaction at the interface, such as surface texture at differing scales, tyre properties and vehicle dynamics.

Woodward et al., 2014 considered the influence of tyre inflation pressure on tyre contact area, length and width. The contact area and length behave in a parabolic manner, whereas contact width behaves linearly, as shown in Figure 2.20.

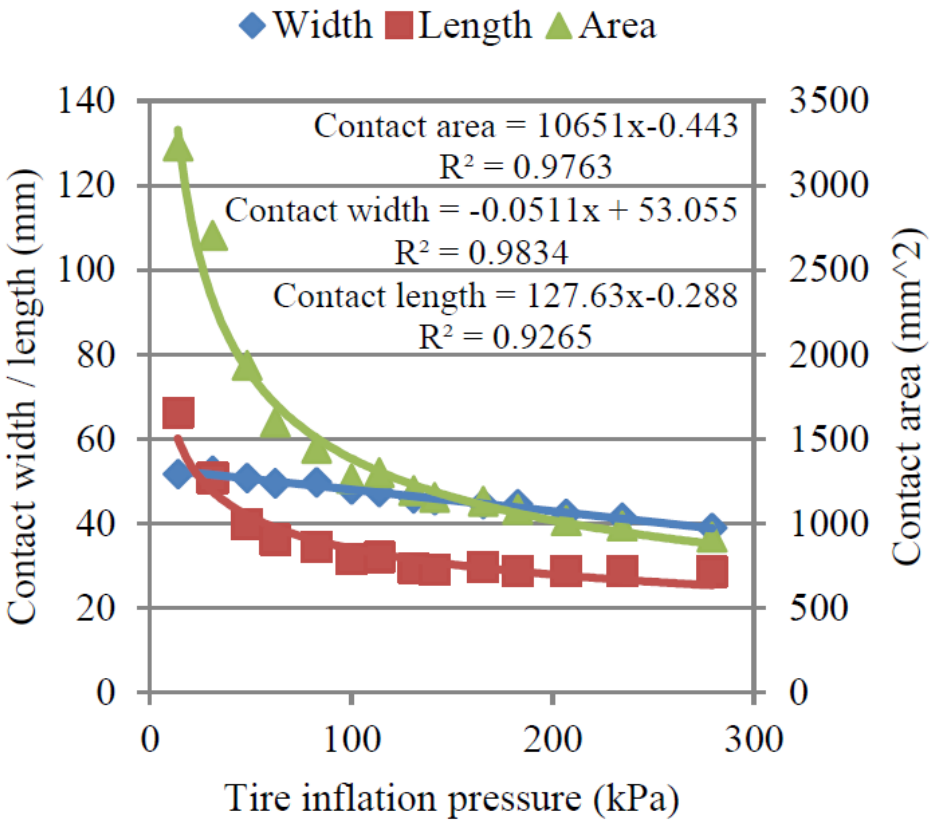

Figure 2.20. The influence of tyre inflation pressure on tyre contact width, length and area (Woodward et al, 2014).

Millar et al., (2011) showed that the engineering performance of a highway surface is not related to the contact area but how the contact pressure is distributed within the contact patch. It was found that not only does the contact area vary with tyre inflation pressure, but there is also a significant variation in contact pressure distribution within the contact patch. The findings raise the question if the term contact area refers to actual contact area or a series of 'contact points' where the actual contact area is much less than stated due to the surface texture. The study raised the need for further consideration of the distribution of contact pressure within the contact patch

2.10.2 Comparison of Aircraft and Passenger Tyres

Whilst aircraft and road vehicle tyres play similar roles in supporting the weight of the road vehicle/aircraft, and each operates under different environmental conditions, which is reflected in their design. The greatest difference between aircraft tyres vs regular vehicle tyres is that aircraft tyres have to resist greater loads when the aircraft lands and takes off (McCarty and Tanner,1983) (Aviation Hunt,2020). For road vehicle tyres, the environmental conditions remain relatively constant and driver dependent, whereas aircraft tyres are exposed to a cyclic exposure to varying temperatures and pressures (Aviation Pros, 2001).

The most critical operation of an aircraft tyre is during landing, where the tyre is forced to match the speed of the aircraft almost instantly. The impact causes rapid flexing where the grooved tread widens and retract due to the tyre absorbing the payload from the aircraft (Georgia and Mayeau,1963). In addition, upon touchdown, tyre surface temperature rises instantly so much that the critical temperature of the rubber compound is exceeded as characterised by a puff of smoke.

Aircraft tyres are manufactured to a higher specification than road vehicle tyres. Tread patterns on-road vehicle tyres are more complex than aircraft tyres. Aircraft tyres are treaded with simple grooves as aircraft perform simple manoeuvres compared to vehicle tyres. It could be argued that this also benefits the aerodynamics of aircraft tyres as the complex treads would provide greater wind resistance than that of simple grooves.

2.10.3 Aircraft Tyre Impact

Experimental data relating to tyre impact in the open literature is rare (Neeves et al., 2010). Aircraft landing gears and aircraft tyres are subjected to impact conditions due to variations in the aircraft sink speed, angle of attack and aircraft mass. The landing gear's job is to absorb the impact energy upon touchdown to minimise any structural damage to the aircraft (Batterbee et al., 2007). Upon touchdown, the aircraft tyres sustain the mass of the aircraft immediately followed by the aloe struts (shock absorbers).

2.11 Tyre Interface Pressure

Douglas (2009) reviewed tyre/surface contact stress measurement research. This identified three main systems based on strain gauge technologies.

- The first was the Stress-In-Motion (SIM) system developed in South Africa. This system was used in many studies including de Beer (1997a), de Beer et al (1997b), Weissman (1999), Machemehl et al (2005), Luo and Prozzi (2005) Wang and Machemehl (2006) and de Beer (2008).
- A second system was developed in Northern Ireland and used in studies by Liu (1992), Siegfried (1998), Woodside et al. (1999), Douglas et al. (2000, 2003).
- A third system was developed in New Zealand based on the Irish system and experiences from using the de Beer SIM system (Douglas, 2009b).

The commonality amongst the research is that they were designed to consider truck tyres and, to a lesser extent, passenger car tyres. The interface was a tyre interacting with instrumented metal pins. The spatial resolution of the data was dependent on the pin spacing. The data collected related to how the tyre and the tread elements interface the metal pins and not the texture of an asphalt surface.

The use of strain gauge pins limited the collection of data; therefore, alternative approaches were adopted to further this area of research. The potential of pressure mapping was first reported ten years ago by Backx (2007), Dunford (2013) and Hamlet et al. (2015) through the use of pressure-sensitive film. This method offered greater insight than the strain pins; however, it required post-processing to produce useable data.

Pressure mapping using sensors was reported by Conville (2010), Millar et al., 2011. Friel (2013), and Woodward et al. (2016). Pressure mapping using sensors enabled the collection and processing of data in real-time. Unlike pressure film, which can only be used as single use, utilising sensors could be reused many times.

2.11.1 Ulster Tyre Road Surface Interface

The Ulster Tyre Road Surface Interface (UTRSI) method was developed in Ulster University laboratory and used to measure actual road/tyre interfaces. The method consists of three elements:

- Vertical Pressure Mapping,
- A Modified Wheel Tracking Device fitted with an ASTM Friction Tyre,
- Asphalt Test Specimens subjected to simulated trafficking.

Woodward et al., 2020 highlighted the potential to compare interface properties of asphalt subjected to simulated trafficking enabling change in interface conditions such as contact area or pressure frequency and pressure distribution to be evaluated. The research highlighted the complexity of an asphalt surface, and therefore considering an idealised surface simplifies the complexity and therefore facilitates understanding at the interface.

2.12 Tyre Temperature

The performance of tyres is influenced by tyre temperature. In motorsports, tyre temperature is of critical importance as it is considered to influence the grip level to the pavement surface (Your Data-Driven, 2020). The grip is influenced by temperature, and there is a balance to be struck in terms of maximum grip levels for the least tyre degradation. As temperature influences grip in motorsport, the tyre is sacrificial in that the tyres are pushed to their maximum to maintain the best time. Therefore, monitoring tyre temperature enables race teams to make informed decisions on the racetrack and gain an advantage over the vehicle's performance.

In aviation, tyre temperature is not monitored for this purpose; however, tyre temperature contributes to tyre degradation and particularly tyre temperature is of importance as extreme temperature contributes to rubber deposition during touchdown (Wang, 2019).

Temperature influences the stiffness of the tyre (Harsh and Shyrokau, 2019), (Kelly and Sharp, 2012) which further influences the tyre's grip by allowing the tyre greater flexibility to envelope the pavement surface. Both air temperature and pavement temperature will contribute to tyre surface temperature. Tyre speed contributes to tyre surface temperature as the frequency of interaction between the pavement and surface is directly influenced by the number of interactions with the pavement texture. As aircraft tyres go through varying cyclic conditions and perform manoeuvres in short and sharp time frames, it is reasonable

to consider that the aircraft tyre surface temperature is highly transient and therefore does not have sufficient time to reach thermodynamic equilibrium.

Temperature measurement of tyres is complex as the temperature under investigation can either be the bulk temperature, the temperature of the tyre carcass relating to the internal temperature of the rubber, or the surface temperature; relating to the tread temperature. The devices considered in this review relate to surface temperature. Conant et al. (1970) stated that as tyre speed increases, the rate of heat generation in the tyre increases, which acts to cause a rise in tyre temperature. However, the accompanying increases in airflow around the tyre cause a decrease in tyre surface temperature. Conant et al., (1970) conclude that the relationship between bulk temperature and surface temperature is highly speed dependent.

Conant et al., (1970) concluded that radial tyres were cooler on the surface than bias tyres and are less sensitive to temperature changes due to speed, inflation pressure and load. Anderson, (1996) supports this conclusion suggesting Bias tyres are adversely affected by changes in load and speed; however, he recommended further work to quantify the temperature profile distinction.

2.12.1 Tyre Impact Temperature

Similar to tyre impact data, references to tyre impact temperature data is rare in the literature. Aircraft tyres generate heat during landing, taxiing and take off due to the flexure of the rubber. The poor thermal conductivity of rubber provides a means for build-up of heat, more so greater heat built up than can be dissipated, particularly for aircraft tyres (Hunter et al., 1987).

Aircraft tyres, upon touchdown, initially skid due to a greater difference between the tangential velocity of the tyre radius and the horizontal landing speed at touchdown (Alroqi et al., 2017) as the tyre is required to match the speed of the aircraft instantly. Pavements cannot provide infinite friction levels, and therefore, as friction is limited, slippage is inevitable. Slippage results in the tyre tread temperature rising immediately within 0.1 seconds. The increase exceeds the critical temperature of the rubber, which is in the region of 200°C (Alroqi et al., 2017); therefore, rubber at the tyre surface is incinerated/vaporised and lost due to deposition by abrasion of the pavement surface.

Alroqi et al. (2017) aimed to eliminate the vaporising of the rubber upon touchdown by reducing the difference between the horizontal landing speed and the tangential difference

of the tyre by introducing a wind turbine to rotate the tyre prior tyre touchdown. The study, whilst appreciating high-temperature occurrences, did not detail temperature Figures nor investigate specific parameters which would contribute to this temperature.

2.12.2 Heat Generation in Aircraft Tyres

Heat generation in aircraft tyres is presented in Goodyear, (2020) manufacturer's guidance and operation manuals. As aircraft tyres operate in extremities in terms of speed and load, heat generation has a greater detrimental effect on the tyre. Figure 2.21 illustrates the internal heat generation in an aircraft tyre.

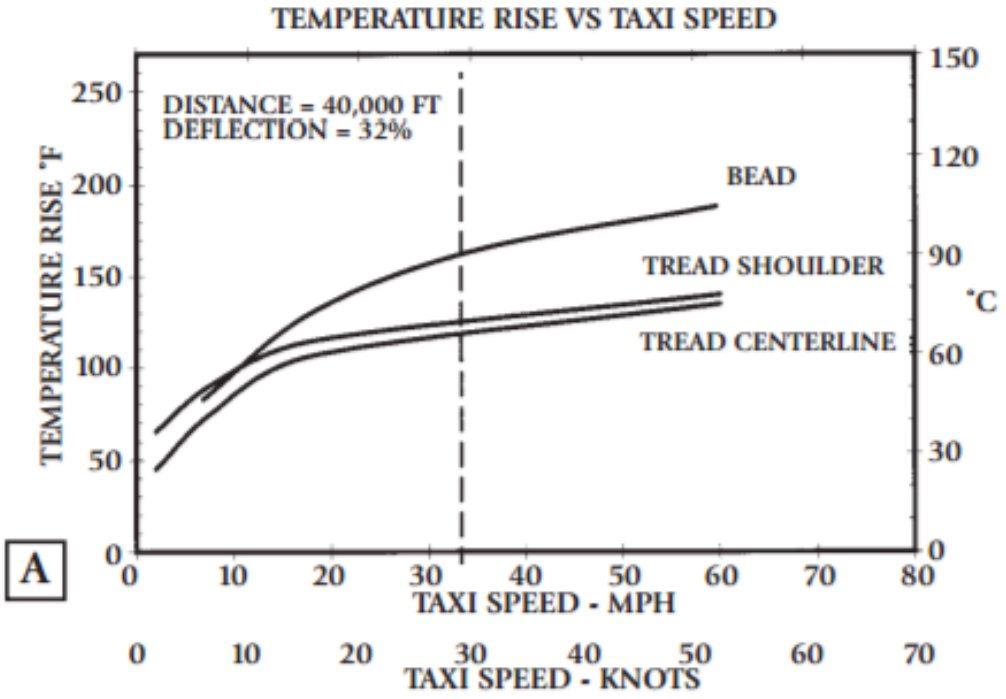

Figure 2.21. Heat generation in an aircraft tyre; Taxi Speed Vs Temperature Rise (Goodyear, 2020)

Figure 2.21 illustrates the heat generation in an aircraft tyre with three thermistors placed inside at the bead, tread shoulder and tread centreline. The general relationship notes that at lower speeds, there is curvature with temperature rise, demonstrating the temperature stabilises / slowly increases with taxi speed. The dotted line represents the maximum

recommended taxi speed for the tyre considered. The relationship between speed and temperature shows that the faster the aircraft travels over a given distance, the hotter the tyres become (Goodyear, 2020). At the recommended speed, the internal tread temperature has risen to 65°C.

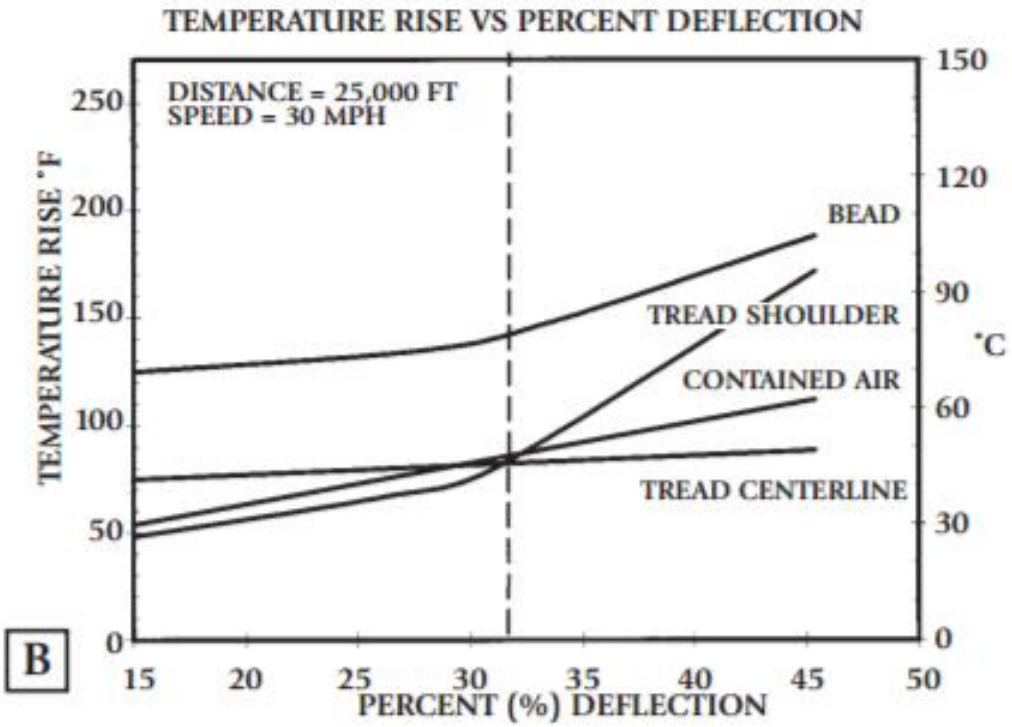

Figure 2.22. Heat generation in an aircraft tyre; Percentage Vs Temperature Rise (Goodyear, 2020).

Figure 2.22 illustrates heat generation in an aircraft tyre with percentage tyre deflection. The dotted line represents the maximum deflection the aircraft tyre is designed to. The data shows that the temperature rises gently within the recommended limit of 32% deflection. Below 32% represents the over inflation, with greater than 32% representing under inflation. The data shows the critical nature of 32% with heat generation for the bead rising rapidly for deflection greater than 32%.

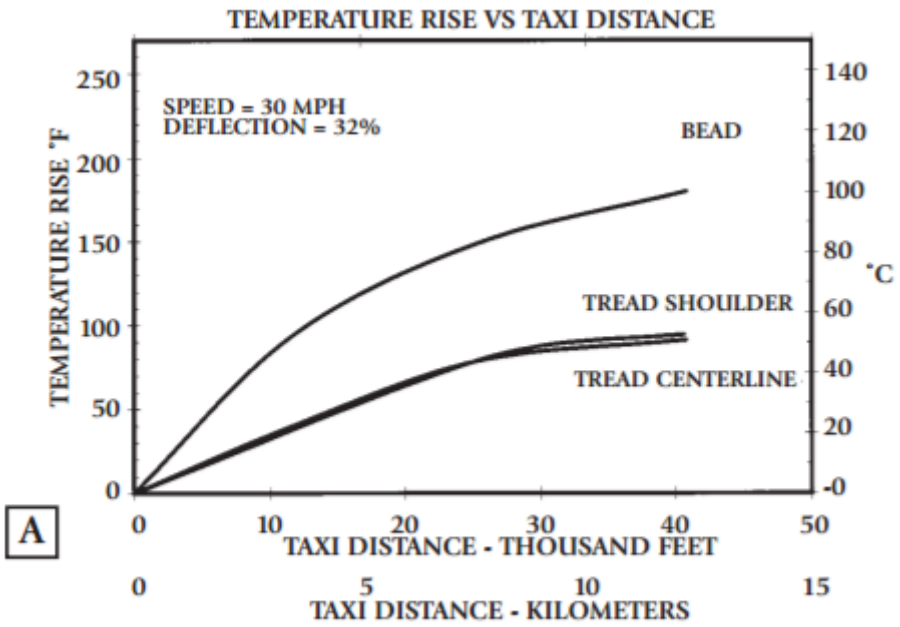

Figure 2.23. Heat generation in an aircraft tyre; Taxi Distance Vs Temperature Rise, 30mph – 32% deflection (Goodyear, (2020).

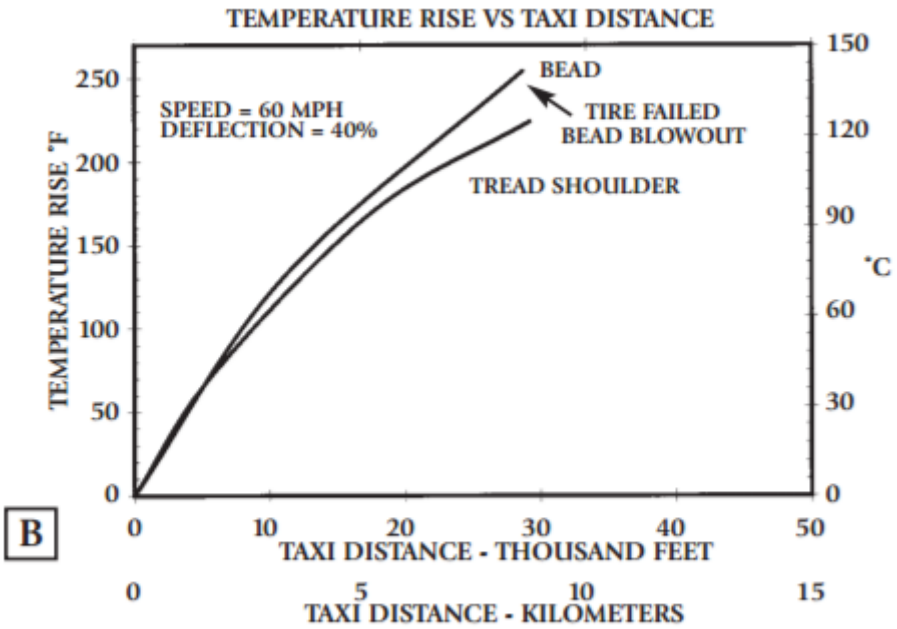

Figure 2.24. Heat generation in an aircraft tyre; Taxi Distance Vs Temperature Rise , 60mph – 40% deflection (Goodyear, 2020).

Figures 2.23 to 2.24 illustrate heat generation in aircraft tyres for taxi distance at 30mph and 60mph respectively. The data illustrates a gradual increase in heat generation on the tread for the slower speed within the operational deflection of the tyre. Tread internal temperature had risen to 50°C for a distance of 15km. As the tyre reaches extreme operating conditions, Figure 2.24 shows the detrimental effect of heat generation with a linear increase in heat generation, causing the tyre to fail at 144°C, having only travelled 9 km.

2.12.3 Rubber Deposition

Upon aircraft touchdown, when the rear landing gears make contact with the pavement surface, rubber is deposited from the tyre to the pavement due to heat and abrasion during the spin-up process of the tyres (Simpson, 1989). At critical rubber temperature, in the region of 200°C, the rubber bonds in the tread break and therefore are easily worn by abrasion forces. In addition to this, under slippage, rubber is also lost to evaporation, which constitutes a third of the total lost rubber from the tyre (Alroqi et al., 2017).

Rubber accumulation is detrimental to the available friction co-efficient as it coats the micro-texture and occludes the macrotexture as rubber build-up increases. The rubber coating alters the geometry of the micro-texture surface by changing sharp asperities to rounded spheres. This change in geometry inhibits the hydraulic pressure generation necessary to penetrate the film of water of wet pavement. Furthermore, this also affects adhesion in dry pavements Graul and Lenke (1985).

Whilst studies focus on removing rubber deposition; few exist as to the theory of deposition in the literature. Rubber deposition is a function of the number of aircraft landings. As the pavement characteristics is an influencing parameter for rubber deposition, Yager (1969) found that transversely grooved pavements do not significantly increase rubber deposition. Simpson (1989) also supports a similar view citing that grooved pavements accumulate less rubber for a given amount of usage than ungrooved pavements.

The link between aircraft impact temperature and rubber deposition has been established. However, as the temperature is a significant contributing factor to rubber deposition, there is no experimental data available in the literature regarding the variables; speed, load, texture, that contribute to impact temperature.

2.12.4 Tyre Temperature Measurement

Various methods of temperature measurement exist, such as infrared measurement and thermocouples, each operating on different principles to obtain temperature. Both contact and non-contact methods are used. This review focuses on non-contact methods.

The infrared temperature measurement system determines temperature from the emitted energy from objects. Different objects emit infrared energy depending on their emissivity. Emissivity varies with temperature and spectral response (wavelength); each material will absorb and reflect different percentages of energy. Darker surfaces such as rubber have an emissivity of 95%, whereas metal surfaces such as polished stainless steel have an emissivity of 14%. Figure 2.25 details the infrared temperature measurement system.

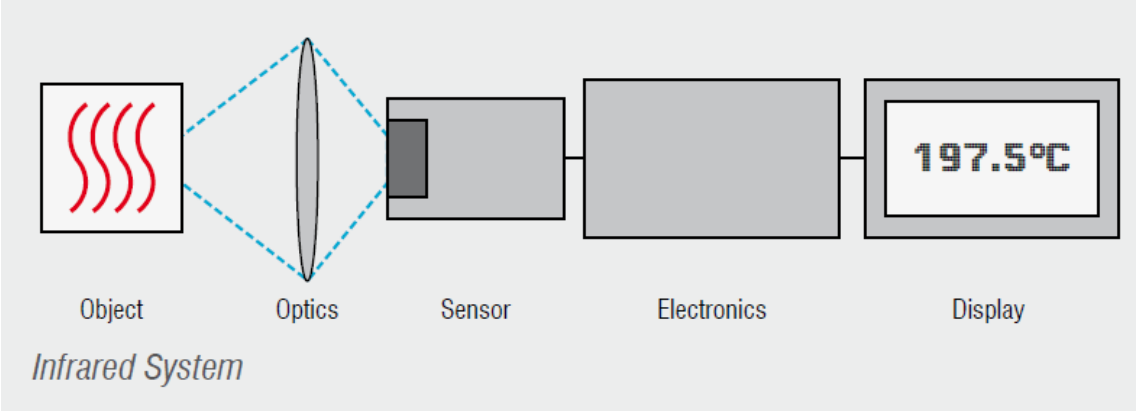

Figure 2.25. Infrared Temperature Measurement System (Flir, 2020).

Infrared temperature measurement can be conducted either through thermal imaging or a pyrometer. Both methods work according to the same principle; they detect infrared radiation and translate it into a temperature reading (Flir, 2020). However, one method may be more appropriate than the other, depending on the application. A pyrometer consists of a spot measurement and provides a single temperature measurement, whereas a thermal imager provides an image with a colour ramp illustrating the temperature difference through colour. The pyrometer consists of a single-pixel reading. The thermal image will consist of many thousands of pixels, with each recording a spot measurement, therefore, detailing a greater quantity of data. Flir, 2020 notes that with a spot measurement, the operator can easily miss crucial information. Figure 2.26 illustrates what both devices 'see'.

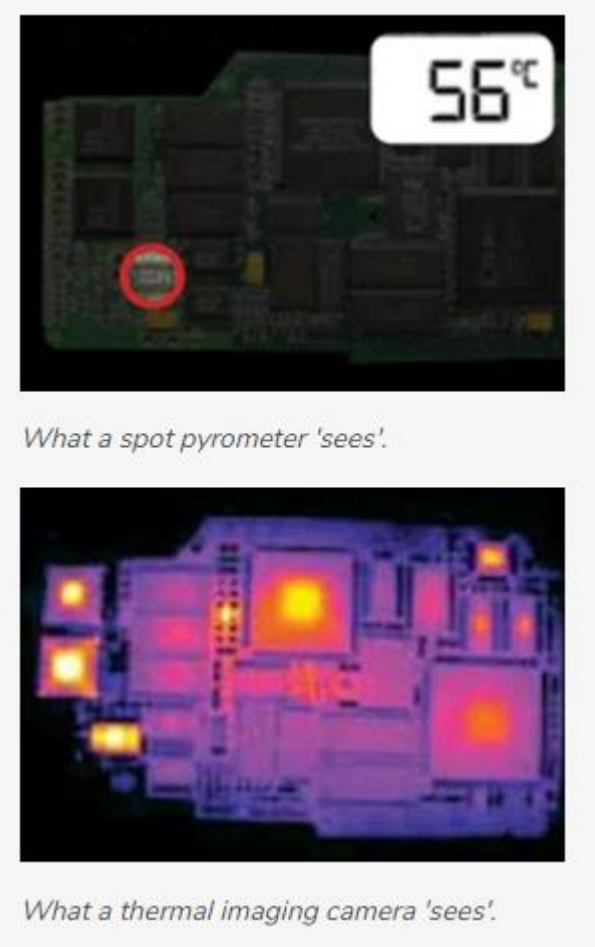

Figure 2.26. The field of view from both methods of measurement (Flir, 2020).

Various factors influence temperature measurement and different temperature measurement devices set up similarly may record different temperatures. Airflow is of interest when measuring tyre surface temperature and is of further significance with tyre speed. Due to the convection of heat at the tyre surface, the air around the surface is of a similar temperature. As speed increases, the flow of air increase surrounding the tyre and therefore, airflow is greater. This flow replaces the surrounding air with new air which has not yet adapted to the surface temperature of the tyre. This airflow affects the heat exchange and therefore increases the greater temperature difference between the surface of the measuring object and the ambient temperature conditions. This difference, therefore, influences the measured temperature (Testo, 2022).

2.13 Critical Review of Literature

The literature review has considered the aspects of tyre/surface interaction. It has highlighted the following areas which need further consideration.

The focus of this research is runway surfaces, however majority of the literature considered related to road pavements due to lack of research relating to runway pavements. Given the similarities between both pavements it is considered literature for roads is relatable to runway pavements.

Marshall Asphalt dates to the second world war. Due to the poor structural performance of asphalt used for airfield applications at that time, the design focus of Marshall Asphalt was strength to withstand increasing wheel loads from aircraft. Therefore, there was no focus on how the material wore. This is still the case, and there is no method to determine how the surface of Marshall Asphalt wears.

Asphalt grooving is a method where grooves are sawn laterally into asphalt pavements. Research has considered the extent to which asphalt grooving improves wet weather skid resistance. However, it omits to consider the performance of asphalt grooving with trafficking and further omits to consider the performance of alternative grooving dimensions. There is no method to determine how grooved Marshall asphalt wears.

The tyre surface interface has been previously considered between an asphalt surface and a vehicle tyre; with technological developments, the methodology has been improved from strain gauge instruments to digital technology. To date, there has been no tyre/pavement research relating to the tyre interface between a tyre and a grooved surface/ grooved asphalt surface.

The British Pendulum BS EN 13036 method is used within the asphalt industry to assess the skid resistance performance of asphalt surfaces. A consistent omission relating to grooved surfaces from research suggests the method has not been considered entirely. There is an ambiguity within the standard relating to the method adaption for grooved surfaces, and there is no diagram to explain this adaption.

Rubber accumulation at the touchdown zone of a runway surface is detrimental to the available pavement friction as it coats the surface of the aggregate micro-texture. The deposition of rubber occurs due to impact temperature when the tyre touches down on the pavement surface. Alroqi et al., 2017 found that the heat generated at the tyre interface

could be reduced by pre-spinning the tyre before touchdown. The study established a link between impact temperature and rubber deposition, and it did not consider how and to what magnitude aircraft parameters such as speed and load conditions contributes to tyre impact temperature.

CHAPTER 3.

RESEARCH METHODS

3.1 Introduction

This chapter considers the research methods used in this thesis. They have been divided into the following:

- ASTM friction tyre / test surface interface using pressure mapping using the Ulster Tyre Road Surface Interface (UTRSI) method.
- Accelerated wear of grooved Marshall Asphalt using the Road Test Machine.
- Determination of 3D areal parameters using Zephyr and Mountains Map software.
- Use of paint removal to investigate interface contact area.
- Measurement of skid resistance using the British Pendulum Tester.
- Tyre impact temperature using the Ulster Loaded Tyre Road Assimilator (ULTRA).

Full details of how these methods were used are given in subsequent chapters.

3.2 Apparatus

The Ulster Tyre Road Surface Interface (UTRSI) test method (Woodward, Millar, Tierney and Ferguson, 2020) was used to investigate the ASTM friction tyre / test surface interface. The UTRSI method was developed over a period of 10 years at Ulster University to address the knowledge gap relating to how a tyre interacts with a surface.

Although the emphasis in development of the UTRSI method was friction, the data can be used to better understand other interface properties relating to both the surface and the tyre. With respect to this thesis the UTRSI method was used to investigate the ASTM friction tyre / grooved surface interface.

The UTRSI method has four main elements i.e. vertical pressure mapping, a modified small wheel tracking device fitted with an ASTM friction tyre and test specimens subjected to slow speed high stress accelerated trafficking that allow changes in time to be assessed. The test tyre used for all investigations in this thesis was an ASTM 1844 friction measuring tyre typically fitted to a GripTester to test runways. The ASTM tyre was unworn.

In the UTRSI method, the tyre is fitted to a modified Wessex wheel tracking device adapted to facilitate tyre/surface interface research. The test equipment is shown in Figure 3.0. The standard vertical load on the ASTM friction tyre when fitted to a GripTester is 20 kg or 0.19 kN (ASTM, 2015). This was achieved by hanging 0.76 kg on the end of the lever arm of the

modified Wessex machine. This was confirmed by measuring with a load cell. All testing was carried out with the recommended tyre inflation pressure of 20PSI.

The test specimen is located on a table that can be moved under the loaded tyre. A flexible XSENSOR pressure mapping system is placed between the tyre and test specimen to measure the distribution of vertical (z-axis) contact pressure within the contact patch. The spatial resolution of the pressure pad cell size is 2.54mm x 2.54mm. Each cell records a pressure value for an area of 6.45mm^2.

The pressure pad is used in conjunction with XSENSOR 3 Pro software to capture the data. Two types of measurement are possible. The first is a simple static measurement of vertical pressure. The second type of measurement involves pushing the test specimen slowly under the tyre whilst recording data frames. As the tyre tracks over the grooved surface, the sensors capture the change in vertical contact pressure.

Figure 3.0 shows the test set up with the ASTM friction measuring tyre resting on the flexible XSENSOR pressure pad. The computer screen shows the contact interface data just recorded. In this example, 250 individual frames have been merged to form the composite image shown on the computer screen as the grooved test surface was pushed slowly underneath the test tyre.

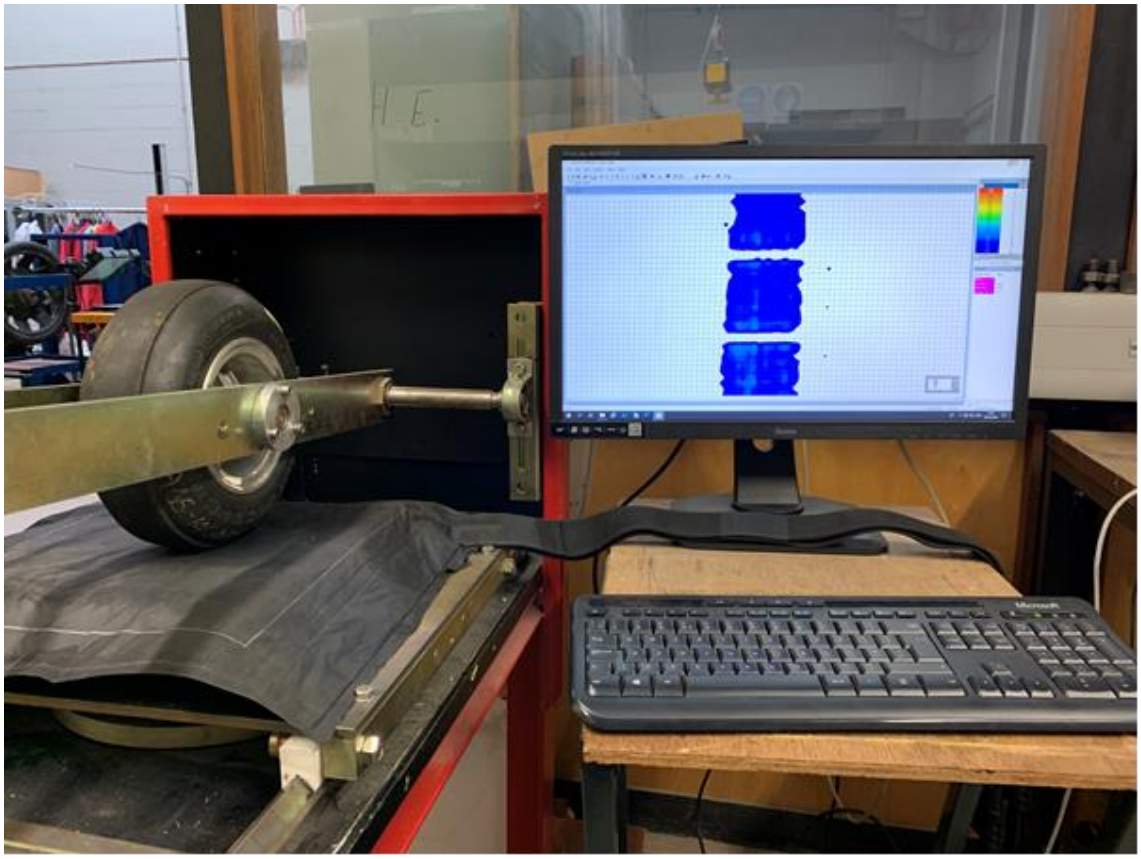

Figure 3.0. Flexible XENSOR pressure pad set up for UTRSI testing.

3.3 Accelerated wear of grooved Marshall Asphalt using the RTM

The Road Test Machine (RTM) was used to subject Marshall Asphalt test surfaces to simulated trafficking in accordance with Appendix H of TRL 176 (Nichols, 1999). The RTM is shown in Figure 3.1. Figure 3.2 shows one of the Marshall Asphalt (MA) test specimens located in the RTM.

The RTM consists of a circular table that can accommodate up to ten slab specimens of 305mm x 305mm x 50mm. The table rotates at a single speed of 10rpm, which equates to 1.1m/s. Two tyres are positioned vertically above the rotating table. Tyres are 195/70R14. Each tyre applies a static load of 5 kN onto the surface of the test specimen. As the table rotates, the tyres track transversely across test specimens.

The RTM is housed in an environmental chamber with a temperature of 10º ± 2 °C. The test specimens were subjected to slow speed, high stress accelerated trafficking. Trafficking was determined as the number of wheel passes the test specimens were subjected to.

Figure 3.1. The Road Test Machine.

Figure 3.2. Grooved Marshall Asphalt Test Specimen in the RTM.

Prior to the start of RTM testing, each MA test surface was measured for wet skid resistance using the British Pendulum Tester (BPT). The surface was photographed for 3D modelling and its interface with an ASTM friction tyre measured using the merged frames version of the UTRSI method.

RTM testing was stopped at 200, 400, 800, 1500, 3,000, 6,000, 10,000, 30,000, 50,000 and 75,000 wheel passes to repeat these test methods to determine how each MA test surface had responded to simulated trafficking. Trafficking intervals were based on a visual observation of the test surfacing during simulated trafficking.

3.4 Determination of 3D areal parameters using Zephyr and Mountains Map software

The UU 3D Test method (Woodward, et al., 2017) was used to determine a range of 2D and 3D areal parameters for the test surfaces. The 3D models were created using Close Range Photogrammetry (CRP). The photographs were captured using a Canon EOS 5D fitted with a 70 mm lens. LED lighting was used.

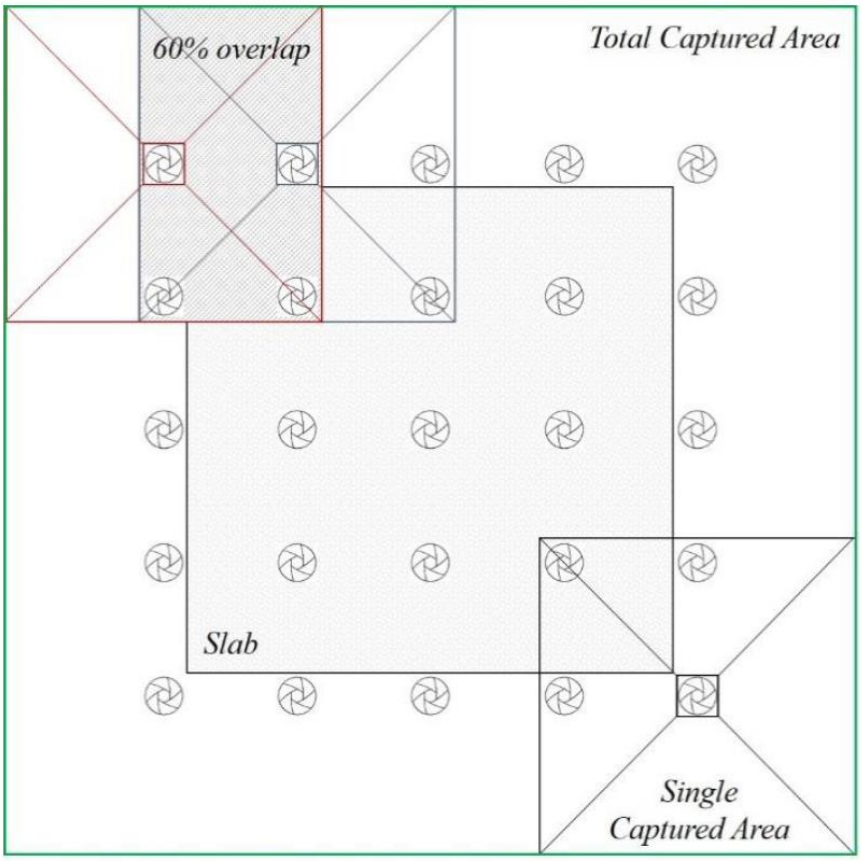

Figure 3.3. Capturing images over lapping technique (Hamilton, 2016).

CRP involves taking a series of images of the test surface under consideration. The software used was Zephyr Pro by the Italian company 3Dflow. The process relies upon images that have at least 60% forward overlap and at least 30% side overlap as shown in Figure 3.3. The process of creating a 3D model using photographs involved four key stages;

- Importing Images: Utilising Zephyrs 'Image Quality Index' function enables images to be ranked according to the image quality. The Image Quality Index grades the imported image based on its quality. A high scoring image does not necessarily regard the image as a good quality image; however, low scoring images were discarded from the model.

- Creation of point Clouds: Two-point clouds are created, a Sparse Point Cloud and Dense Point Cloud respectively.

- Model Orientation and Scaling: The software cannot automatically recognise the area of interest and must be manually orientated. Orientation involved defining the up vector manually by using the triangle method. Scaling of the model involved selecting at least two Control Points from the steel ruler included in the photographs. This allows the 3D model to be scaled in millimetres.

- Exporting the Model: The Dense Point Cloud is exported in txt format for analysis in Digital Surf MountainsMap software.

The Zephyr txt file was imported into Digital Surf MountainsMap Software V 7.4 for analysis. Full details are given in later chapters and workflows included as Numbered Appendices that explain how the 3D models were analysed.

3.5 Use of paint removal to investigate interface contact area

Water-based pink paint was used to investigate the contact interface between the British Pendulum and test surfaces. The technique quantified contact by determining the amount of paint that was removed after a pendulum swing. The contact area i.e., area of paint removal was quantified using Image Pro image analysis software.

A ruler was included in each photograph to scale the image. Image Pro quantified contact area based on differences in colour. Figure 3.4 illustrates how the software determined contact area based on colour differentiation.

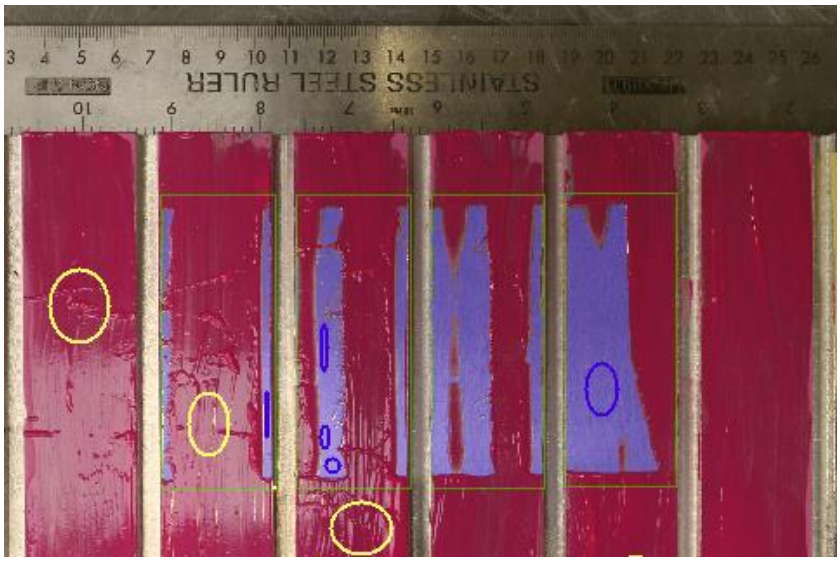

Figure 3.4. Image pro quantification of interface contact based on colour differentiation.

Figure 3.4 shows the area of interest. The image shows the footprint or contact patch of the BPT highlighted in green within each rib. The software quantified contact area by distinguishing colour difference within the image. The yellow ellipsoids were used to programme the software to recognise the pink paint and the blue ellipsoids were used to programme the software to recognise the silver aluminium surface. Based on these two colour differences the software could distinguish the colour difference and determine contact area by quantifying the area of aluminium surface as highlighted in purple/blue.

3.6 Measurement of skid resistance using the British Pendulum Tester

Skid resistance was carried out in accordance with BS EN 13036-4:2011. The equipment is shown in Figure 3.5. A 76.2 mm wide slider and sliding length of 126 mm was used. Room temperature during testing was maintained at 20° C +/- 2° C. In Figure 3.5 pink paint has been added to the test surface to determine the pendulum / test surface contact area.

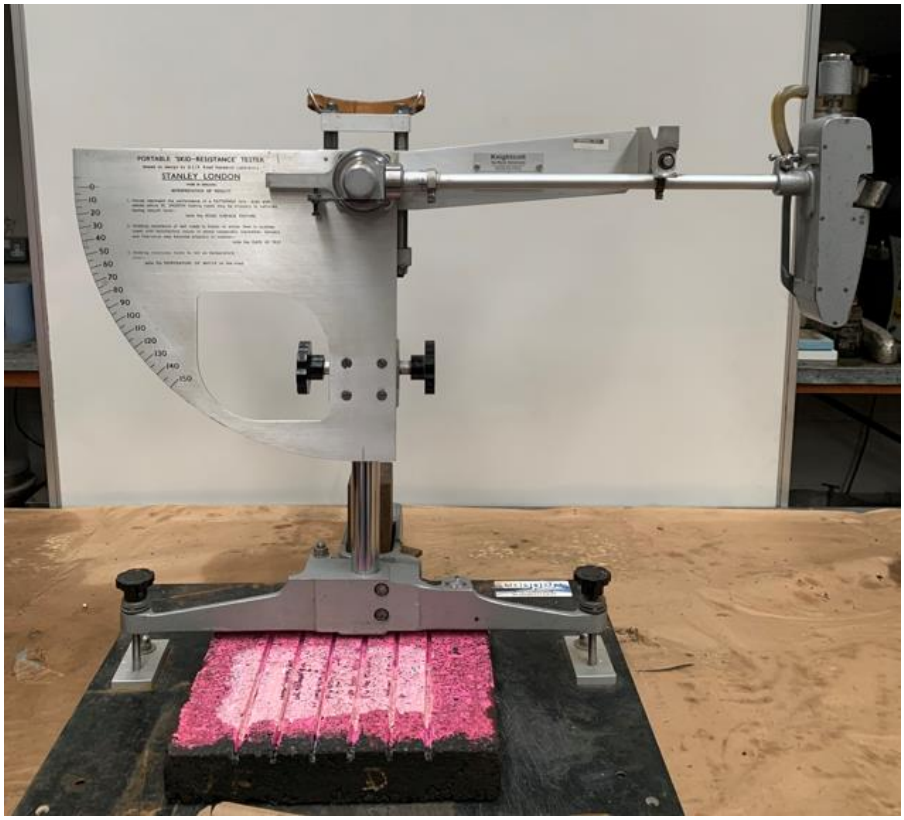

Figure 3.5. The British Pendulum Tester.

Pendulum testing was performed at two angles i.e. according to the standard as well as an addition angle of interaction. The standard method as set out in BS EN 13036 states for surfaces with a regular pattern such as grooves tests should be made with the slider operating at an angle of approximately 80° to the grooves. This statement is open to interpretation as considered in sub section 2.7.1. The pendulum testing angle is demonstrated in Figure 3.6.

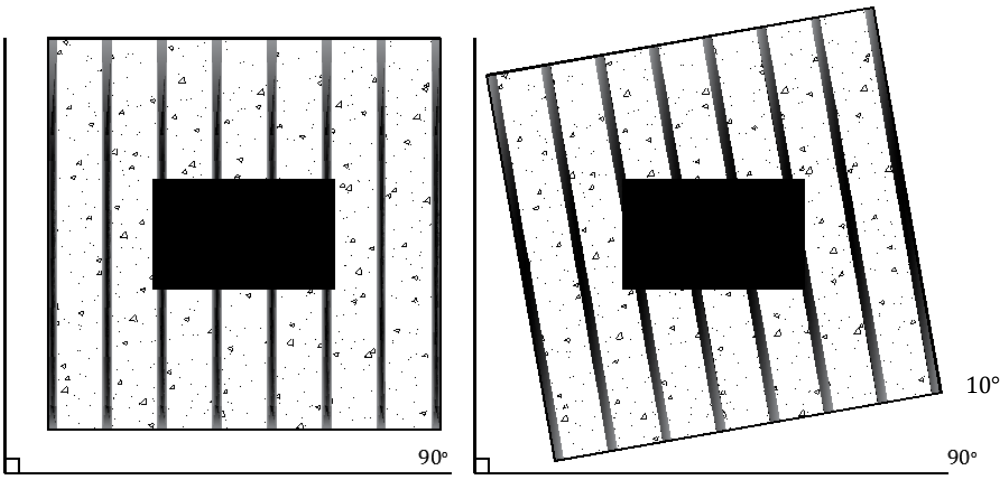

Figure 3.6. Plan view Schematic of the British Pendulum rubber slider interacting with Grooved Marshall Asphalt test specimen at 90° and 10°.

3.7 Tyre impact temperature using the ULTRA

The Ulster Loaded Tyre Road Assimilator (ULTRA) was used to simulate a tyre dropping onto a moving surface. The ULTRA is shown in Figure 3.7.

Figure 3.7. The Ulster Loaded Tyre Road Assimilator.

The ULTRA consists of a steel drum which can rotate to a maximum of 300 revolutions per minute (rpm) or equivalent to 64.3 km/h. A test surface can be fixed to the interior surface of the drum. A loading carriage is mounted at 90° to the steel drum. This holds the ASTM friction measuring tyre that is fitted to the GripTester. The tyre is free to roll on the internal surface of the ULTRA drum. . During a test, the drum was brought to a specified rotation speed and the tyre dropped onto the rolling surface. Two devices were used to measure the tyre surface temperature. The devices are shown in Figure 3.8. A Texsense INF (V/T) 150 ° C uses a data logger to record voltage which is converted to temperature. A Micro-Epilson thermoIMAGER 400 was used to video the surface temperature of the tyre.

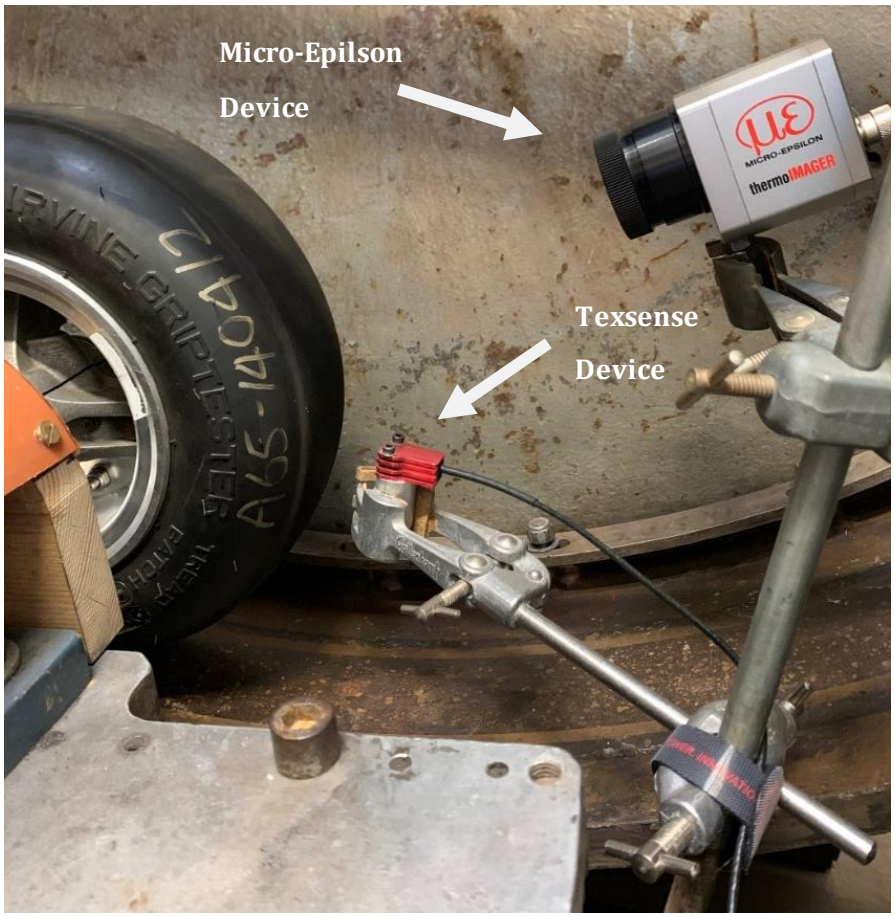

Figure 3.8. Impact temperature measurement equipment.

CHAPTER 4.

TEST SURFACES

4.1 Introduction

This chapter considers different combinations of rib width, groove width and groove depth from a theoretical approach. This has produced a series of look-up tables and an Excel rib / groove calculator. These can be used to obtain a range of parameters such as number of ribs per linear meter, rib area and groove volume per square meter. The second part of this chapter considers the preparation of test surfaces that were investigated and the reasons for their selection.

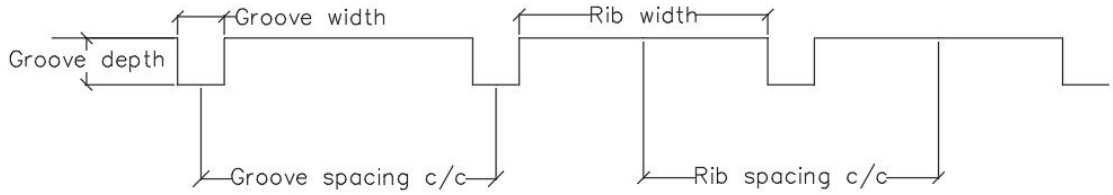

Figure 4.0. Illustration of rib and groove terminology.

4.2 Determination of rib / groove look up tables

The terminology shown in Figure 4.0 has been used throughout. This illustrates the terms rib width, groove width, groove depth, groove spacing and rib spacing. The following look-up tables were derived.

Table 4.0 and Figure 4.1 determine the volume of a single groove 1000 mm long for different groove widths and depths. Table 4.1 and Figure 4.2 is the number of grooves for 1000 mm for different groove spacings and widths.

Table 4.2 is the volume of grooves for a 1000 x 1000 mm area. Figure 4.3 is the area of a single rib 1000 mm long for different rib widths. Table 4.2 and Figure 4.4 is the volume of grooves for a 1000 x 1000 mm area for different rib and groove widths.

Table 4.0 Volume for a single groove 1000mm long

Groove width (mm)	Groove depth (mm)					
	Volume (mm^3)					
	2	4	6	8	10	12
2	4000	8000	12000	16000	20000	24000
4	8000	16000	24000	32000	40000	48000
6	12000	24000	36000	48000	60000	72000
8	16000	32000	48000	64000	80000	96000
10	20000	40000	60000	80000	100000	120000
12	24000	48000	72000	96000	120000	144000
14	28000	56000	84000	112000	140000	168000
16	32000	64000	96000	128000	160000	192000
18	36000	72000	108000	144000	180000	216000
20	40000	80000	120000	160000	200000	240000
22	44000	88000	132000	176000	220000	264000
24	48000	96000	144000	192000	240000	288000
26	52000	104000	156000	208000	260000	312000
28	56000	112000	168000	224000	280000	336000
30	60000	120000	180000	240000	300000	360000

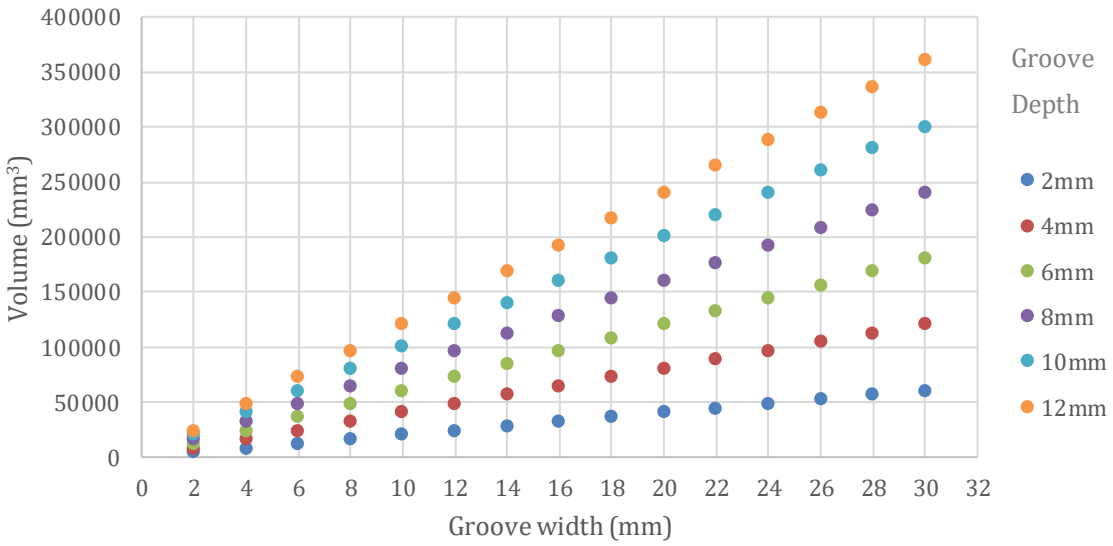

Figure 4.1. Volume of a single groove 1000mm long for different groove widths and depths.

Table 4.1 Number of grooves for 1000 mm

Groove spacing (mm)	Groove width (mm)									
	Number of grooves									
	2	4	6	8	10	12	14	16	18	20
2	250.0	166.7	125.0	100.0	83.3	71.4	62.5	55.6	50.0	45.5
4	166.7	125.0	100.0	83.3	71.4	62.5	55.6	50.0	45.5	41.7
6	125.0	100.0	83.3	71.4	62.5	55.6	50.0	45.5	41.7	38.5
8	100.0	83.3	71.4	62.5	55.6	50.0	45.5	41.7	38.5	35.7
10	83.3	71.4	62.5	55.6	50.0	45.5	41.7	38.5	35.7	33.3
12	71.4	62.5	55.6	50.0	45.5	41.7	38.5	35.7	33.3	31.3
14	62.5	55.6	50.0	45.5	41.7	38.5	35.7	33.3	31.3	29.4
16	55.6	50.0	45.5	41.7	38.5	35.7	33.3	31.3	29.4	27.8
18	50.0	45.5	41.7	38.5	35.7	33.3	31.3	29.4	27.8	26.3
20	45.5	41.7	38.5	35.7	33.3	31.3	29.4	27.8	26.3	25.0
22	41.7	38.5	35.7	33.3	31.3	29.4	27.8	26.3	25.0	23.8
24	38.5	35.7	33.3	31.3	29.4	27.8	26.3	25.0	23.8	22.7
26	35.7	33.3	31.3	29.4	27.8	26.3	25.0	23.8	22.7	21.7
28	33.3	31.3	29.4	27.8	26.3	25.0	23.8	22.7	21.7	20.8
30	31.3	29.4	27.8	26.3	25.0	23.8	22.7	21.7	20.8	20.0
32	29.4	27.8	26.3	25.0	23.8	22.7	21.7	20.8	20.0	19.2
34	27.8	26.3	25.0	23.8	22.7	21.7	20.8	20.0	19.2	18.5
36	26.3	25.0	23.8	22.7	21.7	20.8	20.0	19.2	18.5	17.9
38	25.0	23.8	22.7	21.7	20.8	20.0	19.2	18.5	17.9	17.2
40	23.8	22.7	21.7	20.8	20.0	19.2	18.5	17.9	17.2	16.7

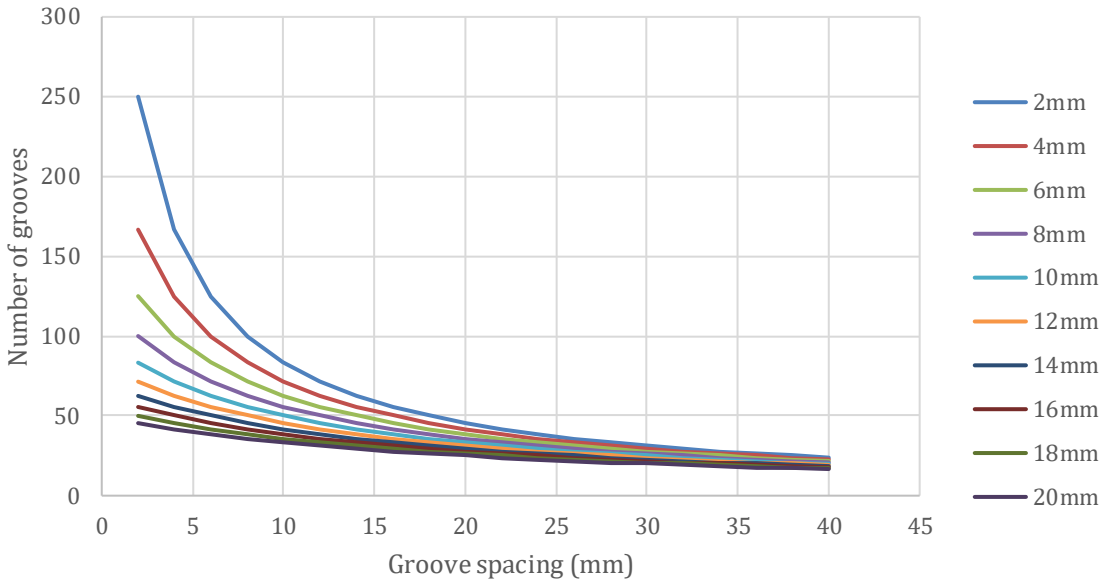

Figure 4.2. Number of grooves for 1000 mm for different groove spacings and widths.

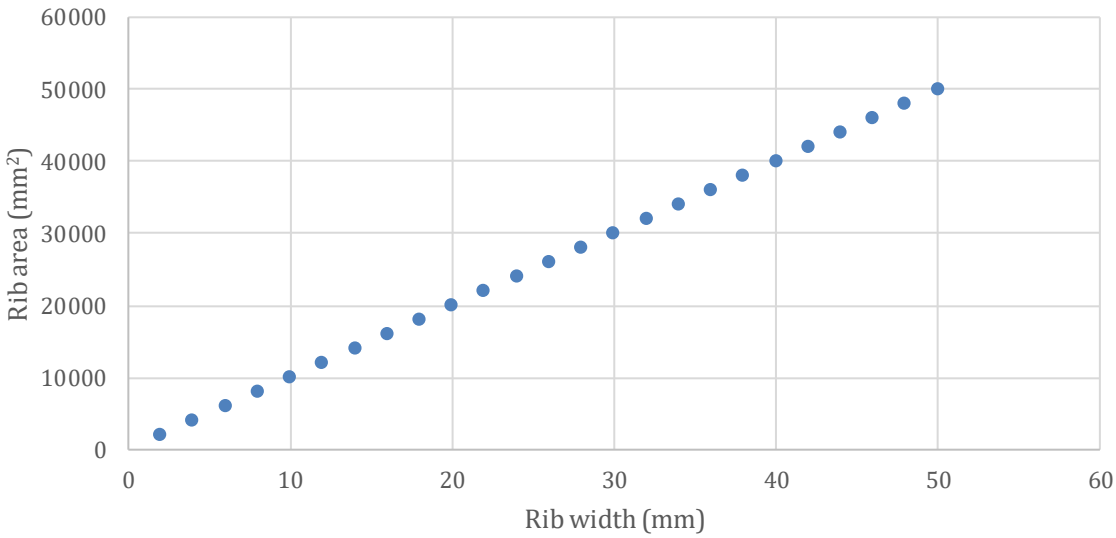

Figure 4.3. Area of a single rib 1000 mm long for different rib widths.

Table 4.2. Volume of grooves for a 1000 x 1000 mm area.

Rib width (mm)	Groove width (mm)						
	Volume of grooves (mm^3)						
	4	6	8	10	12	16	20
2	1333333	1500000	1600000	1666667	1714286	1777778	1818182
4	2000000	2400000	2666667	2857143	3000000	3200000	3333333
6	2400000	3000000	3428571	3750000	4000000	4363636	4615385
8	2666667	3428571	4000000	4444444	4800000	5333333	5714286
10	2857143	3750000	4444444	5000000	5454545	6153846	6666667
12	3000000	4000000	4800000	5454545	6000000	6857143	7500000
14	3111111	4200000	5090909	5833333	6461538	7466667	8235294
16	3200000	4363636	5333333	6153846	6857143	8000000	8888889
18	3272727	4500000	5538462	6428571	7200000	8470588	9473684
20	3333333	4615385	5714286	6666667	7500000	8888889	10000000
22	3384615	4714286	5866667	6875000	7764706	9263158	10476190
24	3428571	4800000	6000000	7058824	8000000	9600000	10909091
26	3466667	4875000	6117647	7222222	8210526	9904762	11304348
28	3500000	4941176	6222222	7368421	8400000	10181818	11666667
30	3529412	5000000	6315789	7500000	8571429	10434783	12000000
32	3555556	5052632	6400000	7619048	8727273	10666667	12307692
34	3578947	5100000	6476190	7727273	8869565	10880000	12592593
36	3600000	5142857	6545455	7826087	9000000	11076923	12857143
38	3619048	5181818	6608696	7916667	9120000	11259259	13103448
40	3636364	5217391	6666667	8000000	9230769	11428571	13333333

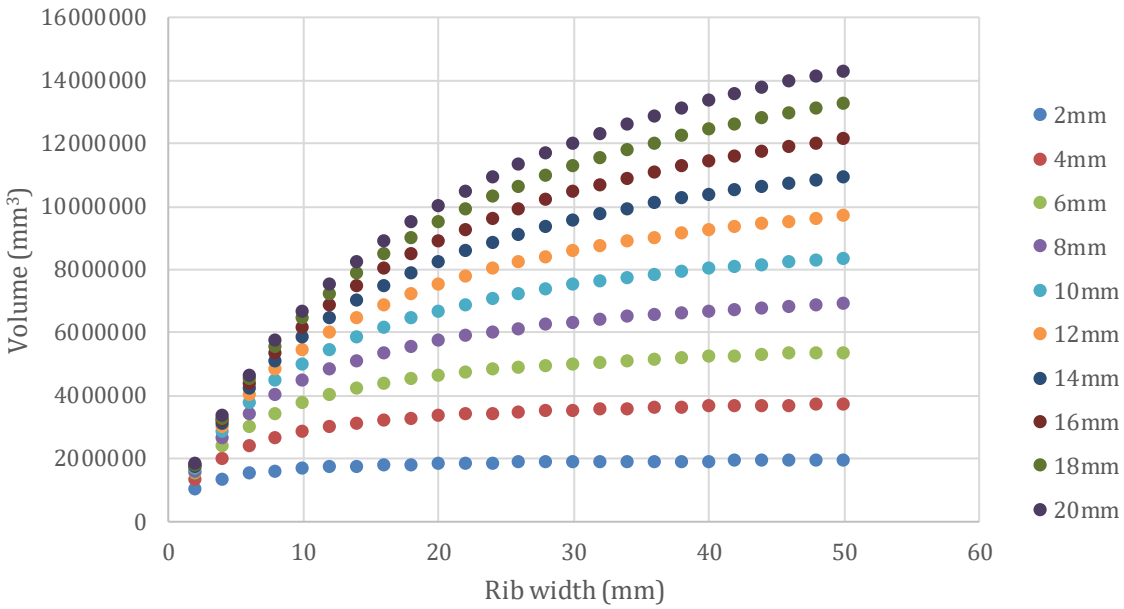

Figure 4.4. Volume of grooves for a 1000 x 1000 mm area for different rib and groove widths.

These look-up tables and their corresponding graphs can be used to help visualise the relationships between different combinations of rib width, groove width and groove depth. They illustrate that it is possible to create a wide range of possible groove combinations and corresponding ability to drain water from a surface.

4.3 Determination of rib / groove calculator

An Excel spreadsheet was developed to calculate a range of parameters depending on these inputs. A screenshot of the Excel Rib / groove calculator is shown in Figure 4.5.

The inputs are rib width, groove width and groove depth. Inputs are also required for calculation length e.g. a length of grooved runway and for calculation width e.g. a specified width of grooved runway.

The Rib / groove calculator uses these inputs to calculate a range of parameters including rib spacing, groove spacing, single groove volume per calculation length, single rib area per calculation width, number of ribs per calculation length, number of grooves per calculation length, groove volume for calculation area and rib area for calculation area.

Rib / groove calculator		
Inputs:	Units	
Rib width	mm	32
Groove width	mm	6
Groove depth	mm	6
Calculation length	mm	1000
Calculation width	mm	1000
Outputs:		
Rib spacing	mm	38
Groove spacing	mm	38
Single groove volume per calculation length	mm^3	36000
Single rib area per calculation width	mm^2	32000
Number of ribs per calculation length		26.3
Number of grooves per calculation length		26.3
Groove volume for calculation area	mm^3	947368
Rib area for calculation area	mm^2	842105
Rib width to groove width ratio		5.3
Rib spacing to groove width ratio		6.3

Figure 4.5. Screen shot of Excel Rib / groove calculator.

The example screenshot shown in Figure 4.5 illustrates the standard ICAO grooving of 38mm centre-centre spacing x 6mm x 6mm groove. The calculation area is for a section of runway 1m x 1m. The example shows that per linear square metre there are 26.3 grooves, 947368mm^3 of groove volume is available for dispersing water and there is 842105mm2 of rib area available for interface contact.

4.4 Test Surfaces

The first part of this chapter used a theoretical approach to understand the inter-relationships between rib with, groove width and groove depth and how they impact the ability of a grooved surface to accommodate water.

In industry there is only a small number of rib / groove dimensions used at airports around the world. The two most common are those specified by the FAA and the CAA. Three types of test surface were used in the research. They were:

- Glass plate to represent a smooth surface.
- Aluminium plate 380mm x 185mm with machine cut rib / groove dimensions.
- Compacted slabs of Marshall Asphalt 305 x 305 x 50mm in size with cut rib / groove dimensions.

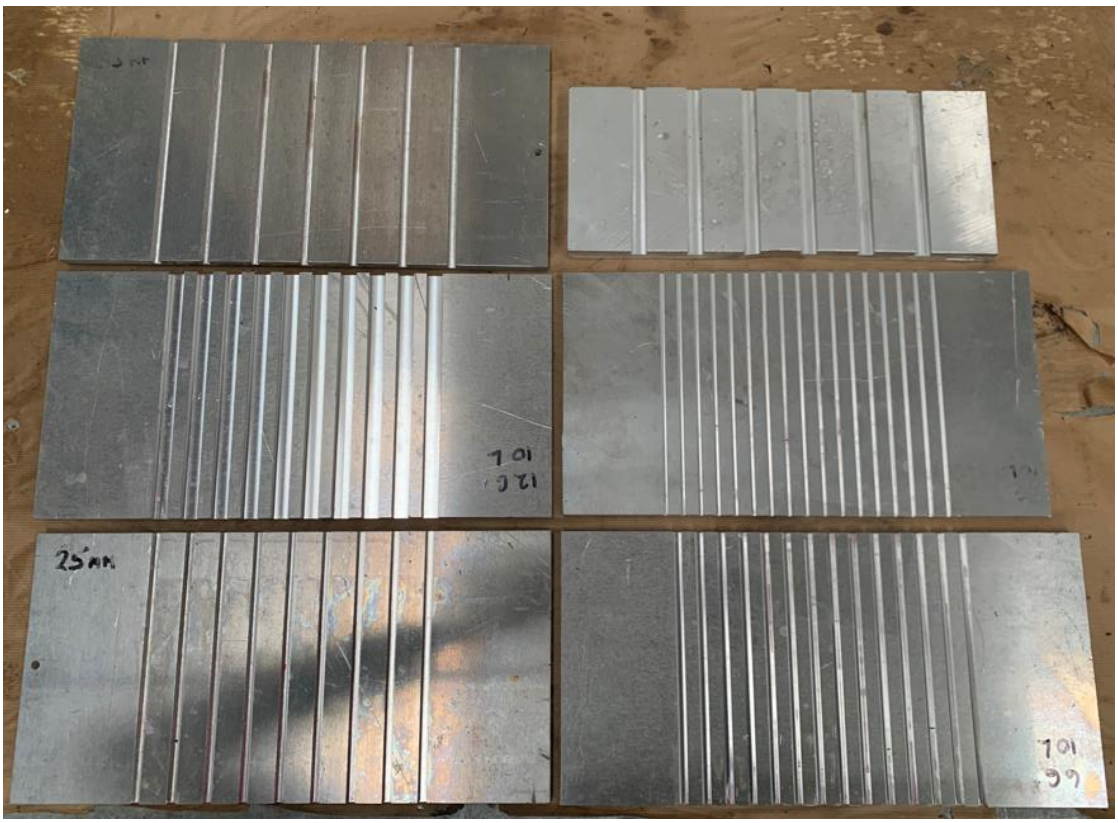

Figure 4.6. A selection of the grooved aluminium plates.

Figure 4.6 shows a selection of the grooved aluminium plates used in the thesis. Pre-mixed Marshall Asphalt (MA) was supplied by Lagan Bitumen Ltd. The MA was reheated to 200° C for 3 hours. The asphalt material was compacted in accordance with EN 12697-33 (2003) using a Cooper roller compactor to form slabs 305 x 305 x 50 mm in size. Grooves were cut into the surface of each MA test specimen using an MK-101 brick saw.

The full mix design properties are not reported herein as it is commercially sensitive information. The Marshall Asphalt (MA) used was a 14mm Marshall Asphalt Surface Course with 6.2% 70/100 bitumen content. The mix was prepared as per Specification 13 Marshall

Asphalt for Airfields Mix Design (MOD, 2009). The MA mix consisted of 14mm, 10mm, 6mm aggregate, aggregate fines, sand, limestone filler, hydrated lime, and 70 / 100 pen bitumen. The aggregate used was a Northern Ireland Silurian greywacke resembles poorly sorted angular grains of sand / quartz and feldspars. The aggregate blend percentages and grading fell within specification limits and are shown in Table 4.3.

Table 4.3 Aggregate Particle Size Distribution and Grading Table

Sieve Size	**Loughrans 6.3 / 14**	**Loughrans 4 / 10**	**Loughrans 2 / 6.3**	**Loughrans CRF**	**Lagan Cement Sand**	**Mc Graths Filler**	**Limits**		**Combined Grading**
AGGREGATE PROPORTIONS (%)									
	16.50%	**0.00%**	**28.90%**	**39.80%**	**11.00%**	**3.80%**			**100.00%**
20	100	100	100	100	100	100	100	100	100
14	90	99	100	100	100	100	86	100	98
10	12	77	99	100	100	100	78	90	85
6.3	0.3	3	63	100	100	100	66	79	73
2	0.3	0.3	0.7	87	99	100	43	57	50
1	0.3	0.3	0.3	62	99	100	31	46	40
0.5	0.3	0.3	0.3	37	97	100	21	36	29
0.125	0.3	0.3	0.3	10	41	100	7	15	12
0.063	0.3	0.3	0.3	3	3.4	90	3	7	5.1

The Softening Point of the 70 / 100 pen bitumen was 46.6 ºC. This was within specification limits of 43-51°C as per EN 1427. The Penetration of the bitumen was 86mm which was within specification limits of 70-100mm as per EN 1426.

Examples of grooved MA test surfaces are shown in Figure 4.7. The test surface is painted pink and white as other testing was explored on the test surfaces.

Figure 4.7. A selection of the grooved MA test surfaces

A summary of the test surfaces and their dimensions is shown in Table 4.4. This shows the different combinations of rib width, groove width and groove depth. For example, AP2 and AP4 were test surfaces representing the FAA and CAA standard dimensions. Also shown is the rib spacing and groove spacing.

The Rib / groove calculator was used to calculate the parameters shown in Table 4.5 for each test surface.

Table 4.4 Summary of test surfaces.

Test surface reference	Material	Grooved / Non-grooved	Rib width (mm)	Groove width (mm)	Groove depth (mm)	Rib spacing C-C (mm)	Groove spacing C-C (mm)
GP	Glass plate	Non-grooved	0	0	0	0	0
AP1	Aluminium plate	Grooved	32	3	6	35	35
AP2 (FAA)		Grooved	32	6	6	38	38
AP3		Grooved	32	12	6	44	44
AP4 (CAA)		Grooved	19	6	6	25	25
AP5		Grooved	10	3	6	13	13
AP6		Grooved	10	6	6	16	16
AP7		Grooved	10	12	6	22	22
MAA	Marshall Asphalt	Grooved	12	10	8	22	22
MAB		Grooved	10	10	8	20	20
MAC		Grooved	15	10	8	25	25
MAD		Grooved	29	6	8	35	35
MAE		Grooved	15	5	4	20	20
MAF		Grooved	22	3	4	25	25
MAH		Grooved	25	3	4	28	28
MAK		Non-grooved	0	0	0	0	0

Table 4.5. Calculated parameters for each test surface.

Test surface reference	Number of grooves per metre (m)	Groove volume per millimetre cubed (mm3)	Rib area per millimetre squared (mm2)
GP	0.0	0	1000000
AP1	28.6	514286	914286
AP2 (FAA)	26.3	947368	842105
AP3	22.7	1636364	727273
AP4 (CAA)	40.0	1440000	760000
AP5	76.9	1384615	769231
AP6	62.5	2250000	625000
AP7	45.5	3272727	454545
MAA	45.5	3636364	545455
MAB	50.0	4000000	500000
MAC	40.0	3200000	600000
MAD	28.6	1371429	828571
MAE	50.0	1000000	750000
MAF	40.0	480000	880000
MAH	35.7	428571	892857
MAK	0.0	0	1000000

Figures 4.8 to 4.10 allow comparison of the test surfaces. The CAA and FAA test surfaces are highlighted in red and green respectively. Figure 4.8 shows the number of grooves per metre (i.e. 1000mm). This ranges from 22 to 77 grooves. The Glass Plate (GP) and un-grooved Marshall Asphalt control (MAK) have no grooves. The FAA and CAA test surfaces have 26 and 40 grooves respectively.

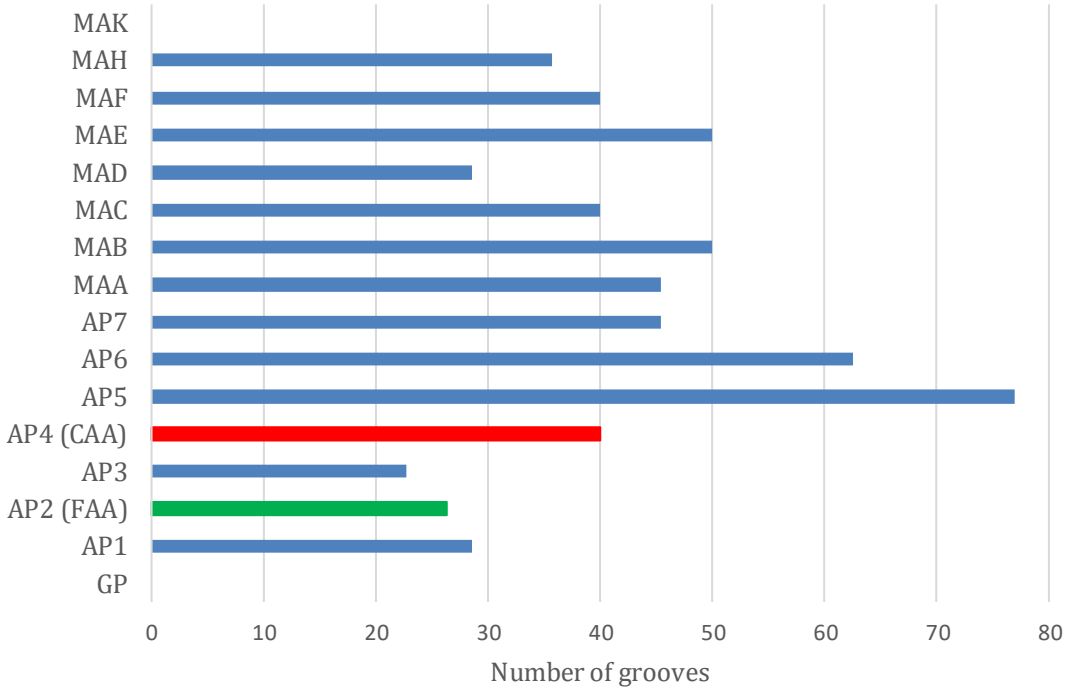

Figure 4.8. Number of grooves per metre.

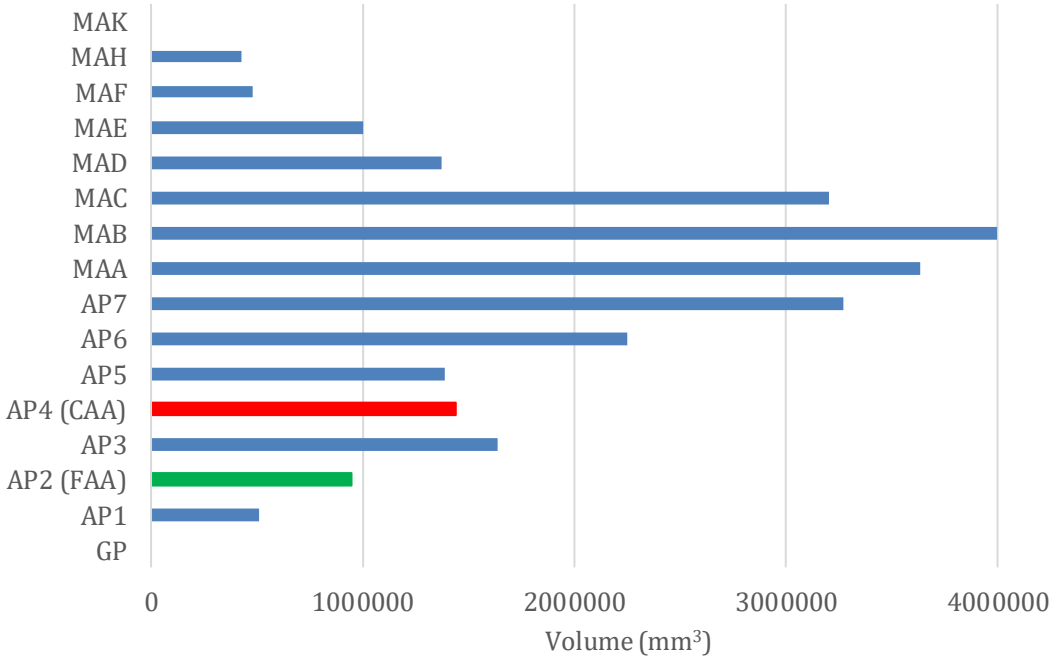

Figure4.9. Volume of grooves per square meter.

Figure 4.9 shows the groove volume per square metre as a means of comparison. The volume ranges from 514286 mm^3 for test surface MAH to 4000000 mm^3 for test surface MAB. The CAA groove pattern has a greater volume compared to the FAA groove pattern.

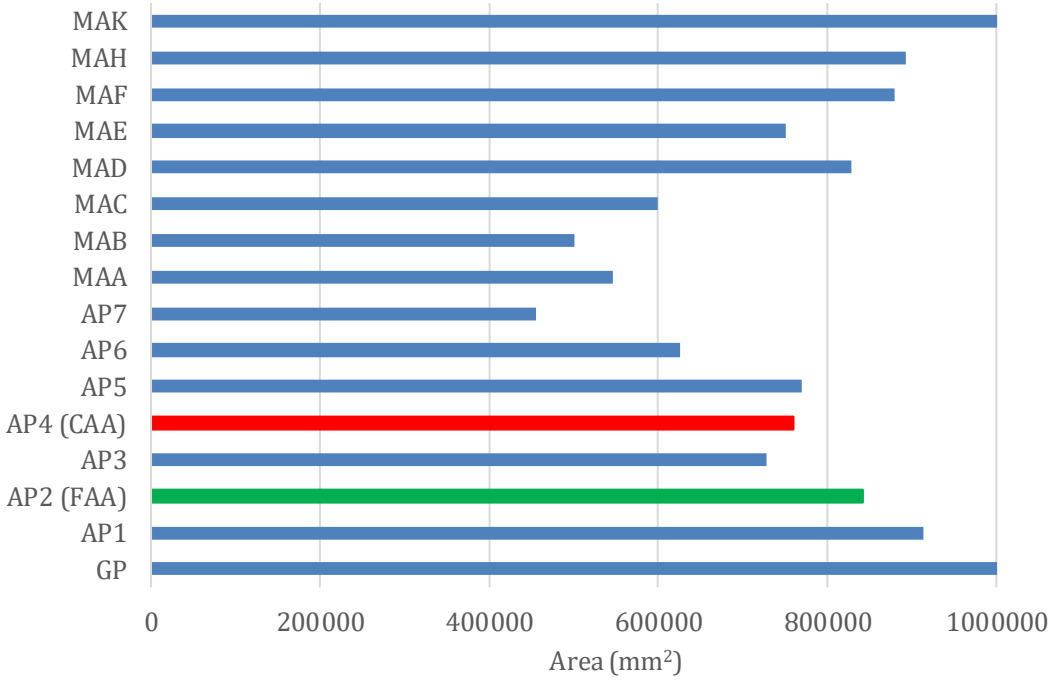

Figure 4.10. Area of ribs per square meter.

Figure 4.10 compares the rib area per square meter. This ranges from 45454 mm^2 for test surface AP7 to 892857 mm^2 for test surface AP1. The CAA groove pattern has a less rib area compared to the FAA groove. The control surfaces i.e. GP and MAK have zero volumes of grooves and 1000000 mm^2 area of rib.

These Figures illustrate that the FAA and CAA test surface rib / groove dimensions are conservative. It is theoretically possible to increase the volume of grooving using alternative combinations and so increase the ability of a grooved runway to displace water under a moving tyre.

It has been demonstrated it is possible to achieve differing combinations of grooves by alternating the grooving characteristics. The ratio of rib width to groove spacing is expressed as a ratio to as shown in table 4.6

Table 4.6 Test surfaces used expressed as a ratio of rib width / groove spacing.

Test surface reference	Material	Grooved / Non-grooved	Rib width (mm)	Groove width (mm)	Rib width / Groove spacing Ratio
GP	Glass plate	Non-grooved	0	0	
AP1	Aluminium plate	Grooved	32	3	0.91
AP2 (FAA)		Grooved	32	6	0.84
AP3		Grooved	32	12	0.73
AP4 (CAA)		Grooved	19	6	0.76
AP5		Grooved	10	3	0.77
AP6		Grooved	10	6	0.63
AP7		Grooved	10	12	0.45
MAA	Marshall Asphalt	Grooved	12	10	0.55
MAB		Grooved	10	10	0.50
MAC		Grooved	15	10	0.60
MAD		Grooved	29	6	0.83
MAE		Grooved	15	5	0.75
MAF		Grooved	22	3	0.88
MAH		Grooved	25	3	0.89
MAK		Non-grooved	0	0	

Each rib width / groove spacing ratio was determined by dividing the rib width by the total width of the rib and the groove. For example for MAA 12/(12+10)= 0.55.

CHAPTER 5.

INVESTIGATION OF THE ASTM FRICTION TYRE / IDEALISED SURFACE INTERFACE USING PRESSURE MAPPING

5.1 Introduction

This chapter investigates the ASTM friction tyre interface with two types of idealised test surface using the Ulster Tyre Road Surface Interface method (UTRSI). The first test surface was a glass plate which was used to represent a smooth texture-less surface. The second surface was aluminium plate with machined grooves of known rib and groove dimensions. The use of these idealised test surfaces reduced the number of variables present at the ASTM tyre / grooved surface interface.

5.2 Investigation equipment / methods

Investigation of the ASTM tyre / smooth glass established a baseline in terms of interfacial contact pressure for just the ASTM friction tyre. There was no influence of grooving or surface texture. The tyre circumference was divided into four positions to allow determination of the static z-axis contact patch interfaces measured using the XSENSOR pressure pad shown in Figure 5.0

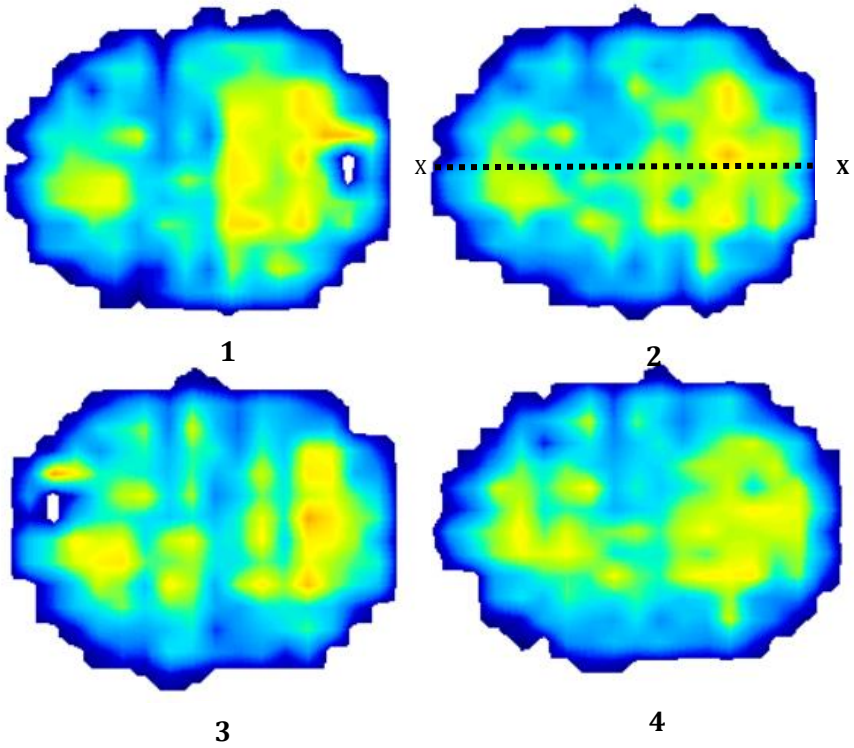

Figure 5.0. Static tyre interface contact patches for tyre positions 1, 2, 3 and 4.

Colour thresholding is used to show pressure variation within each contact patch. They show the contact patch for the four positions around the ASTM tyre to be similar. The contact patch is elliptical, with the X-X axis representing the width of the tyre. The contact pressure is centralised, with the periphery of the contact patch having lower contact pressures.

Table 5.0 details the tyre contact area, maximum pressure and average pressure at each tyre contact position. This shows contact area and pressure are not consistent at each tyre position. These minor variations in distribution are typical of most tyres and may be due to tyre manufacture. The average contact area using standard loading of 0.19kN was 1104.8 mm^2. The average maximum pressure was 34.7PSI. The average pressure was 23.4PSI. The range in contact area was 71mm2. The range in maximum pressure was 1.6PSI. The standard deviation is small at 29.5mm^2 suggesting the contact path at each position to be similar.

Table 5.0. XSENSOR static contact pressure data for tyre positions 1 to 4

Tyre Position	Contact Area (mm^2)	Maximum Pressure (PSI)	Average Pressure (PSI)
1	1071.0	35.4	23.8
2	1096.8	34.5	22.6
3	1109.7	36.3	23.6
4	1141.9	32.6	23.6
Average	1104.8	34.7	23.4
Range	71	3.7	1.1
Std deviation	29.5	1.6	0.5

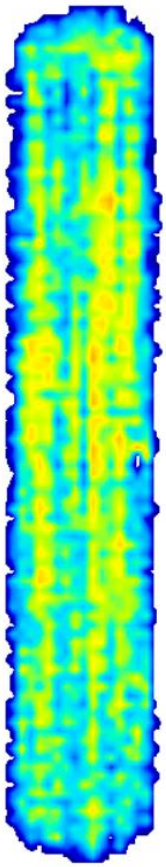

Figure 5.1. Merged dynamic XSENSOR contact patch.

Figure 5.1 shows the merged contact patch for 250 individual frames when the glass surface was pushed slowly under the tyre. Similar to the static contact patch, the vertical pressure distribution is centralised and reduces suddenly towards the edges of the contact patch. Four frames were selected to determine if there was a difference between the static and dynamic test conditions. The four frames are shown in Figure 5.2.

Visual comparison of the frames shown in Figure 5.0 for the static test and Figure 5.2 for the dynamic test show no significant differences in pressure distribution. Table 5.1 shows the XSENSOR data for the 4 frames extracted from the dynamic test. The average contact area was 970.9mm^2, the maximum contact pressure was 33.5PSI, and the average contact pressure was 23.4PSI.

Comparison of the two datasets in Table 5.0 and 5.1 found the average contact area to have decreased by 12% for the dynamic test. The average maximum pressure values reduce by 3 %. The average pressure values are the same, with both static and dynamic tests giving an average of 23.4PSI. Similar to the static contact patch the standard deviation of the contact

area for the dynamic was determined as 28.12mm$^{2.}$ This is small suggesting the contact area between the four frames to be similar.

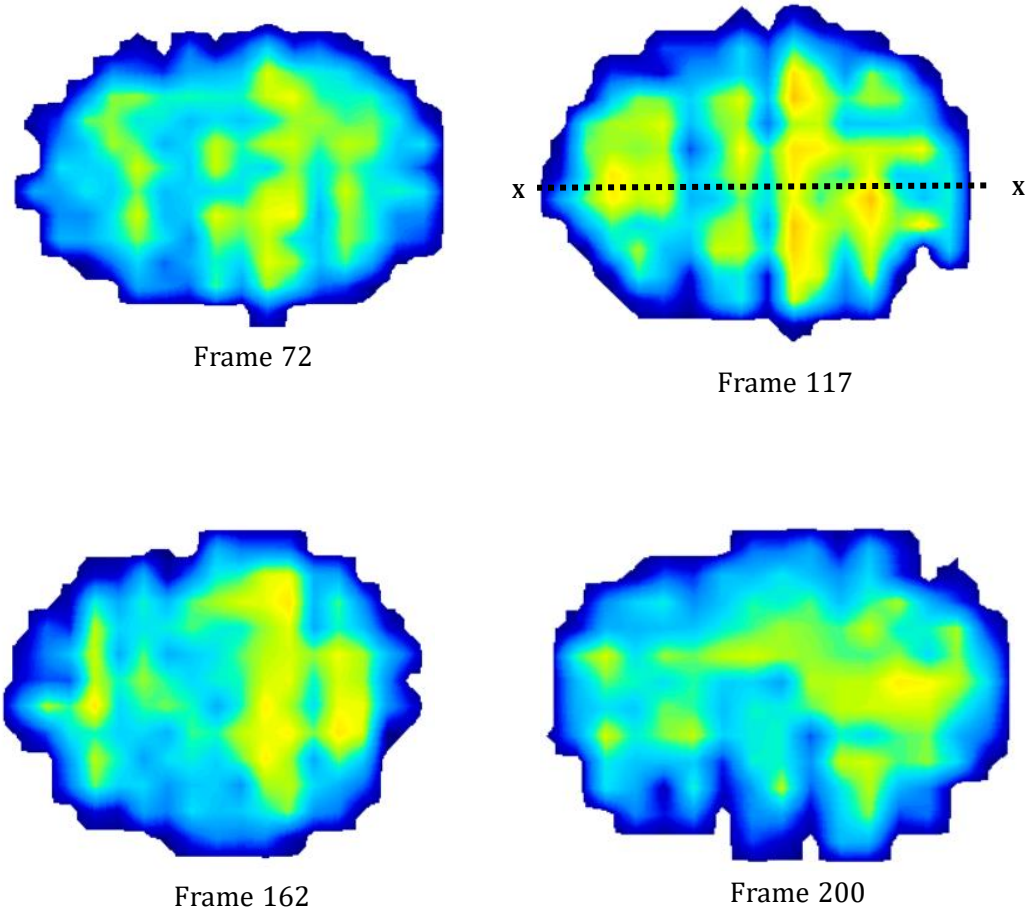

Figure 5.2. Example XSENSOR contact patch frames.

Table 5.1. XSENSOR dynamic contact patch extracted frame data.

Frame No.	Contact Area (mm^2)	Maximum Pressure (PSI)	Average Pressure (PSI)
72	961.29	32.1	23.2
117	993.55	35.4	24.2
162	993.55	33.4	23.2
200	935.48	33.0	23.1
Average	970.97	33.5	23.4
Range	58.06	3.27	1.10
Std deviation	28.12	1.39	0.51

5.3 Investigation of aluminium plate idealised grooved test surface.

The investigation of the contact patch for an ASTM friction tyre and idealised grooves machine cut into aluminium plates allowed understanding of the influence of rib width and groove width. The rib width and groove width dimensions for the aluminium plate surfaces are shown in Table 4.5.

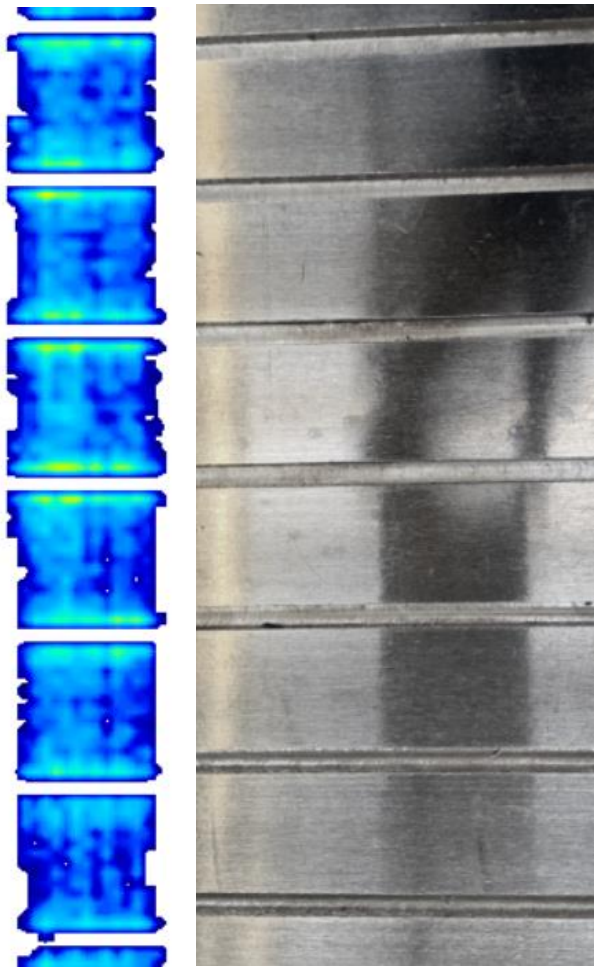

(a) (b)

Figure 5.3. Comparison of merged XSENSOR pressure pad for 32mm rib width groove pattern (a) and metal plate showing machine cut grooves (b).

Figure 5.3 compares a photograph of an aluminium plate with machined grooves and its corresponding merged contact patch measured by the XSENSOR pressure pad.

A minimum pressure threshold of 5PSI has been utilised in the XSENSOR software. Colour thresholding shows variation in pressure as the grooved surface moves under the ASTM

tyre. This illustrates how the grooved pattern cut into the aluminium plate influences the ASTM contact patch.

5.4 Preparation of pressure pad data for analysis

A total of 111 XSENSOR pressure pad tests were carried out. The merged data files were exported as .csv files into Excel for analysis. An example of a merged data file is shown in Figure 5.4. This shows data for each XSENSOR pressure pad cell.

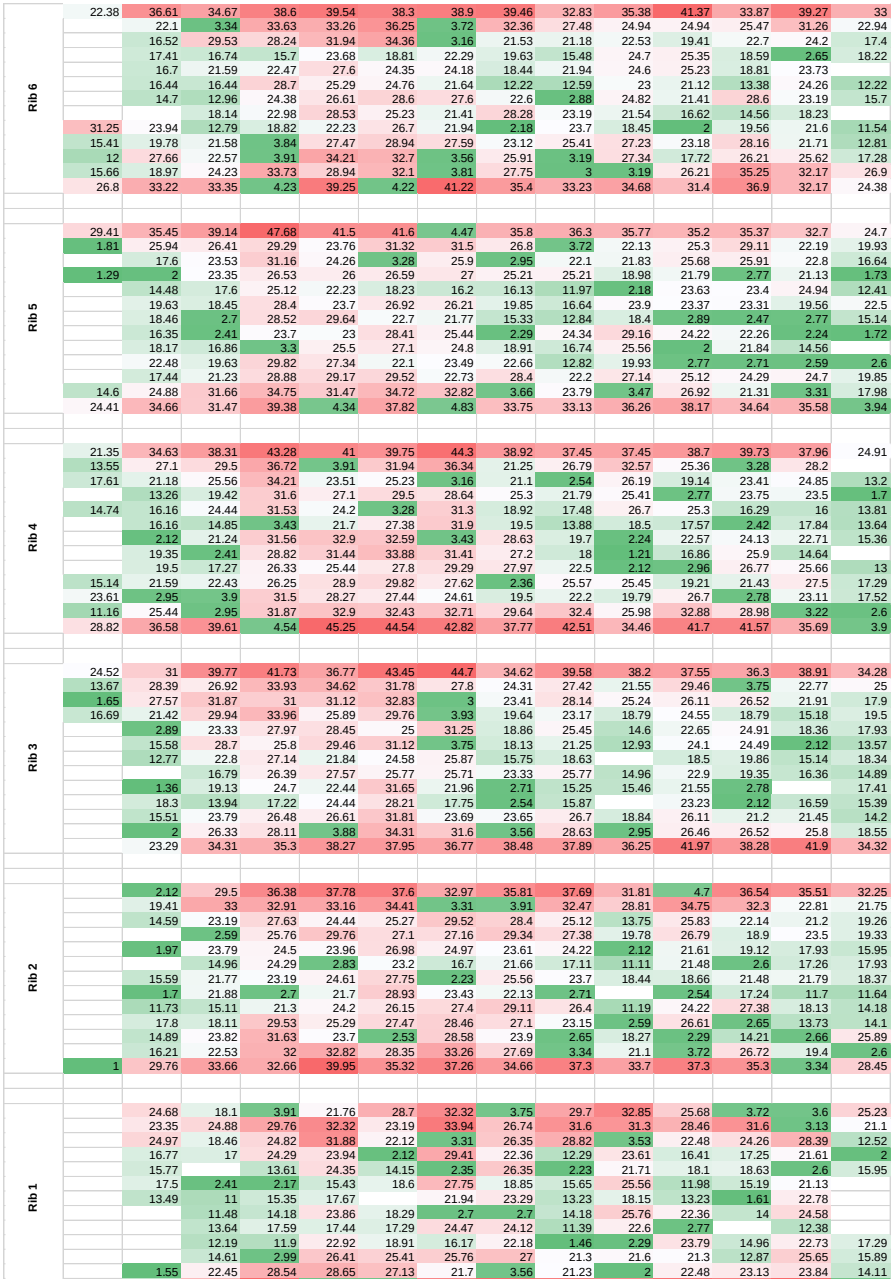

Figure 5.4. Merged XSENSOR rib / groove pressure pad data imported into Excel and conditionally formatted.

The example data shows six ribs and their groove widths. Conditional formatting has been used to illustrate the variation in the pressure data. Each cell is 2.54 mm x 2.54 mm allowing spatial measurements such as contact area and length to be determined.

Figure 5.5 shows a schematic of the leading and trailing edges of the ASTM tyre interaction with the grooved specimen.

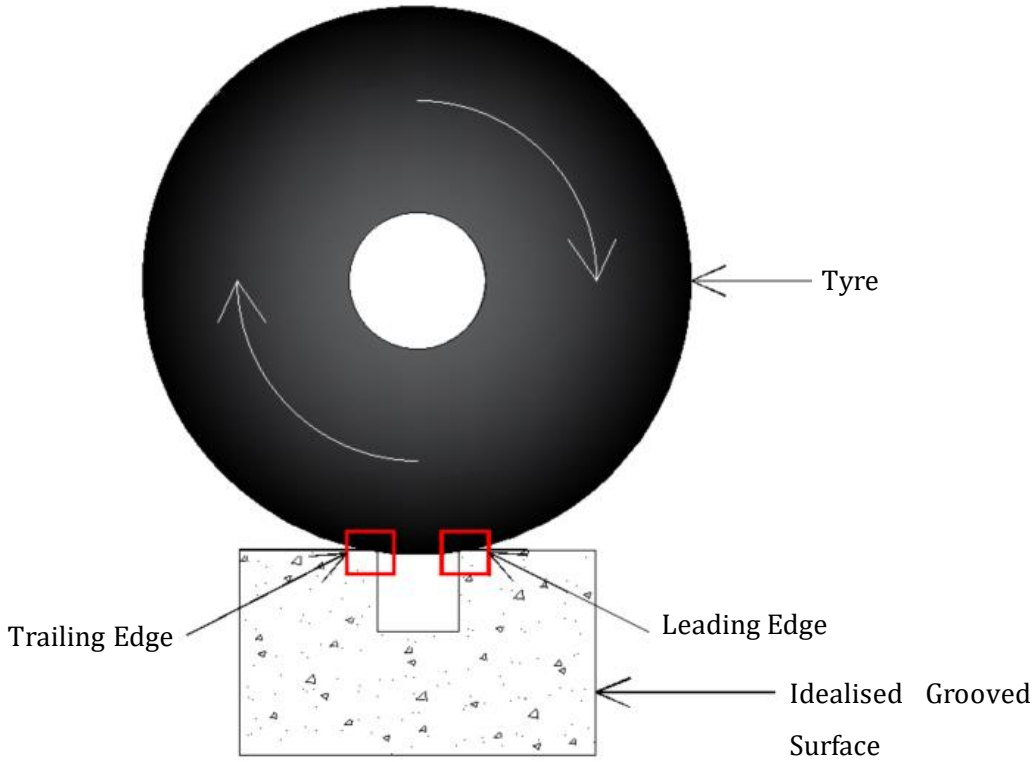

Figure 5.5. Leading and trailing edge tyre / groove interface.

5.5 Investigation of rib width

The rib width investigation considered the leading, central and trailing edge pressure distributions for the 32mm, 19mm and 10mm rib width test specimens. The groove width was 6 mm wide x 6 mm depth. Tables 5.2, 5.3 and 5.4 show pressure data for the three rib widths. This relates to test surfaces AP2, AP4 and AP6.

Table 5.2 shows pressure data for the six 32mm wide ribs measured for test surface AP6. Each 32 mm wide rib has 13 rows of pressure pad cell data. Each row of data has been averaged to illustrate the variation in pressure from the leading to the trailing edge of each rib as it moved under the ASTM tyre. The average pressure represents the average of the average. For example the data for rib 1 represents the average pressure across the width of rib 1. The average of average was adopted in this case as it was considered the relationship shouldn't be affected as the data is quantitative. The raw data and data preparation for Table 5.2 – 5.4 is presented in Appendix A.

Table 5.2. Pressure data for six 32 mm rib widths.

Pressure Data						Average pressure for six 32 mm wide ribs
Rib 1	Rib 2	Rib 3	Rib 4	Rib 5	Rib 6	
29.64	32.55	34.56	38.71	35.10	34.33	34.1 (trailing edge)
21.70	25.10	25.58	27.69	27.60	28.01	25.9
19.80	21.17	22.12	23.99	23.50	25.73	22.7
16.55	21.60	17.91	23.38	20.88	23.80	20.7
15.73	20.37	18.62	22.32	19.94	20.87	19.6
17.06	17.87	19.89	21.21	21.31	19.09	19.4
14.98	20.72	18.62	23.61	19.60	21.33	19.8
17.69	17.53	21.83	19.44	21.54	18.69	19.5
17.73	20.54	22.11	21.88	18.22	20.54	20.2
19.64	22.40	23.44	22.03	21.68	19.04	21.4
23.98	22.13	25.96	23.26	22.64	23.46	23.6
26.93	28.33	27.03	27.14	25.35	27.51	27.0
26.50	32.40	37.18	36.94	36.39	36.01	34.2 (leading edge)

Table 5.3. Pressure data for six 19 mm rib widths.

Pressure Data						Average pressure for six 19 mm wide ribs
Rib 1	Rib 2	Rib 3	Rib 4	Rib 5	Rib 6	
24.91	27.21	27.85	32.02	33.57	35.32	30.1 (trailing edge)
26.16	26.02	27.81	26.22	29.72	28.90	27.5
20.07	22.68	23.47	23.36	24.24	26.14	23.3
20.55	21.24	20.84	22.38	23.55	25.01	22.3
18.88	21.57	20.39	21.34	25.40	23.04	21.8
22.07	21.93	22.21	23.56	26.32	24.68	23.5
24.34	24.25	23.42	27.98	28.60	25.02	25.6
33.64	33.03	33.53	36.54	37.09	33.25	34.5 (leading edge)

Table 5.4. Pressure data for six 10 mm rib widths.

Pressure Data						Average pressure for six 10 mm wide ribs
Rib 1	Rib 2	Rib 3	Rib 4	Rib 5	Rib 6	
38.28	22.14	37.35	33.54	17.97	9.27	26.4 (trailing edge)
33.81	33.97	31.39	31.67	33.50	35.77	33.4
29.10	30.85	29.65	28.96	31.95	28.84	29.9
32.73	29.34	34.49	32.15	31.69	28.04	31.4
25.22	31.92	11.91	25.32	34.80	33.09	27.0 (leading edge)

The average pressure for the 32 mm wide ribs shows greatest pressure at the leading and trailing edge as the test surface is moved slowly under the ASTM tyre. Pressure is lowest in the centre of each rib. Table 5.3 shows the same to occur for the 19 mm rib width for test surface AP4. Table 5.4 shows that the leading edge is lowest for the 10mm rib width and the pressure increases as the tyre moves to the trailing edge.

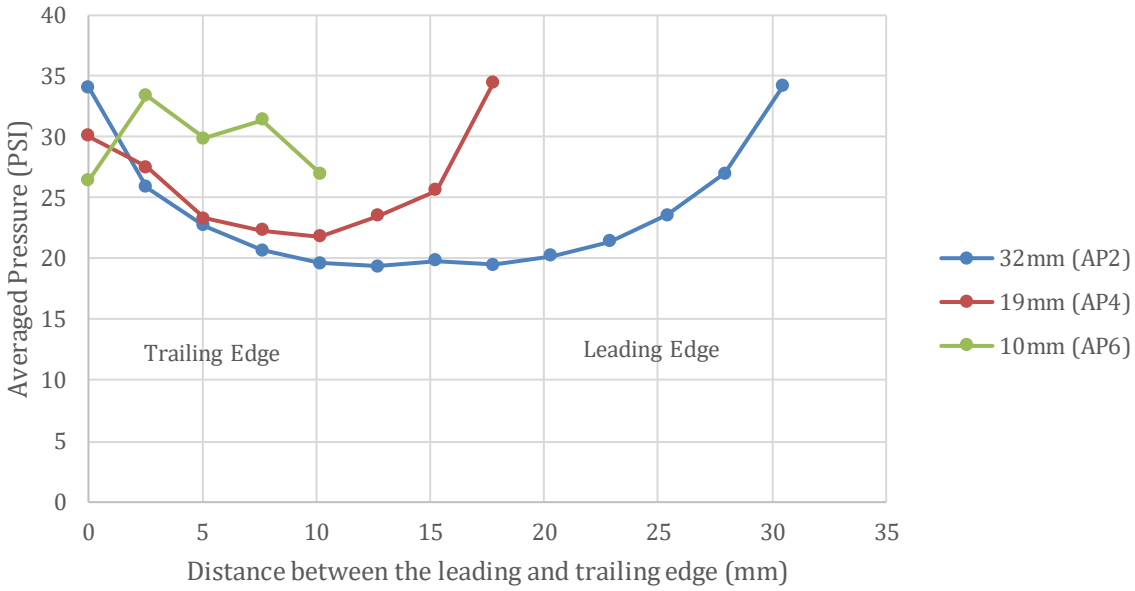

Figure 5.6. Comparison of 32mm (AP2), 19mm (AP4) and 10mm rib widths (AP6).

Figure 5.6 compares the three rib widths by plotting pressure with distance between the leading and trailing edges. The 32 mm rib width shows pressure to be similar at each edge and to reduce significantly towards the centre of the rib. The same trend was found for the 19 mm rib width. As rib width is reduced to 10 mm, there is a change in the trend with higher values in the centre of the rib. The data shows rib width influences the pressure distribution within the ASTM contact patch.

5.6 Investigation of groove width

This investigated groove widths of 12, 6 and 3mm for rib widths of 32mm and 10mm. Figure 5.7 compares the 3 groove widths for the 32mm rib width. This shows there to be a pattern in the data with the widest groove having the greatest effect. The 12 and 6mm groove widths had similar leading and trailing edge values.

There was significant reduction towards the centre for the 12mm grove width (AP3), with less reduction for the 6mm width (AP2). The 3mm groove width (AP1) interface pressure remained relatively consistent with only a small increase towards both edges.

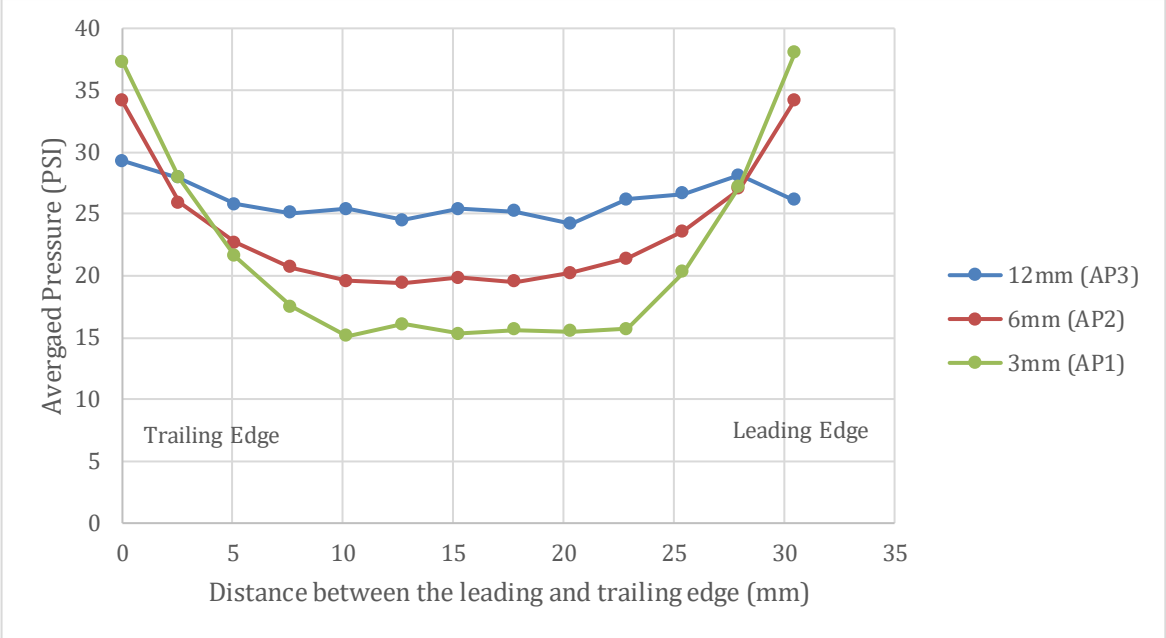

Figure 5.7. Comparison of 12mm (AP3), 6mm (AP2) and 3mm (AP1) groove widths for the 32mm rib widths.

Whilst the 12mm groove width (AP12) has the greatest interface pressure at both groove edges, it had the lowest pressure in the central area of the rib. This suggests that the 12mm groove width for the 32mm rib width causes greater enveloping of the tyre into the groove resulting in higher interface pressure at the edges. Reducing groove width reduces interface pressures at both the leading and trailing edges.

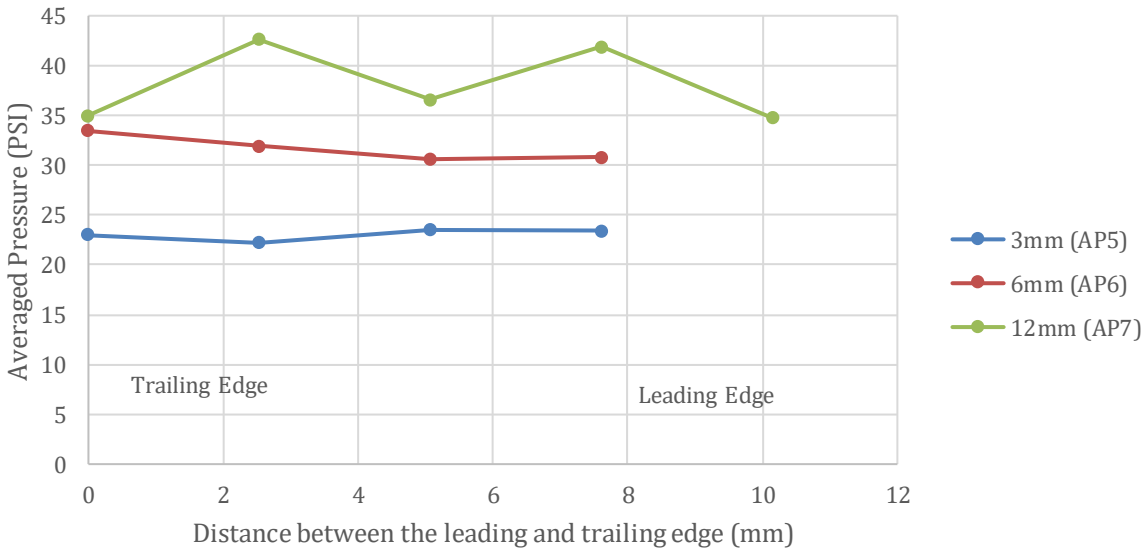

Figure 5.8. Comparison of 12mm (AP7) , 6mm (AP6) and 3mm (AP5) groove widths for the 10mm rib width.

Figure 5.8 compares the 3 groove widths for the 10mm rib width i.e., AP7, AP6 and AP5. The plots for the 10mm rib width are significantly different to the 32mm rib width. There is no obvious increase in pressure at the leading or trailing edges for the 10mm rib width. However, interface pressure increases as the groove width increases.

5.7 Comparison of pressure pad data

The cumulative frequency of the interface pressure was used as a method to compare pressure pad data. The interface pressure for each of the four static ASTM tyre positions (see Figure 5.0) resting on the glass plate is plotted in Figure 5.9. The data shows the measured pressure to range from 10 and 40PSI. There was slight variation in the pressure distribution for each position of the ASTM tyre.

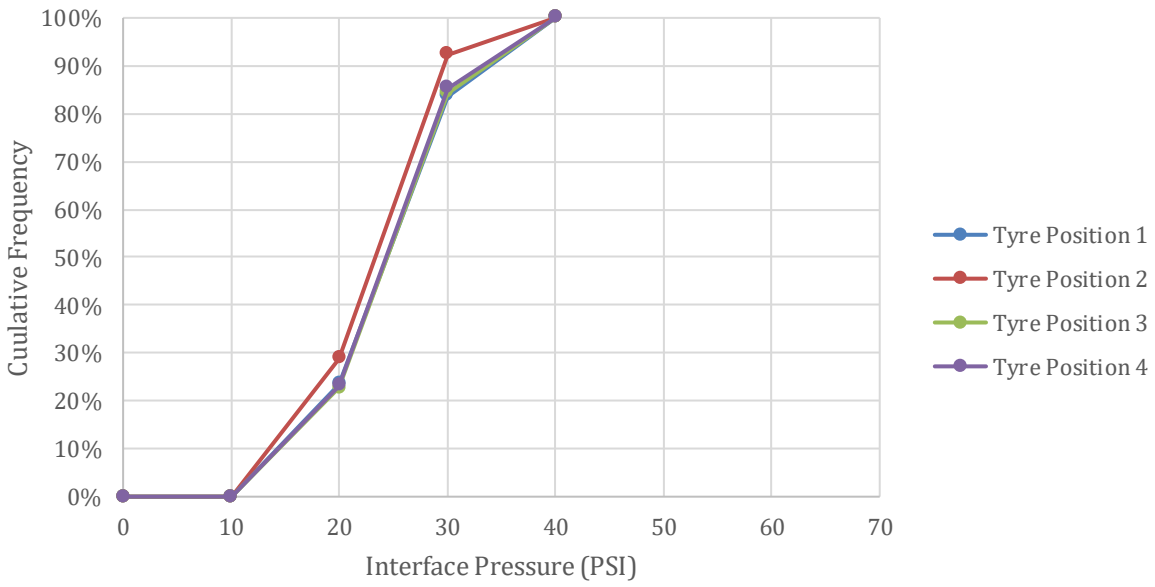

Figure 5.9. Frequency distribution for 4 static ASTM tyre positions on a glass plate.

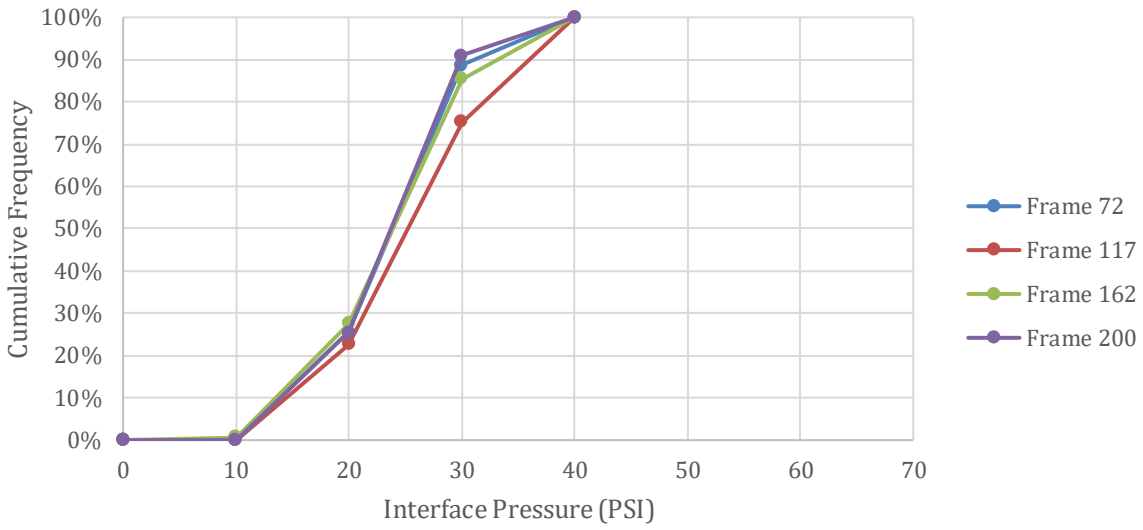

Figure 5.10. Frequency distribution for 4 dynamic tyre positions on a glass plate.

Figure 5.10 compares the cumulative frequency interface pressure for the 4 frames (see Figure 5.2) selected from the merged pressure pad file for the glass plate. This also shows the pressure to range from 10 and 40PSI with slight variation for each extracted frame. The plots in Figure 5.9 and 5.10 are similar.

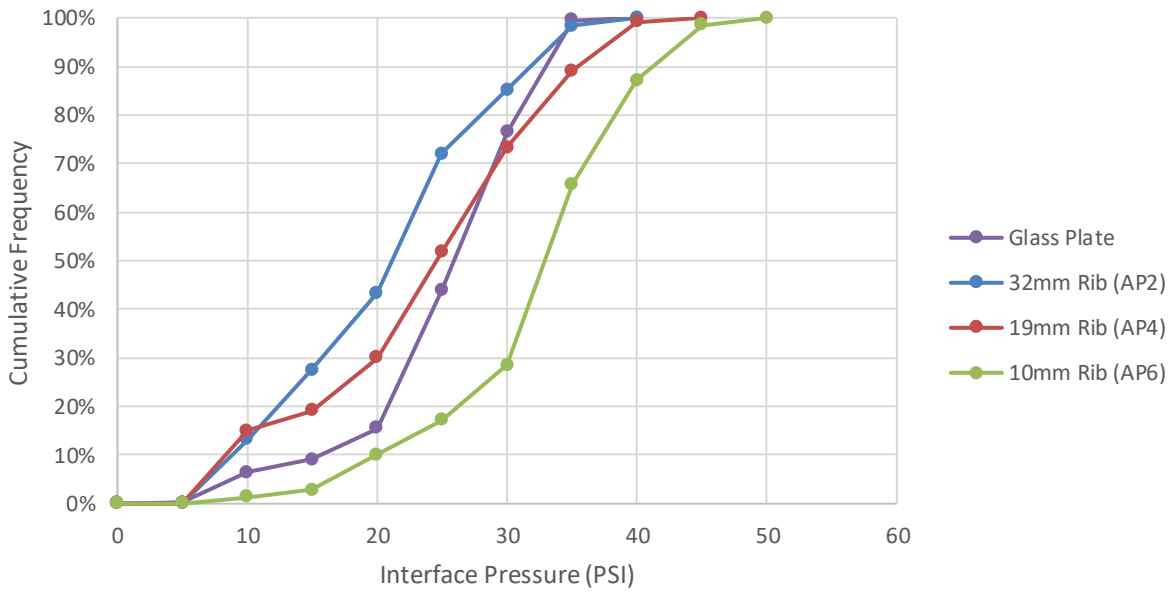

Figure 5.11. Comparison of cumulative frequencies for glass plate, 32mm (AP2), 19mm (AP4) and 10 mm data (AP6).

Figure 5.11 compares the cumulative frequencies for the 32 mm, 19mm and 10mm rib width (see Figure 5.6) with tyre position 1 for a glass plate. This illustrates how rib width influences the frequency distribution of the pressure pad data for test surfaces AP2, AP4 and AP6.

Figure 5.11 shows a significant difference in the 4 plots. The curve for the 32mm rib width (AP2) plots to the left of the glass plate curve. The curve for the 10mm rib width (AP6) plots to the right of the glass plate curve. The curve for the 19mm rib width (AP4) plots to the left of the glass plate curve up to 25PSI where it then shifts to the right.

This illustrates how rib width may influence the ASTM friction measuring tyre / grooved surface interface.

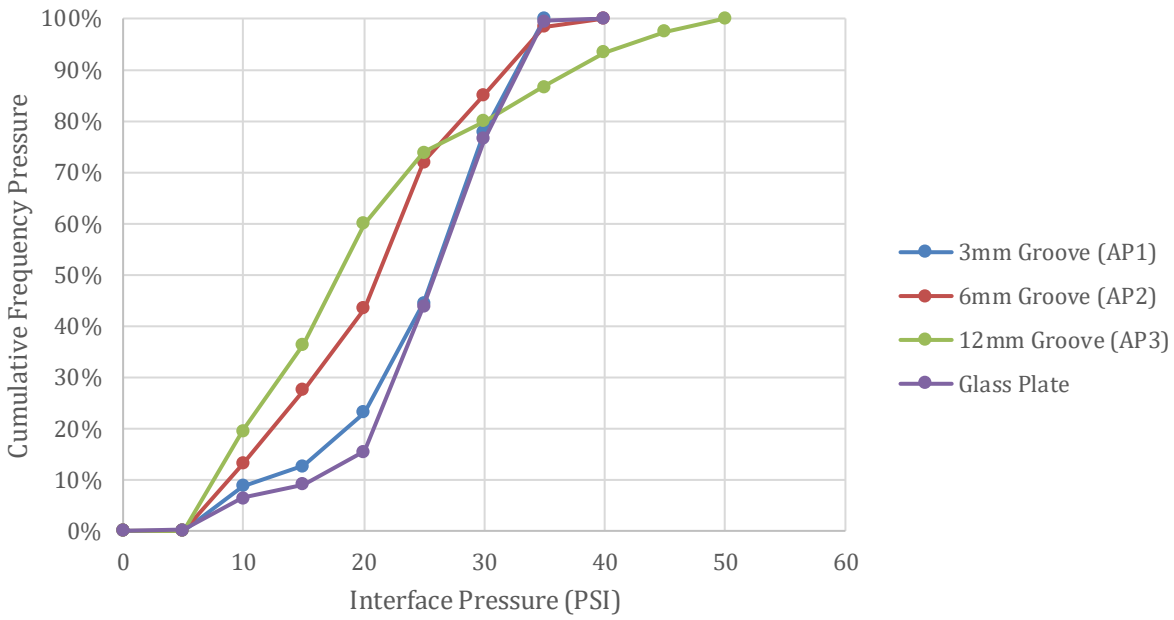

Figure 5.12. Comparison of cumulative frequencies for glass plate, 3mm (AP1), 6 mm (AP2) and 12 mm (AP3) groove width data for 32 mm rib width.

Figure 5.12 compares the cumulative frequency for the 32 mm rib width idealised surface with the groove widths of 3, 6 and 12 mm. The plots show the curves for the glass plate and the 3mm groove width (AP1) to be similar.

With increasing groove width the curves plot progressively to the left. The 6 mm curve then plots similar to the glass plate and 3 mm data at the highest values; 100% cumulative

frequency. The 12mm data moves to the right due to the higher pressures along its leading and trailing edges.

Figure 5.13 compares the cumulative frequency curves for the 12mm, 6mm and 3mm groove widths with the glass plate. The rib width remains constant at 10mm. The pressure frequency curves show that the glass plate and 3mm groove width (AP5) to be similar. The 12mm (AP7) and 6 mm groove width (AP6) curves plot to the right of the glass plate curve. This reflects the reduced rib area for the 10 mm rib compared to the much greater rib area for the 32 mm rib.

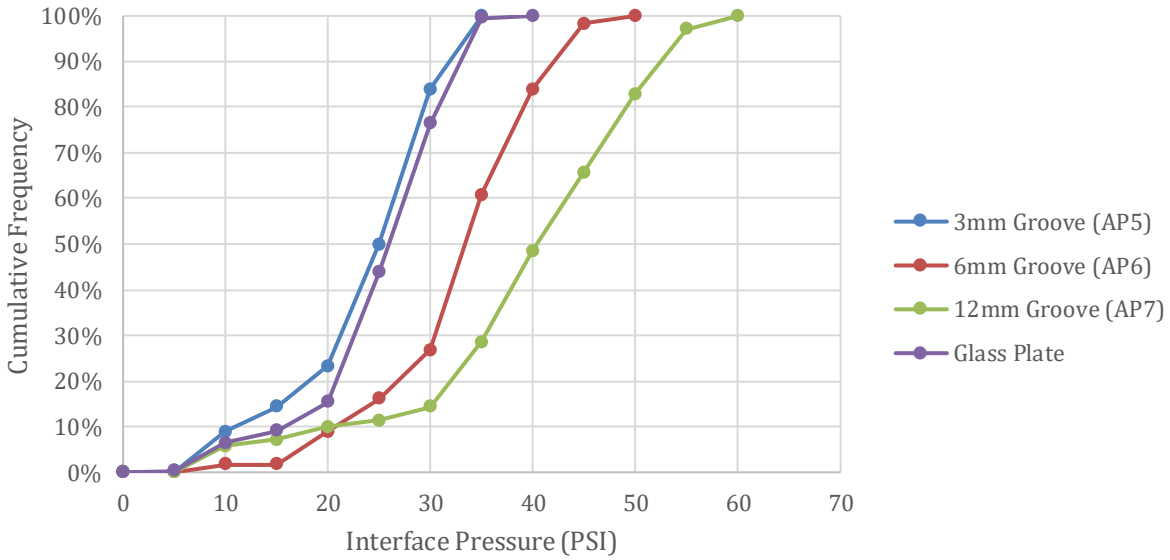

Figure 5.13. Comparison of cumulative frequencies for glass plate, 3mm (AP5), 6 mm (AP6) and 12 mm (AP7) groove width data for 10 mm rib.

The 3mm groove width (AP5) is similar to the glass plate as the tyre cannot envelop the groove giving similar pressure values to the glass plate. As groove width increases there is more enveloping giving the higher interface pressures at the edges of the rib.

5.8 Summary

- The UTRSI method was able to measure the ASTM tyre / surface interface for each of the test surfaces.
- Rib width was found to influence the ASTM tyre / surface interface. The highest interface pressure was found for the 10mm rib width, followed by 19mm, with 32mm having the lowest.
- Groove width was found to influence the ASTM tyre / surface interface. The wider the groove the greater the pressure at both leading the trailing edges.
- The use of cumulative frequency distribution curves allowed comparison of the different rib / groove combinations.

CHAPTER 6.

EVOLUTION OF THE ASTM FRICTION TYRE / GROOVED MARSHALL ASPHALT INTERFACE DUE TO SIMULATED WEAR USING PRESSURE MAPPING

6.1 Introduction

This chapter investigates evolution of the ASTM friction tyre / grooved Marshall Asphalt (MA) interface for test surfaces subjected to simulated wear using the Ulster University Road Test Machine (RTM). This interface investigation uses the merged XSENSOR data measured each time RTM testing was stopped. Digital Surf MountainsMap software was used to visualise the measured interface between the friction tyre and the test surfaces.

Four test surfaces were chosen to investigate evolution of the ASTM friction tyre / test surface interface. The four test specimens were:

- Test Surface MAA – this represents an extreme rib width to groove width ratio, i.e., 12mm rib width : 10mm groove width. This surface suffered excessive wear during simulated trafficking. Pendulum testing had to be stopped after 6000 wheel passes due to degradation of the ribs of the test surface.

- Test Surface MAD – this represents the dimensions recommended by ICAO and FAA, i.e. 32mm rib width : 6mm groove width.

- Test Surface MAF – this represents the smallest groove width considered in this thesis i.e., 22mm rib width : 3mm groove width.

- Test Surface MAK – this surface was not grooved and acted as a MA control.

6.2 Investigation equipment / methods

XSENSOR X3 Pro software can remove pressure values below a given threshold. The calibrated range of the flexible pressure pad is 10 to 250PSI. The default minimum threshold is 5PSI. Analysis was carried out to determine whether the 10PSI default threshold was suitable for the trafficked MA test surfaces.

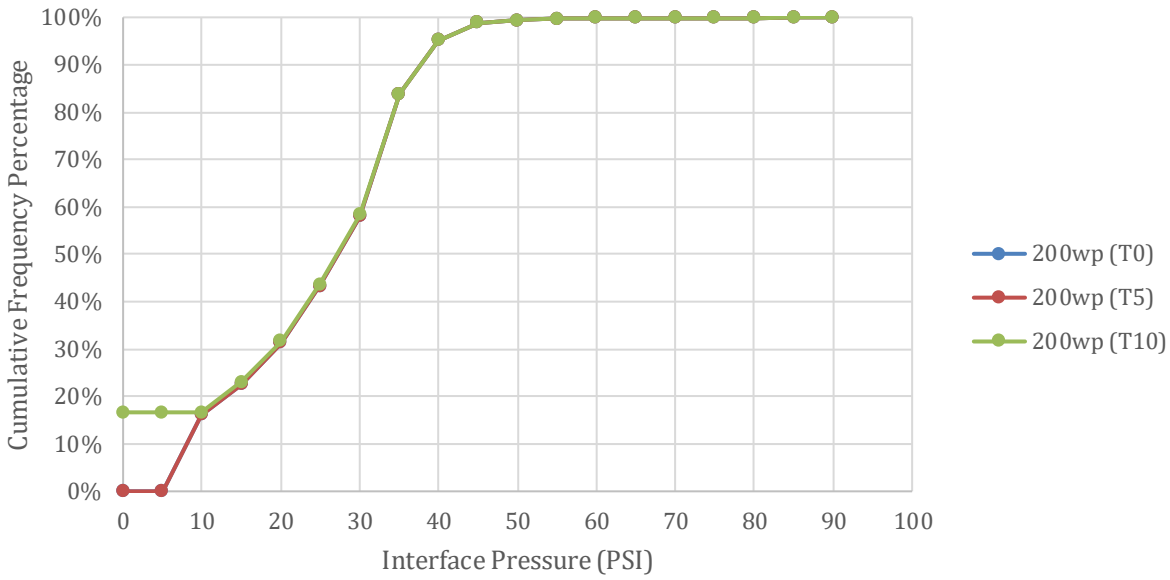

Figure 6.0. Cumulative Frequency Percentage for Test Surface MAK at 200 wheel passes with thresholds of 0PSI, 5PSI and 10PSI.

Figure 6.0 shows the cumulative frequency percentage of interface pressure for test specimen MAK at 200 wheel passes with thresholds of 0, 5, and 10PSI. The three data sets plot the same for pressures above 10PSI. The plots show there is no measured pressure for thresholds of 0 and 5PSI. However, 17% of the data occurs between an interface pressure of 5 and 10PSI. Subsequent analysis of merged pressure pad data used a threshold value of 5PSI.

6.3 Test Surface MAK non-grooved Marshall Asphalt control

Test surface MAK was not grooved and acted as a control. Figure 6.1 compares the merged XSENSOR pressure pad data with a photograph of the MAK test surface after 200 wheel passes. This shows the surface of MAK to consist predominately of a fine graded mastic with a small number of exposed coarse aggregate particles. These exposed coarse aggregate particles result in the areas of higher pressure in the XSENSOR data.

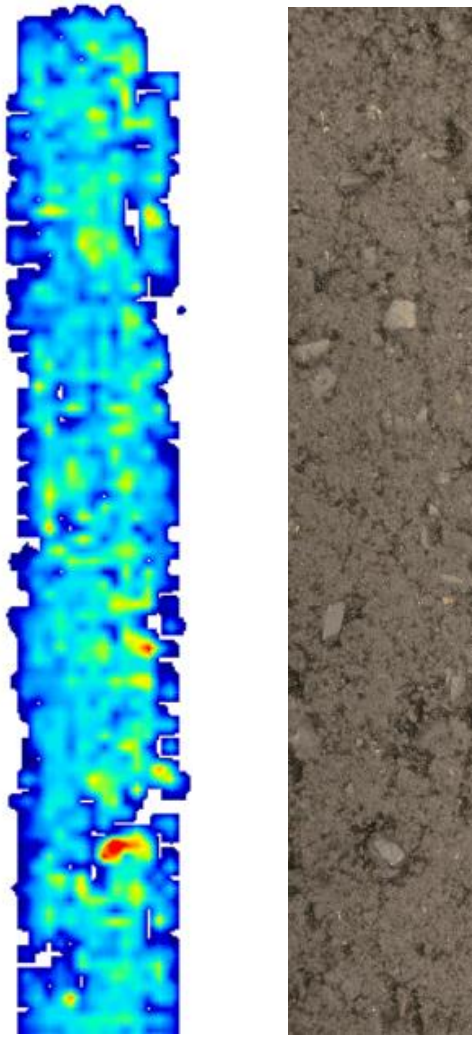

(a) (b)

Figure 6.1. Test specimen MAK after 200 wheel passes (a) merged XSENSOR pressure pad data, (b) photograph.

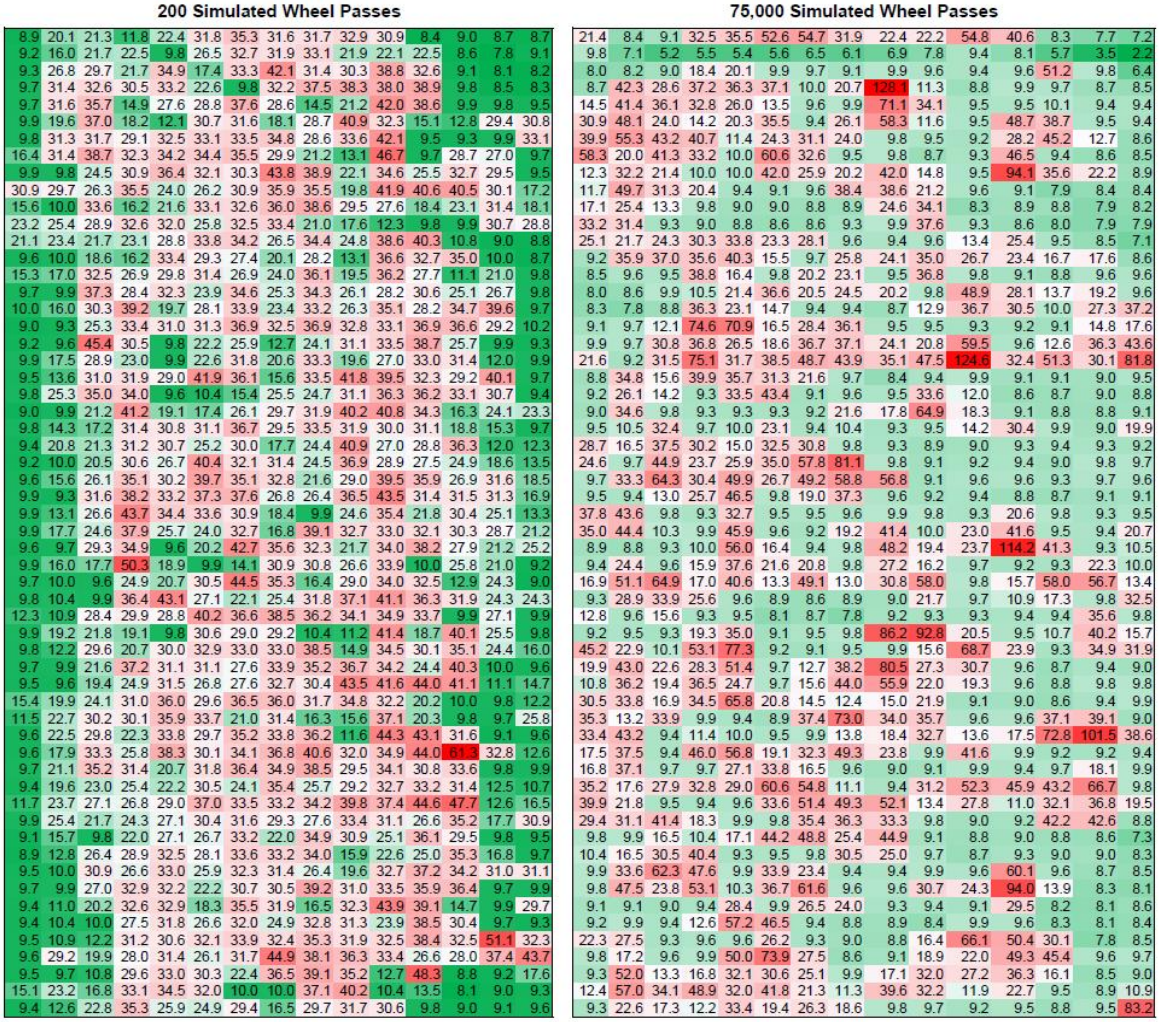

Figure 6.2. Comparison of XSENSOR data for test specimen MAK after 200 and 75,000 wheel passes.

Figure 6.2 compares the XSENSOR pressure data for test surface MAK after 200 and 75,000 wheel passes, this shows the pressure distribution to have changed.

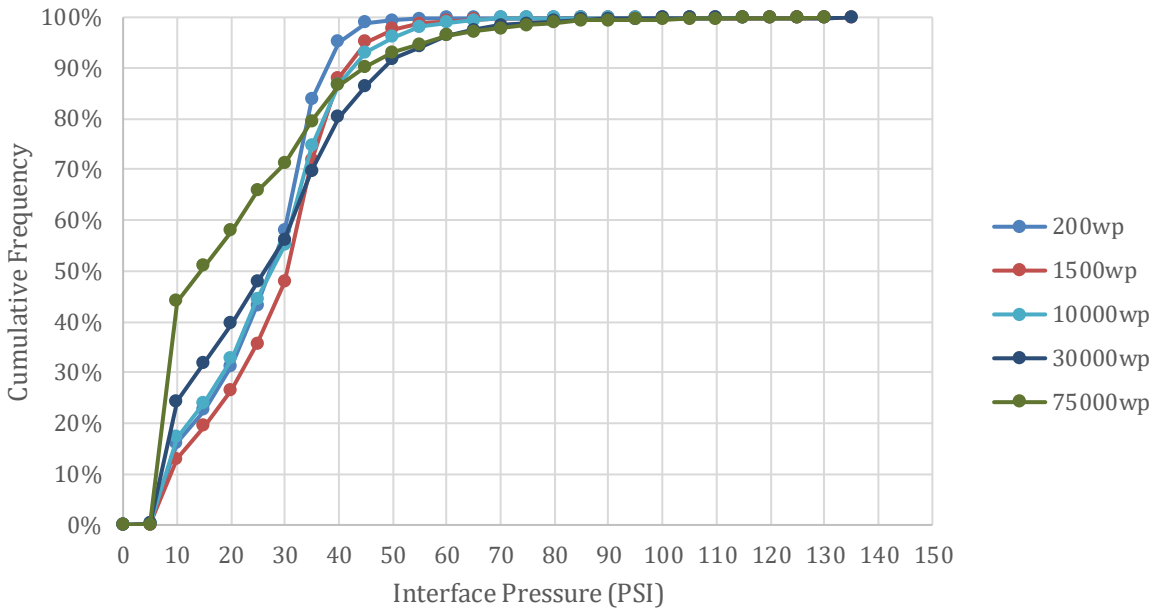

Figure 6.3. Evolution of pressure due to simulated trafficking for test specimen MAK.

Figure 6.3 shows the evolution of ASTM friction tyre / surface interface pressure due to simulated trafficking for the non-grooved test surface MAK. Interface pressure was found to range between 5 and 135PSI. With increased trafficking there is an increase in both the lower contact pressures and the higher contact pressures.

This represents the development of surface texture as the un-grooved asphalt is trafficked. The film of bitumen is worn off and the surface texture of aggregate particles becomes exposed. As trafficking continues, the matrix of fines between the aggregate particles begins to wear away. The number of contact points decreases as the matrix is worn contributing to a greater frequency of lower contact pressures. The high pressure values are associated with individual aggregate particles.

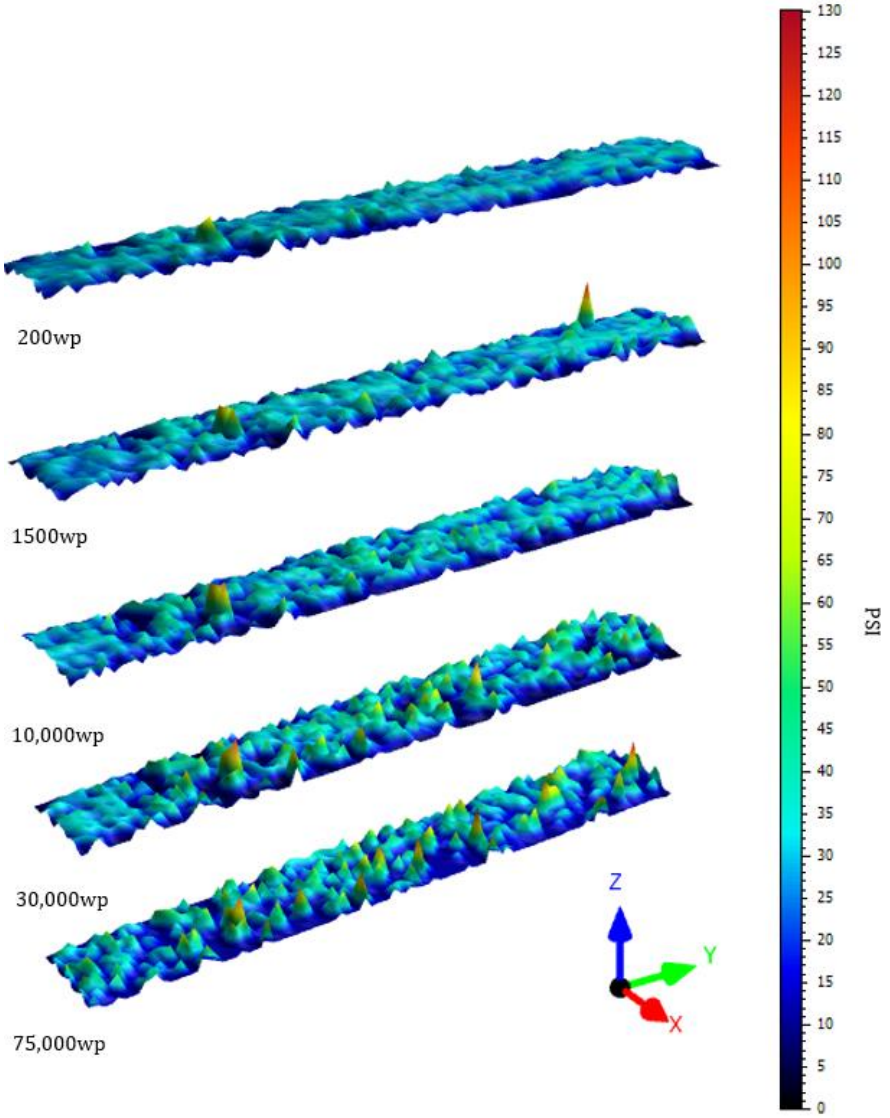

Figure 6.4. 4D Stacked Image for 200, 1500, 10,000, 30,000 and 75,000 wheel passes for test surface MAK.

Digital Surf MountainsMap software was used to generate a 4D stacked view of the merged pressure pad files. The 4D stacked view facilitated visual representation of the surface change due to simulated trafficking. Figure 6.4 shows a 4D stacked view of pressure contact for 200, 1500, 10,000, 30,000 and 75,000 wheel passes for test surface MAK.

The evolution of surface texture of the un-grooved asphalt surface can be seen. The number of points of elevated pressure increase as the surface wears and the coarse aggregate becomes exposed. The development of interface pressure for single aggregates can be seen.

6.4 Test Specimen MAD – FAA Standard Groove Dimension

Test specimen D represents the standard grooving dimensions recommended by FAA – 6mm x 6mm x 38mm centre-centre spacing. Figure 6.5 illustrates the pressure imaging data for test surface MAD and a photograph of the surface. The merged pressure pad image shows the greatest pressure pre trafficking occurs at the leading and trailing edges of the rib. The lowest contact pressure occurs in the centre of the rib width. This is similar to the idealised grooves cut in the aluminium plate.

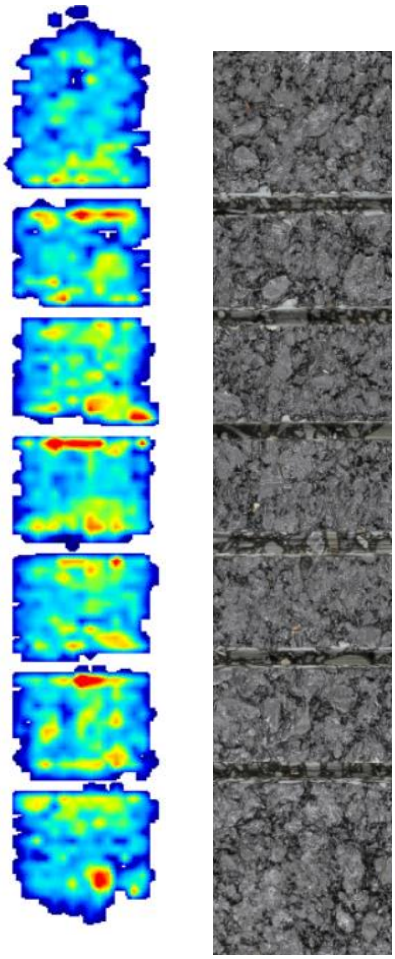

(a) (b)

Figure 6.5. Test surface MAD before trafficking (a) merged XSENSOR pressure pad data, (b) photograph.

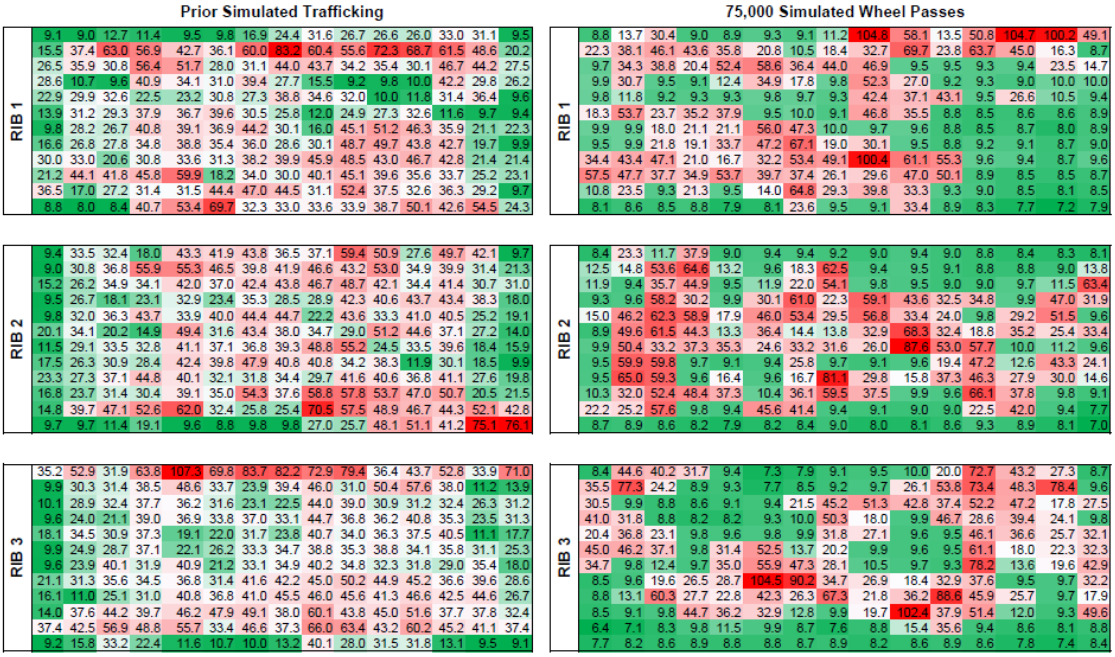

Figure 6.6. Comparison of XSENSOR data for test surface MAD, prior to trafficking and after 75,000 simulated wheel passes.

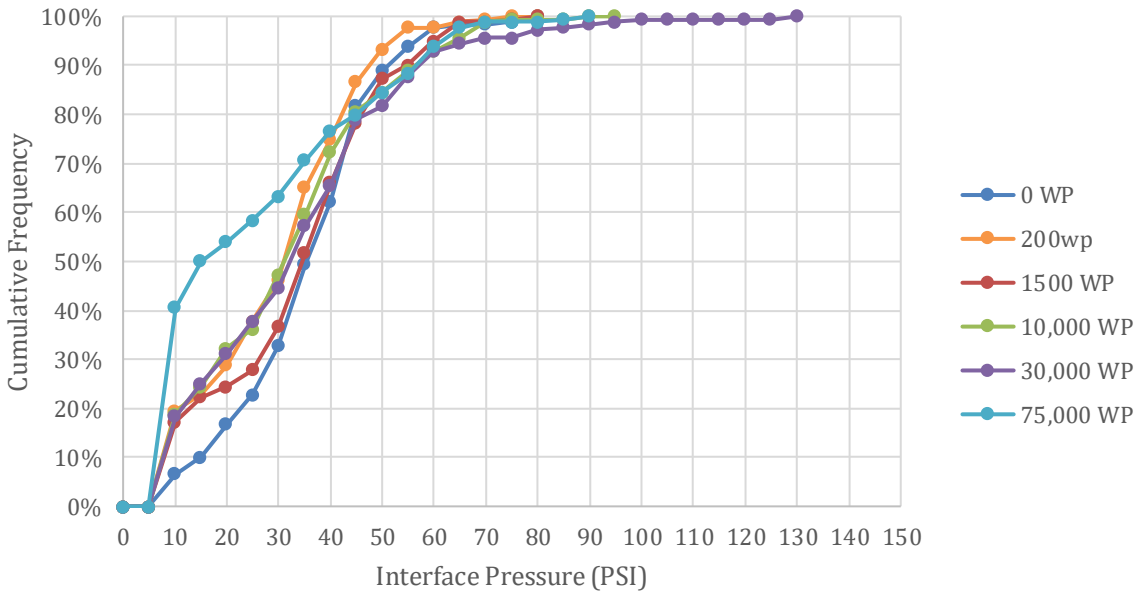

Figure 6.7. Evolution of pressure due to simulated trafficking for test specimen MAD.

Figure 6.6 compares the prior to trafficking and after 75,000 wheel passes using conditional formatting. This shows a significant change in the distribution of pressure within each rib.

Prior to trafficking it is greatest at the leading and trailing edges of the rib. After 75,000 wheel passes the leading and trailing edges of the rib have been worn resulting in lower pressures. The finer aggregate / mastic around the coarse aggregate particles in the rib have become worn resulting in the higher pressures recorded in the central parts of each rib.

Figure 6.7 shows the evolution of interface pressure due to simulated trafficking for test surface MAD. Interface pressure ranges between 5 and 130PSI. As simulated trafficking increases, the pressure curves plot to the left and then upwards for values less than 50 PSI. At 0 wheel passes, 37% of the pressure data is less than 30PSI. After 75,000 wheel passes 64% of the pressure data is less than 30PSI.

The peak pressures varied during simulated trafficking. For example, at 0 wheel passes it was between 75-80PSI, at 10,000 it was between 90-95PSI, at 30,000 it was between 125-130PSI and at the end of trafficking at 75,000 is had reduced to 85-90PSI. This is due to exposure of aggregate particles due to wear and re-orientation of particles.

Table 6.0. Pressure data for 5 rib widths for test surface MAD prior to trafficking.

Pressure Data					Average pressure for 5 ribs
Rib 1	Rib 2	Rib 3	Rib 4	Rib 5	
19.15	35.67	61.13	42.45	55.36	42.75 (trailing edge)
52.13	39.09	33.58	38.83	32.38	39.20
37.72	36.69	30.51	39.24	34.75	35.78
24.30	30.18	32.21	32.73	28.77	29.64
26.25	33.98	29.00	34.68	33.69	31.52
24.82	32.63	30.40	33.28	34.61	31.15
32.91	33.12	30.48	33.43	35.34	33.06
32.64	30.52	37.64	28.99	33.97	32.75
35.15	33.86	36.04	34.81	31.38	34.25
35.83	38.56	41.68	36.96	32.45	37.09
33.89	44.16	47.67	42.77	41.67	42.03
35.46	28.81	19.28	17.02	21.69	24.45 (leading edge)

Table 6.1. Pressure data for 5 rib widths for test surface MAD after 75,000 wheel passes.

Pressure Data					Average pressure for 5 ribs
Rib 1	Rib 2	Rib 3	Rib 4	Rib 5	
38.76	11.95	23.33	19.02	16.80	21.97 (trailing edge)
33.01	21.15	31.98	32.99	30.82	29.99
27.82	21.42	27.94	28.03	35.79	28.20
17.39	32.62	22.93	38.50	18.76	26.04
17.13	36.23	22.52	30.04	21.44	25.47
21.53	32.58	27.90	28.70	24.67	27.07
17.04	34.03	27.78	24.71	31.35	26.98
20.76	23.86	32.64	22.00	25.23	24.90
36.75	31.25	34.29	29.02	28.37	31.94
33.06	31.08	29.74	35.51	16.59	29.19
19.94	21.94	10.94	14.68	21.47	17.79
11.05	8.39	8.43	8.41	8.92	9.04 (leading edge)

Tables 6.0 and 6.1 compare the pressure distributions for test surface MAD before and after simulated trafficking. Prior to trafficking the greatest pressure is at the edges. As the edges wear the higher pressure values move towards the centre of the ribs due to increasing tyre enveloping.

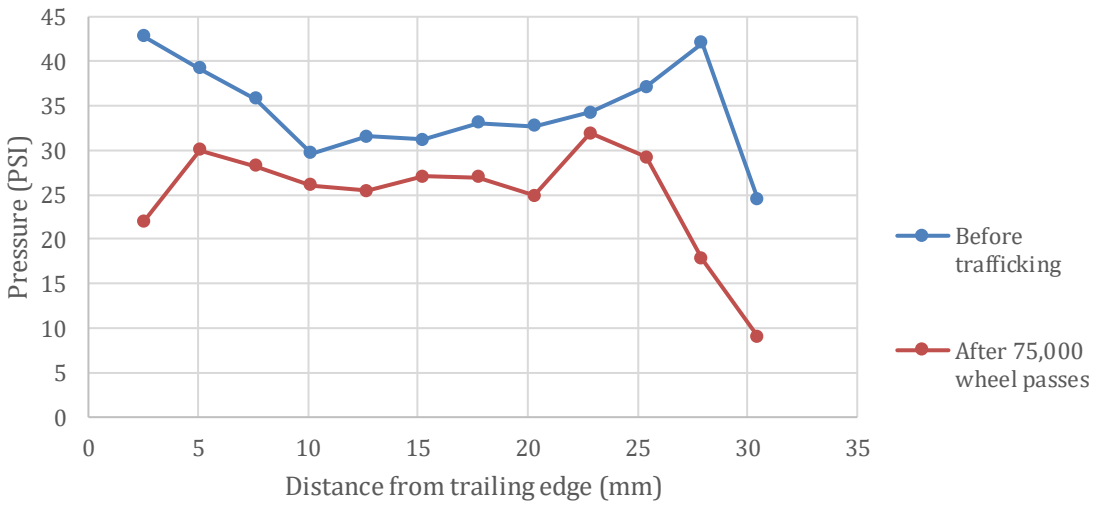

Figure 6.8. Change in averaged pressure distribution due to simulated trafficking for test surface MAD.

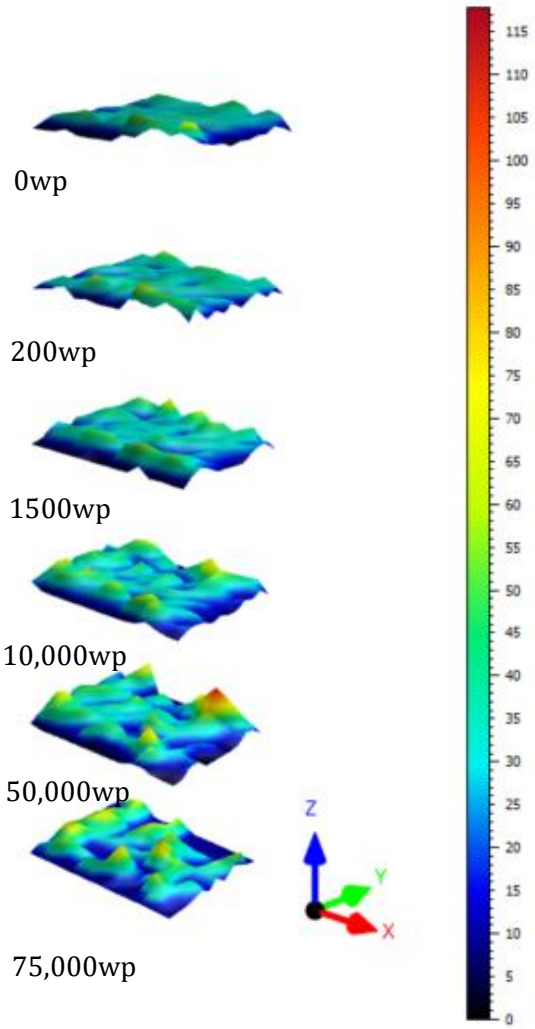

Figure 6.9. 4D Stacked image for same rib of test surface MAD.

Figure 6.8 compares the averaged pressure data for the 5 ribs before and after 75.000 wheel passes. This shows an overall reduction in average pressure and the higher pressures moving from the edges towards the centre of the rib.

Figure 6.9 shows a 4D Stacked view of pressure for the same rib of test surface MAD at 0, 200, 1500, 10,000, 50,000 and 75,000 wheel passes. This shows how the pressure distribution evolves as the rib is worn during simulated trafficking.

6.5 Test Surface MAF

Test surface MAF has a rib width of 22 mm and a groove width of 3mm. Figure 6.10 compares the merged pressure pad with a photograph of the surface before trafficking. The merged pressure pad image shows limited increase in pressure associated with the rib edges. The 3mm groove width makes it difficult for tyre enveloping. The 3mm groove width is just within the 2.54 mm spatial resolution of the pressure pad. The merged pressure image shows the prominent pressure influence of a single aggregate shown as red,

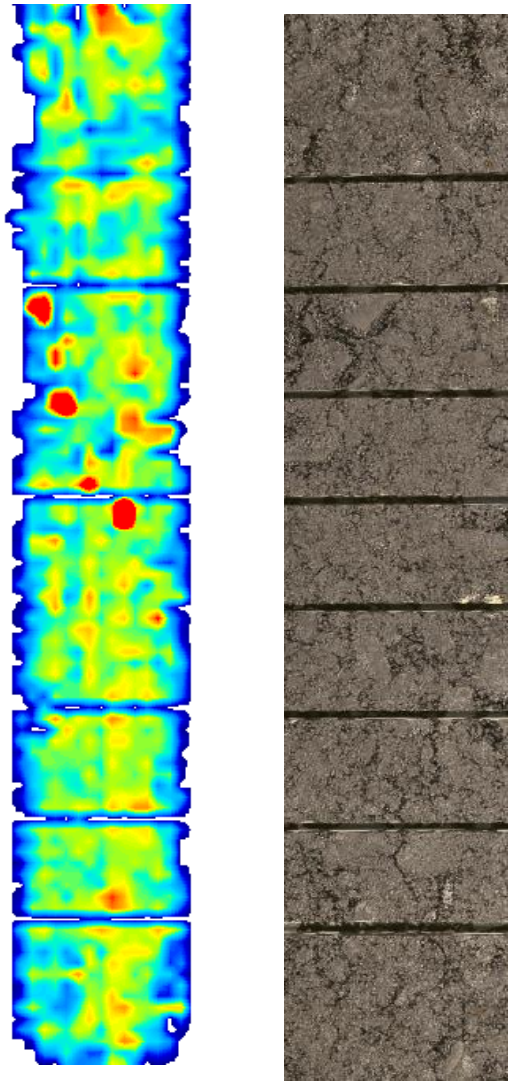

(a) (b)

Figure 6.10. Test surface MAF before trafficking (a) merged XSENSOR pressure pad data , (b) photograph.

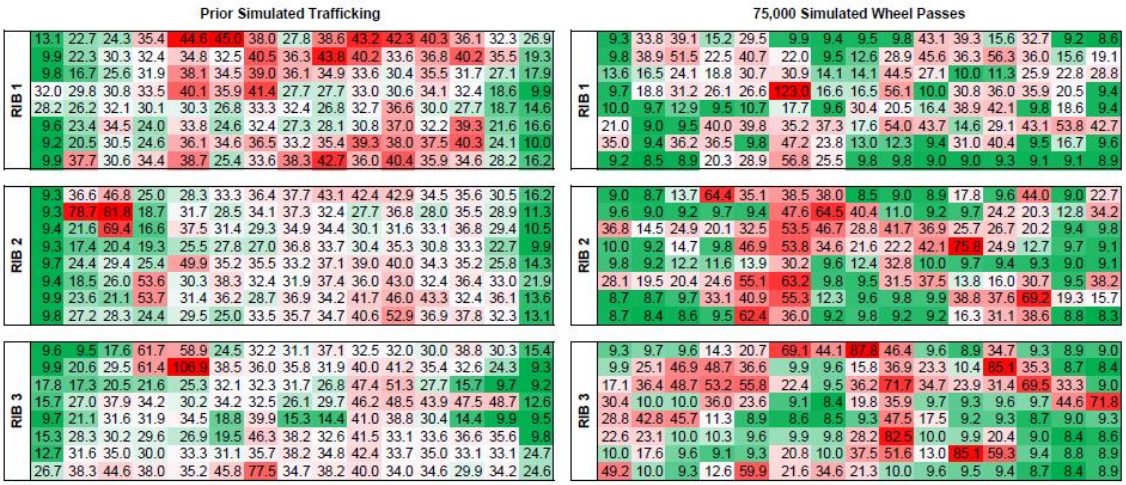

Figure 6.11. Comparison of XSENSOR data for test surface MAF, prior to trafficking and after 75,000 simulated wheel passes.

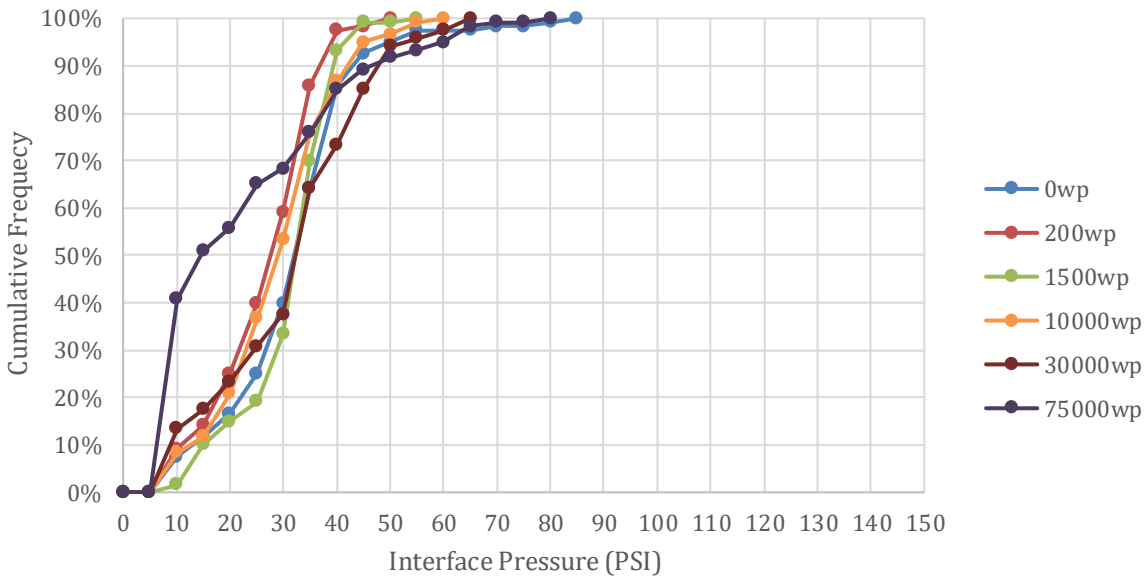

Figure 6.12. Evolution of pressure due to simulated trafficking for test specimen MAF.

Figure 6.11 compares the conditional formatted pressure data before trafficking and after 75,000 wheel passes. Figure 6.12 plots the frequency distribution curves. The interface pressure ranges from 5 to 85PSI. The curves are similar with the exception of 75,000 wheel passes where the surface has experienced most trafficking.

Table 6.2. Pressure data for 7 rib widths for test surface MAF prior to trafficking.

Pressure Data							Average pressure for 7 ribs
Rib 1	Rib 2	Rib 3	Rib 4	Rib 5	Rib 6	Rib 7	
34.04	33.24	30.75	40.21	32.21	33.88	34.15	34.07 (trailing edge)
32.55	34.71	36.88	42.15	30.26	28.34	31.18	33.72
29.51	30.39	25.75	28.30	31.90	33.12	31.86	30.12
30.50	25.30	34.32	32.31	32.40	31.19	29.27	30.75
28.43	31.21	24.08	28.99	31.12	30.33	31.57	29.39
27.67	32.04	30.46	33.03	32.62	28.89	30.45	30.74
29.98	32.57	32.29	31.64	31.87	31.33	33.73	31.92
32.17	30.76	38.42	32.36	31.41	34.30	34.71	33.45 (leading edge)

Table 6.3. Pressure data for 7 rib widths for test surface MAF after 75,000 wheel passes.

Pressure Data							Average pressure for 7 ribs
Rib 1	Rib 2	Rib 3	Rib 4	Rib 5	Rib 6	Rib 7	
20.94	22.45	26.09	15.65	19.68	11.31	11.11	18.17 (trailing edge)
29.68	21.39	27.37	22.56	26.52	22.41	19.76	24.24
22.21	28.54	36.84	19.17	25.66	24.49	29.40	26.61
31.14	26.47	22.52	25.62	28.47	24.90	28.65	26.82
17.75	13.21	18.30	28.66	22.81	25.94	27.38	22.01
32.67	27.15	18.15	32.93	26.44	26.07	30.30	27.68
22.65	25.22	23.99	22.07	34.76	22.48	23.26	24.92
15.47	18.26	18.86	16.63	27.46	27.06	27.84	21.65 (leading edge)

Tables 6.2 and 6.3 compare the pressure distributions for test surface MAF before and after simulated trafficking. Prior to trafficking there is a fairly uniform distribution across the ribs. The 3mm groove has limited affect. After 75,000 wheel passes, the edges of the 3mm grooves have some wear causing a reduction in pressure at both edges.

Figure 6.13 compares the averaged pressure data for the 7 ribs before and after 75.000 wheel passes. This shows a reduction in average pressure and the wear of the 3mm grooves.

Figure 6.14 shows a 4D Stacked view of pressure for the same rib of test surface MAD at 0, 200, 1500, 10,000, 50,000 and 75,000 wheel passes. This shows how the pressure distribution evolves as the rib is worn during simulated trafficking.

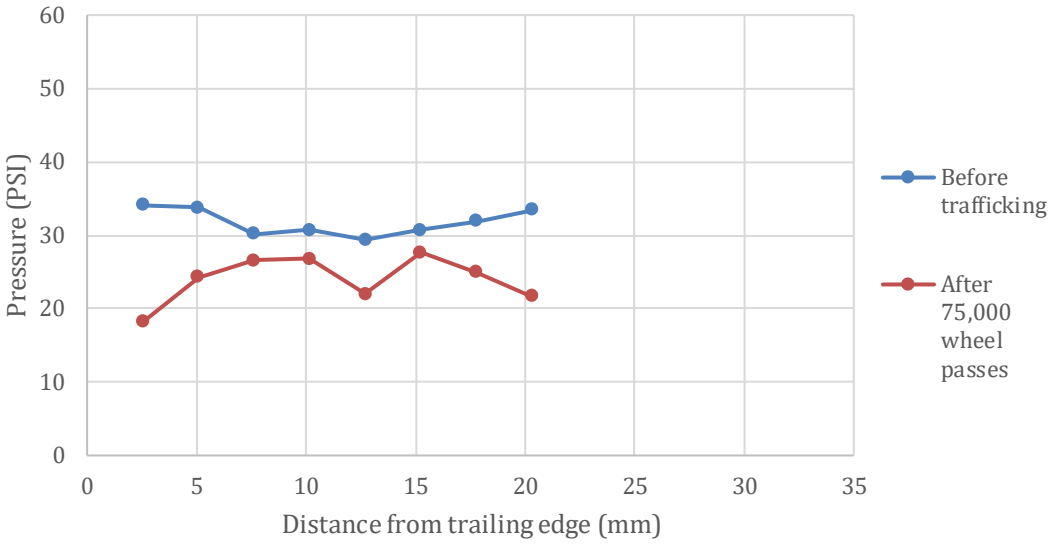

Figure 6.13. Change in averaged pressure distribution due to simulated trafficking for test surface MAF.

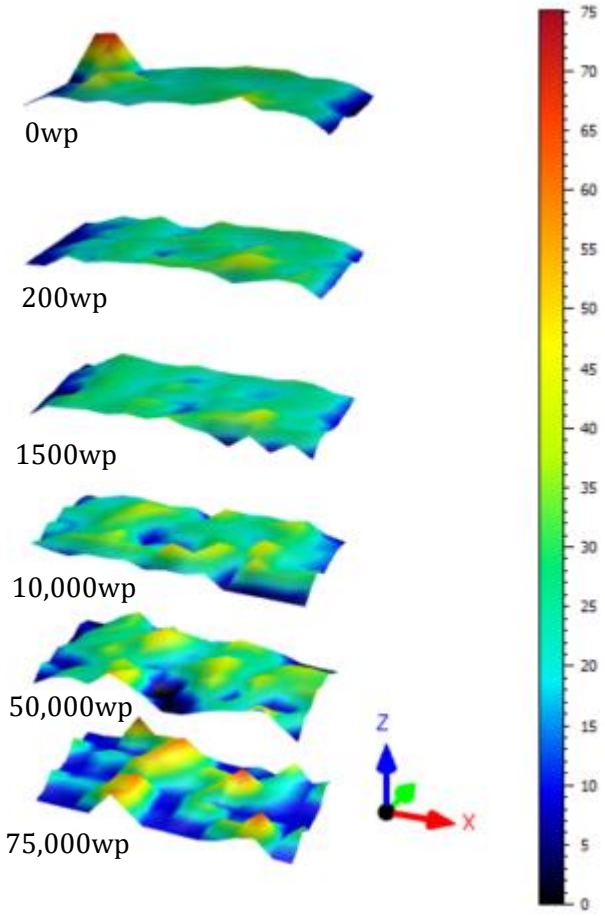

Figure 6.14. 4D Stacked image for same rib of test surface MAF.

6.6 Test Surface MAA

Test surface MAA has a rib width of 12mm and a groove width of 10mm. Figure 6.15 compares the merged pressure pad with a photograph of the surface before trafficking. The merged pressure pad image shows high values for each rib and its aggregate particles.

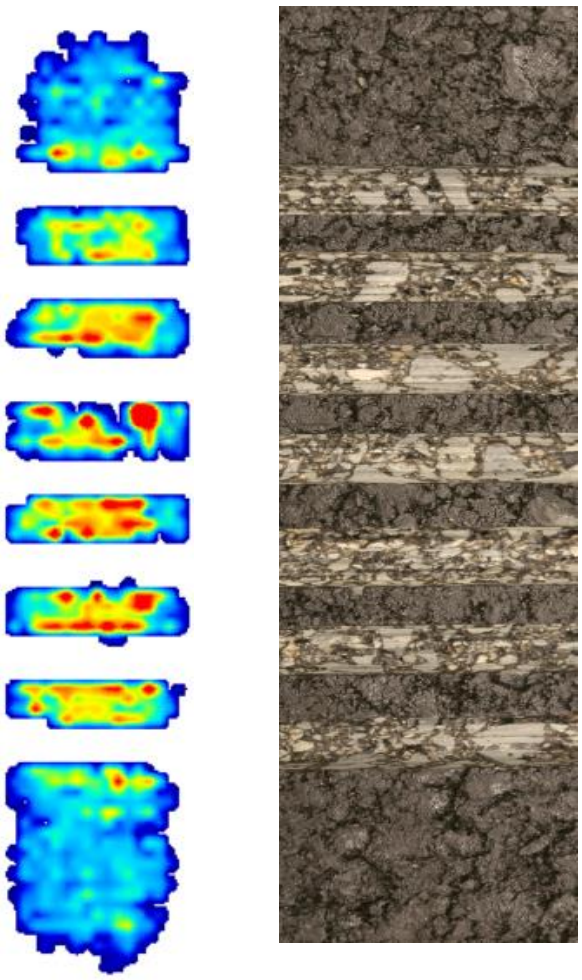

(a) (b)

Figure 6.15. Test surface MAA before trafficking (a) merged XSENSOR pressure pad data, (b) photograph.

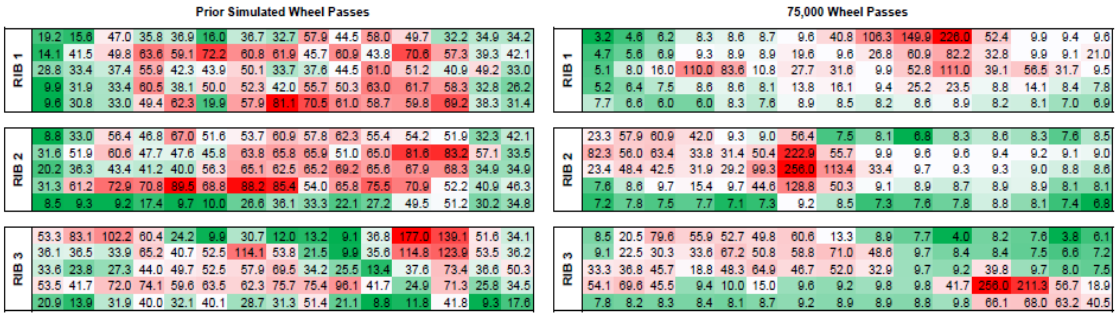

Figure 6.16. Comparison of XSENSOR data for test surface MAA, prior to trafficking and after 75,000 simulated wheel passes.

Figure 6.16 compares the pressure data for test surface MAA before and after 75,000 wheel passes. The data before trafficking shows high contact pressures experienced by the 12mm rib width and 10mm groove widths. After 75,000 wheel passes the narrow rib had suffered considerable wear with very high pressures recorded for the few remaining individual aggregate particles.

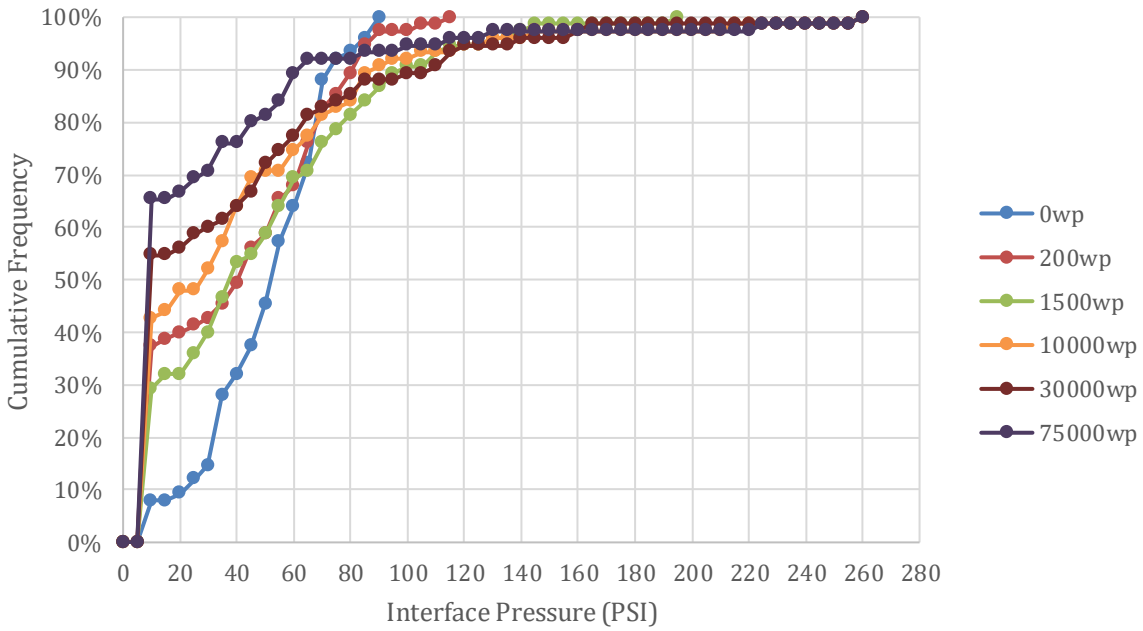

Figure 6.17. Evolution of pressure due to simulated trafficking for test specimen MAA.

This excessive and rapid wear experienced by the 12mm rib is illustrated in the comparison of cumulative frequency curves plotted in Figure 6.17. Interface pressure ranges from 5 to 260PSI.

Table 6.4. Summarizes the average interfacial contact pressure along the width of the asphalt groove for test specimen MAA prior trafficking.

Pressure Data						Average pressure for 6 ribs
Rib 1	Rib 2	Rib 3	Rib 4	Rib 5	Rib 6	
36.75	48.92	55.76	63.07	58.25	66.04	54.80 (trailing edge)
52.18	56.79	55.20	51.91	56.05	50.02	53.69
42.86	51.39	41.94	62.87	47.19	52.03	49.71
44.41	64.91	58.13	52.21	69.86	45.03	55.76
48.87	25.01	26.71	9.30	10.65	8.78	21.55 (leading edge)

Table 6.5. Summarizes the average interfacial contact pressure along the width of the asphalt groove for test specimen MAA subjected to 75,000 wheel passes.

Pressure Data						Average pressure for 6 ribs
Rib 1	Rib 2	Rib 3	Rib 4	Rib 5	Rib 6	
43.56	21.49	25.80	13.07	10.40	11.20	20.92 (trailing edge)
21.07	44.11	29.31	57.79	40.92	19.36	35.43
40.22	48.81	30.88	41.03	57.69	26.74	40.90
11.43	22.36	55.11	12.16	24.38	10.17	22.60
7.69	7.73	22.19	8.25	8.29	8.13	10.38 (leading edge)

Tables 6.4 and 6.5 compare the pressure distributions for test surface MAA before and after simulated trafficking. Prior to trafficking the averaged pressures are much higher than the other test surfaces. The 10mm groove is having a significant effect. After 75,000 wheel passes, the 12mm ribs have suffered excessive wear particularly at both edges.

Figure 6.18 compares the averaged pressure data for the 6 ribs before and after 75.000 wheel passes. This shows reduction in average pressure and wear of the ribs.

Figure 6.19 shows a 4D Stacked view of pressure for the same rib of test surface MAA at 0, 200, 1500, 10,000, 50,000 and 75,000 wheel passes. This shows how the pressure distribution evolves as the rib is worn during simulated trafficking.

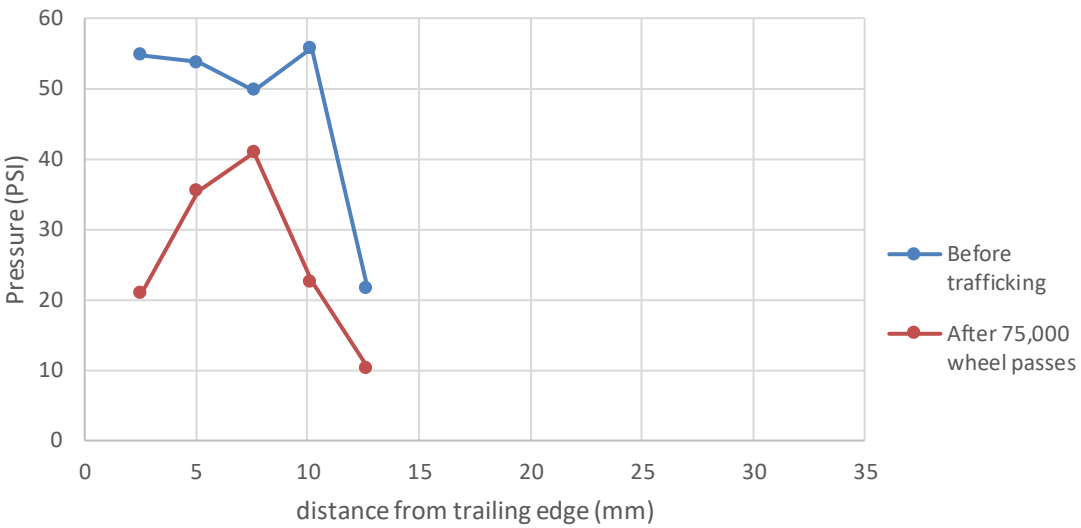

Figure 6.18. Change in averaged pressure distribution due to simulated trafficking for test surface MAA.

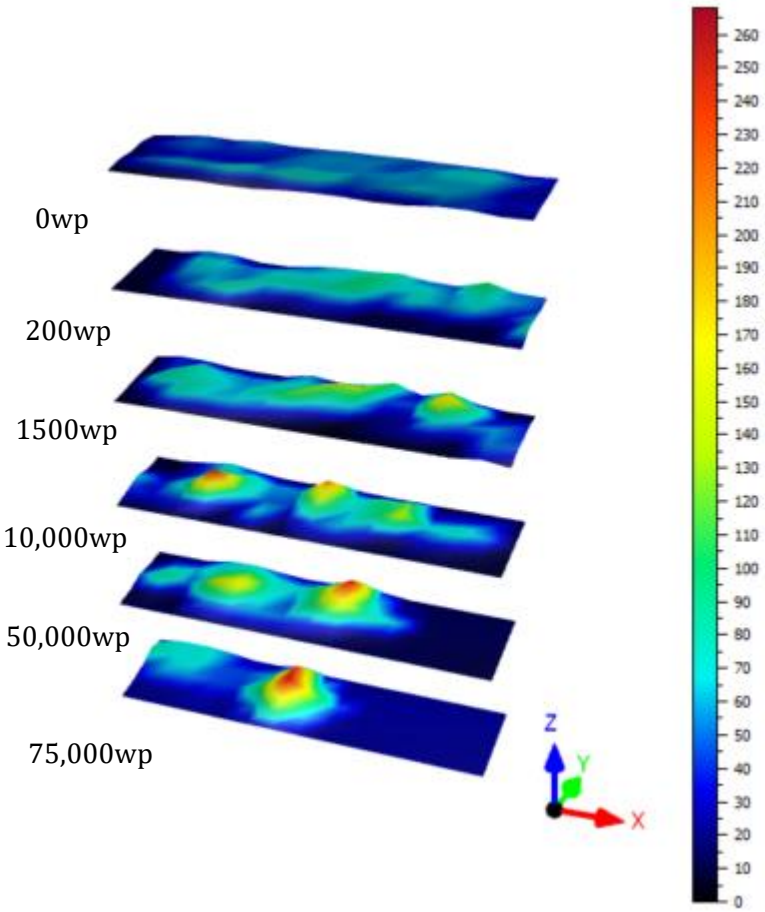

Figure 6.19. 4D Stacked image for same rib of test surface MAA.

6.7 Comparison of Groove Dimensions

Figures 6.20 to 6.23 compare evolution of cumulative frequency curves at 0, 200, 1500 and 75,000 wheel passes. Figure 6.20 compares the test surfaces prior to RTM testing. Test surface MAK and MAF are almost identical. This is due to the 3mm gap width.

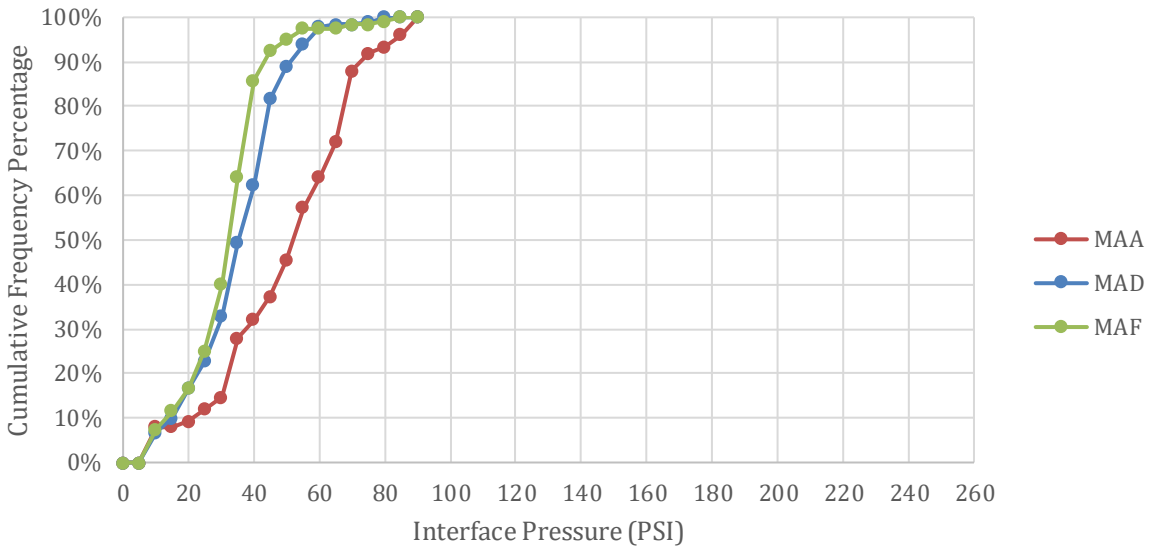

Figure 6.20. Comparison of cumulative frequency curves prior to simulated trafficking.

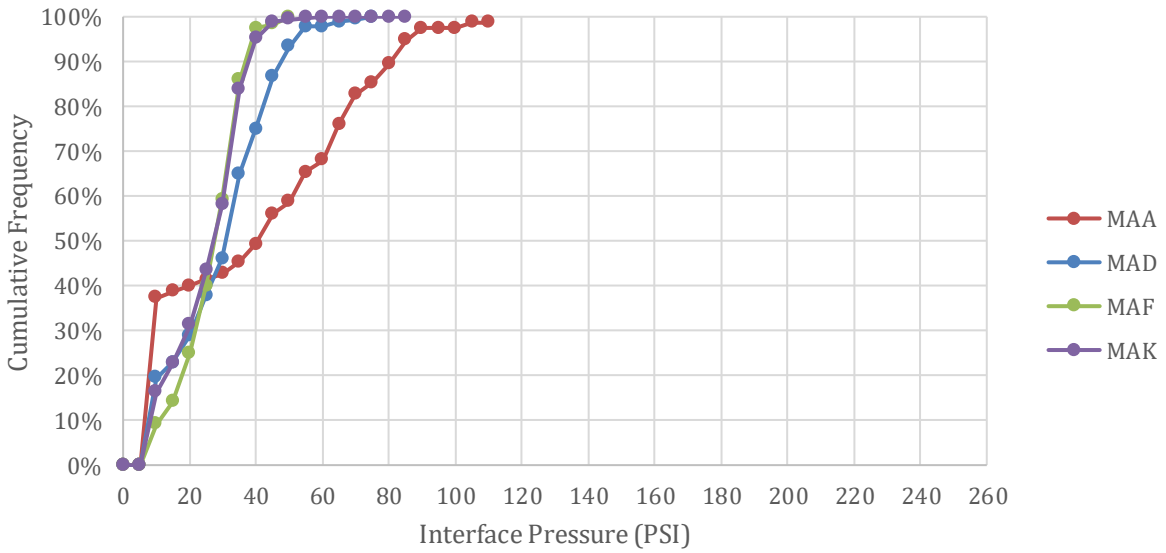

Figure 6.21. Comparison of cumulative frequency curves after 200 wheel passes.

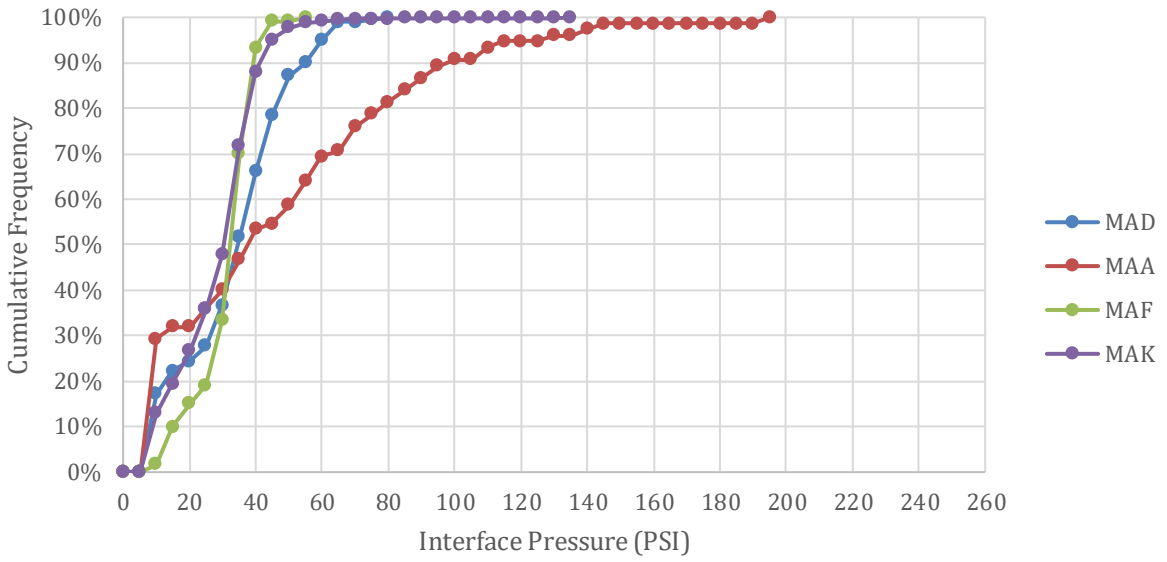

Figure 6.22. Comparison of cumulative frequency curves after 1500 wheel passes.

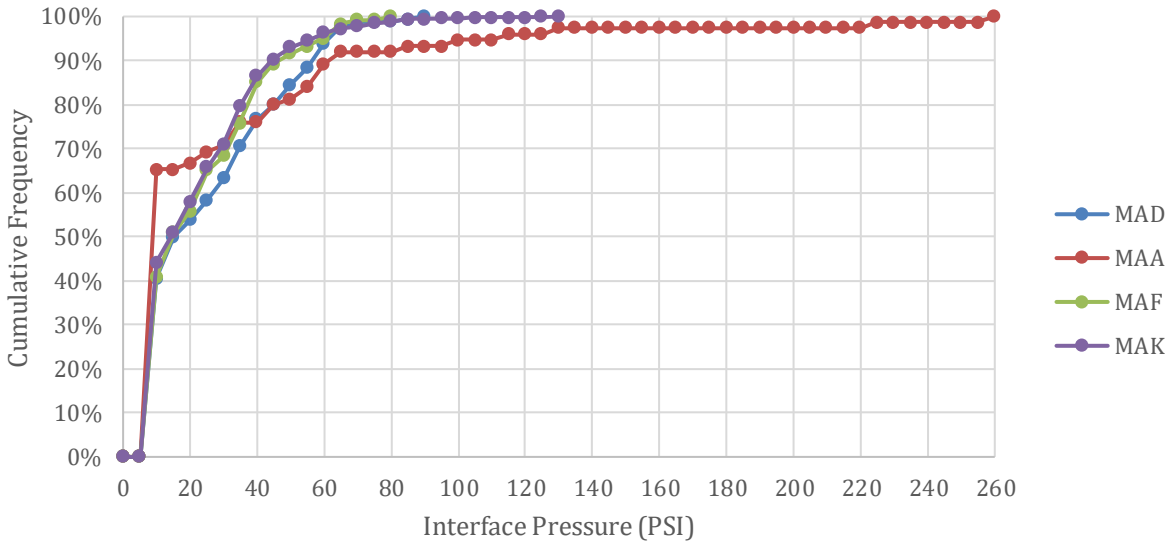

Figure 6.23. Comparison of cumulative frequency curves after 75,000 wheel passes.

Figure 6.21 – 6.23 compares the cumulative frequency curves 200, 1500 and 75,000 wheel passes. Test surfaces MAD, MAF and MAK are still comparable. However, MAA is starting to suffer wear. This becomes more pronounced as simulated trafficking continues.

6.8 Summary

- The distribution of pressure across the asphalt groove prior simulated trafficking shows greater pressure is concentrated either on or in the immediate periphery of the leading and trailing edges of the groove. Interface Pressure dissipates towards the centre of the groove.
- At 75,000 wheel passes the pressure relationship identified is the same for test specimen D. However, this changes for MAF and MAA. For test specimen MAF and MAA the higher pressure severity moves towards the centre.
- The data considered collectively does not support the hypothesis ideology that either the leading or trailing edge generates higher interface pressures, either pre or post trafficking.
- Interface pressure values differ for each test specimen groove dimensions.
- The general relationship of cumulative frequency of interface pressure Vs simulated trafficking shows that cumulative frequency of lower interface pressures increases, and the cumulative frequency of higher interface pressures also increase.
- The cumulative frequency data shows that test specimen MAF and MAK are almost identical, with interface pressures increasing with decreasing rib width / groove spacing ratio.
- The pressure envelope amongst the cumulative frequency data decreases as the data aligns closer with increased simulated trafficking. The pressure interface relationship amongst the different groove dimensions remains consistent with increased trafficking i.e., Test specimen A has the greatest frequency of lower contact pressures than the remaining ribs and simultaneously has the greatest quantity of higher frequency pressures than the remaining ribs.
- The groove dimensions vs pressure statistics show that there is a rank order. The rank of the highest interface pressure for the groove specimens is MAA > MAD > MAF> MAK. The rib width / groove spacing ratio suggests that the smaller groove width contributes to lower interface pressures and vice versa.

CHAPTER 7.

EVOLUTION OF GROOVED MARSHALL ASPHALT SKID RESISTANCE

7.1 Introduction

This chapter investigates the evolution of skid resistance for the grooved Marshall Asphalt test surfaces. Skid resistance was determined using the pendulum at 0° and 10° as specified in BS EN 13036-4. Details of the Marshall Asphalt test surfaces are given in Table 4.5. The Road Test Machine (RTM) was used to simulate traffic and wear the test surfaces. Pendulum testing was carried out at 0, 10, 100, 200, 400, 800, 1500, 3000, 6000, 10,000, 20,000, 30,000, 50,000 and 75,000 wheel passes. Trafficking intervals were based on a visual observation of the test surfaces during simulated trafficking.

7.2 PTV for grooved Marshall Asphalt test surfaces

The British Pendulum was used to determine the change in skid resistance due to simulated trafficking. Slider 57 was used. The number 57 represents the hardness of the rubber used. Slider 57 would normally be used as it is similar to car tyre rubber. The rubber pad dimensions are 76.2 ± 0.5 mm wide, 24.4 ± 1.0 mm and 6.35 ± 0.5 mm thick. The swing length was 126 ± 1mm. Testing was carried out at a laboratory temperature of 20 ± 2°C.

BS EN 13036-4 states for surfaces bearing a regular pattern such as grooved asphalt testing should be made with the slider operating at an angle of approximately 80° to the grooves; essentially offsetting the normal operating angle by 10°. Four testing scenarios were considered.

- Testing condition 1 – PTV 90° Angle – Dry Conditions
- Testing condition 2 – PTV 80° Angle – Dry Conditions
- Testing condition 3 – PTV 90° Angle – Wet Conditions
- Testing condition 4 – PTV 80° Angle – Wet Conditions

Figures 7.0, 7.2, 7.4 and 7.6 plot the development of PTV data for the 4 test conditions. The PTV data is given in Appendix B. A significant amount of PTV change is possible during the early periods of RTM testing. This can be difficult to see in a standard scatter plot. If the x-axis is plotted on a log-scale then this early life change is much easier to visualise. Figures 7.1, 7.3, 7.5 and 7.7 plot the same data using wheel passes on a log scale.

Figures 7.10 and 7.12 plot the difference between PTV measured at 80 and 90 degrees. A positive number means the 80 PTV value is greater. Figures 7.11 and 7.13 plot the same data using a log scale to better show early life changes.

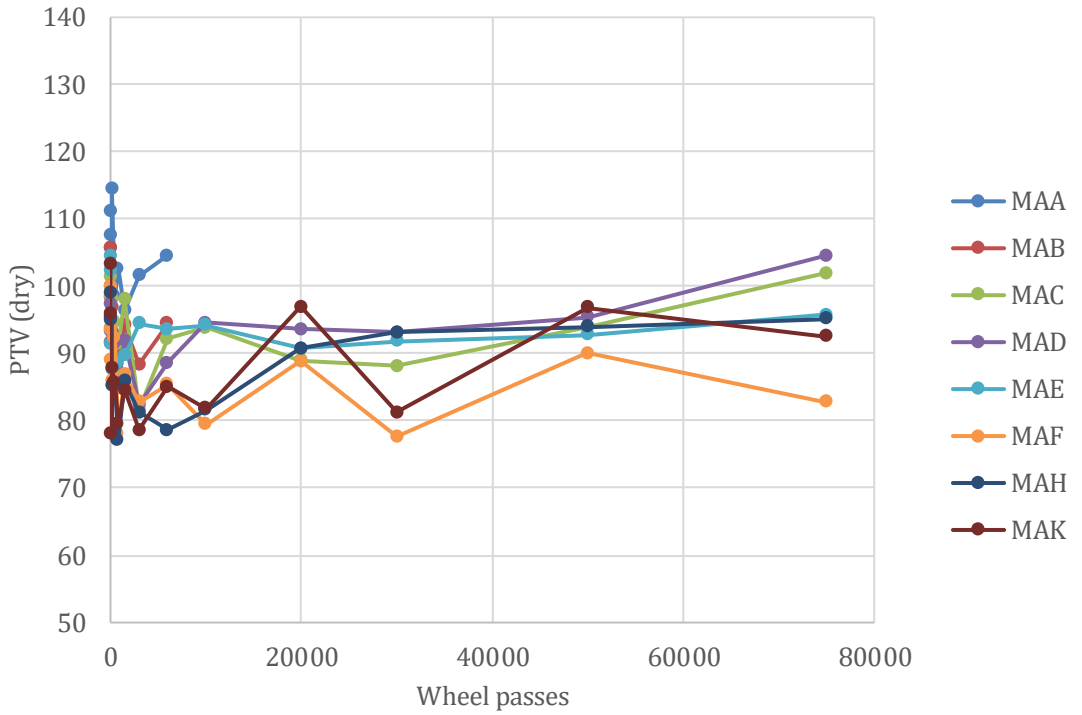

Figure 7.0. Test condition 1 - PTV 90° angle, dry.

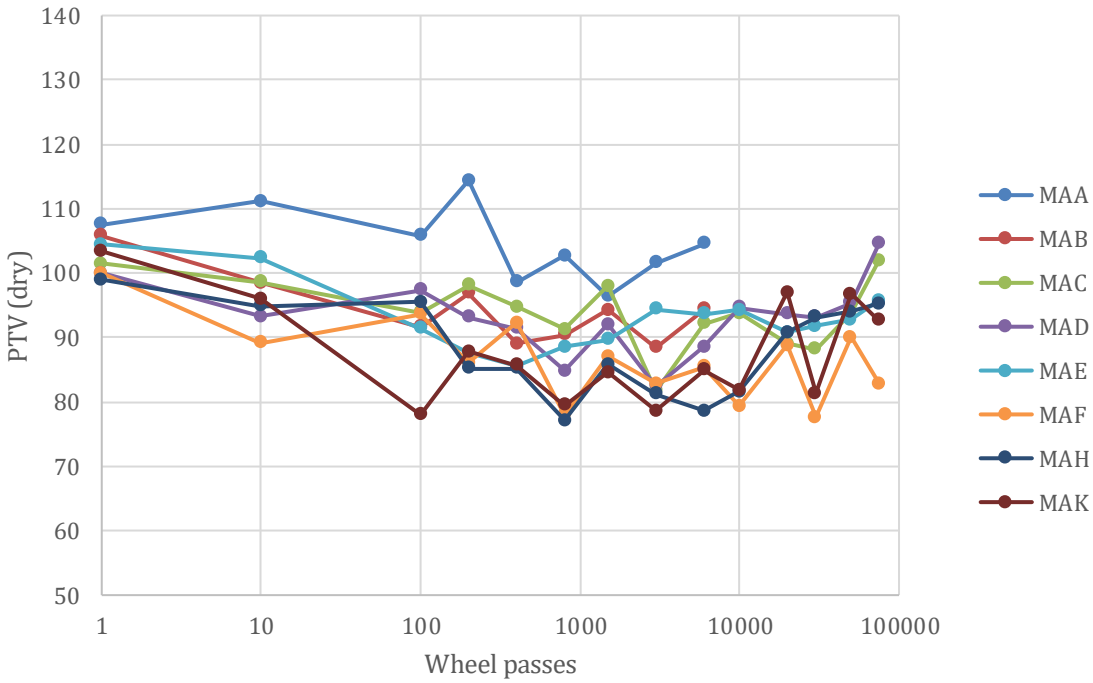

Figure 7.1. Test condition 1 - PTV 90° angle, dry, log scale.

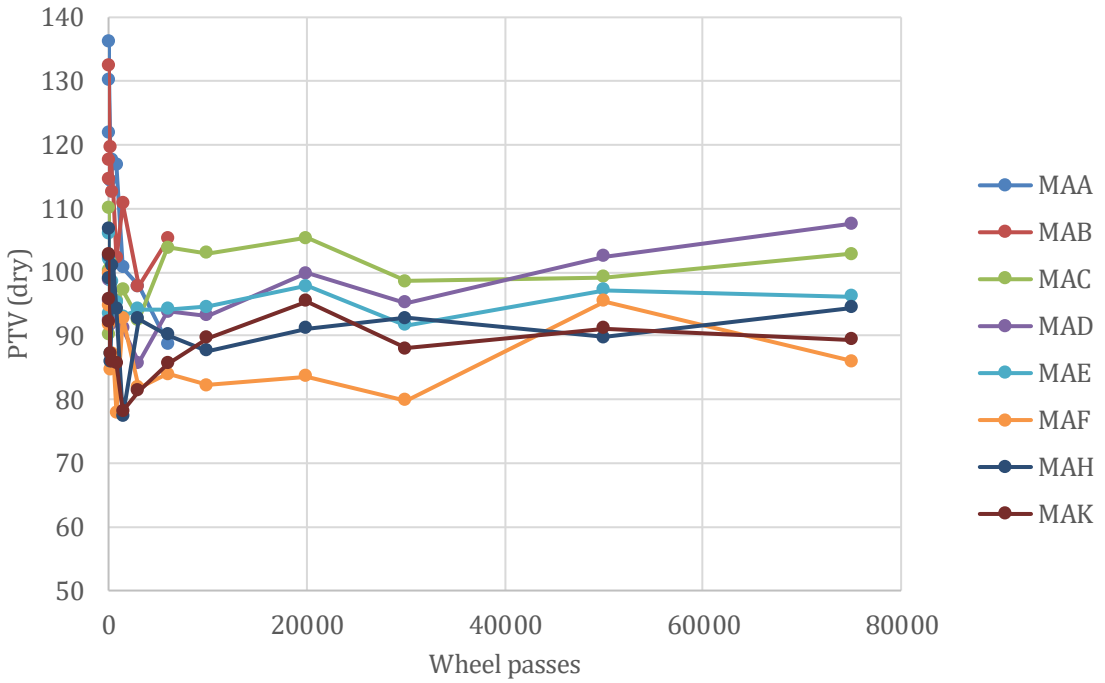

Figure 7.2. Test condition 2 - PTV 80° angle, dry.

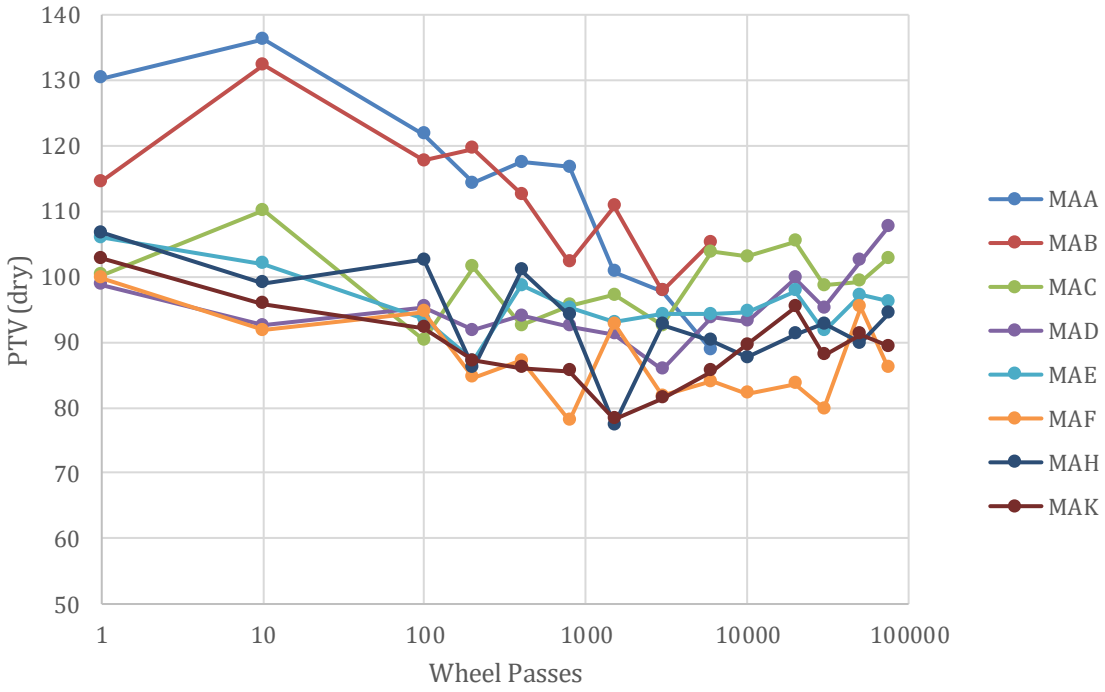

Figure 7.3. Test condition 2 - PTV 80° angle, dry, log scale.

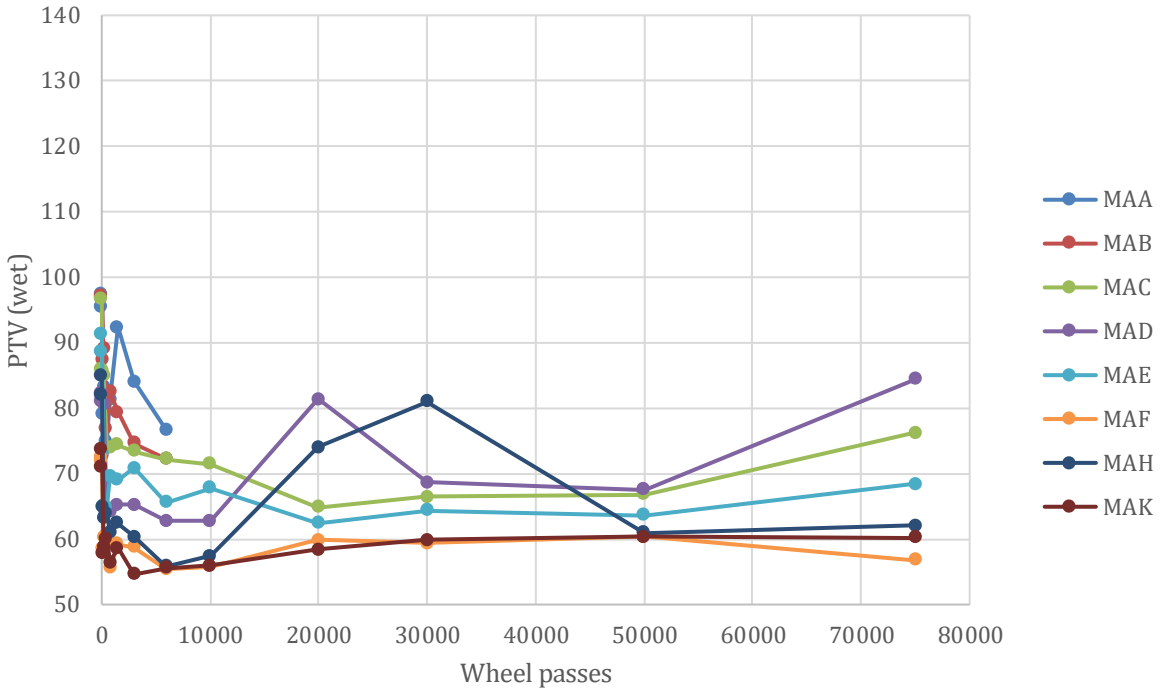

Figure 7.4. Test condition 3 - PTV 90° angle, wet.

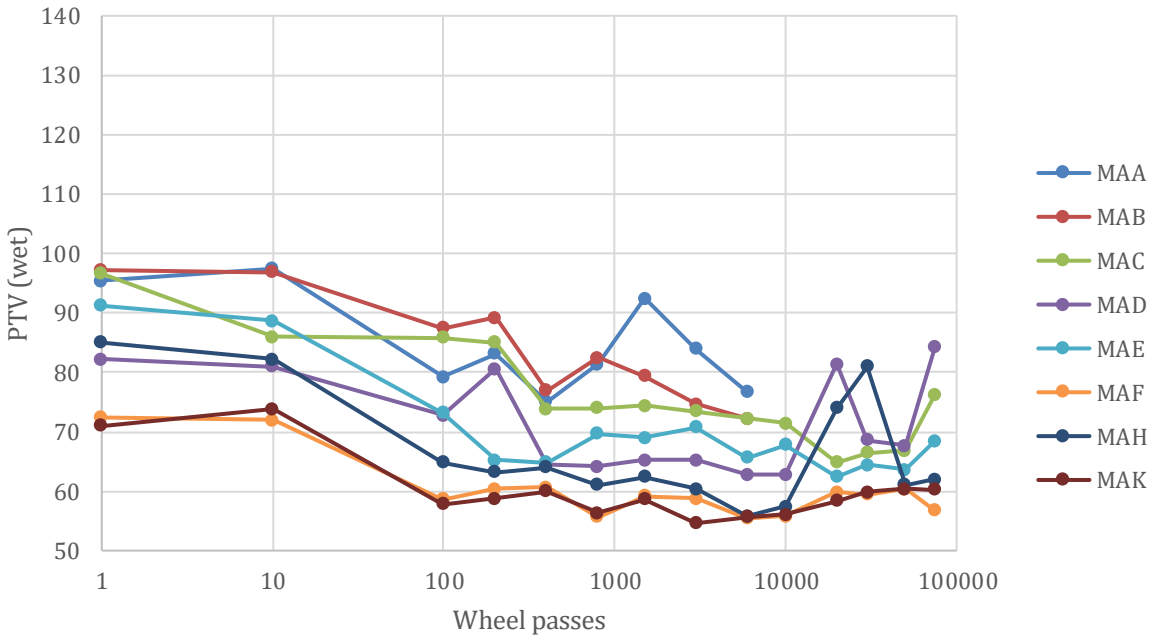

Figure 7.5. Test condition 3 - PTV 90° angle, wet, log scale.

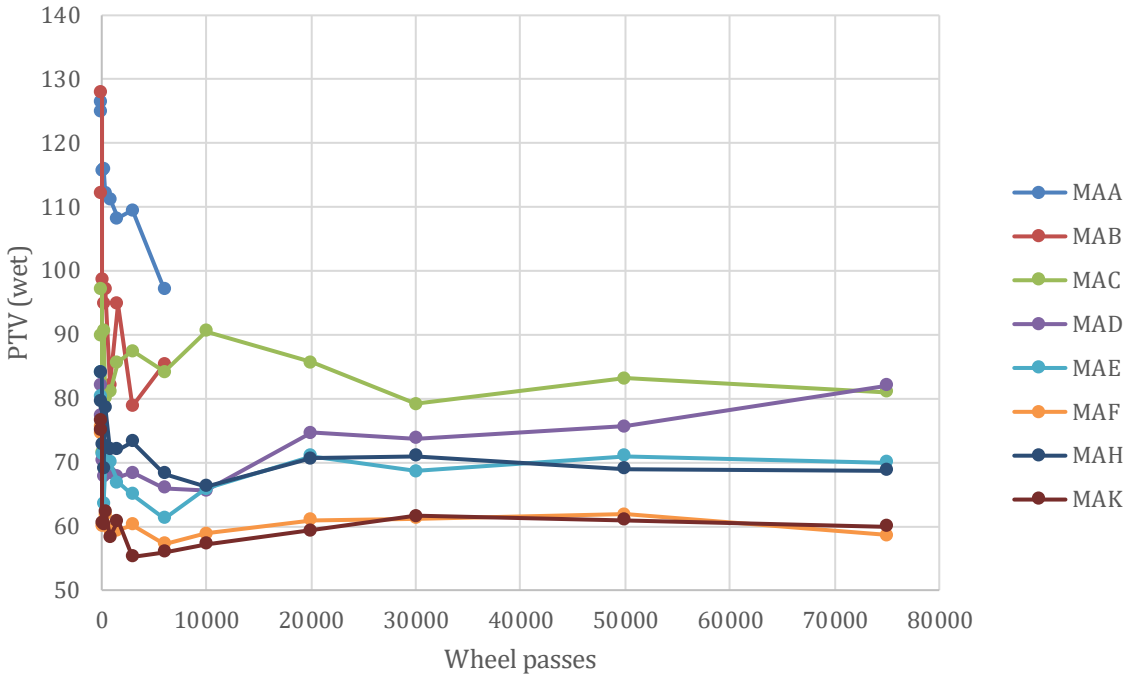

Figure 7.6. Test condition 4 - PTV 80° angle, wet.

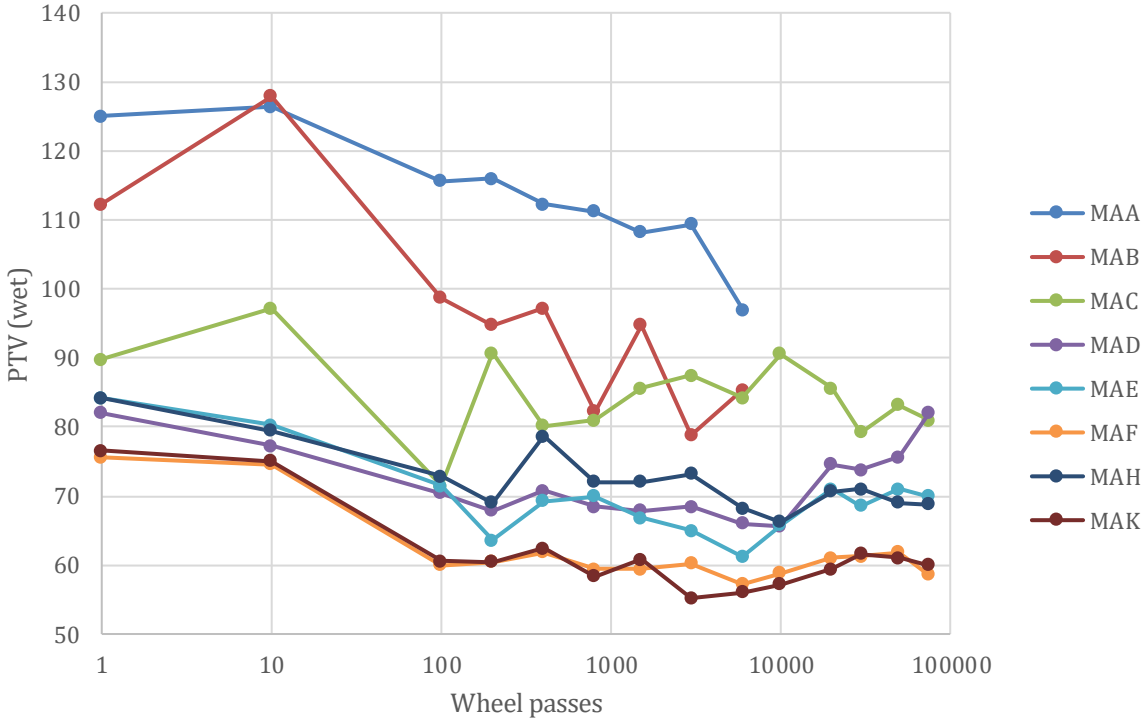

Figure 7.7. Test condition 4 - PTV 80° angle, wet, log scale.

The plots show that all groove dimensions (rib and groove width) considered contribute positively to skid resistance. However, the level of improvement is based on the groove dimensions. All plots show that test surface MAA and MAB generate the greatest PTV. The data shows that testing stopped at 6,000 wheel passes due to the ribs being worn.

Similarly, all plots show that MAF and MAK contribute to the lowest pendulum values. These test specimens represent the un-grooved control and the test specimen with a 3mm groove. The plot shows test surface MAK and MAF to be almost identical and remain relatively constant, this demonstrates the limited influence of the 3mm groove width on PTV. Whilst test surface MAA and MAB were similar in dimensions the effect of grooving on the pendulum interaction is evident in the difference of PTV values as they are both significantly different.

A general comparison between the dry and wet conditions demonstrates there is greater fluctuations within the data for each test specimen. This is demonstrated as the spikes shown in the data plots. These may be attributed to wear of the groove as aggregates may become re-orientated or removed due to simulated trafficking.

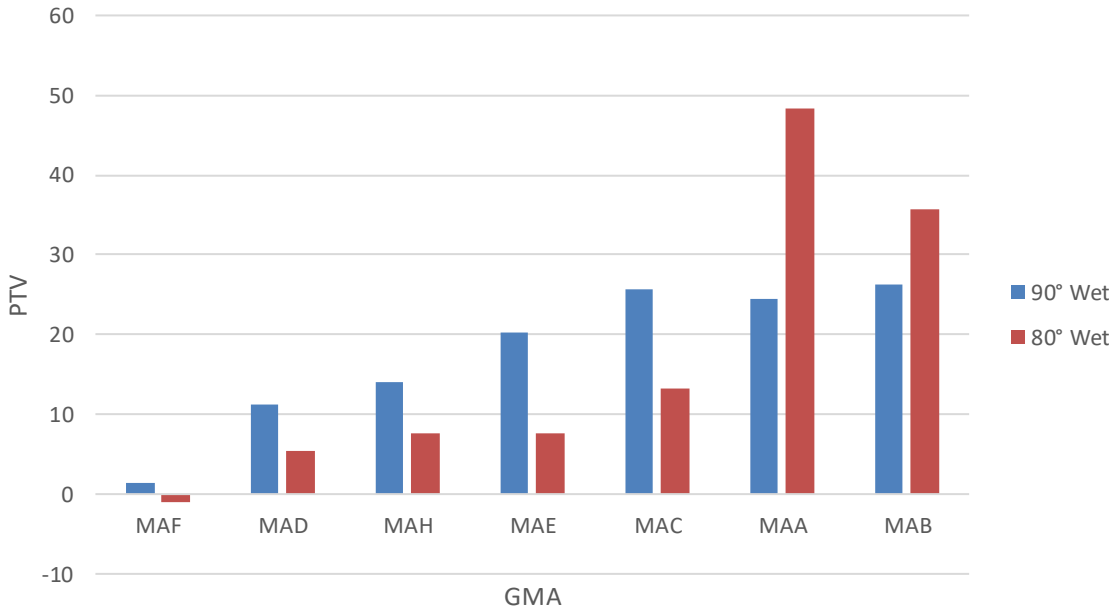

Figure 7.8 Difference between un-grooved control and grooved test specimens for wet conditions

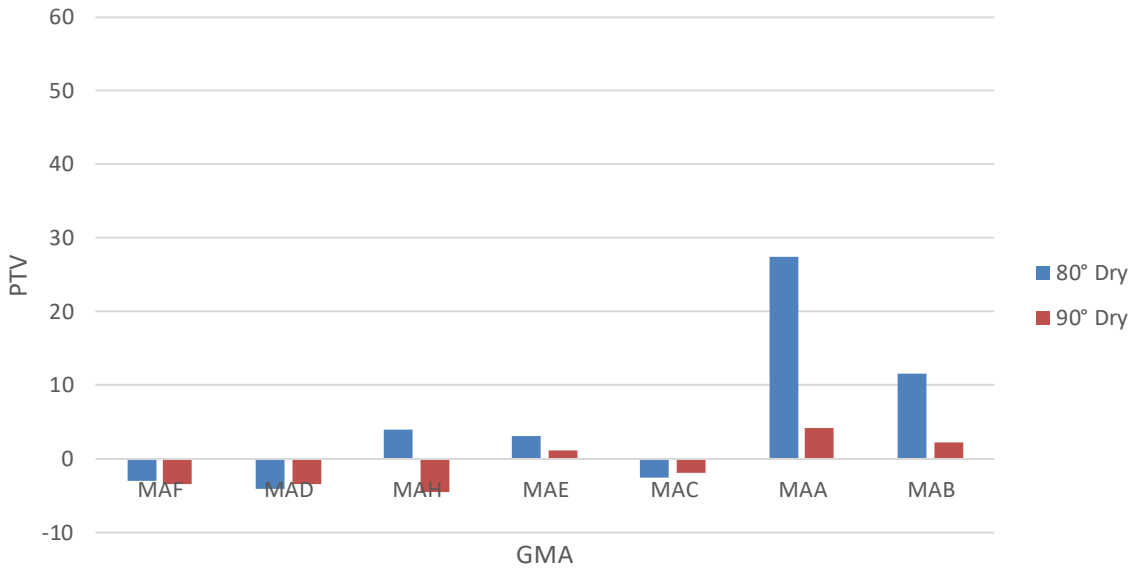

Figure 7.9. Difference between un-grooved control and grooved test specimens for dry conditions

Figure 7.8 and 7.9 plot the difference between the initial pendulum testing prior to simulated trafficking for the un-grooved control and the grooved test specimens for both rotation angles for wet and dry conditions respectively. Figures 7.10 plot the difference between 80 and 90 degree PTV, dry and 7.11 plot the same data using wheel passes on a log scale. The wet conditions shown in Figure 7.12 and 7.13 demonstrate that all groove dimensions apart from MAF contribute positive PTV.

The level of improvement would appear to depend on groove dimensions. The plots show that for some test specimens testing at 90 degrees generates higher PTV than 80 degrees whereas for other test specimens testing at 80 degrees generates higher PTV than 90 degrees.

The dry conditions show that generally there is lower PTV difference apart from test specimens MAA and MAB. Generally, the plots show the dry conditions to be somewhat complicated with MAF, MAD and MAC and increases with MAA and MAB. The plots show conflicting PTV values for MAH with an increase and decrease in PTV dependent on the rotation angle.

The difference between the dry conditions illustrate that generally 80 degrees generate higher PTV where as for the wet conditions a greater number of data point show 80 degrees to generate lower PTV.

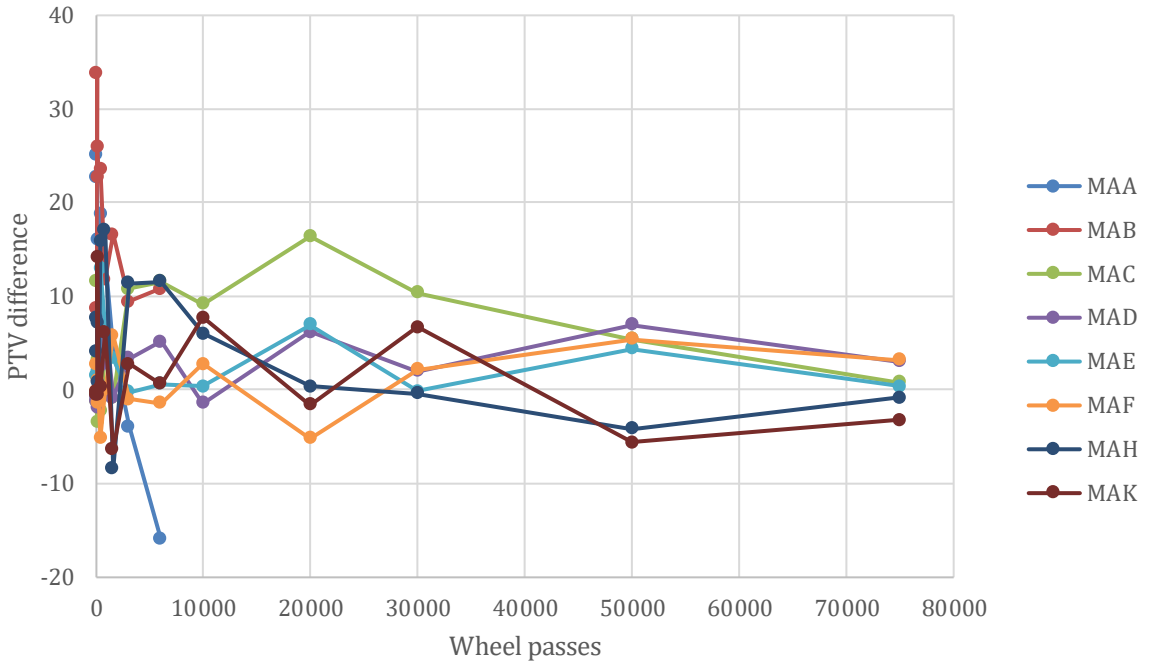

Figure 7.10. Difference between 80 and 90 degree PTV, dry.

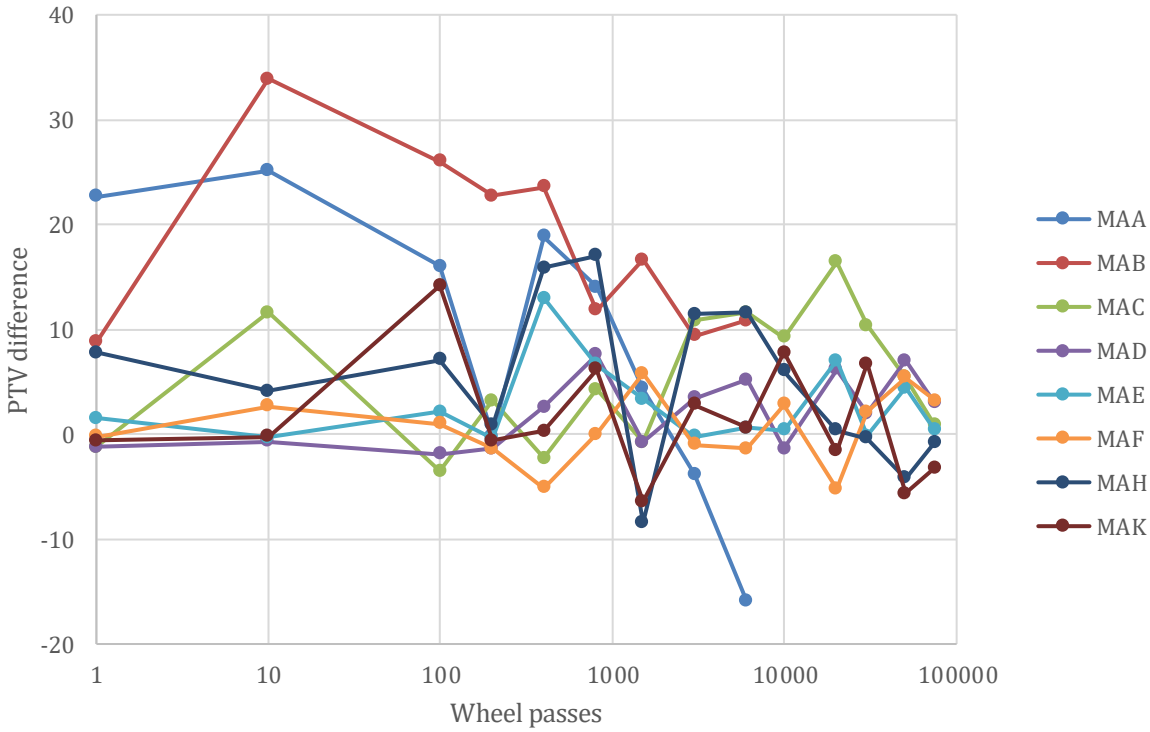

Figure 7.11. Difference between 80 and 90 degree PTV, dry, log scale.

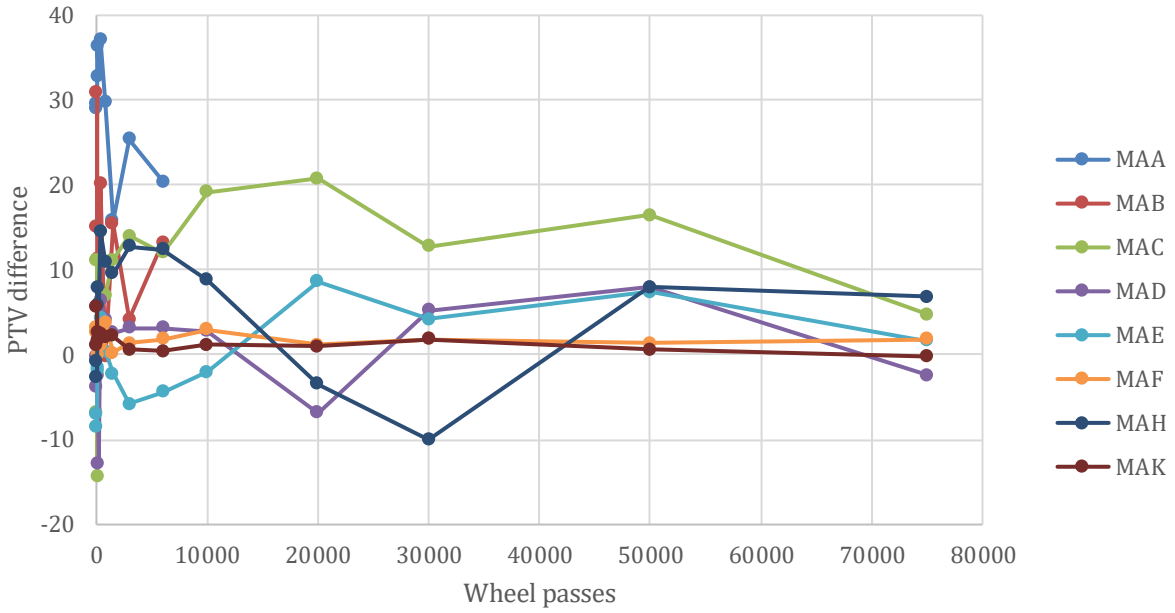

Figure 7.12. Difference between 80 and 90 degree PTV, wet.

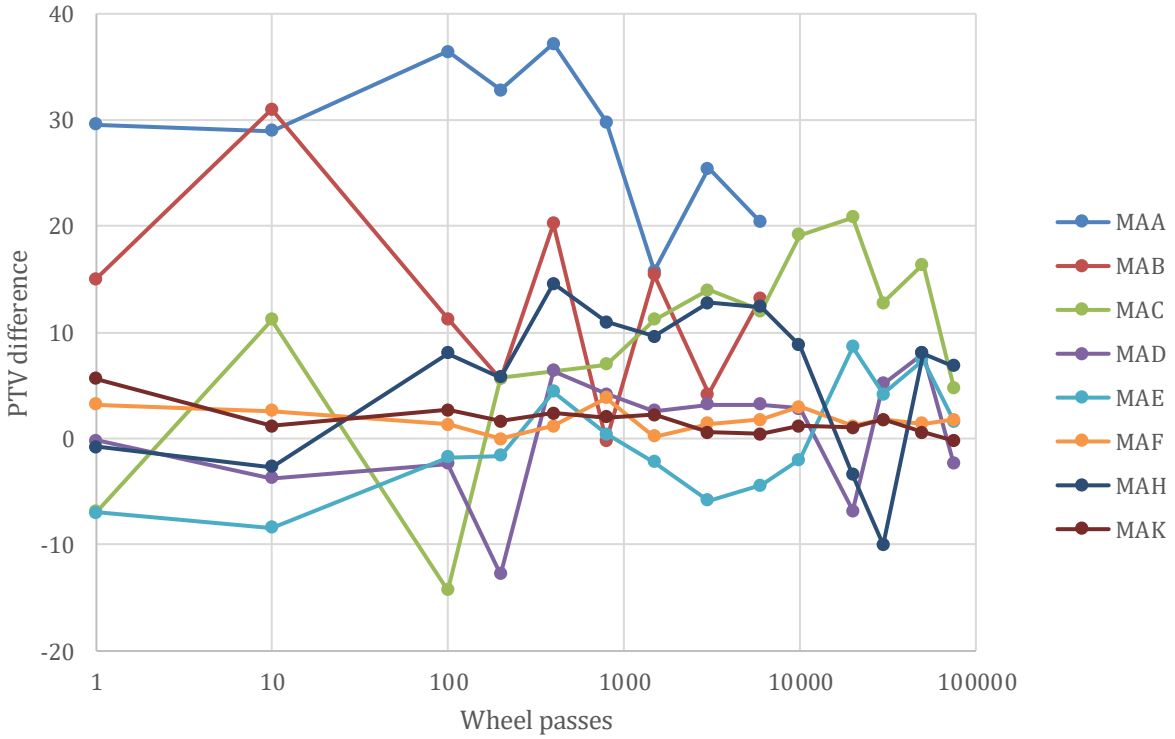

Figure 7.13. Difference between 80 and 90 degree PTV, wet, log scale.

Table 7.0. Average difference between 80 and 90 degree PTV testing.

Test condition	Test surface							
	MAA	MAB	MAC	MAD	MAE	MAF	MAH	MAK
Dry	9.02	18.18	5.42	2.11	2.73	0.62	4.87	1.45
Wet	28.49	12.86	8.59	0.52	-0.47	1.76	5.78	1.65

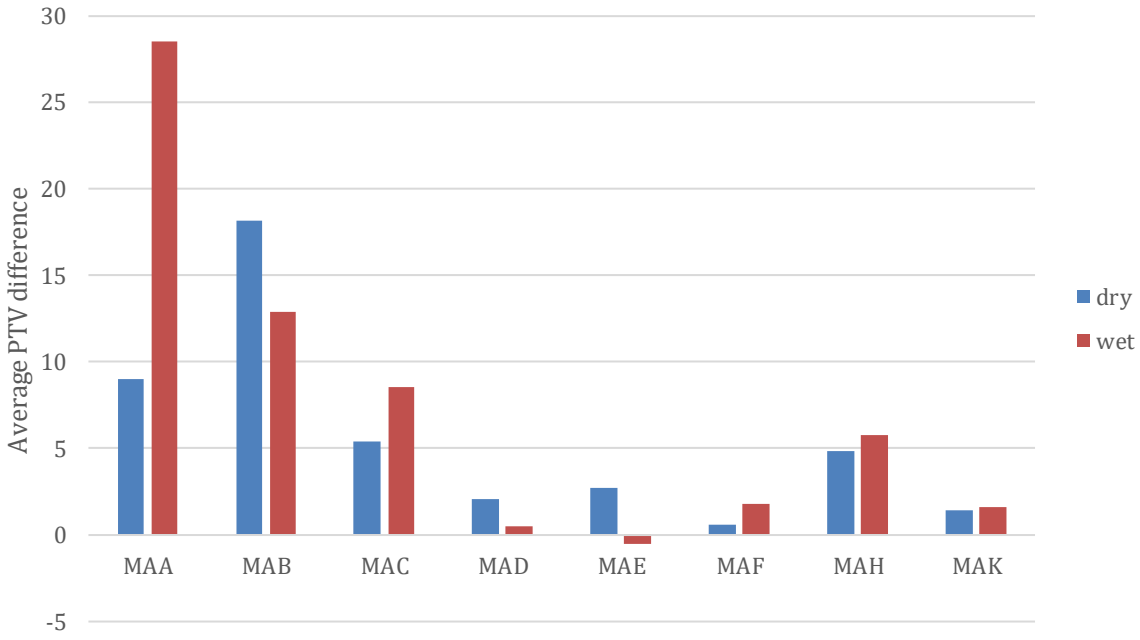

Figure 7.14. Comparison of test surfaces

Table 7.0 and Figure 7.14 shows the average PTV difference between 80° and 90° degree testing. Testing between 80° and 90° is considered in sub section 3.6. This was calculated by determining the average of the total PTV for all wheel passes tested and calculating the average difference between testing at 80° degrees and 90°. The average data for 90° degrees is subtracted from 80°.

The table shows those test surfaces with a significant groove to rib ratio for example MAA and MAB to have the greatest difference between 80° and 90° testing. The plots show that for the control test surface that 80° and 90° testing had limited influence on PTV by a margin of just1.5 PTV units.

The data presented in Figure 7.14 shows two distinct regions within the data; MAA, MAB, and MAC show significantly higher average PTV differences as opposed to MAD, MAE, MAF, MAH and MAK, which show lower average PTV differences. The plot suggests that groove to rib dimensions less than MAC had a limited increase in PTV. The data could imply there is an optimum rib width / groove spacing ratio between this point. Figure 7.14 demonstrates that the measurement of PTV is sensitive to the grooving dimensions.

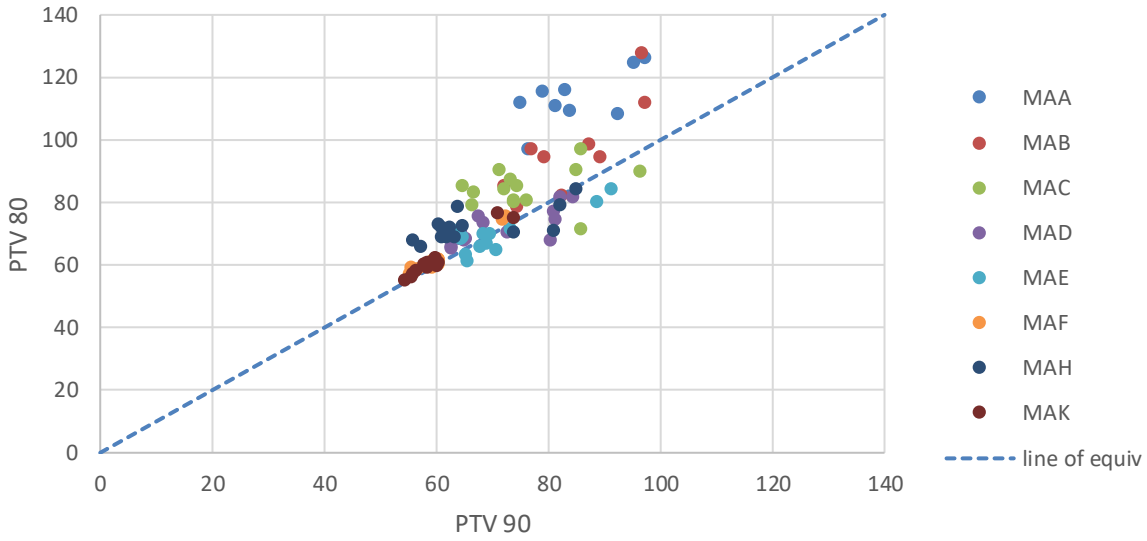

Figure 7.15. Comparison of PTV data tested at 80 and 90 degrees

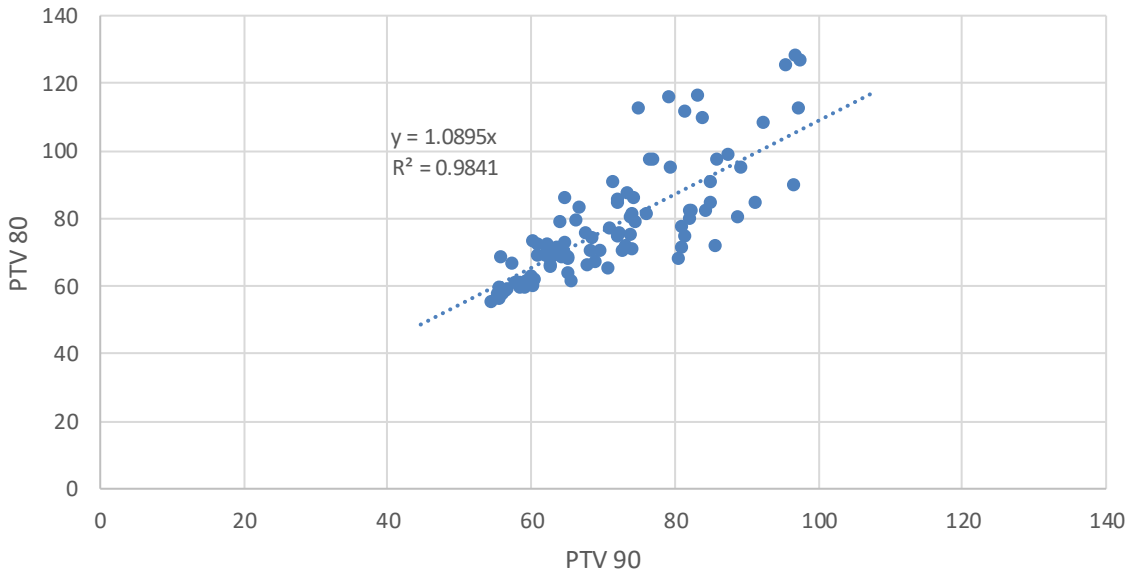

Figure 7.16. Relationship of PTV data tested at 80 and 90 degrees

Figures 7.15 and 7.16 show the relationship between the data tested at 80 and 90 degrees. The data shows that PTV broadly aligns along the line of equivalence. However, the plot demonstrates that the greatest concentration of data points to be on the side of 80 suggesting testing at 80 degrees generates higher PTV values. The plot demonstrates the broad range of PTV values amongst the different groove dimensions. It has been demonstrated that it is possible to achieve greater PTV depending on the groove dimensions.

7.2.1 Groove Dimension Vs PTV

Comparison of Groove width against PTV and Rib width individually against PTV is not appropriate as both contribute to PTV during pendulum testing. Therefore, a comparison of the rib width / groove spacing ratio was considered to better understand of how the dimensions contribute to PTV.

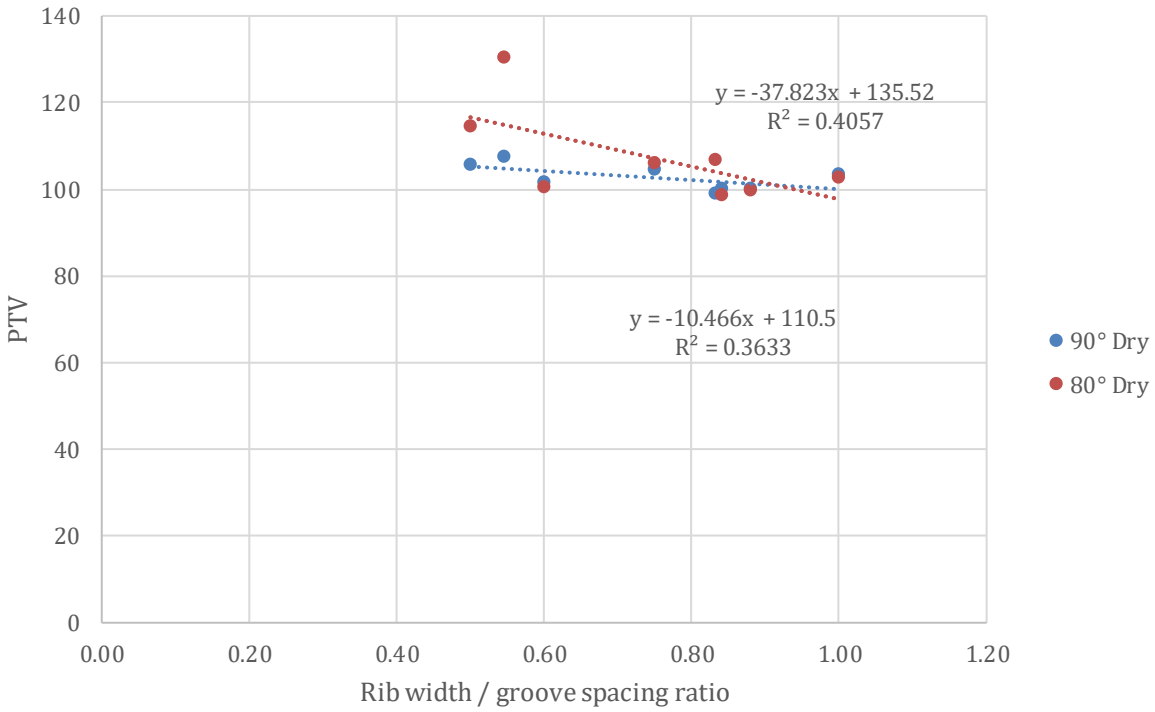

Figure 7.17. Rib width / groove width spacing ratio against dry PTV prior to simulated trafficking

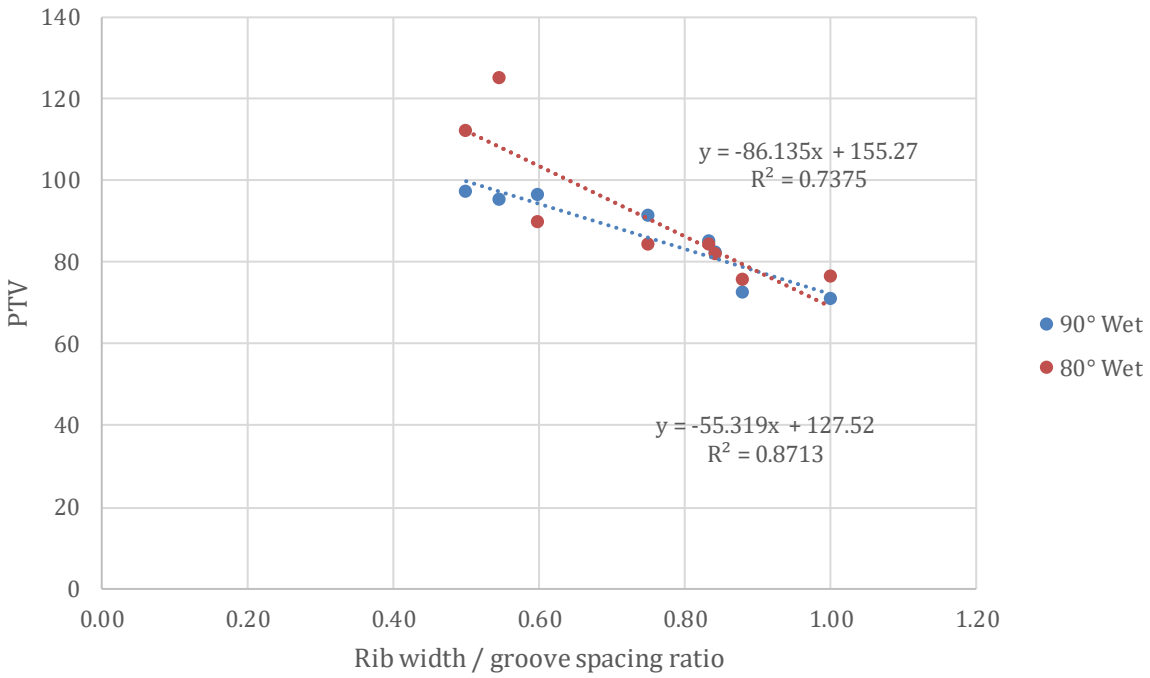

Figure 7.18. Rib width / groove width spacing ratio against wet PTV prior to simulated trafficking

Figure 7.17 and 7.18 plot rib width / groove width spacing ratio against dry and wet PTV respectively prior to simulated trafficking. The data represents the initial pendulum values. The plot shows that PTV decreases for both wet and dry conditions as the rib width / groove spacing ratio increases. The smaller ratio represents an extreme groove to gap ratio. A larger ratio represents a smaller rib width / groove spacing ratio. The plots show the decrease for dry conditions is much less of a gradient than that for wet conditions. The plots suggest a larger rib width / groove spacing ratio contributes the greater PTV values.

7.3 Summary

- Skid resistance of GMA generally decreases when subjected to simulated trafficking.
- Grooving contributes positively to skid resistance; however, the extent of improvement is dependent on the groove dimensions.
- A narrow groove demonstrates comparable skid resistance values to that of an ungrooved control surface.
- Skid resistance measurement at 80 degrees and 90 degrees generates different skid resistance values. Generally, the data shows that 80 degrees generates higher skid resistance values.
- An increase rib width / groove spacing ratio results in a decrease in skid resistance values.

CHAPTER 8.

EVOLUTION OF GROOVED MARSHALL ASPHALT AREAL PARAMETERS

8.1 Introduction

This chapter investigates the evolution of areal surface texture parameters for three of the eight Marshall Asphalt test surfaces. Areal surface texture parameters relates to a defined area where the texture of the asphalt test specimens were recovered through 3D photogrammetry and analysed through Digital Surf MountainsMap software. Photographs of each test surface were taken at 0, 10, 100, 200, 400, 800, 1500, 3000, 6000, 10,000, 20,000, 30,000, 50,000 and 75,000 wheel passes. Zephyr software was used to create a 3D model. This was imported into Digital Surf, MountainsMap software for analysis. A process flow diagram of this is demonstrated in Appendix F.

Test specimens under consideration were imported as a studiable in .txt format. Operators were applied to prepare the test specimen for analysis. The first Operators used in this investigation involved Levelling of the model by the Least squares plane. The levelling operator was applied by the subtraction method. Subtraction is recommended where only small tilt angles exist. As the model has been previously orientated, this was the most suitable. The next Operator was Extract area. This focused on the Area of Interest (AOI) i.e. the area interfaced by the British Pendulum. The AOI for test specimen MAD after being subjected to 200 wheel passes is shown in Figure 8.0.

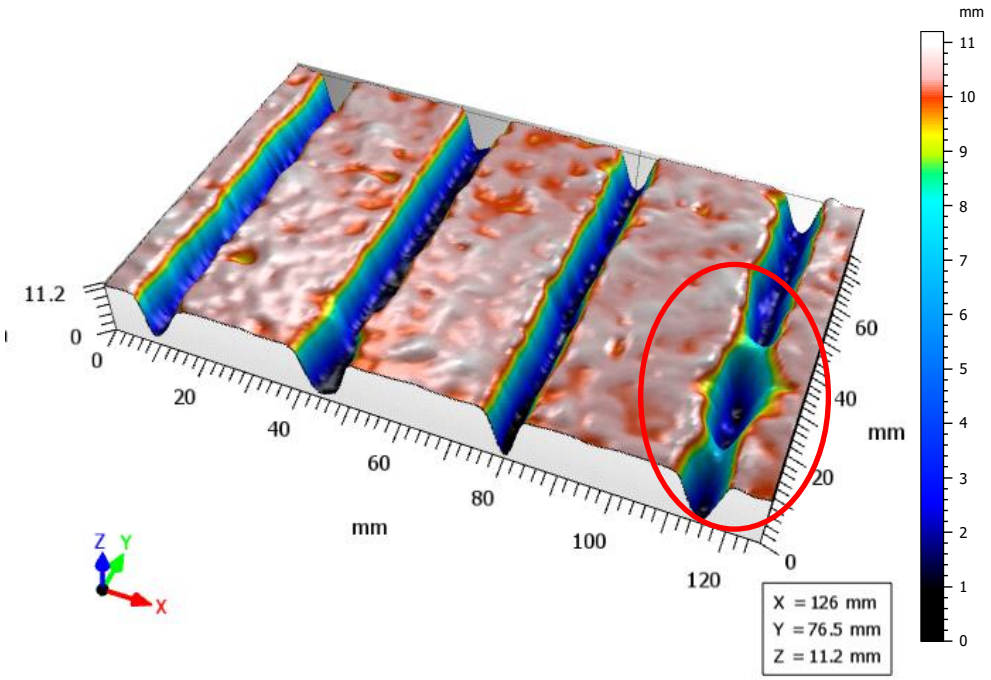

Figure 8.0. 3D view of test specimen D subjected to 200 wheel passes.

The 3D model shows that the maximum depth of the groove is 11.2mm. The scale colour palette illustrates the bottom of the groove to be dark blue/black, whereas the top of the rib is white/red. In this example, the 3D model shows asphalt material grooving stuck between the grooves at the right-hand side of the AOI highlighted in red. A range of Studies were performed on each 3D model including Step Height analysis and Volume parameters.

8.2 Step Height Analysis

Step Height analysis was used to investigate the rib and groove dimensions. A positive step represents the rib with a negative step representing the groove. Analysis involved extracting a series of profiles from the AOI. An example is shown in Figure 8.1. The V shape of the groove base can be attributed to occlusion.

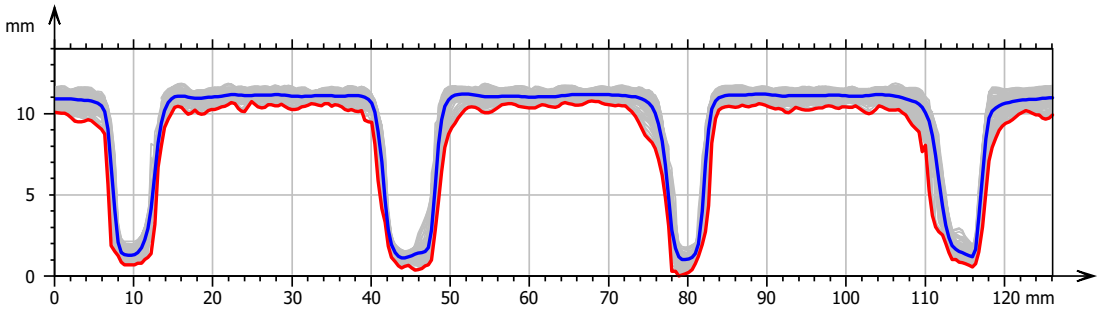

Figure 8.1. Series Profile example for test specimen MAD before simulated trafficking.

Figure 8.1 illustrates the 245 cross-sectional line profiles through the AOI of test specimen MAD. The mean line profile is shown in blue, with the lower profile shown in red. The ribs and grooves are clearly shown. A single rib was selected as shown in Figure 8.2. This allows measurement of the rib.

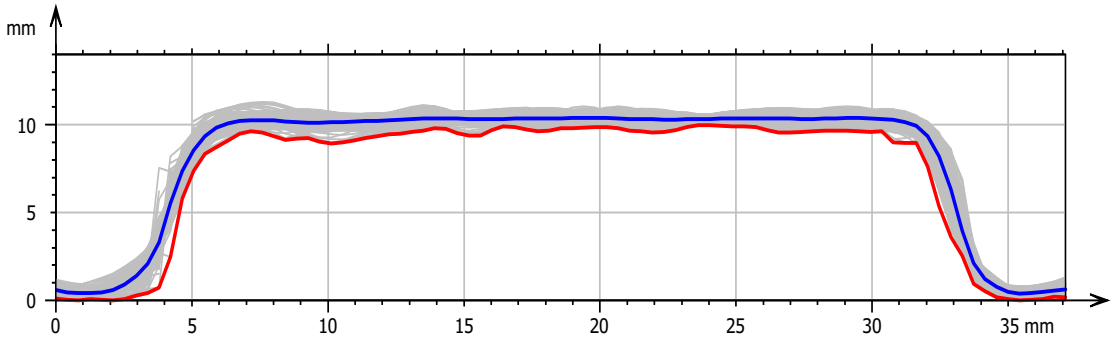

Figure 8.2. Selected rib for analysis.

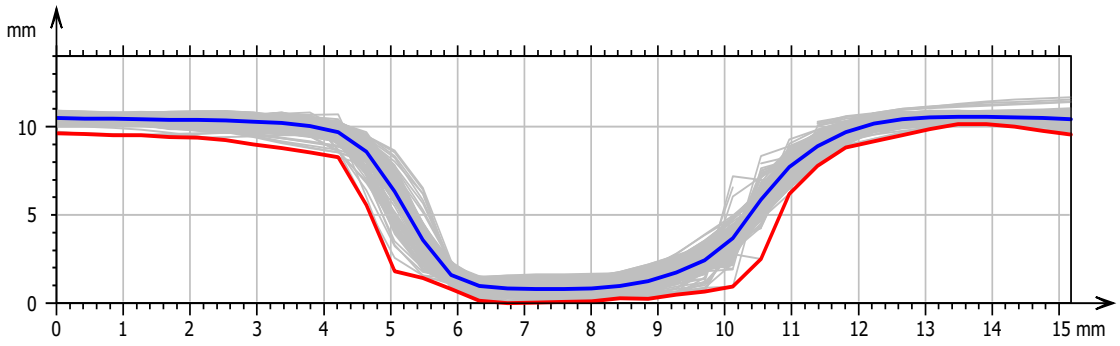

Figure 8.3. Selected groove for analysis.

Figure 8.3 shows a single groove selected for analysis. The width of the rib and groove was determined with a 5% step edge threshold; 5% of the edges of the groove/rib were excluded. This was to limit the influence of the curvature phenomena as shown in both the rib and groove profiles.

8.2.1 Analysis of the Rib - Positive Step

The positive step represents the rib. Figure 8.4 plots the change in rib width for test specimens MAA, MAD and MAF with increasing number of wheel passes.

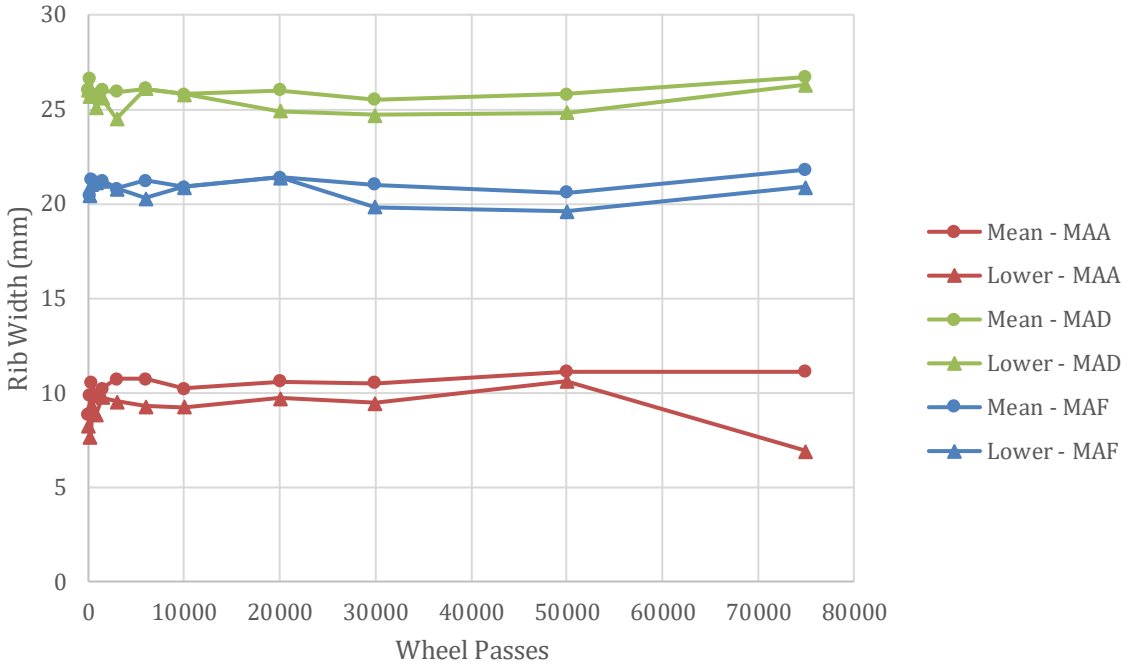

Figure 8.4. Rib width of test specimens MAA, MAD and MAF against wheel passes.

Figure 8.4 shows the rib width data for each test specimen for the mean and the lower extracted profile. The mean represents the average width of the total profiles and the lower represents the lowest profile. The plot shows the mean profile width of test specimen MAA to be approximately 10mm, MAD to be 26mm and MAF to be 21mm.

Manual measurements before trafficking determined the rib width of test specimen MAA to be approximately 12mm, MAD to be 28.5mm and MAF to be 21.8mm i.e. the 3D model measurements broadly align with the manual measurements within a tolerance of 2mm for MAA 2.5mm for MAD and 0.8mm for MAF.

Figure 8.4 shows the rib width remains relatively constant until testing stopped at 75,000 wheel passes. The outlier in the data for the lower profile of test specimen MAA was due to partial breakdown of the rib. The graph shows this partial breakdown of the rib is not

demonstrated in the mean profile, thus demonstrating the need to consider a lower profile within the data set.

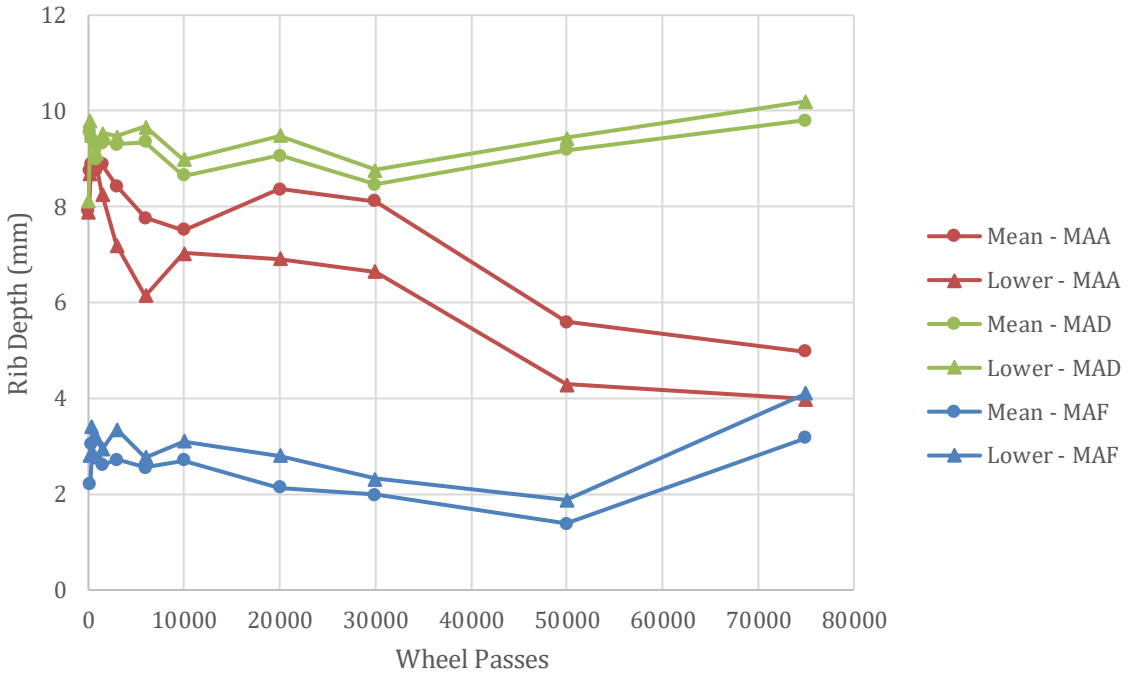

Figure 8.5. Rib Depth of test specimens MAA, MAD and MAF against wheel passes.

Figure 8.5 shows the rib depth data for each test specimen for the mean and the lower profile. Prior trafficking / at zero wheel passes, the maximum rib depth of test specimen MAA for the mean profile was 8mm, MAD was 9.5mm, and MAF was 2.2mm. Manual measurements before trafficking determined the depth of test specimen MAA to be 9.4mm, MAD to be 9mm and MAF to be 4.2mm. The 3D model measurements broadly align with the manual measurements within a tolerance of 1.4mm for MAA, 0.5mm for MAD and 2.2mm for MAF. As mentioned previously, this discrepancy is less due to the 5% model profile reduction where 5% of the edges of the groove are not considered due to the curvature at the groove edges.

The plot shows a general reduction in depth for each test specimen up until a point. This is demonstrated for test specimen MAA up to 75,000 wheel passes, up to 50,000 wheel passes for MAF and up to 30,000 wheel passes for MAD.

A possible explanation for the loss of rib depth until a certain number of wheel passes is simulated trafficking wears the matrix of fines between the aggregate particles. The matrix in nature is more susceptible to wear than the aggregate due to its finer material composition. Therefore, it is the least resistant to wear. This loss of matrix is likely to

account for the reduction in groove depth as reduction is only a few mm. The reduction of depth up until a point is less likely due to the aggregate loss as the reduction would be expected to be much greater. The point at which the matrix of fines influences the depth is likely related to the rib width / groove spacing ratio.

The greatest depth reduction is observed for test specimen MAA. Test specimen MAA has the smallest rib width / groove spacing ratio; therefore, as identified in chapter 5, the smaller ratio has higher interface pressures as the ratio facilitates greater depths of tyre embedment. Therefore there is greater stress on the rib. The ability of the rib to withstand this stress is less likely after the 6000 wheel passes, as the initial reduction could correspond to the loss of the matrix of fines, after which there is a fluctuation. However, a general reduction could correspond to the loss of aggregate particles within the groove.

The hypothesis that rib width / groove spacing ratio influences the wear of the groove, as demonstrated through groove depth, is also applicable for test specimens MAD and MAF.

The reduction of depth due to the loss of the matrix of fines occurs up to 50,000 wheel passes for test specimen MAF and up to 30,000 for test specimen MAD. Therefore, test specimen MAF has greater resistance to wear than test specimen MAD.

The data suggests the point at which depth reduction changes is influenced by rib width / groove spacing ratio. As found in chapter 5, the interface pressure for MAF with a rib width / groove spacing ratio of 0.88 is greater than MAD of 0.83, albeit, by only 0.04, the interface pressure is not as severe due to less enveloping. Therefore, there is less stress and ultimately less wear, therefore less groove depth reduction.

The loss of the matrix if fines due to trafficking reduces the depth at which the aggregate particles is embedded into the bulk of the asphalt surface making them less resistant to wear. This process makes the aggregate vulnerable as erosion of the matrix influences the depth of embedment, further increasing the vulnerability of the aggregate as the stress on the aggregate increases as the depth of enveloping increases. This is experienced after 50,000 wheel passes for MAF and 30,000 for MAD. The plot shows an increase in depth after a certain number of wheel passes, particularly at the greater wheel pass intervals. At this point, the exposure of prominent aggregate due to erosion of the matrix of fines is likely to contribute to this perceived depth increase.

8.2.2 Analysis of the Groove - Negative Step

The negative step represents the groove. The groove width influences the depth to which enveloping of the tyre occurs. Figure 8.6 illustrates the groove width of test specimens MAA, MAD and MAF against wheel passes.

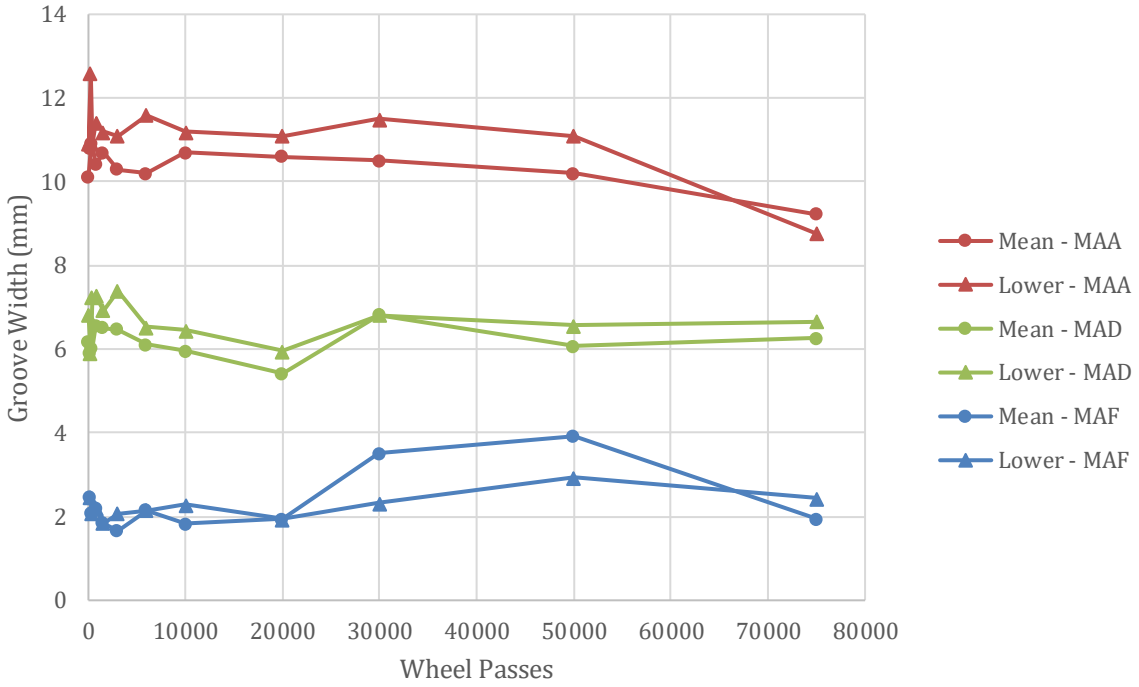

Figure 8.6. Groove width of test specimens MAA, MAD and MAF against wheel passes.

Figure 8.6 shows the groove width data for each test specimen for the mean and the lower profile. Prior trafficking / at zero wheel passes the width of the groove of test specimen MAA for the mean profile was 10.1mm, MAD was 6.2mm, and MAF was 2.5mm. Manual measurements before trafficking determined the width of test specimen MAA to be 10.3mm, MAD to be 6.2mm and MAF to be 2.16mm. The 3D model measurements align with the manual measurements with only a small horizontal measurement degree of error/discrepancy of 0.2mm for MAA, 0mm for MAD and 0.34mm for MAF.

The plot shows that all test specimens broadly maintain their groove width with fluctuations within a margin of around 1/2mm except for test specimen MAA after 50,000 wheel passes. Fluctuations in the data could represent the immediate edges of the groove

where they are more susceptible to change due to the tyre enveloping into the groove. As identified in chapter 5, the greatest stress occurs at the immediate edges of the groove.

The greater width changes observed for test specimen MAA are likely due to groove breakdown influencing the groove width measurement.

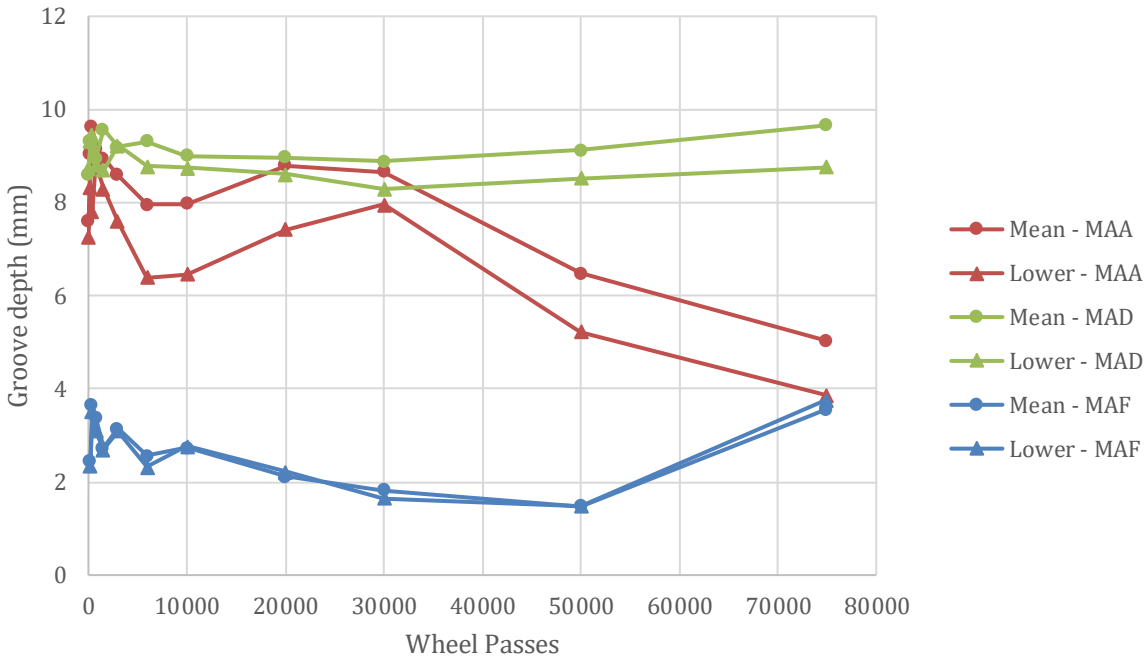

Figure 8.7. Groove depth of test specimens MAA, MAD and MAF against wheel passes.

Figure 8.7 shows the maximum groove depth data for each test specimen for the mean and the lower profile. Prior trafficking / at zero wheel passes, the maximum groove depth of test specimen MAA for the mean profile was 9mm, MAD was 8.6mm, and MAF was 2.5mm. Manual measurements before trafficking determined the depth of test specimen MAA to be 9.4mm, MAD to be 9mm and MAF to be 4.2mm. The 3D model measurements broadly align with the manual measurements within a tolerance, there is a vertical measurement degree of error/discrepancy of 0.4mm for MAA, 0.4mm for MAD and 1.7mm for MAF. As mentioned previously, this discrepancy is less due to the 5% model profile reduction.

The plot shows a general reduction in depth for test specimens MAA and MAF with some fluctuations. There is a discrepancy in that data at 75,000 wheel passes for MAF where the

depth increases. This is likely an error contributed by occlusion, where the penetration of light to the bottom of the groove was limited due to the groove width. In the 3D model, the profile was shown as a 'V' shape rather than a 'U' shape where the walls of the groove were shown to taper, whereas, in reality, they were cut straight. This phenomenon raises the question of whether a step analysis for narrow groove width is appropriate or where mitigation measures such as LED lighting and alternative photographic tilt angle at which are used to reduce/inhibit this phenomenon.

Test specimen MAA shows the greatest depth difference, from 9mm to 5/4mm. This is not surprising given the dimensions of the rib width / groove spacing ratio; therefore, it is quite slender and more susceptible to breakdown. Test specimen MAD shows a small reduction in depth up to 30,000 wheel passes; however, the depth is arguably constant/stable in the region of 9mm.

The groove depth is of importance in such data as it facilitates the bulk removal of water. A reduction in groove depth reduces the volume which the groove can handle. In this case, MAD maintains its depth, therefore, maintains its volume. In contrast, MAA reduces in depth, as does MAF, therefore significantly affecting its ability to remove the bulk volume of water during wet conditions.

8.3 Abbot Firestone Analysis

The Abbot-Firestone Curve quantifies the volume of peak material (Vmp), the volume of core material (Vmc), volume of core voids (Vvc) and volume of valley voids (Vvv). These are illustrated in Figure 8.8. The Abbot-Firestone curve illustrates the cumulative curve of the distribution of volume. The plot shows the bearing volume at different height percentages above the surface form.

Chapter 7 had considered the change in pendulum values due to simulated trafficking. Quantification of change in surface parameters was not within the capabilities of the pendulum test. Therefore, there was no indication of why pendulum values were changing the PTV data.

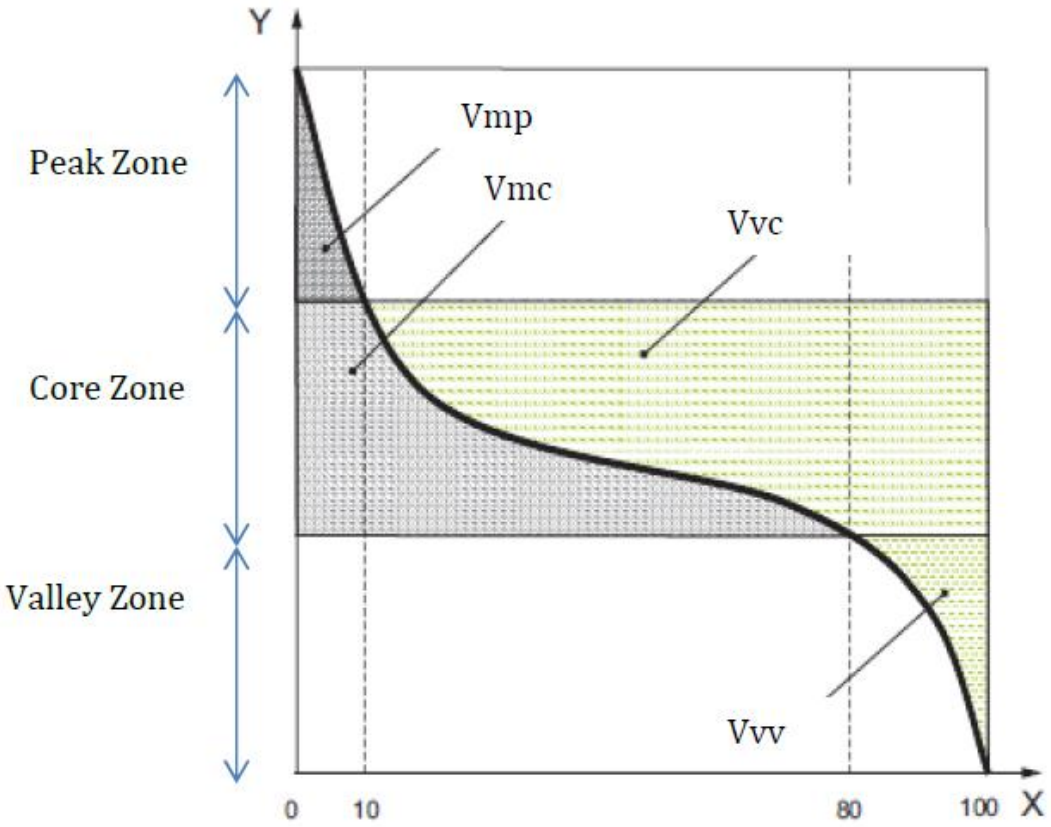

Figure 8.8. The Abbott Firestone Curve (Abbott and Firestone, 1933).

The AFC is a simple plot representing a texture profile (Abbott and Firestone, 1933). This shows the volume of surface texture material at depth into the surface. The default limits p and q are typically 10 % and 80 %. Depth into the surface texture is split into three zones, peak, core and valley, dependent on the position of the AMBR limits p and q. P and q are shown as 10 and 80 respectively on the X axis. Change in the Abbot-Firestone Volumetric parameters was investigated to determine whether it may help explain the variation in pendulum values.

Vmp is the peak material volume of the scale limited surface. Vmp represents the volume of material of the areal material ratio p (%). Vmp is measured in ml/m^2. The areal material ratio parameters that divide the peaks and valleys from the core material are specified in area roughness parameters.

In this investigation, Vmp was considered to represent the upper peaks of the asphalt surface. These peaks are considered to be in contact with the tyre at tyre-pavement interface (Mc Quaid, 2016). Kogbara et al. 2018 concluded that Vmp had a good correlation

with GripNumber. Therefore, Vmp was chosen to determine whether it could explain the development of PTV during simulated trafficking.

8.3.1 Vmp of test specimen MAK

Test specimen MAK represents the ungrooved control. Figure 8.9 plots pendulum and Vmp data for increasing number of wheel passes for test specimen MAK. The log scale is used to better illustrate the trafficking intervals. The plot shows PTV decreases from an initial PTV of 71 before trafficking to 59 at 200 wheel passes.

This decrease in PTV corresponds to a similar decrease in Vmp from an initial value of 9 ml/m² to 5 ml/m² at 200 wheel passes. The data follows a similar trend where PTV decreases, Vmp increases, and vice versa until 10,000 wheel passes. After 10,000 wheel passes, a large increase in Vmp from 5.9 ml/m2 to 9.8 ml/m² at 75,000 wheel passes only corresponds to an increase of 4 PTV points.

Figure 8.9. Pendulum Values and Vmp against wheel passes for test specimen MAK (log scale).

Considering the data change in terms of the asphalt surface, Vmp is the volume of material in the aggregate peaks. Initially, excess bitumen coats the surface of the aggregate and the

peaks / microtexture is concealed in a coating of bitumen. This coating would correspond to an initial high volume of peaks as the bitumen has created a smoother surface.

As the asphalt surface is trafficked, the bitumen becomes worn away and the microtexture on the aggregate becomes exposed. This microtexture has a lower volume than the peaks coated in bitumen and corresponds with a decrease in pendulum value. At this early stage of simulated trafficking, these early life changes could also be influenced by the initial smearing and bedding in the bitumen on the surface of the aggregate. Figure 8.10 illustrates a schematic of the bitumen coating the peaks of the aggregate. The red dotted line represents p on the Abbot-Firestone curve on shown in figure 8.8.

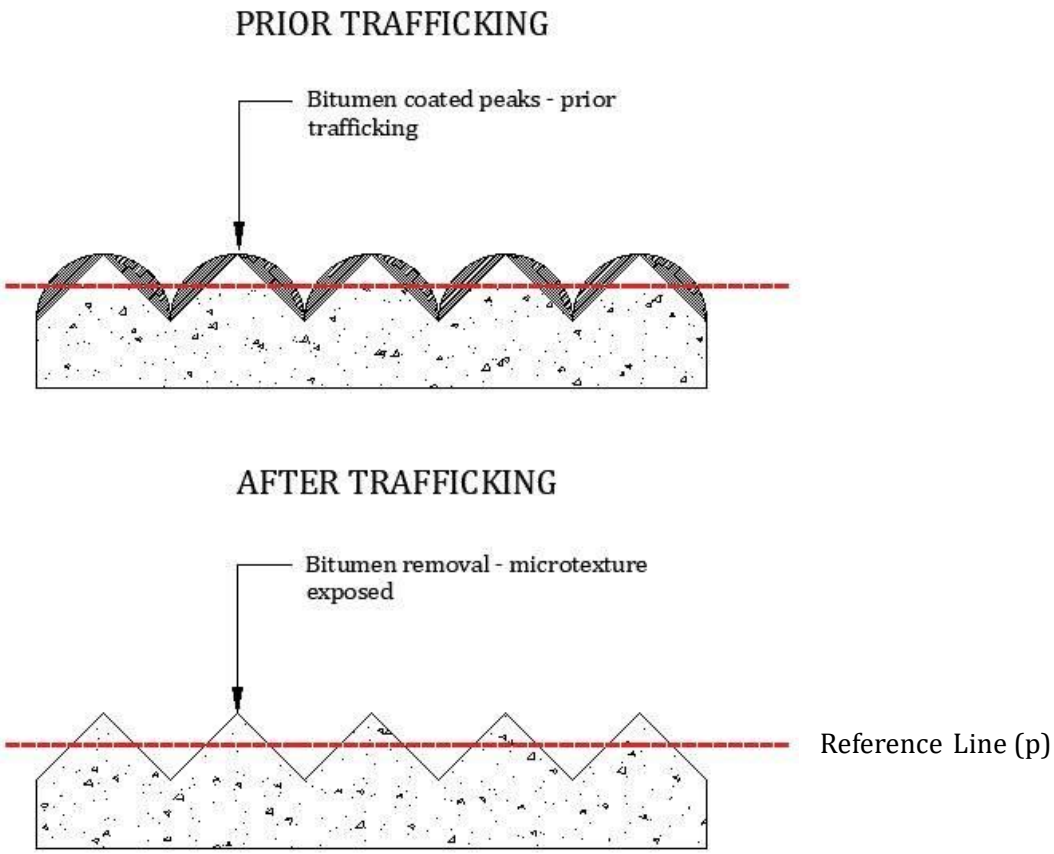

Figure 8.10. Vmp schematic – bitumen removal from surface of aggregate.

As trafficking continues the PTV would be expected to increase due to the removal of bitumen exposing the aggregate. When the bitumen is worn from the aggregate, the peaks become exposed, corresponding to a Vmp reduction. Continued trafficking would appear to

increase the volume in the peaks as the surface volume increases due to the peaks becoming rounded and worn.

Vmp is considered to relate to the micro-scale of surface texture as it relates to the upper surface of the aggregate peaks. Using Vmp to consider the change of PTV at greater wheel pass intervals is questionable. At higher wheel pass intervals, the surface is likely to become worn and degraded; therefore, the Vmp may display erratic data. This is likely the case after 10,000 wheel passes.

8.3.2 Vmp of Test Specimen MAA

Test specimen MAA represents an extreme rib to groove ratio. Figure 8.11 shows PTV and Vmp data plotted with increasing number of wheel passes for test specimen MAA. Pendulum testing was only carried out until 6000 wheel passes as rib degradation made it impossible to maintain the recommended swing length. This wear of the rib has influenced the PTV and Vmp data. The considerable variation of Vmp reflects particle loss. This example illustrates a different phenomena to occur depending on rib / groove dimensions.

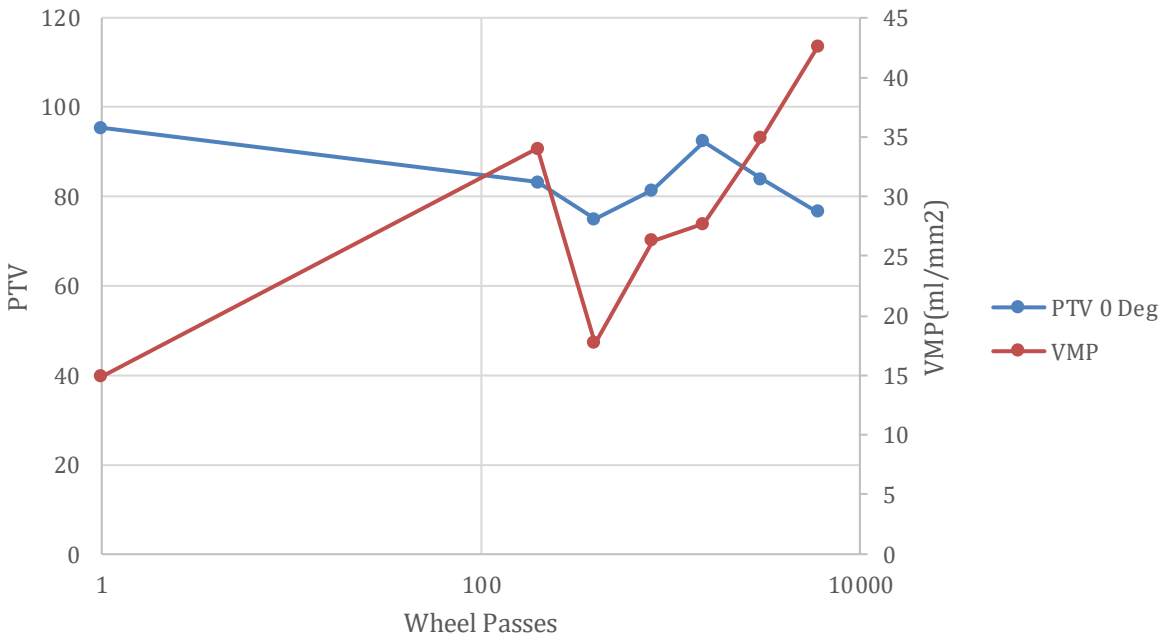

Figure 8.11. Pendulum and Vmp data against wheel passes for test specimen MAA (log scale).

8.3.3 Vmp of Test Specimen MAD

Test specimen MAD represents similar dimensions recommended by ICAO. Figure 8.12 shows pendulum data, and Vmp data against wheel passes for test specimen MAD. The plot shows PTV decreases from an initial PTV of 82 to 80 at 200 wheel passes. This reduction corresponds to a Vmp increase from an initial value of 10 ml/m2 to 12ml/m2. After 200 wheel passes, a reduction in Vmp corresponds to a reduction in PTV. PTV stabilises after 400 wheel passes in the region of 64~62 PTV whilst Vmp fluctuates but generally increases. After 10,000 wheel passes, an increase in Vmp corresponds to an increase in PTV and vice versa.

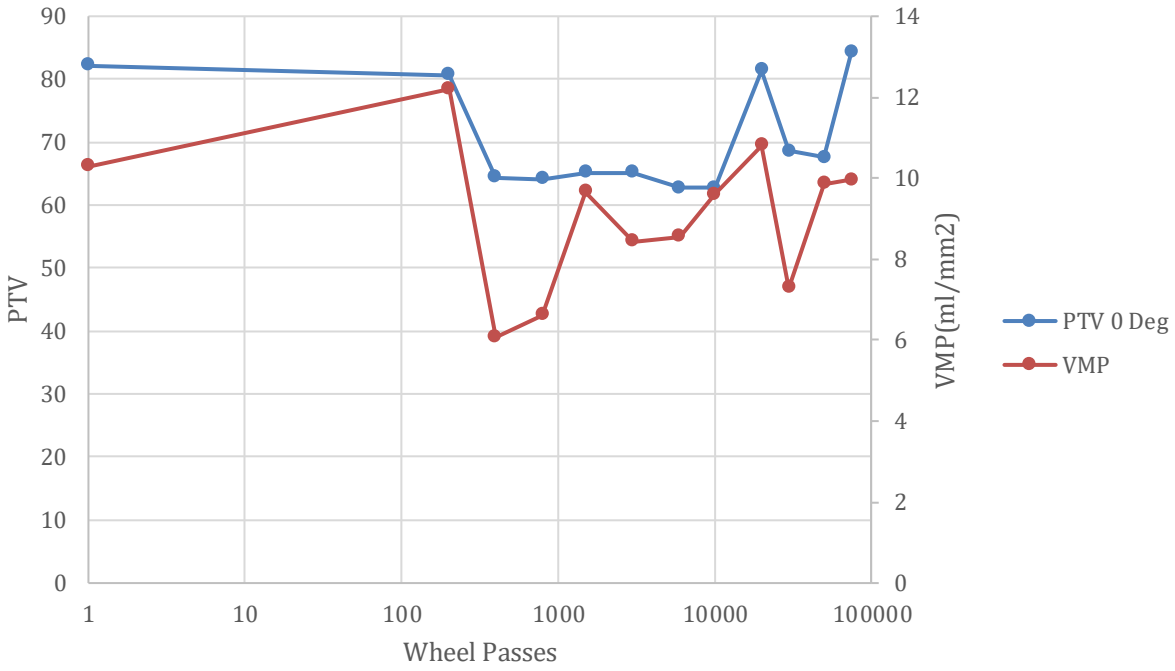

Figure 8.12. Pendulum Values and Vmp against wheel passes for test specimen MAD (log scale).

As the volume of the material in the peaks changes between 20,000 and 50,000, the change could indicate potential degradation in the matrix of fines as the material is worn. As PTV remains stable, this would support the ideology of the changes in the matrix of fines. When the pendulum interacts with the test specimens, the prominence of the aggregates indicates pendulum values and not the matrix of fines.

8.4 Vmp for Test Specimen MAF

Test specimen MAF represents a rib width / groove spacing with a narrow groove width. Figure 8.13 shows pendulum data, and Vmp data against wheel passes for test specimen MAF. The plot shows PTV decreases from an initial PTV 72 to 60 at 200 wheel passes. This reduction corresponds to a Vmp increase from an initial value of 9 ml/m2 to 5ml/m2. This relationship is consistent up until 10,000 wheel passes. After 10,000 wheel passes, Vmp increases; however, PTV remains relatively stable between 55 and 60 PTV.

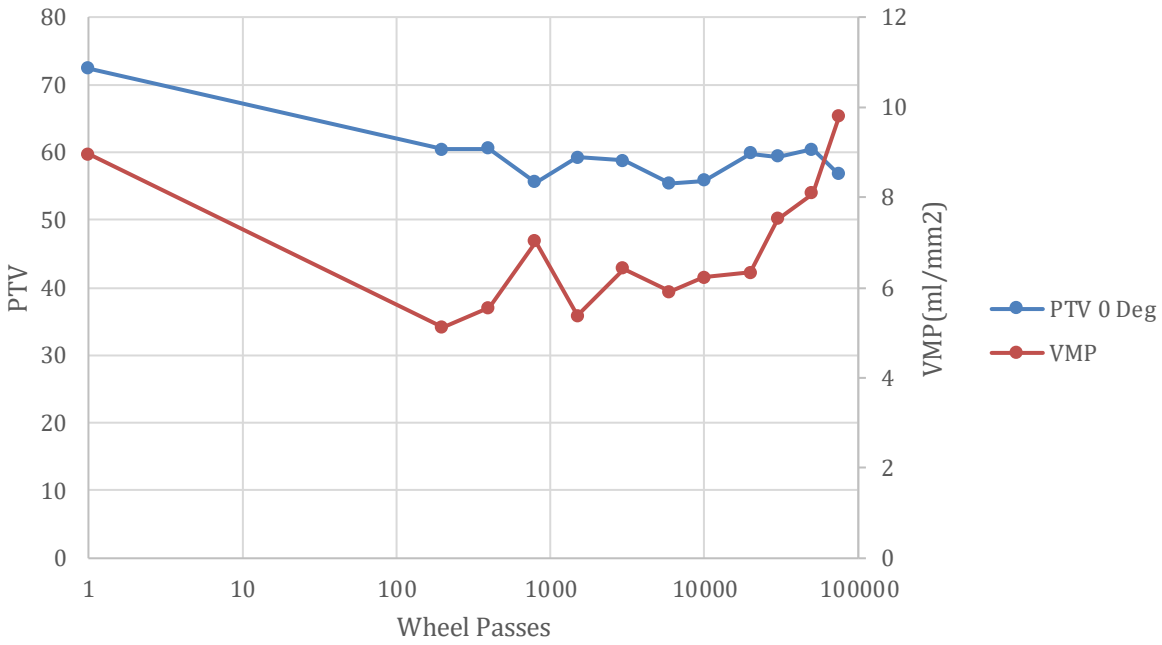

Figure 8.13. Pendulum Values and Vmp against wheel passes for test specimen MAF (log scale).

As mentioned previously, the PTV data for test specimen MAK and test specimen MAF is almost identical. The relationship between PTV and Vmp for both also demonstrates this consistent relationship. The trend identified is similar to that of the control specimen MAK; however, for MAK, the data is more closely aligned. Test specimen MAF has a 3mm groove and therefore is closest to the control.

The change in data with the asphalt surface indicates similar to that previously identified, where the bitumen coating the surface of the aggregate contributes an initial high Vmp. Trafficking removes this excess bitumen and exposes peaks in the aggregate. The slight

change in PTV is indicative of the surface still maintaining excess bitumen with the addition of the influence of the grooving.

Similar to test specimen MAK, the aggregate properties are resisting wear and therefore maintaining the PTV value. However, the Vmp fluctuates over a greater volume range, and it could be suggested that grooving contributes to this fluctuation.

8.5 Summary

- Vmp can assist in the explanation of the change in pendulum values with simulated trafficking.
- The use of Vmp is more critical in the earlier stages of trafficking as the surface is generally not extensively influenced by degradation or wear.
- The use of Vmp at higher wheel passes may not be appropriate as the loss of aggregate or material may give rise to misleading data as the reference line from which Vmp is determined will be affected by the loss of aggregate.
- Generally, before trafficking, Vmp values are high. This value changes as the surface interface changes with simulated trafficking. The Vmp generally reduces as the excess bitumen coating the surface is worn from the surface of the aggregate. As the microtexture of the surface of the aggregate becomes exposed, this corresponds to a decrease in Vmp. There is a period of stability as the microtexture resists the trafficking action. Vmp can fluctuate significantly more at higher wheel pass intervals due to surface degradation.

CHAPTER 9.

INVESTIGATING GROOVED SURFACE INTERFACE WITH BRITISH PENDULUM SKID RESISTANCE TESTER

9.1 Introduction

This chapter investigates the interface between the British Skid Resistance pendulum tester and grooved test specimens using the paint removal technique. The paint removal after pendulum testing was quantified using Image-Pro analysis. Paint removal was indicative of contact area. The investigation was in two parts. The first part used idealised grooved aluminium plates to consider the effect of test specimen rotation angle, rib width and groove width on contact area. The second part investigated testing GMA test specimens subjected to simulated trafficking.

The chapter demonstrates a lot of new findings when utilising the British Pendulum Tester. It can be inferred that whilst weaknesses have been demonstrated when utilising the British Pendulum Tester there is no suitable alternative and therefore it continues to be utilised.

9.2 Initial Investigation

The first part of the investigation used 10mm thick aluminium plates with seven idealised groove patterns. The plates geometric properties are shown in Table 9.0. The spacing ratio represents the rib width to groove spacing. The smallest ratio corresponds to a larger groove width with smallest rib width and similarly the largest ratio corresponds to a larger rib width with smallest groove width. The pendulum testing used the 76.2 ± 0.5 mm wide slider with a swing length of 126 ± 1mm as detailed in BS EN 13036.

Table 9.0. Idealised aluminium plate groove dimensions

Rib width (mm)	Groove width (mm)	Groove Depth (mm)	Groove spacing c/c (mm)	Rib width / Groove spacing ratio
32	3	6	35	0.91
32	6	6	38	0.84
32	12	6	44	0.73
19	6	6	25	0.76
10	3	6	13	0.77
10	6	6	16	0.63
10	12	6	22	0.45

Figure 9.0. Testing arrangement for plate rotation angle of 0º

Figure 9.0 shows the testing arrangement for a plate rotation of 0º. A water based paint was applied to the surface of a test specimen. Two rotation angles were assessed, 0 degrees perpendicular to the grooves, and 10 degrees with respect to the grooves. Removal of paint during the test was used to indicate the area of contact.

Figures 9.1 and 9.2 compare paint removal during the pendulum test for a non-grooved test specimen at different rotation angles. The direction of swing was right to left. Both Figures show total paint removal in the contact interface.

The contact patch for both tests is visually the same. Measurement using Image Pro found their contact area to be similar at 9100 mm^2. This initial experiment concluded that test angle did not affect the smooth aluminium test specimen.

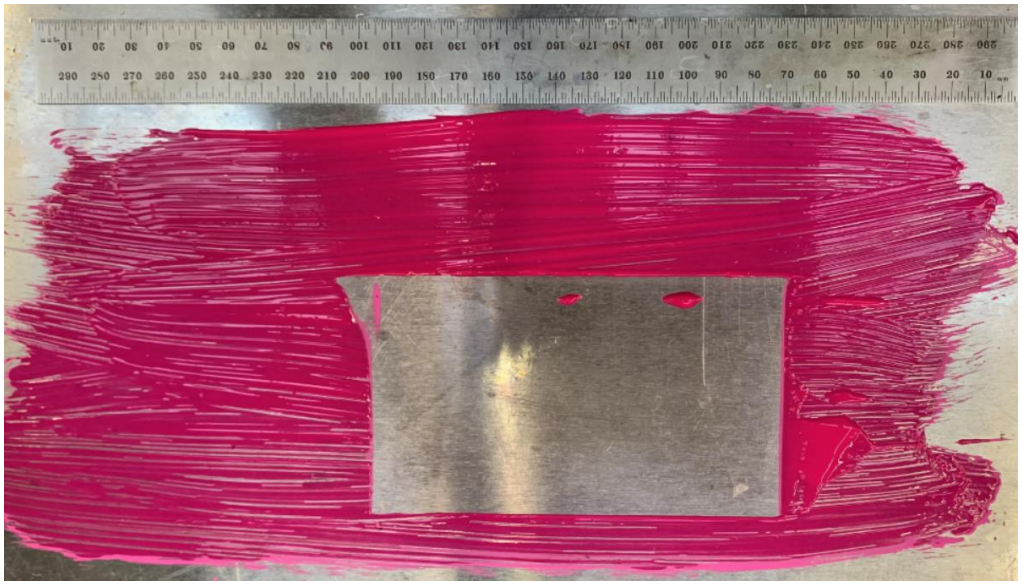

Figure 9.1. Paint removal for non-grooved idealised aluminium surface at 0.

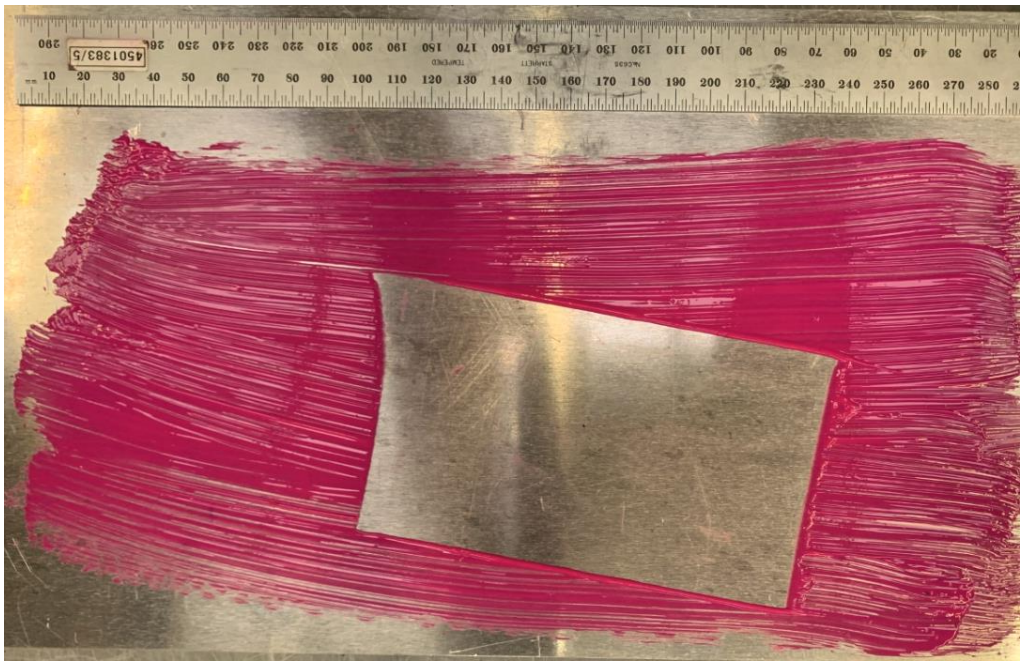

Figure 9.2. Paint removal for non-grooved idealised aluminium surface at 10°.

Figures 9.3 and 9.4 compare paint removal during the pendulum test for standard ICAO grooving dimensions of 6 mm groove width and 32 mm rib width at 0º and 10º. The pendulum was arranged so that the start of the contact coincided with the centre of a rib first. Both images visually illustrate how grooving the test specimen can impact the slider contact with the surface.

Figure 9.3. Paint removal for 6mm groove width and 32mm rib width tested at 0°.

Figure 9.4. Paint removal for 6 mm groove width and 32mm rib width at 10°.

Both paint removal patterns show the pendulum slider bouncing over the grooved surface as evidenced by the intermittent contact. At the 0° rotation angle, more paint was removed

during the first part of the swing and much less for the out-swing. The paint removal for the 10° rotation angle test was comparable in this respect.

It is suggested that this removal pattern is attributable to the rapid early dissipation of energy when the slider hits the surface harder. The energy is reduced as the pendulum slider impacts the edges of the grooves.

Paint removal provides insight into the contact patch and its interface with the grooved surface and the area of contact the pendulum value is derived from. This initial testing warranted the need to investigate the pendulum testing of grooved surfaces further.

9.3 Pendulum Contact Area

Pendulum testing at 5 rotation angles increasing from 0° to 12° in 3º increments was investigated using the ICAO standard grooving dimensions for an idealised aluminium plate surface. The test specimen was rotated to facilitate the change in angle of interaction. The contact area for each testing angle was determined using Image-Pro. The test results are summarised in Table 9.1 and plotted in Figure 9.5.

Also shown is a percentage change in contact area compared to the un-grooved test specimen. The 0 % contact area for the un-grooved test specimen was used as a control. The difference in contact area due to the rotation angle was expressed as a percentage change. This contact change was compared to that contact of a non-groove surface i.e full contact.

Table 9.1. Effect of test specimen rotation on contact area for the ungrooved control and the 6 mm groove width and 32mm rib width test specimen.

Rib width/Groove spacing ratio	Rotation of test specimen (degrees)	Contact area (mm^2)	Contact change (%)
0.84	0	3926	-57%
0.84	3	6048	-34%
0.84	6	5901	-35%
0.84	9	5133	-44%
0.84	12	8042	-12%
1.00	0	9100	0%
1.00	12	9100	0%

Table 9.1 shows the effect of test specimen rotation on contact area for the 6 mm groove width and 32mm rib width test specimen. The rib width / groove spacing ratio of 1.0 contact area was measured to be 9100mm^2 . This measurement differs from that determined by the actual pendulum swing length of 9600mm^2 based on the pendulum slider dimensions detailed in Chapter 7.2. This discrepancy is likely due to practicality of carrying out pendulum testing.

Contact change was calculated by the following.

$$\left(\frac{9100 - 3926}{9100}\right) = 0.57 * 100 = 57\%$$

The Rib width/Groove spacing ratio of 1.0 represents the ungrooved control test specimen whereas 0.84 represents the grooved test specimen. The data shows a 57 % reduction in contact area for a change in Rib width/Groove spacing ratio from 1.00 to 0.84 for 0 degree rotation.

Pendulum testing at 0 degrees for the grooved surface derives a pendulum value from 57% less contact area than that of the control surface. The data in general shows contact change percentage difference is reduced as the test specimen rotation angle increases, therefore contact is increasing. The data shows contact change is limited between 3 and 6 degrees. This change is likely related to the point at which the slider initially interfaces the rib which influences the bouncing of the pendulum. Nine degrees represents a decrease in contact area – likely due to the grooved interface at this angle, whilst an improvement in contact area from 0 degrees, 9 degrees has likely reintroduced bouncing as compared to 3 and 6 degrees.

It is suggested this reduction is due to the influence of reduced contact of the pendulum slider as the impact on the grooved edges is reduced with rotation. The contact with the ribs becomes more consistent and the bouncing effect is reduced. The pendulum slider is sliding along the groove edges rather than impacting them,

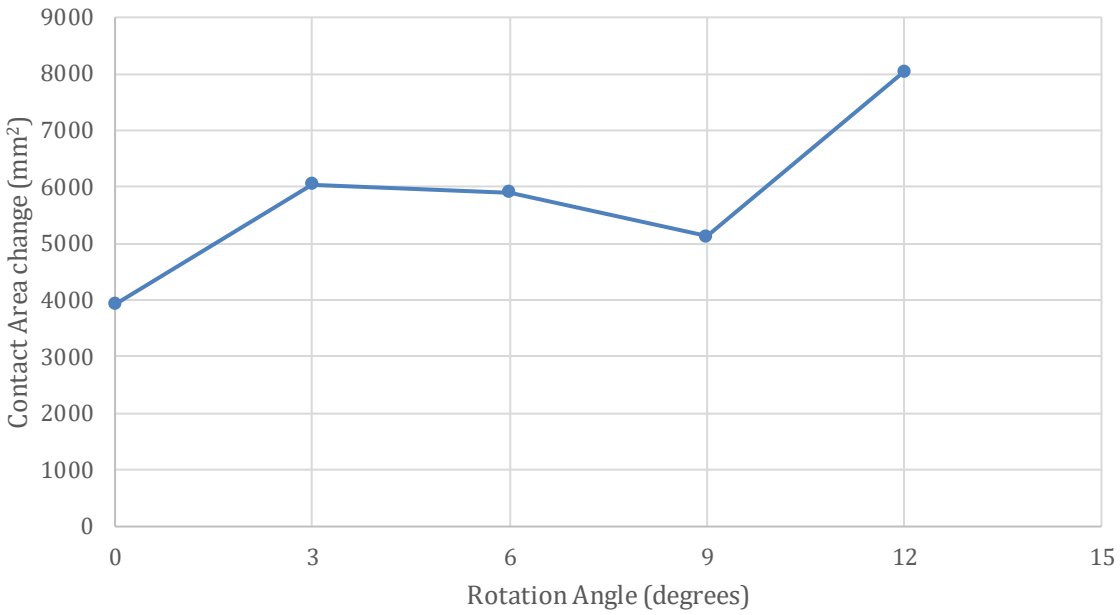

Figure 9.5. Change in contact area with test specimen rotation angle for FAA parameters.

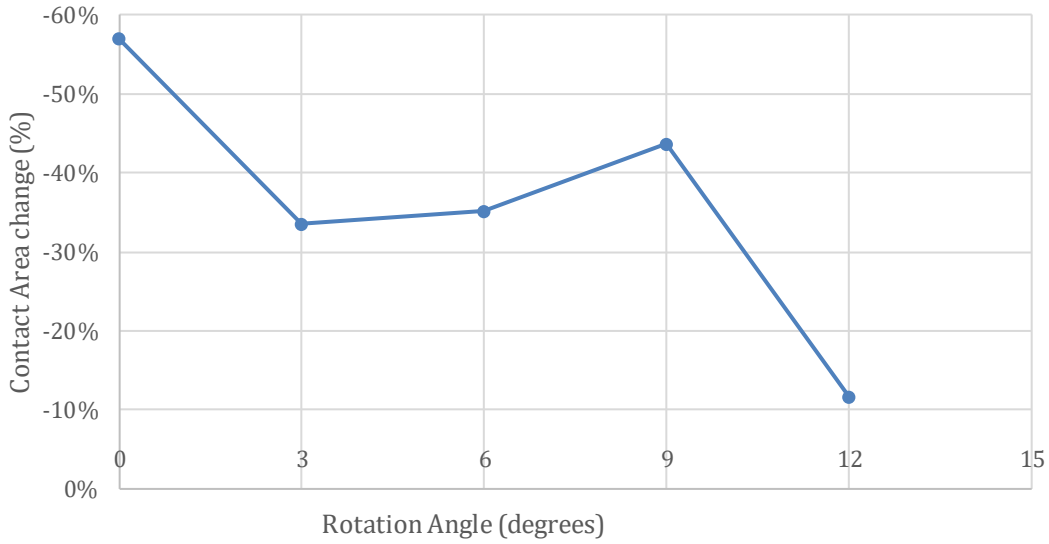

Figure 9.6. Percentage change in contact area with increasing rotation angle for FAA parameters.

Figure 9.5 and 9.6 show the change and percentage change of contact area with increasing rotation angle. The data shows in general a reduction in the percentage difference of contact area as the rotation angle increases. This reduction illustrates greater paint removal which is indicative of greater contact. The data demonstrates a stepped like effect throughout each rib width / groove spacing ratio apart from 0.45. This stepped effect may be due to the pendulum slider interfacing the edge of the groove/rib, sliding along the edge rather than enveloping them.

The percentage change data shown in Table 9.1 / Figure 9.6 suggests this interaction is sensitive to rotation angle. Therefore, whilst the contact area generally increases small changes in the rotation angle can significantly impact the contact area.

For example, during the testing process there was an effort made for the pendulum slider to interface the centre of the rib first. This became impracticable as rotation angles increased. This was reflected in the data for inter-groove ratio of 0.63 at 9 degrees where some bouncing of the pendulum slider may have occurred. The data demonstrated that for a rib width / groove spacing ratio of 0.45 that the opposite relationship occurs where the contact area decreases with rotation. This is likely due to the groove width facilitating a degree of enveloping and therefore increasing the bouncing effect.

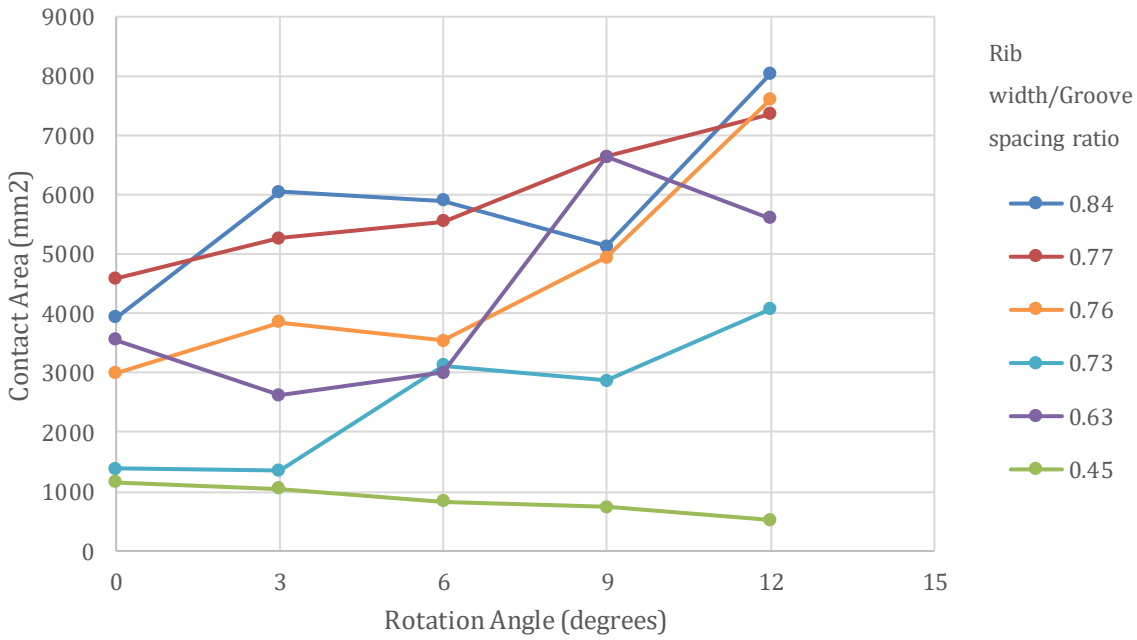

Figure 9.7. Change in contact area for all idealised groove test specimens.

Figure 9.7 shows the change in contact area for all of the idealised grooved specimens. The data shows the same general relationships identified for the rib width / groove spacing of 0.84. The data shows increase in contact area as the test specimen rotation increases. However, the data for a Rib width/Groove spacing ratio of 0.45 demonstrates a gradual decline in contact area as compared with other ratios.

Its contact area decreases with increasing test specimen rotation angle. This is likely due to the increased density of ribs / grooves which corresponds to an increase in impact points. The data for a ratio of 0.76 is closest to the control contact area with a rotation angle of 12 degrees. This suggests that for each rib width / groove spacing ratio there may be an optimum rotation angle which provides the greatest contact area whilst also mitigating the effect of the pendulum slider bouncing.

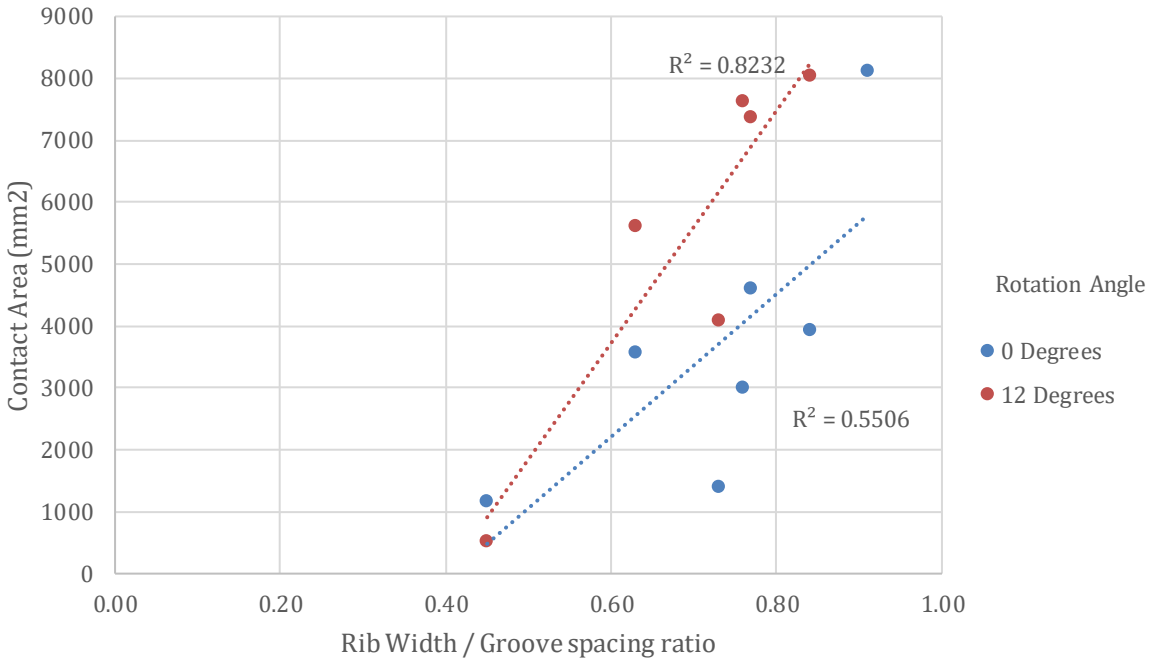

Figure 9.8. Rib width/Groove spacing ratio against Contact Area for rotation angles of 0 and 12 degrees.

Figure 9.8 shows Rib width/groove spacing against Contact Area for rotation angles of 0 and 12 degrees. The plot shows that contact area increases with increasing Rib width/groove spacing ratio. It also shows that a rotation of 12 degrees results in greater contact area than at 0 degrees. There is also less divergence of the data points from the trendline.

9.4 Comparison of idealised surface and Marshall Asphalt paint removal patterns

Figures 9.9 to 9.11 compare the paint removal patterns for the 38 mm centre – centre idealised aluminium plate test specimen with its equivalent Marshall Asphalt test specimen at rotation angles of 6, 9 and 12 degrees. The paint removal patterns are broadly comparable. They show how the pendulum bounces across the grooved test surface due to interaction with the surface. The number of bounces as determined by the visual inspection decreases as the test specimen rotation angle is increased.

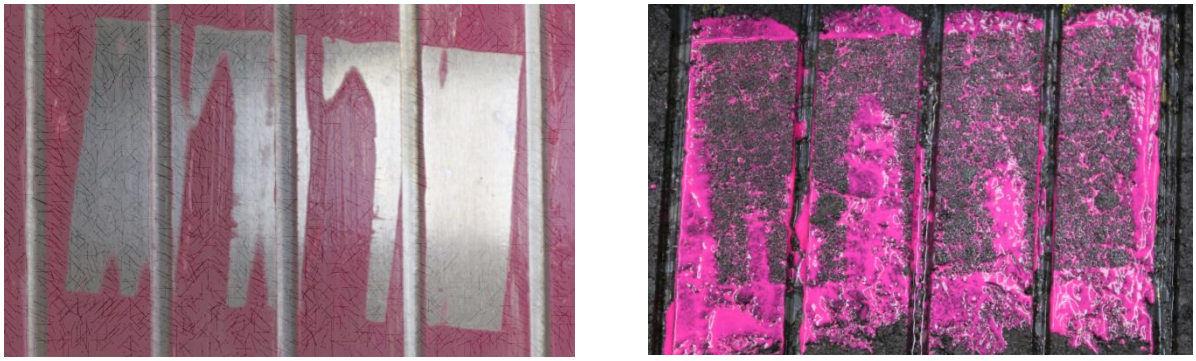

Figure 9.9. Contact phenomena for the pendulum on 38mm ribs and 6mm groove pattern at 6º

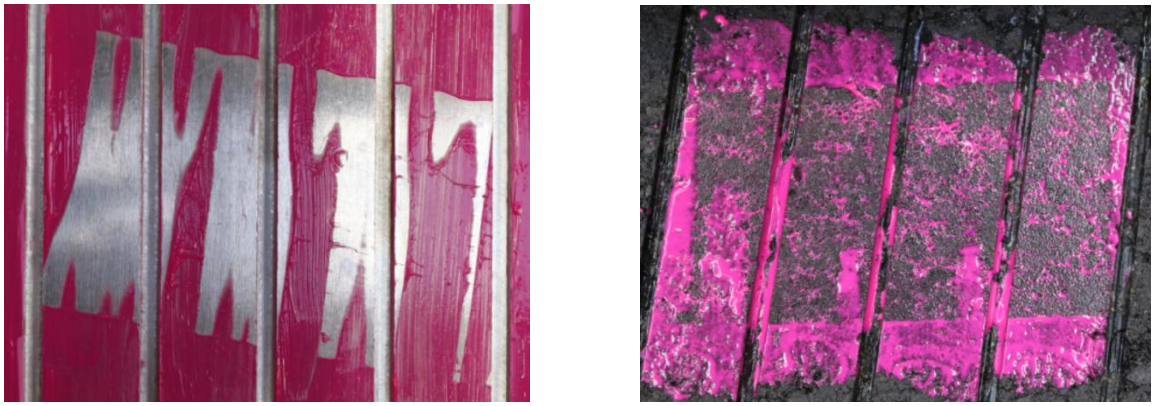

Figure 9.10. Contact phenomena for the pendulum on 38mm ribs and 6mm groove pattern at 9º

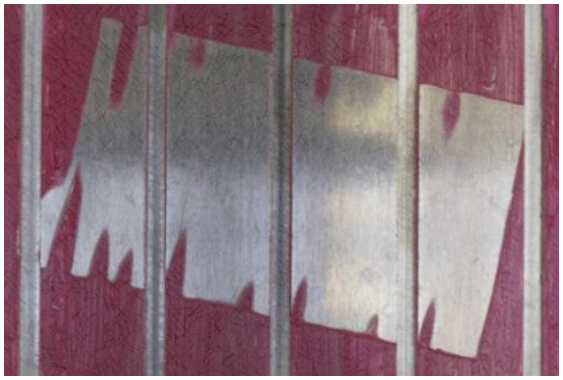

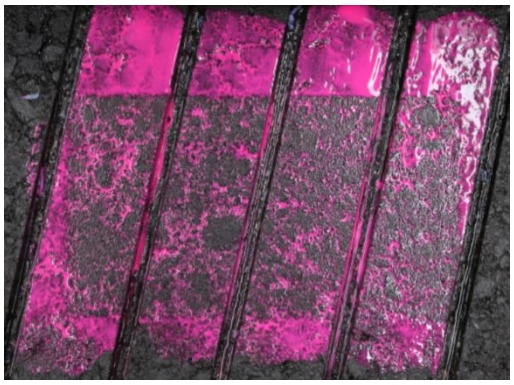

Figure 9.11. Contact phenomena for the pendulum on 38mm ribs and 6mm groove pattern at 12°

The images show the idealised surface which is rotated and then pendulum tested Vs the Marshall Asphalt test surface which is grooved at an angle and pendulum tested.

9.5 Pendulum Test Value of Idealised Surfaces

Pendulum testing was carried out at rotation angles of 0, 3, 6, 9 and 12 degrees. Table 9.2 summarises the PTVs for idealised aluminium test specimens with different groove ratios. Figure 9.13 plots the data.

Table 9.2. Idealised grooved aluminium PTV data for different Rib width/Groove spacing ratios and rotations.

Rib width/Groove spacing ratio	Rib width	Groove width	Rotation (degrees)				
	(mm)		0	3	6	9	12
0.77	10	3	64	56	57	43	36
0.63	10	6	74	86	97	92	47
0.45	10	12	72	88	93	114	115
0.91	32	3	43	-	-	-	-
0.84	32	6	49	40	39	35	25
0.73	32	12	96	90	76	79	71
0.76	19	6	67	56	67	46	28
1.00	Control		14	15	14	14	14

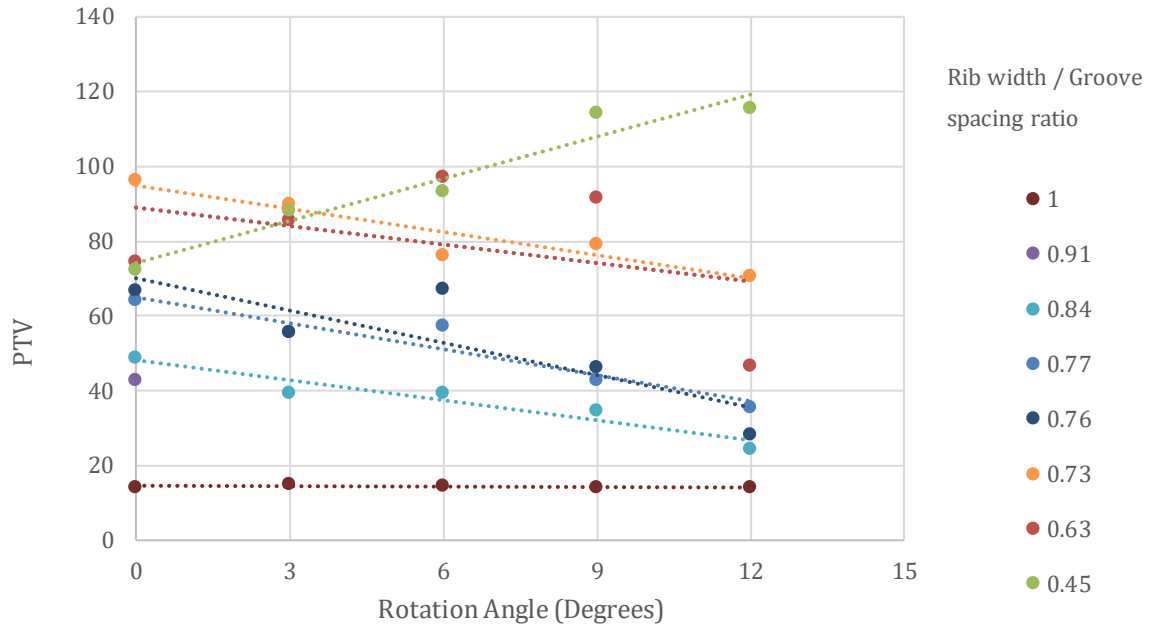

Figure 9.12. Plot of Pendulum Test Value (PTV) and rotation angle.

Figure 9.12 shows a plot of Rotation Angle (RA) against Pendulum Test Value (PTV). The data shows there was no change in PTV for the un-grooved specimen when changing the test specimen rotation angle. The control specimen had the lowest PTV. This was expected as it is a smooth surface.

The remaining rib width / groove spacing ratios show there was a decrease in PTV as the test specimen's rotation angle increased. The one exception was rib width / groove spacing ratio 0.45, with PTV increasing with rotation angle.

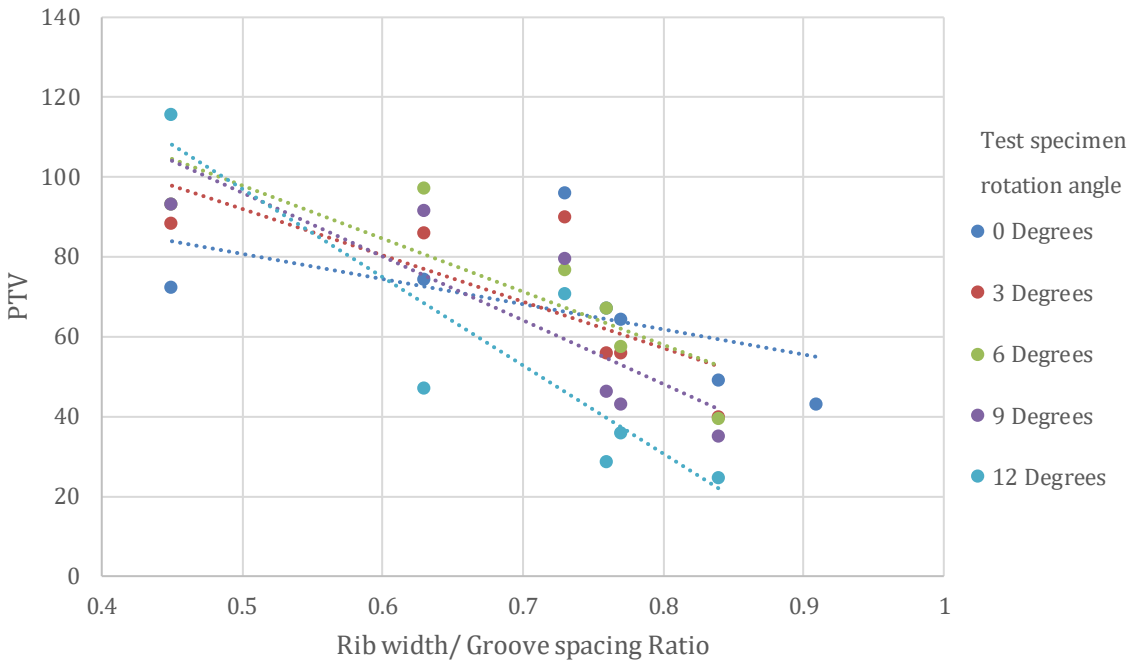

Figure 9.13. PTV of idealised grooves Vs rib width / groove spacing ratio.

Figure 9.13 plots PTV of idealised grooves Vs rib width / groove spacing ratio for the different test specimen rotation angles considered. The plots show that rib width / groove spacing ratio has a different effect on PTV for the rotation angles considered.

The plot show there is no dominant rotation angle which generates the highest PTV across all groove spacing ratios. The data suggests rotation angle for providing greatest PTV is rib width / groove spacing ratio specific.

9.6 Comparison of contact area and PTV

Comparison of contact area, PTV, test specimen rotation angle and rib width / groove spacing ratio were carried out. The main findings are summarised in Figure 9.14, which combines these four variables in a single plot.

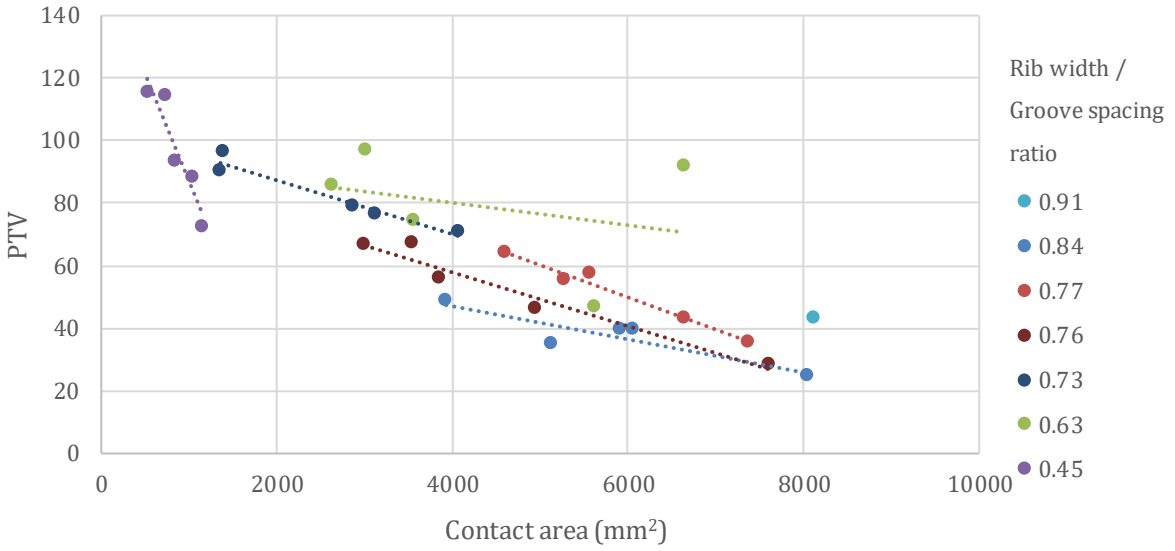

Figure 9.14. Measured Contact Area Vs Measured Pendulum Value for all Rib width / Groove spacing ratios.

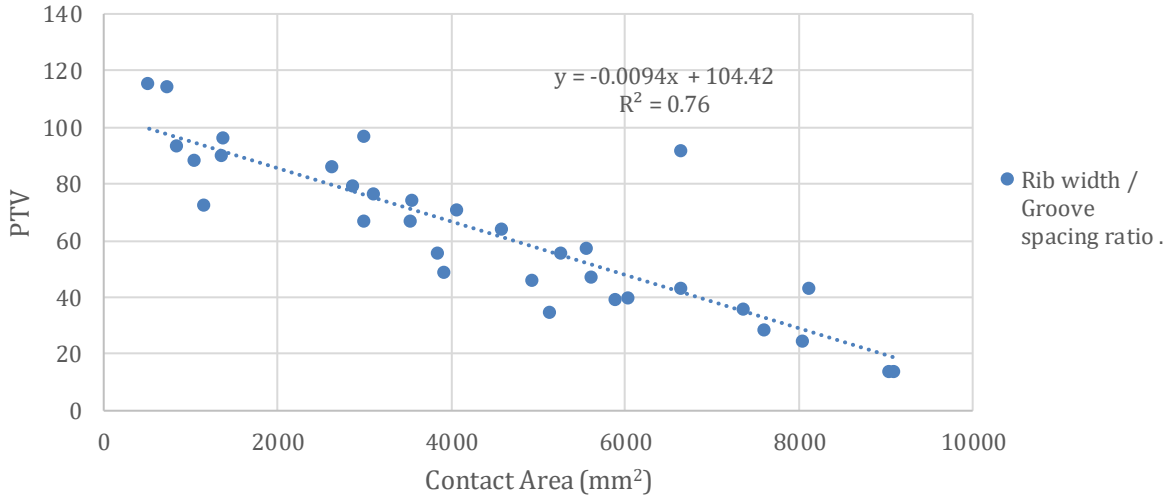

Figure 9.15. Master plot showing the general relationship between measured contact area Vs measured pendulum value for all Rib width / Groove spacing ratios.

Figure 9.14 shows the contact area vs pendulum value for all rib width / groove spacing ratios. The data shows an overall decrease in PTV as the contact area increases. This reduction applies to each groove ratio. The general trend shown on the master plot in Figure 9.15 demonstrates that PTV broadly declines with increased contact area regardless of the rib width / groove spacing ratio. The plot shows that different rib width / groove spacing ratio provides different levels of PTV with the lower inter groove ratio providing the greatest PTV. This was unexpected given that greater contact should equate to greater resistance and a higher pendulum value. The plot demonstrates the significance of groove dimensions suggesting groove dimensions ~ rib width / groove spacing ratio primarily contributes to PTV than that of the rib contact area as those with the higher PTV have lower rib width / groove spacing ratio and those with higher rib width / groove spacing ratio have lower PTV.

9.7 Idealised Grooves Multiple Regression Predictive Model

A multiple regression analysis of the data used to plot Figure 9.14 was conducted using Microsoft Excel. The dependent variable – PTV tester data including the independent data - Rib width / Groove spacing ratio and test specimen rotation angle variables were used to generate an Analysis of the Variance (ANOVA) table. The statistics from the ANOVA table were used to generate the prediction model below;

$$y = m_1 x_1 + m_2 x_2 + c$$

Where;

$y = PTV$

$c = mathmatical\ constant$

$m_1 = Rib\ width\ /\ Groove\ spacing\ ratio\ Coefficient\ /constant$

$x_1 = Rib\ width\ /\ Groove\ spacing\ (input)$

$m_2 = Rotation\ Angle\ Coefficient/constant$

$x_2 = Rotation\ angle\ (input)$

The equation with the constant statistical co-efficient is;

$$y = -156.924x_1 + -0.99714x_2 + 181.2613$$

The multiple regression co-efficient demonstrate a negative rib width / groove spacing ratio co-efficient and rotation angle co-efficient. The negative co-efficient demonstrates

statistical evidence of an inverse relationship between the variables. For example an increase in dependent variable corresponds to a decrease in independent variable.

An example to predict PTV using this equation is:

$$y = (-156.924 * 0.77) + (-0.99714 * 3) + 181.2613 = 57.43$$

The regression model is statistically strong with an R^2 of 0.74 as determined from the regression statistics of the ANOVA table. The ANOVA table and associated data is appended to Appendix C. The standard error of the model is 15.53 PTV points. This standard error represents the average value the measured PTV values deviates from the regression line.

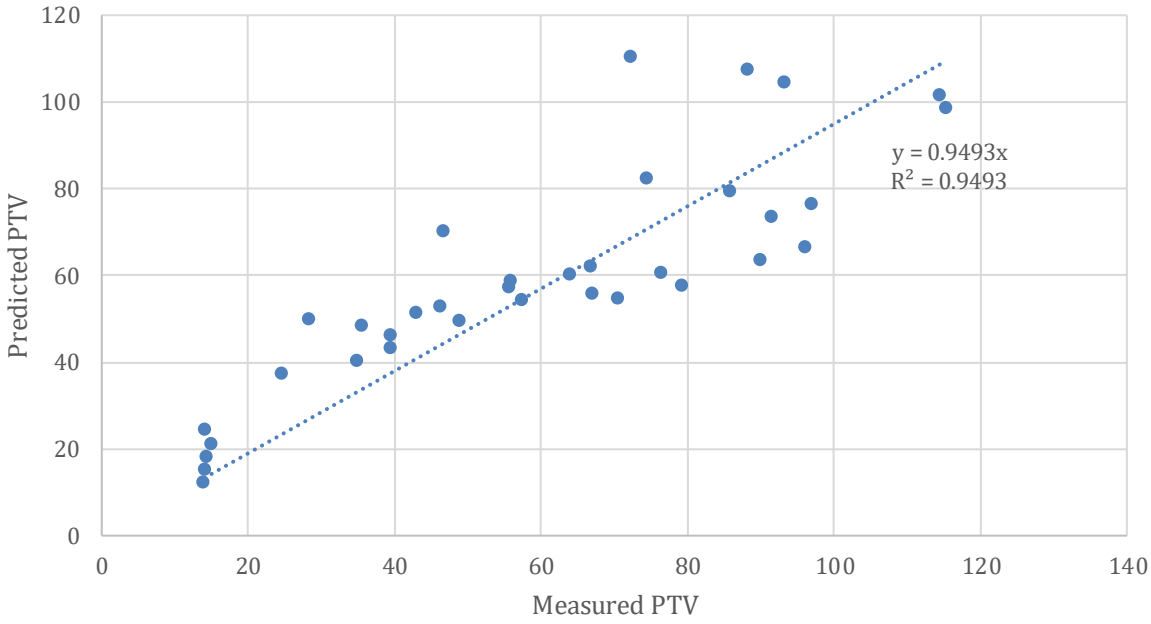

Figure 9.16. Measured PTV Vs Predicted PTV.

Figure 9.16 shows the measured PTV against the predicted PTV. The plot shows the PTV data points for less than 60 PTV adhere reasonably closely to the equality line. Beyond 60 PTV, the points become more sparse. This would suggest the model can reasonably predict PTV accurately of 60 PTV or lower. Above 60 PTV more data points would be required to predict PTV higher than 60.

Whilst the model does suggest a strong statistical significance ($R^2 > 0.7$), Fwa et al., (2003), Liu et al., (2004), found the use of the British Pendulum for measuring grooved surfaces to

exhibit unreliable pendulum behaviour. Therefore, the model should be considered with a degree of caution and is recommended for further work.

9.8 Grooved Marshall Asphalt (GMA) Tyre Interface Angle

Standard ICAO groove dimensions of 6mm x 6mm x 38mm centre to centre spacing were sawn into three Marshall Asphalt test specimens at offset angles of 6°, 9° and 12°. Skid resistance was determined by the standard method for a non-grooved surface. This was to ensure consistency in the method of this investigation into differing angles of interaction.

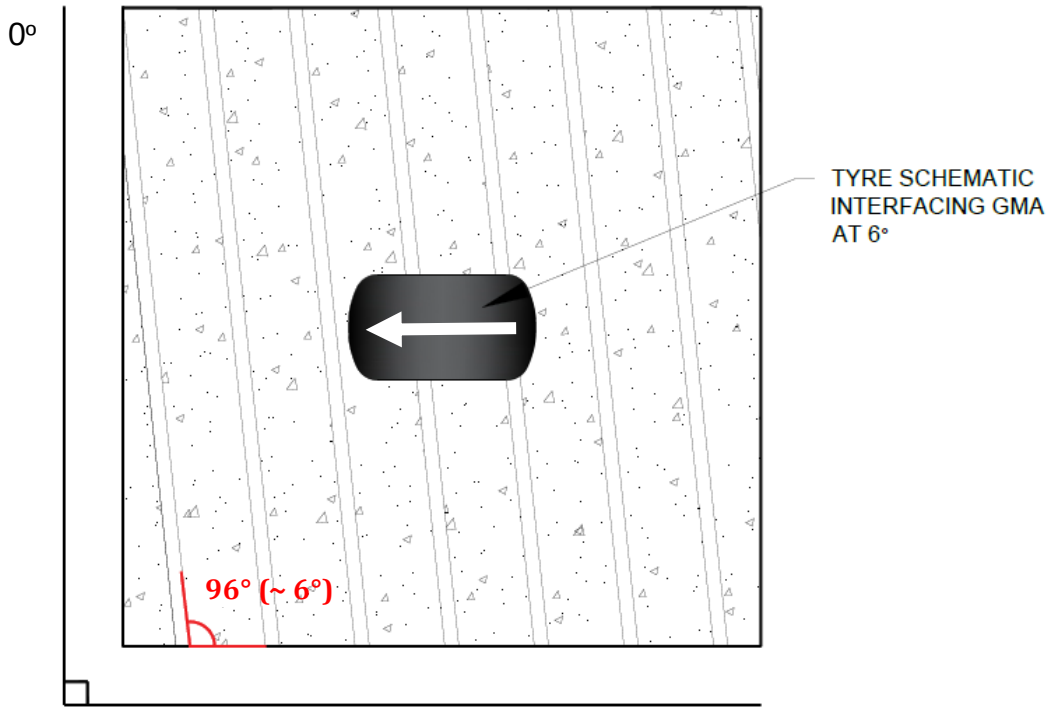

Figure 9.17. Plan view schematic of a tyre interacting with Grooved Marshall Asphalt at 6°.

Figure 9.17 illustrates a plan view schematic of a tyre interacting with Grooved Marshall Asphalt where the Grooves are offset angle of at an angle of 6° anticlockwise. The three test specimens were subjected to simulated trafficking using the RTM.

9.9 PTV of Tyre interfacing GMA with offset grooves at offset angles of 6°, 9° and 12°

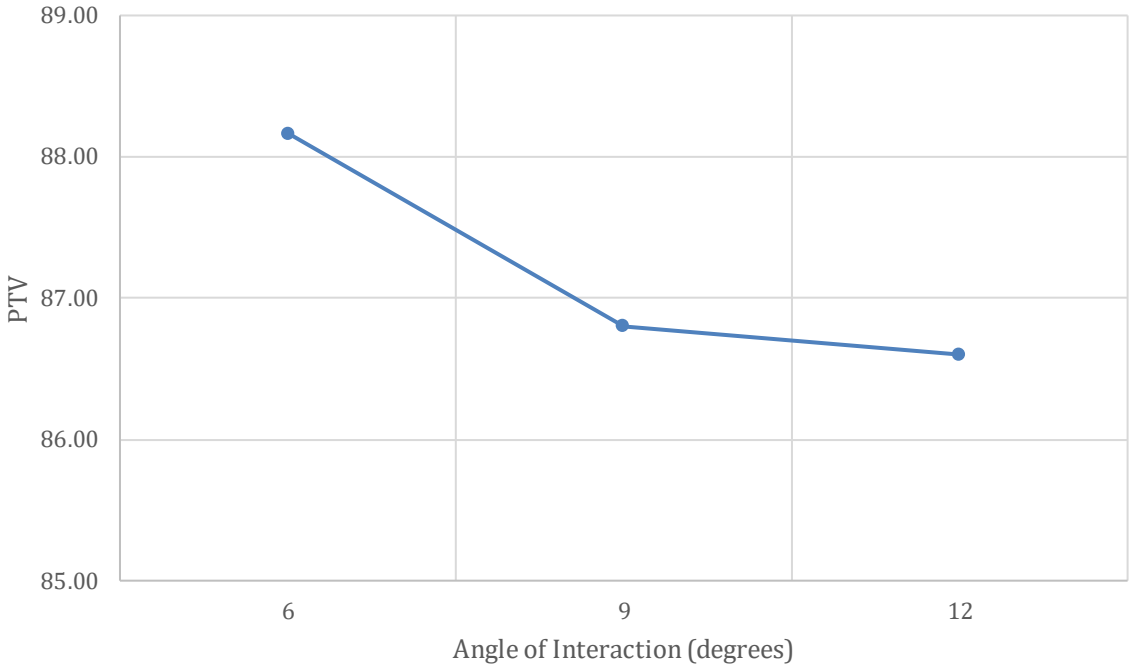

Figure 9.18. PTV for grooves at offset angles of 6°, 9° and 12° before simulated trafficking for FAA standard grooving.

Figure 9.18 plots the PTV for grooves at offset angles of 6°, 9° and 12° before simulated trafficking. The plot shows that before trafficking changing the offset from 6 to 12 degrees caused a small decrease in PTV of 1.57 units.

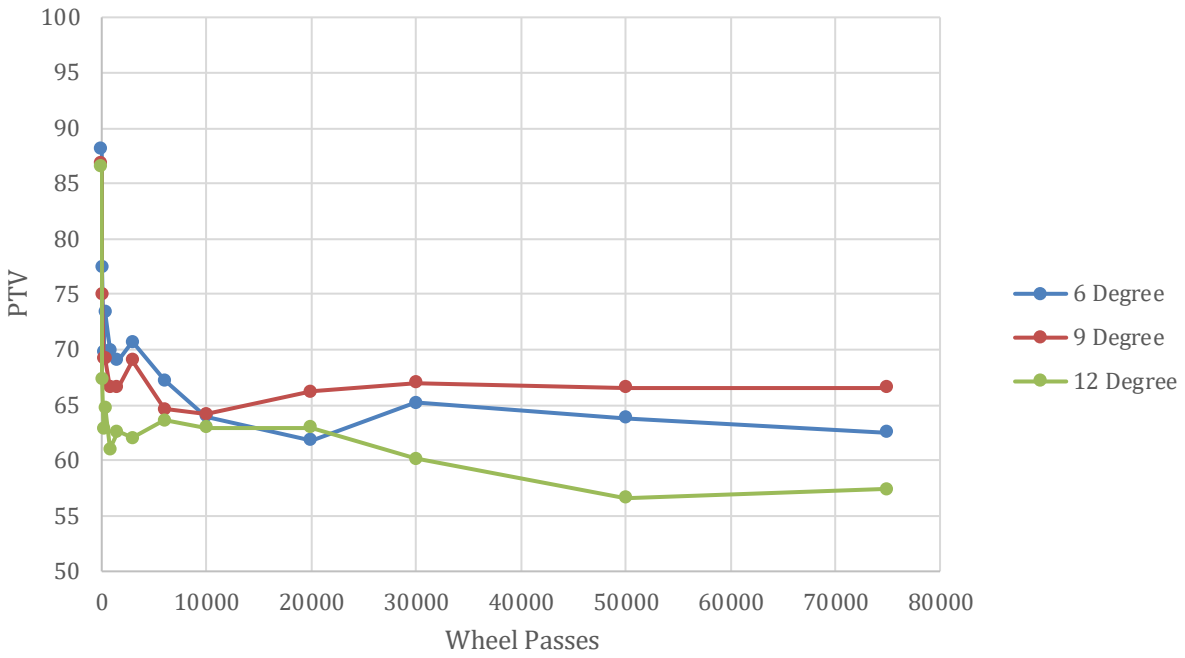

Figure 9.19. Angled GMA subjected to 75,000 simulated wheel passes.

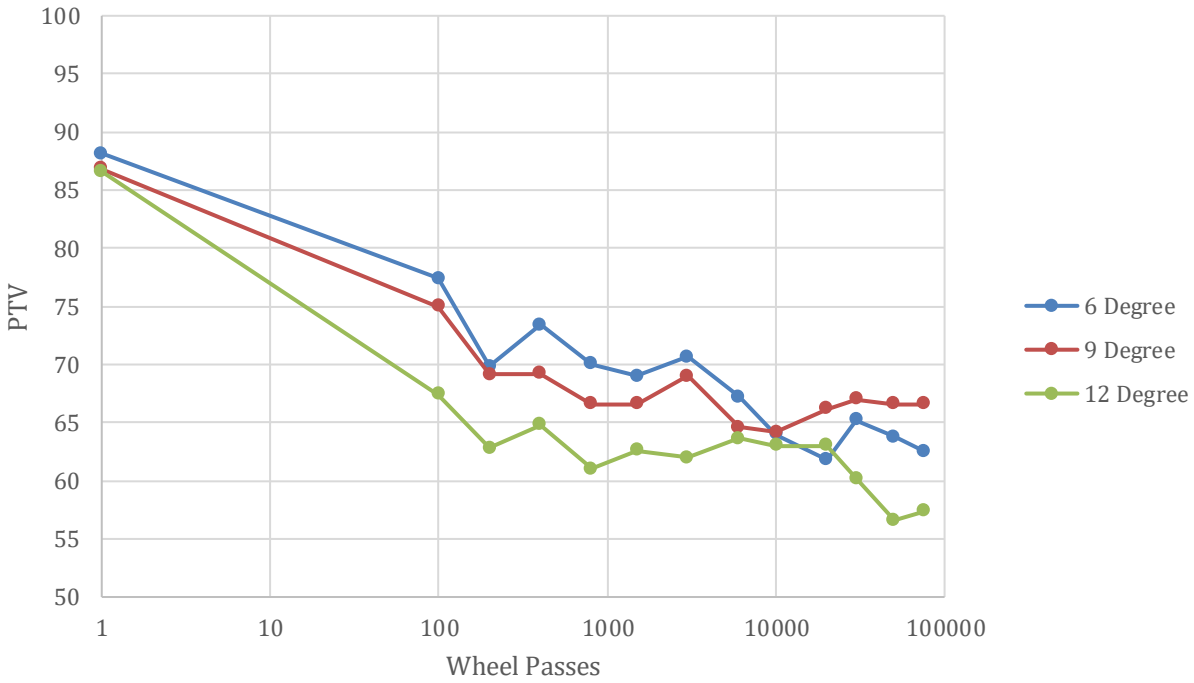

Figure 9.20. Angled GMA subjected to 75,000 simulated wheel passes (log scale).

Figure 9.20 plots the RTM data in 100,000 wheel passes using a log scale. The log scale was similar to that used in chapter 7 as the relationship within data is easier to visualise. The data shows a log-scale decrease in PTV with increasing number of wheel passes. There is a significant drop in PTV from 85+ to 67 ~ 57 PTV. The 6 and 9 degree plots are similar with the 12 degree data giving the lowest PTV. The data suggest that whilst 6° initially provides the best early life PTV values, 9° almost matches 6° but provides marginally lower PTV values. However, at higher trafficking intervals, 9° offers higher PTV values. This suggests 9° offers higher longevity of PTV values.

In terms of a runway pavement, offset grooving may improve the operational efficiency by reducing maintenance associated with improving runway skid resistance.

Table 9.3. PTV Percentage change of PTV for three operating angles.

Operating Angle (°)	Prior Trafficking - 10,000 Wheel Passes (%)	Prior Trafficking - 75,000 Wheel Passes (%)	Difference (%)
6	27	29	+ 2
9	26	23	- 3
12	27	34	+ 7

Table 9.3 shows the PTV percentage change from initial skid resistance value up to 10,000 and initial skid resistance value up to 75,000 wheel passes. The data shows that for 6° initial skid resistance decreases in the region of 27% up to 10,000 wheel passes. As simulated trafficking increases to 75,000, the further change in skid resistance is modest by an additional 2%. 9° shows that PTV is similar to 6°; however, as demonstrated in Figure 6.19, PTV increases. Therefore, the overall PTV decrease is less. 12° shows a greater change in PTV at 75,000 wheel passes of 34% reduction.

The data suggest that 6° and 9° has a greater ability to maintain higher PTV. As all test specimens have the same groove dimensions, all changes in PTV can be explained by groove angle.

9.10 Rotation Angle (RA) Vs Interface Angle (IA)

The principle of rotation angle and interface angle are fundamentally different. The data presented up until sub section 9.8 demonstrates relationships from data where the test specimen is rotated at different angles and then pendulum tested. This relates to the rotation angle. However, sub-section 9.9 demonstrates data where the tyre traffics GMA where the grooves are sawn at different off set angles. Therefore, this relates to the interface angle.

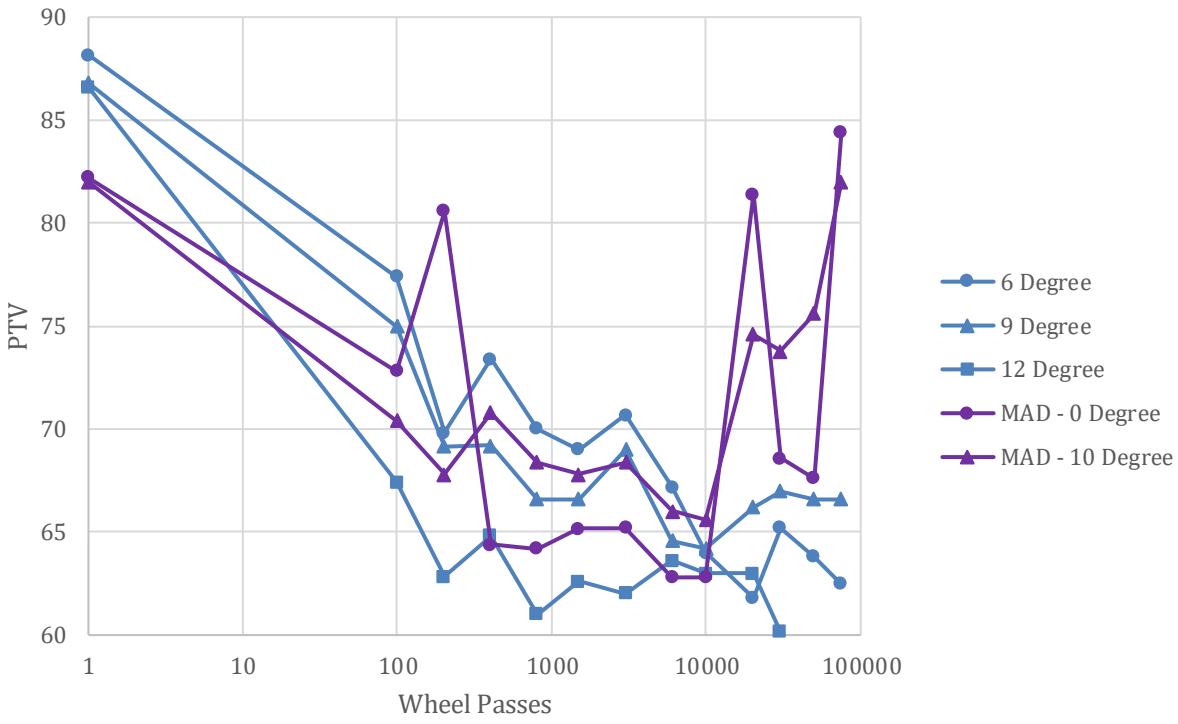

Figure 9.21. Marshall Asphalt Grooved at 6°, 9°, 12° and Test Specimen MAD subjected to 75,000 simulated wheel passes (log scale).

Figure 9.21 plots the pendulum data for angled GMA subjected to simulated trafficking at interface angles of 6°, 9°,12° and test specimen MAD where the test specimen is trafficked at 0° and the pendulum values determined when the test specimen is rotated at 0° and 10°.

The plot for the Interface Angle (IA) data shows a general decrease in PTV as simulated trafficking increases with fluctuations within the data.

The Rotation Angle (RA) shows a similar relationship up to 10,000 however there are two erratic fluctuations within the data. The RA data profile exhibits erratic behaviour at 200 and 20,000. These data points were likely influenced by rougher surface because of wear or groove breakdown as both 0° and 10° rotation angles show similar erratic behaviour. The data shows within a wheel pass envelope of between 400 and 10,000 wheel passes that a RA of 6° offers the highest PTV.

To an airport operator, the ability of the asphalt to maintain its skid resistance throughout trafficking is highly desirable as this reduces maintenance costs and eventually delays the replacement of the runway. Therefore, considering which angle offers the greatest consistent PTV may be of interest.

Table 9.4. Rate of PTV decrease based on a linear relationship.

	Angle (°)	0 - 10,000 wheel passes		0-75,000 wheel passes	
		R^2	Equation	R^2	Equation
IA	6	0.32	-0.0002x +72.1	0.40	-0.0013x + 75.355
	9	0.09	-8E-05x + 70.202	0.29	-0.0011x + 72.826
	12	0.24	-0.0002x + 66.24	0.09	-0.0007x + 67.693
RA	0	0.12	0.0001x + 69.049	0.31	-0.0012x + 71.947
	10	0.38	0.0001x + 69.583	0.27	-0.0007x + 71.519

Table 9.4 shows the linear relationship of data in Figure 9.21. Whilst the R^2 can be considered poor as it is generally less than 0.7. Normally in statistics the R^2 provides a statistical indication of the relationship between the dependent and independent variables. In this case whilst the R^2 is poor it is not of consideration as it is the gradient of the trend line within the data that is of interest as this is used to compare the rate of PTV decrease.

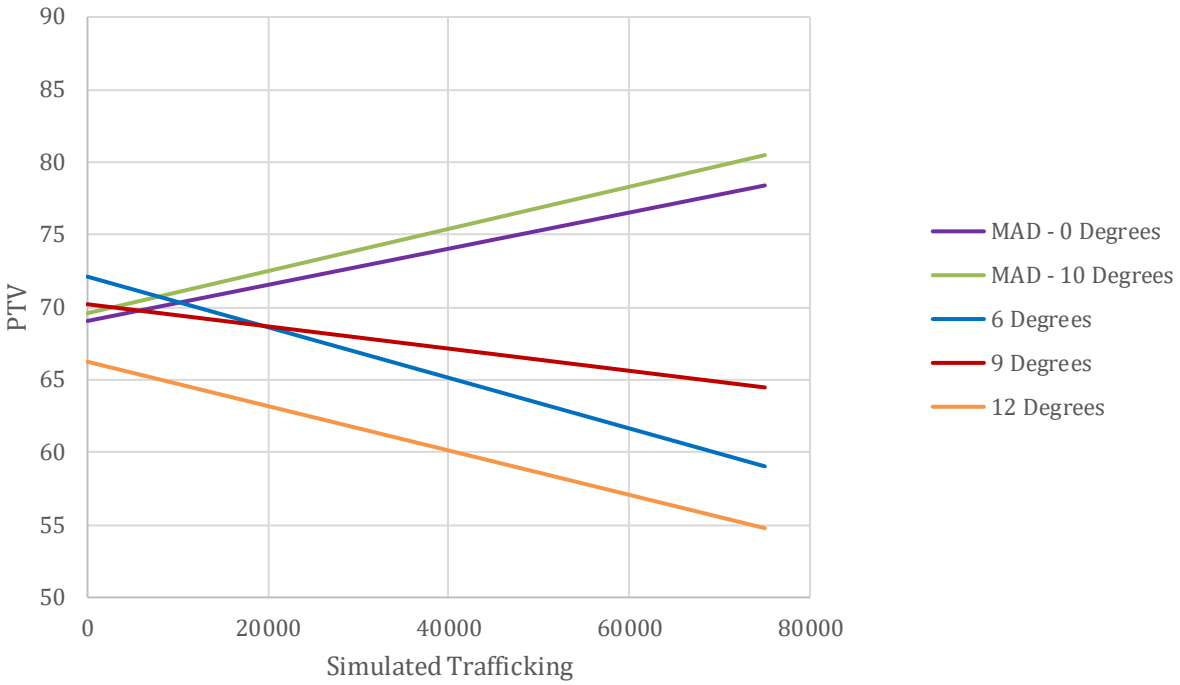

Figure 9.22. Comparison of linear trend line gradients for PTV with wheel passes.

Figure 9.22 shows the linear trend line gradient of the data presented in Figure 9.21. The plot shows the PTV increase for test specimen MAD (29mm rib, 6mm, groove). This increase is deceptive (i.e it is perceived to increase as shown by the trend, however, in reality it does not). The erratic data at wheel pass of 200 and 20,000 likely contributed to the gradient identified in Figure 9.22.

The plot shows that 6° and 12° are almost parallel with little difference in the gradient of the line. However, 9° shows the highest PTV with the lowest rate of decrease as suggested by the linear trend. Therefore, not only does 9° maintain greater PTV stability at higher trafficking intervals, but it also has the lowest rate of PTV decrease.

9.11 Summary

- Changing the test specimen rotation angle from 0° to 10° has no effect on contact area for the idealised non-grooved test specimen.
- Grooving influences the interface of the pendulum. Grooving causes the pendulum to bounce over the grooved surface with greater contact occurring when the pendulum initially interacts with the grooved surface and less contact on the out swing.
- Pendulum contact area increases as the test specimen rotation angle increases from 0° to 12°.
- Pendulum values for an idealised groove surface with standard ICAO dimensions derives a pendulum value from 57% less contact area for 0° whereas this percentage reduces to 12% for the test specimen rotation angle of 12°.
- Comparing the paint removal for an idealised surface to a GMA surface for the same rotation angles shows the paint removal is broadly comparable.
- The angled concept demonstrates that changing the interface angles offers potential whole life skid resistance benefits and further work in this area is required.

CHAPTER 10.

LABORATORY INVESTIGATION OF AIRCRAFT IMPACT TEMPERATURE

10.1 Introduction

This chapter investigates tyre impact temperature. Impact temperature contributes to the deposition of rubber on the runway surface upon aircraft touchdown. Tyre impact temperature is considered the instantaneous heat of the tyre when it makes contact with the runway surface. The investigation focuses solely on impact temperature. The investigation simulates the process of landing an aircraft tyre within the constraints of a laboratory setting.

This chapter considers the effect of Tyre Loading, Speed, Surface Texture and Tyre off Set on tyre impact temperature. Two methods of measurement were used to capture tyre impact temperature. Both methods operate on different principles of measurement. Texsense INF (V/T) 150 ° C records voltage and uses a data logger to convert this into temperature. Micro-Epilson thermoIMAGER 400 records the surface temperature of the tyre based on the emitted infrared energy.

10.2 Investigation Equipment / Methods

The methods and equipment used for this investigation is further considered below.

10.2.1 Test Tyre

This investigation used a standard ASTM 1844 friction measuring tyre fitted to the GripTester, a fixed slip longitudinal friction measuring device. This device is used at many airports around the world to measure runway wet skid resistance. Given its close association with airports and the operational safety of runways, a GripTester tyre was felt to be appropriate for this investigation. Figure 10.0 below demonstrates the scale of the GripTester tyre compared to a standard Airbus A320 tyre.

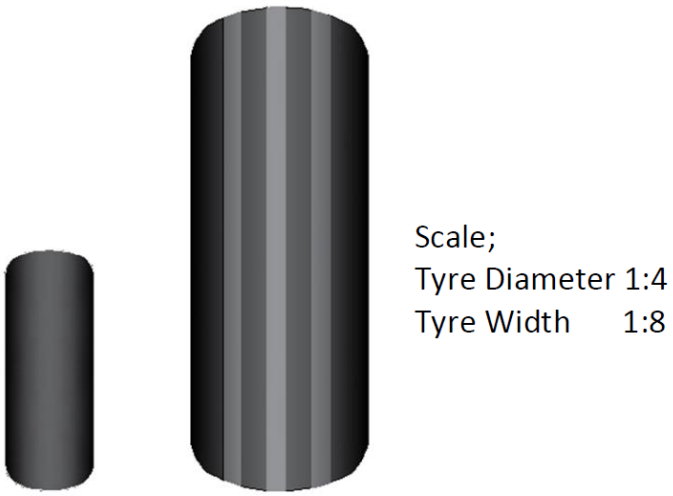

(a) (b)

Figure 10.0. (a)ASTM 1844 Friction Measuring Tyre, (b) Standard Airbus A320 Rear Landing Gear Tyre.

The variation of surface texture was facilitated with the use of three grades of sandpaper grit. This included Fine Sand Paper – grit size 162µm, Medium Sand Paper – grit size 269µm, Coarse Sand Paper – grit size 425µm. Application of tyre loading was facilitated with the use of 10kg loading plates.

10.2.2 Ulster Loaded Tyre Road Assimilator

The ULTRA was used to simulate a tyre dropping onto a moving surface. The ULTRA is Variable Speed Internal Drum Machine consisting of a steel drum of approximately 1.22m diameter. The drum rotation speed is controlled by a Danfoss FC302 VLT Automation Drive up to a maximum of 300 revolutions per minute (rpm) or equivalent to 64.3 km/h.

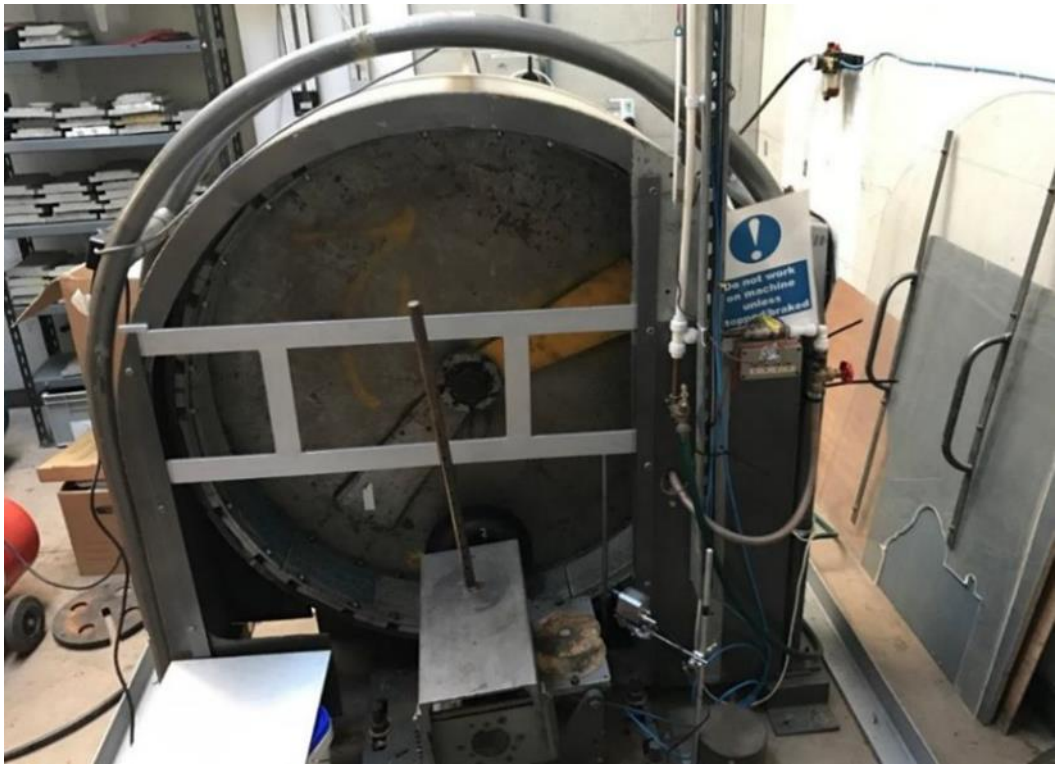

Figure 10.1. The ULTRA rolling road apparatus

The ULTRA was used to simulate a tyre dropping onto a moving surface.

10.2.3 Static Vertical Loading

Total static vertical loading acting through the tyre from the loading carriage was determined using a Novatech F204 load cell with a digital Red Lion strain gauge indicator.

Figure 10.2. Determination of total static vertical load using Novatech F204 load cell with a digital Red Lion strain gauge indicator

The Novatech F204 is a bi-directional load cell show in figure 10.2 measures both tension and compression and is used within the motor industry. It consists of an axial strain cylinder and has a maximum limit of 10kN.

The Red Lion strain gauge indicator consists of a digital voltmeter combined with a high-gain, differential input amplifier that has provision for wide range scaling adjustment.

The set-up enabled standardisation of the total load acting through the tyre. The total load of the carriage was initially determined, followed by the additional applied loading of 10kg loading plates up to a maximum of 100kg. Red Lion values generated for each successive 10kg increment were used to produce a standard graph. The red lion values were compared for the tyre loading conditions to calculate the load applied to the tyre. The R^2 was used to calculate the total loading.

The Red Lion values were recorded for both loading and unloading of the 10kg plates. The Red Lion value was then converted to a total load value in the form of Kilonewtons (kN). This is displayed in Appendix D.

10.2.4 Test Variables

It can be appreciated that various factors influence the thermal signature of tyre impact temperature during aircraft landing conditions. This investigation looks at single parameters. The variables considered in this thesis are;

- Speed (km/h)
- Load (kN)
- Texture
  - ULTRA Drum - Smooth Metal Surface
  - Fine Sand Paper (Average Grit Size162µm)
  - Medium Sand Paper (Average Grit Size 269µm)
  - Coarse Sand Paper (Average Grit Size 425µm)
- Tyre off set
  - 0° (Normal operating angle)
  - 4°

10.2.5 Speed (km/h)

The speed of the ULTRA was determined by working within the limits of the ULTRA. The maximum drum speed was 64.3km/h. The initial speed conditions for the smooth ULTRA test surface were 10, 20, 30, 40, 50 and 60km/h.

Speed conditions were revised for further testing as it was felt that using three-speed conditions provided sufficient data to determine the relationships amongst the data. Thus speed conditions for the sandpaper surfaces were reduced to 20, 40 and 60km/h.

10.2.6 Load (kN)

The loading of the tyre was determined by the ability of the loading carriage to retain additional load.

The applied loading conditions were 20, 40, 60, 80, 100kg for the smooth ULTRA surface. This equated to a total loading of 0.53, 0.76, 1.0, 1.29 and 1.55 kN acting through the tyre.

Loading conditions were revised for further testing as considered that the loading conditions should reflect the operating conditions of the grip tester friction measuring tyre. Therefore, it was determined that the loads considered were greater than the standard operating load of grip tester friction tyre. The standard operating load of a grip tester friction tyre was 20kg which equates to 0.19kN. Thus total loading of the ULTRA was reduced to 0.19, 0.33 and 0.43 kN.

10.2.7 Surface Texture

Initially to reduce the influence of pavement texture on tyre impact temperature, the smooth surface of the ULTRA was considered. However, after consultation with Jet2 Ltd Engineering department (personal communication, April 11, 2019) it was felt that whilst the smooth surface kept the data simplistic, it may also give inaccurate results as the coefficient of friction for rubber can be reduced considerably for smooth surfaces. Thus three grades of micro grit sandpaper were introduced to facilitate the introduction of texture. The sand paper introduced is composed of aluminium oxide with different grit sizes. The three micro grits considered were;

- P100 – Fine Sand Paper (Average Grit Size162µm)
- P60 - Medium Sand Paper (Average Grit Size 269µm)
- P40 - Coarse Sand Paper (Average Grit Size 425µm)

Sandpaper was chosen as the tyre industry use sandpaper to facilitate texture conditions when investigating tyre behaviour on different surfaces.

10.2.8 Tyre Off Set

The angle of the tyre interaction on the surface is also considered to account for the interaction where an aircraft may have to land in crosswind conditions. The standard condition is where the tyre is in line with the horizontal speed of the aircraft (0°) and, in this case, in line with the rotating direction of the drum and for offset conditions, the tyre was

offset at approximately 4°. 4° was considered an appropriate offset to work safely within the constraints of the ULTRA drum.

10.3 Method of Temperature Measurement

This investigation used two methods of non-contact measurement operating on different principles of measurement.

- Texsense INF (V/T) 150 °C records voltage and uses a data logger to convert this into temperature.
- Micro-Epilson thermoIMAGER 400 records surface temperature of the tyre based on the emitted infrared energy.

Figure 10.3. Impact temperature measurement set up

Due to the constraints of the ULTRA set up, the temperature measurement equipment recorded the temperature of impact after the tyre had approximately rotated 270° after impact. Figure 10.3 shows the temperature measurement set up for the two different devices.

10.3.1 Texsense INF (V/T) 150°C

The Texsense INF consists of two elements for tyre temperature measurement; a single point infra-red temperature and a GPS data logger. Both devices have been developed and used for motorsport applications.

Figure 10.4. Texsense INF (V/T) 150 ° C temperature measurement device.

Figure 10.4 shows the Texsense INF temperature measurement device. It has a temperature measuring capability in the range of 0°C to 150°C with a response time of 50 ms. At a distance of 50 mm, the spot measurement has a 12.5 mm diameter. Within this area, the device takes an average spot temperature measurement. This device operates on the principle of measuring voltage. The device outputs a signal from 0 to 5 volts. This voltage is converted to temperature using a calibration table provided by the manufacturer.

10.3.2 Micro-Epilson thermoIMAGER 400

The Micro-Epilson thermoIMAGER 400 is a thermal imaging camera that calculates temperature based on emitted infrared energy. The thermal imaging works with adjoining propriety software TIM Connect.

Figure 10.5. Micro-Epilson thermoIMAGER 400 temperature measurement device.

The two-dimensional detector (FPA - focal plain array) enables the measurement of an area of interest, and this is projected as a thermographic image using standardized palettes. It has a measuring capability of 20°C to 900°C with a maximum functioning capacity of 80Hz a second. For this investigation, the thermoIMAGER was placed at approximately 11cm from the tyre, which enabled a view across the tyre's width.

10.3.3 Experimental Procedure

The ULTRA was set to the desired speed condition, and the loading plates were placed onto the loading carriage for the desired loading condition. The methods of measurement were set to record, and the tyre dropped onto the rotating surface.

10.4 Data Preparation

Raw data collected for a smooth surface at 60km/h is presented in Figure 10.6. Figure 10.6 shows ambient temperature conditions prior to the tyre is dropped onto the rotating ULTRA surface; the spike in the data represents the impact temperature when the tyre is dropped. The difference in ambient conditions (y-axis) and the difference in tyre drop (x-axis) can be seen. To facilitate comparison, the ambient conditions were standardised to 20°C this was done by subtracting the average room temperature - 20°C from the collected data as illustrated in Figure 10.7. To further facilitate comparison, the x-axis was manipulated to show the impact temperature occurring at 1 second, as shown in Figure 10.8.

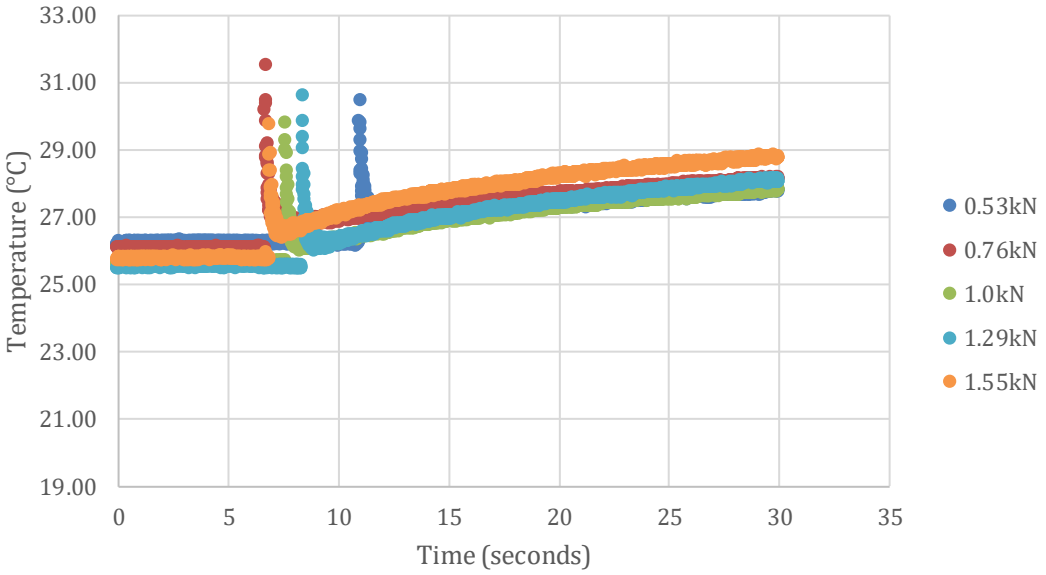

Figure 10.6. 60km/h Texsense Device Raw Data Set for a smooth surface.

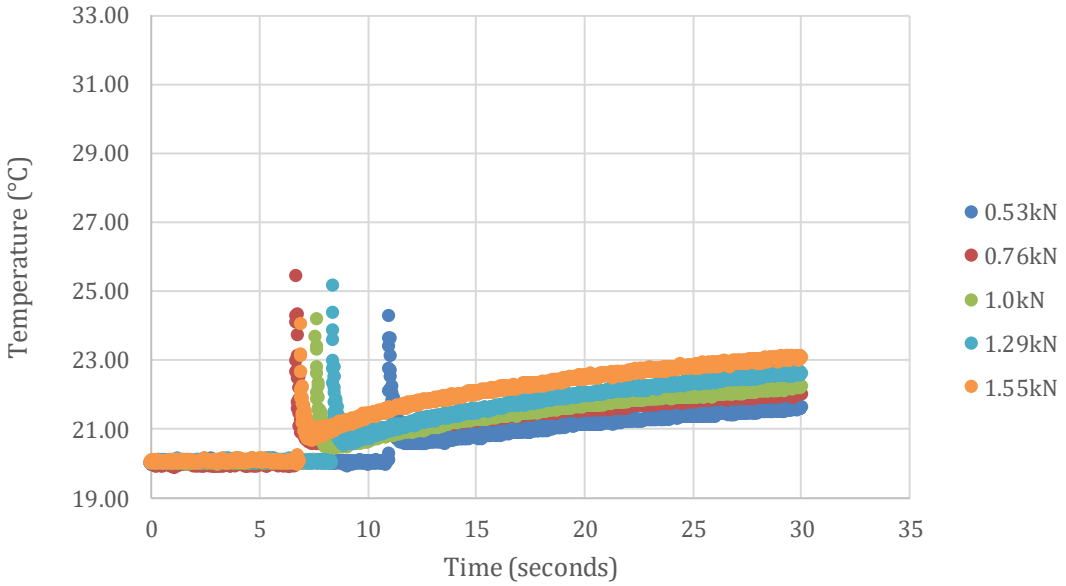

Figure 10.7. 60km/h Texsense Device Raw Data y-axis Standardised to 20°C for a smooth surface.

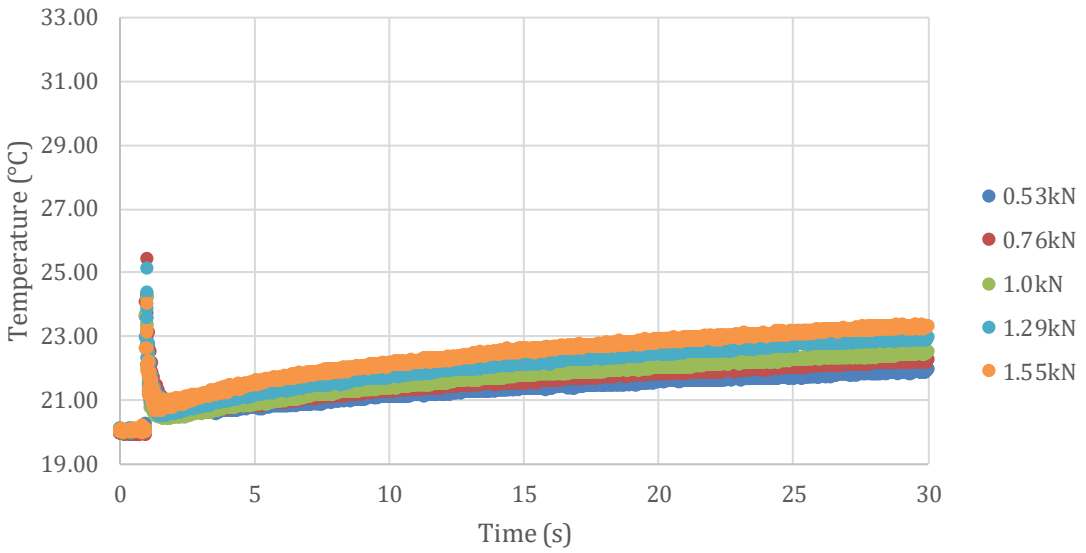

Figure 10.8. 60km/h Texsense Device Raw Data Standardised to 20°C for both axis for a smooth surface.

10.4.1 Experimental Data

A series of experiments were performed for five loading conditions and six test speeds for the smooth surface, three loading conditions and 3 test speeds for the three sandpaper surfaces, three loading conditions, and 3 test speeds with a 4 degree offset angle. A minimum of 3 runs was carried out for each test condition for the smooth surface, and a minimum of 2 runs was carried out for the sandpaper surfaces.

Figures 10.9 to 10.11 illustrate how the Texense sensor dataset recording at 100 Hz can be progressively used to explain what happens in the interface for the landing aircraft tyre/runway contact patch. This example is for measurements recorded with the ULTRA drum rotating at 20, 40 and 60 km/h. The tyre inflation pressure is 20 PSI with a 0.53 kN load. The hydraulic control is used to drop the statically loaded ASTM friction tyre onto the rotating internal lip of the ULTRA drum. The static tyre makes a sudden impact with the rotating drum simulating the tyre of a landing aircraft. The Texense sensor records tyre surface temperature as it starts to rotate.

.

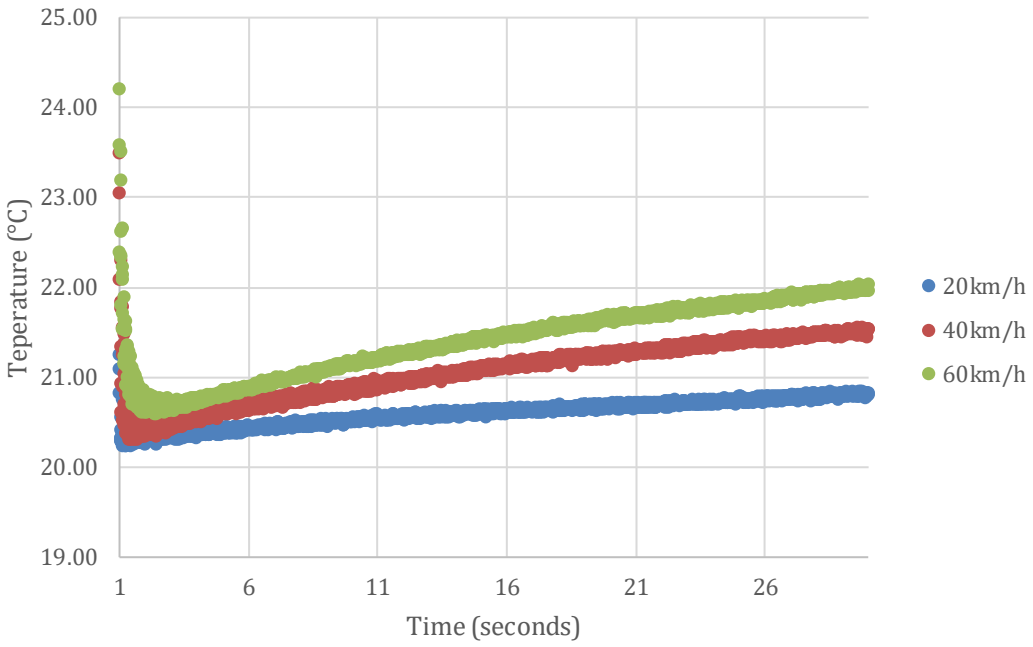

Figure 10.9. Tyre drop data recorded for 30 seconds

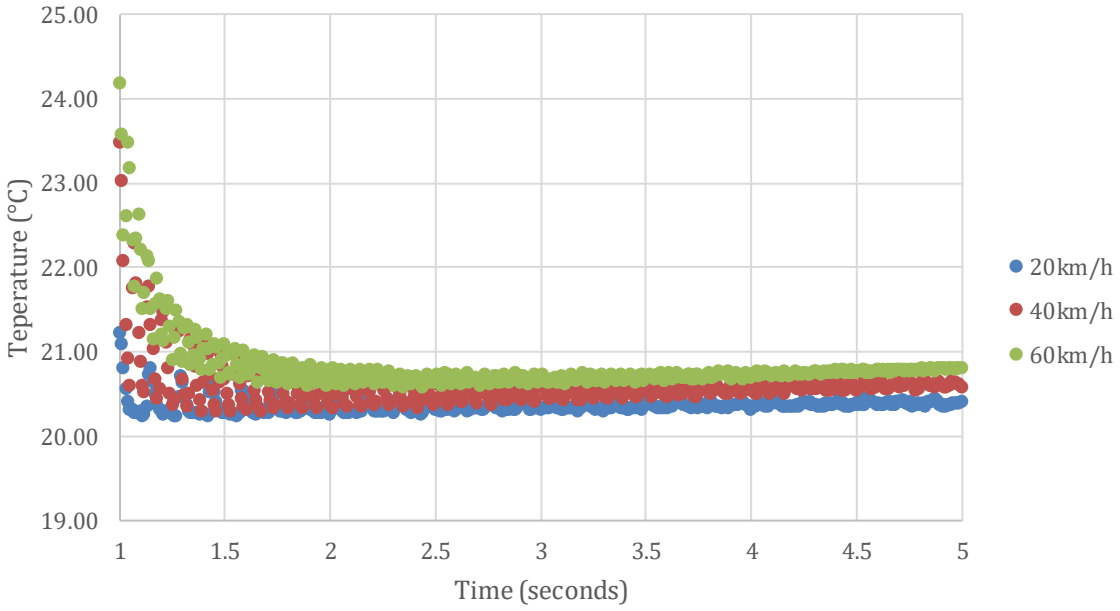

Figure 10.10. Tyre drop data for 5 seconds

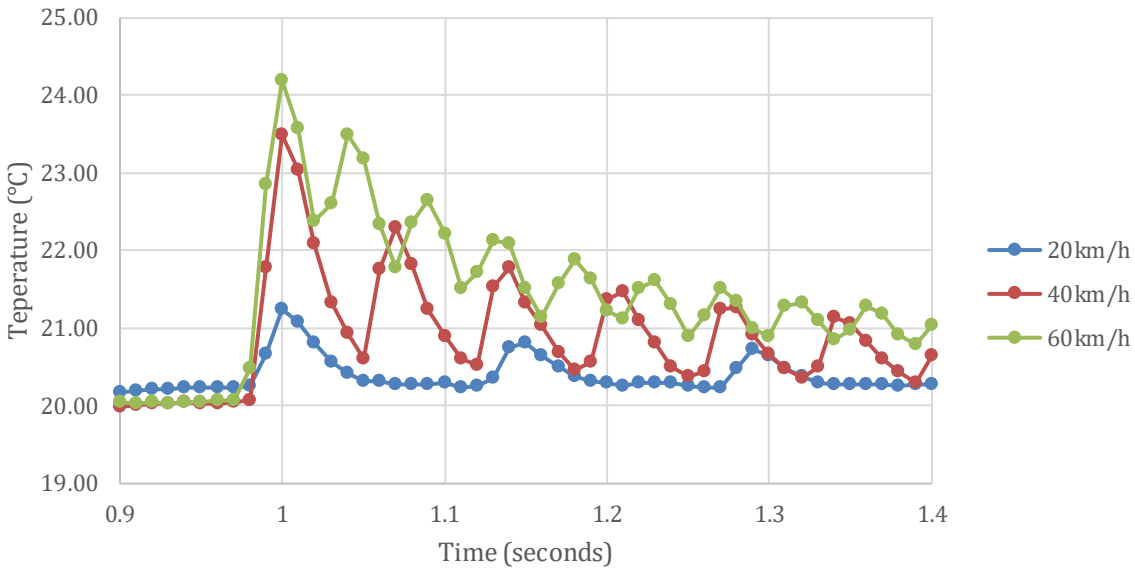

Figure 10.11. Tyre drop data for 0.5 seconds

Figure 10.9 shows what happens during the first 30 seconds of the test. The data shows the surface temperature of the stationary tyre before dropping to be approximately 20 °C reflecting ambient laboratory conditions. The 100 Hz data then shows what appears to be an almost instant increase in temperature as the loaded tyre is dropped onto the rotating surface and makes initial contact at each test speed.

With continued tyre rotation, the measured temperature of the contact patch drops quickly, showing cooling of the tyre surface. As the test continues, the tyre surface temperature rises towards an equilibrium rolling condition, as Tierney et al. (2017) identified.

Figure 10.10 shows 5 seconds of this dataset from 1 second before the tyre drops to 4 seconds after the tyre drop. This shows an almost instant increase in temperature followed by a drop to just above ambient in about 2 seconds. Figure 10.11 shows just 0.5 seconds of recorded 100 Hz temperature data. It shows approximately 0.08 seconds of ambient temperature immediately before the loaded tyre is dropped 15 mm to the rotating surface.

A maximum temperature for the first contact patch is measured approximately 0.03 seconds later. The remaining temperature data is after this last for approximately the next 0.4 seconds. The 100 Hz tyre surface temperature, shows the contact patch and its elevated temperature as the tyre rotates.

The data shows 3 tyre rotations for 20 km/h, 6 tyre rotations for 40 km/h and 9 rotations for 60 km/h. Each plot shows the maximum recorded temperature to fall quickly to a common value within this 0.4 second period.

The data discussed in this chapter refers to the temperature recorded at the initial point of contact when the tyre is dropped onto the rotating surface. This will be known as tyre impact temperature. Tyre impact temperature is shown as the initial spike in the temperature in the above Figures. To account for differences in ambient laboratory temperature, a Δ temperature value has been used to plot the initial maximum tyre surface temperature within the contact patch compared to the starting standardised temperature for each test condition. The Δ temperature value was determined by subtracting the ambient temperature conditions from the impact temperature.

10.5 Speed Vs Impact Temperature

10.5.1 Smooth ULTRA Surface

The primary variables considered in this research were the influence of speed on tyre impact temperature and the influence of Loading on tyre impact temperature. The following considers the influence of speed on tyre impact temperature for a smooth surface, coarse sandpaper surface and a coarse sandpaper surface with a tyre offset at 4 degrees.

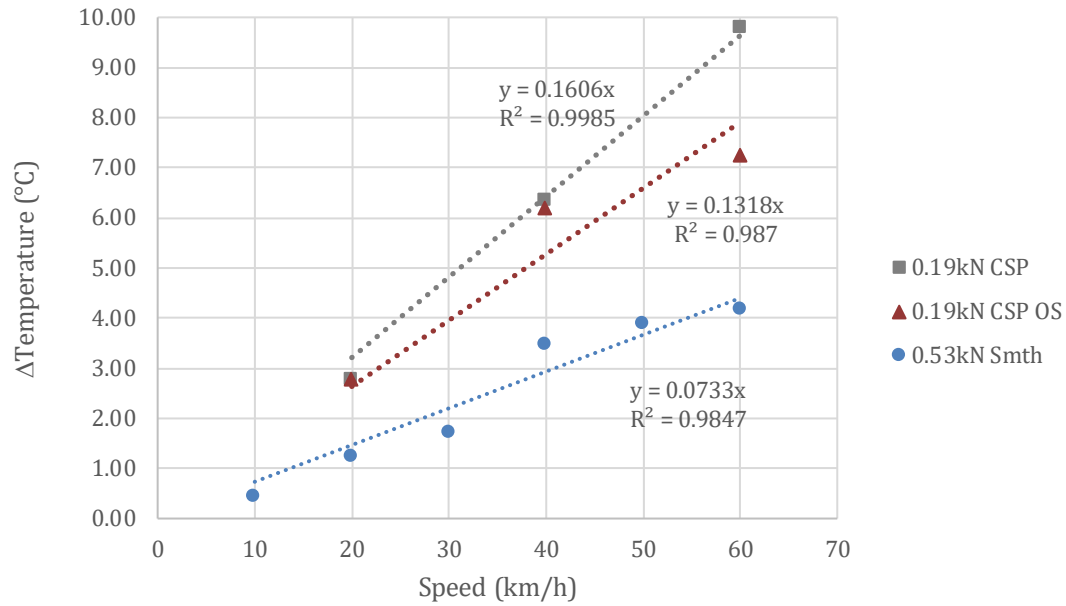

Figure 10.12. Influence of Speed on Tyre Impact Temperature based on Texsense INF (V/T) method of measurement for a smooth surface, coarse sand paper surface texture and a 4 degree tyre offset (load condition 1: 0.19 kN and 0.53 kN).

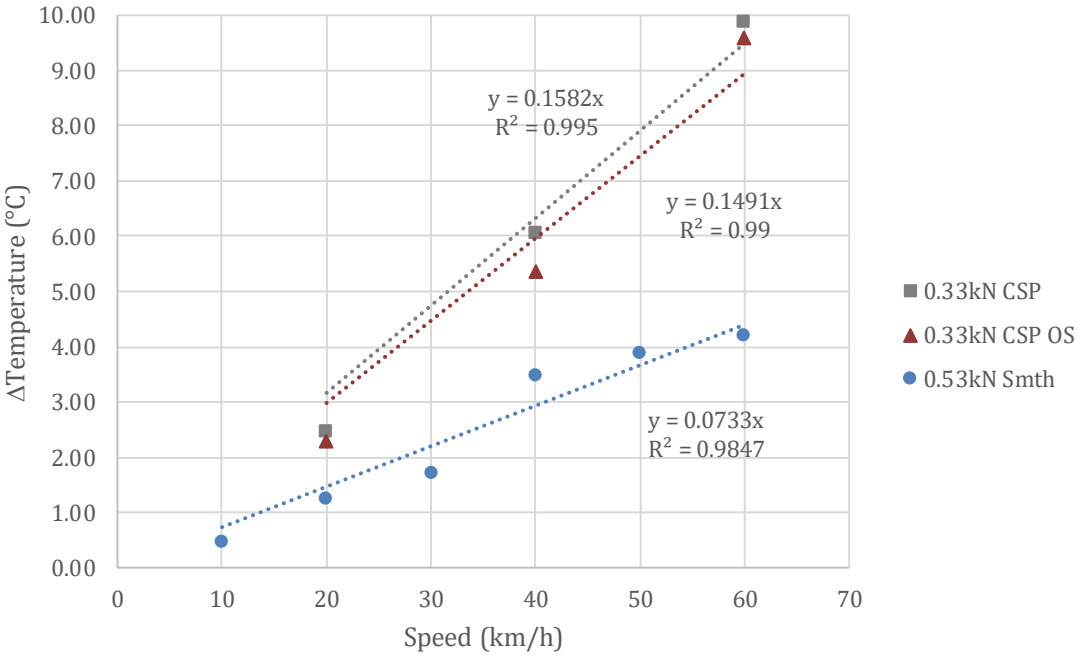

Figure 10.13. Influence of Speed on Tyre Impact Temperature based on Texsense INF (V/T) method of measurement for a smooth surface coarse sand paper

surface texture and a 4 degree tyre offset (load condition 2: 0.33 kN and 0.53 kN).

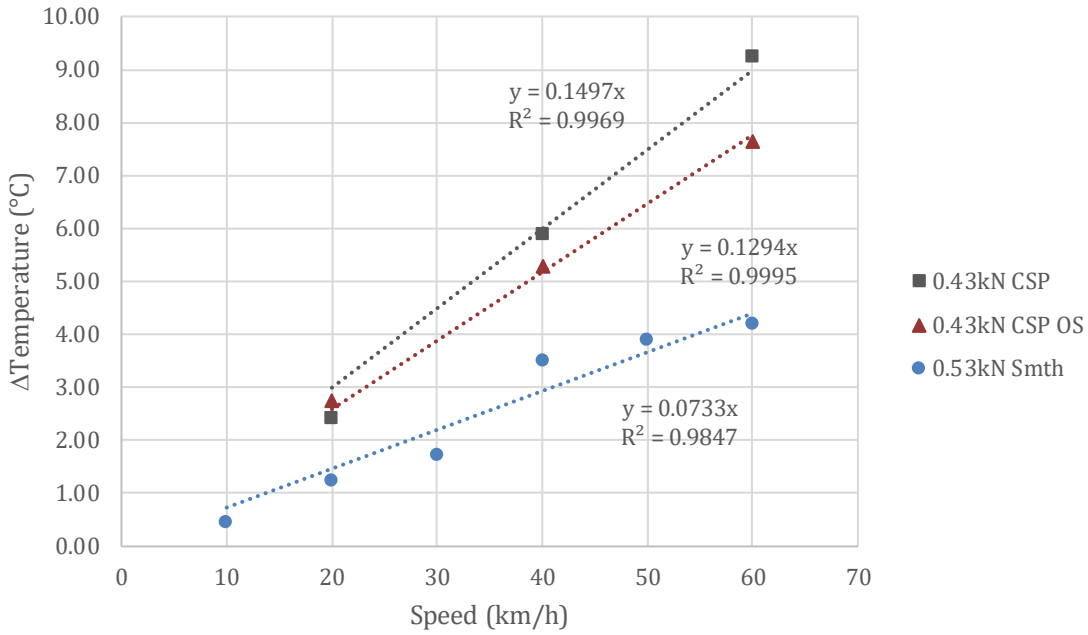

Figure 10.14. Influence of Speed on Tyre Impact Temperature based on Texsense INF (V/T) method of measurement for a smooth surface coarse sand paper surface texture and a 4 degree tyre offset (loading condition 3: 0.43 kN and 0.53 kN).

Figures 10.12 to 10.14 illustrate the influence of speed on tyre impact temperature for the Texsense INF measurement device at 3 loading conditions. The temperature considered is the change in temperature (Δ). CSP represents Coarse Sand Paper, CSP OS represents Coarse Sand Paper with an Off Set angle and Smth represents the Smooth metal ULTRA surface.

Figures 10.12 to 10.14 follow the same relationship that as Speed conditions increase, the tyre impact temperature also increases. This correlation is supported with the R^2 values achieving an R^2 of at least 98%, suggesting that impact temperature is highly correlated by speed.

Figure 10.12 shows impact temperature for the smooth ULTRA surface ranged from 0.46°C to 4.19°C from 10km/h to 60/km/h for loading of 0.53kN. This increased for the coarse sandpaper where impact temperature ranged from 2.79°C at 20km/h to 9.82°C at 60km/h for 0.19kN loading. Impact temperature for tyre offset of approximately 4° reduced from 2.79°C to 2.77°C at 20km/h and from 9.82°C to 7.26°C at 60km/h for 0.19kN loading.

The gradient of impact temperature increase differs amongst the loading values considered as highlighted by the value on the equation. The smooth texture surface of the ULTRA has the lowest gradient as suggested by the y=0.0733 compared to the highest of y=0.160 for 0.19kN loading. This would suggest that a textured surface causes a greater scale of impact temperature as speed increases. Initially, there is almost no difference between the coarse sandpaper surface and the coarse sandpaper surface with a 4° tyre offset at 20km/h at 0.19kN; however, the difference becomes apparent at higher speeds where impact temperature decreases from 9.82°C to 7.26°C at 60km/h.

The increase in loading conditions from 0.19kN in Figure 10.12 to 0.43kN in Figure 10.14 for the coarse sandpaper surface did not have a notable effect on impact temperature; however, small changes are accounted for in the scale of impact temperature increase. The gradient of impact temperature suggests that as tyre loading increases from 0.19kN to 0.43kN for the coarse sandpaper surface, the scale of impact temperature decreases as suggested by y value decreasing from y=0.160 at 0.19kN to y=0.158 at 0.33kN and y=0.149 at 0.43kN.

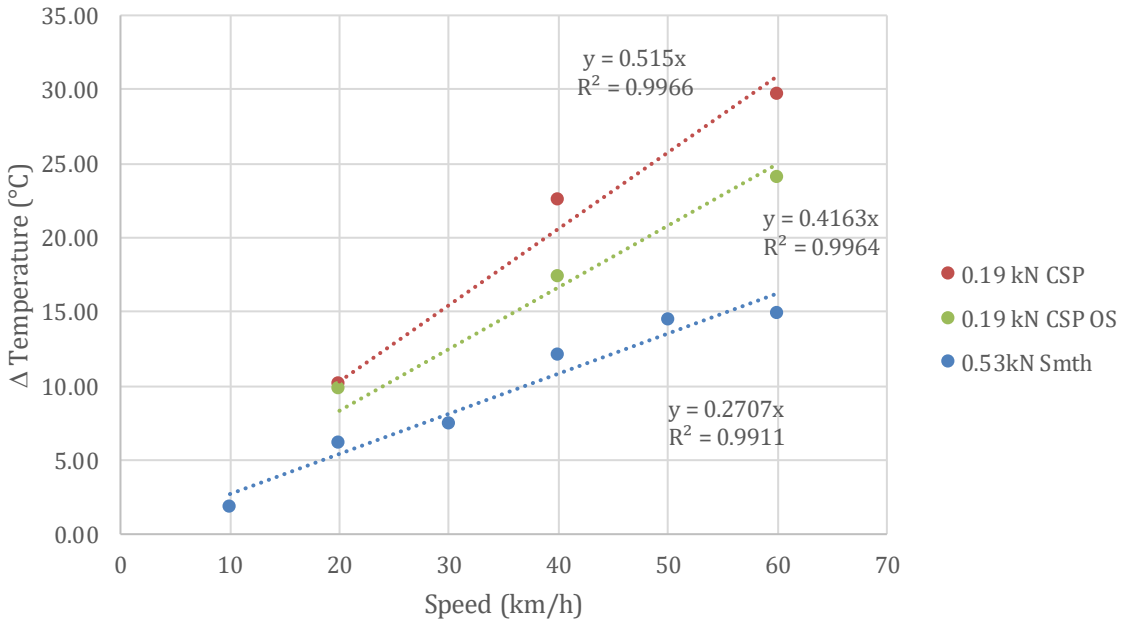

Figure 10.15. Influence of Speed on Tyre Impact Temperature based on Micro-Epilson thermoIMAGER 400 method of measurement for a smooth surface, coarse sand paper surface texture and a 4 degree tyre offset (load condition 1: 0.19 kN and 0.53 kN).

.

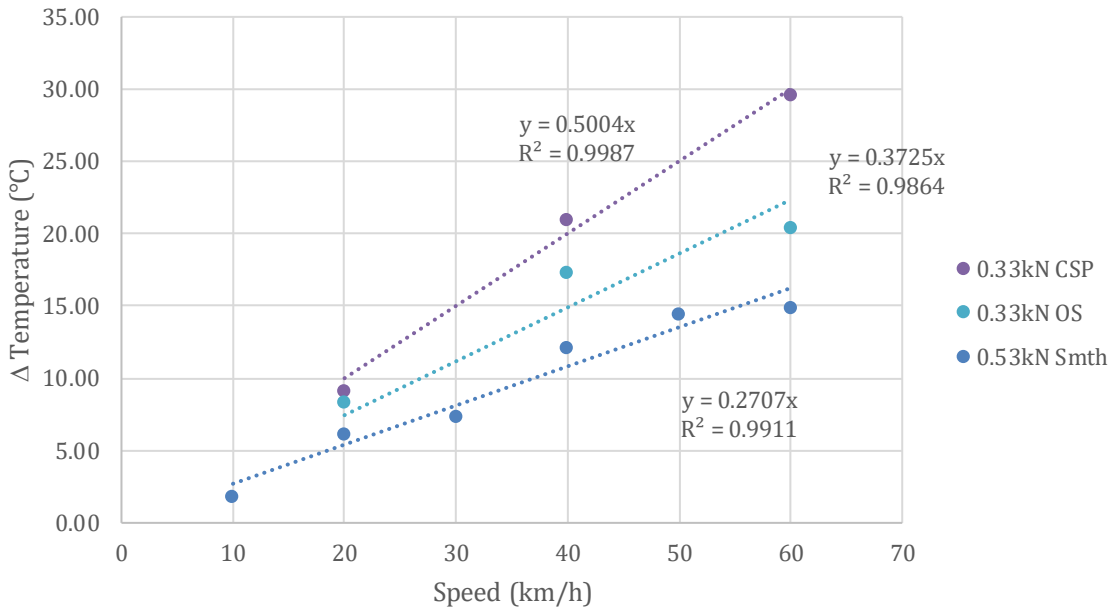

Figure 10.16. Influence of Speed on Tyre Impact Temperature based on Micro-Epilson thermoIMAGER 400 method of measurement for a smooth surface, coarse

sand paper surface texture and a 4 degree tyre offset (load condition 2: 0.33 kN and 0.53 kN).

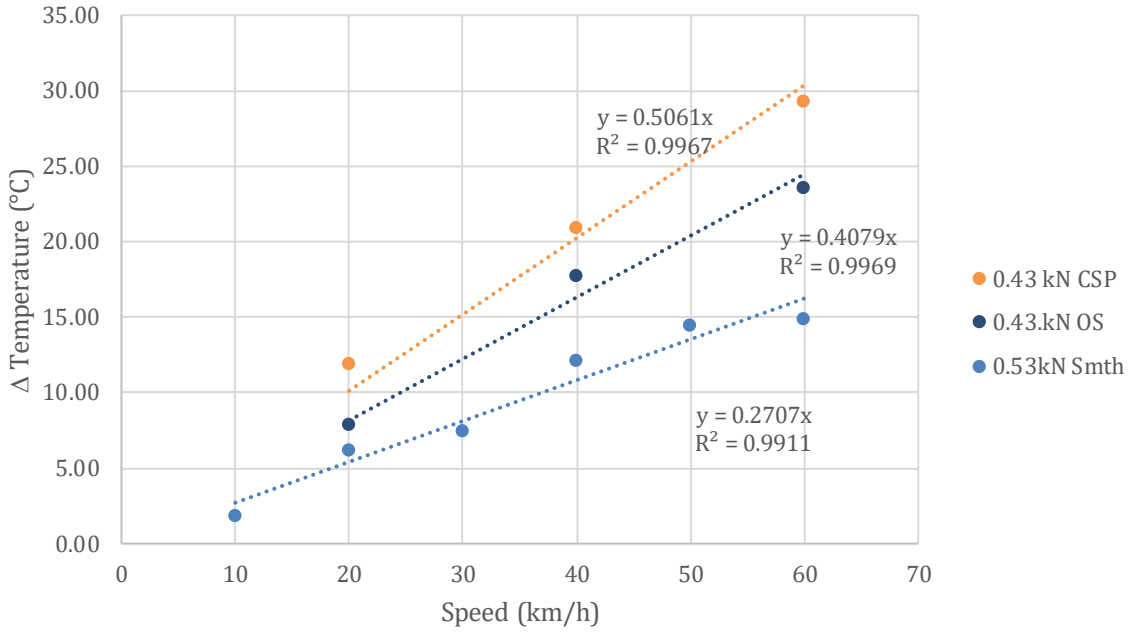

Figure 10.17. Influence of Speed on Tyre Impact Temperature based on Micro-Epilson thermoIMAGER 400 method of measurement for a smooth surface, coarse sand paper surface texture and a 4 degree tyre offset (loading condition 3: 0.43 kN and 0.53 kN).

Figures 10.15 to 10.17 illustrate the influence of speed on tyre impact temperature for the Micro-Epilson thermoIMAGER measurement camera. The temperature considered is the change in temperature (Δ). Similarly to previously identified for Texsense measurement device, the thermoIMAGER records the same relationship as Speed conditions increase, the tyre impact temperature also increases. Similarly to the previous correlation, this correlation is strengthened with the R^2 values achieving an R^2 of at least 95% and therefore suggesting that impact temperature is highly correlated by speed.

Impact temperature for the smooth ULTRA surface ranged from 1.89°C to 14.90°C from 10km/h to 60/km/h for loading of 0.53kN. This increased for the coarse sandpaper where impact temperature ranged from 10.10°C at 20km/h to 29.70°C at 60km/h for 0.19kN loading. Impact temperature for tyre offset of approximately 4° reduced impact temperature from 10.10°C to 9.75°C at 20km/h and from 29.70°C to 24°C at 60km/h.

The gradient of impact temperature increase differs amongst the loading values considered as highlighted by the value on the equation. The smooth texture surface of the ULTRA has the lowest gradient as suggested by the y=0.270 compared to the highest of y=0.515 for CSP 0.19kN loading. Similarly to previously identified, this would suggest a textured surface causes a greater scale of impact temperature as speed increases. For both 0.19kN and 0.33kN initially, the impact temperature for both 20km/h for the tyre offset is arguably the same, achieving an impact temperature of around ten °C and nine °C, respectively; however,, at 0.43kN, there is greater differentiation initially. For the lower load considered, the difference amongst impact temperature for the CSP and CSP OS is almost the same for 40km/h and 60km/h; however, the difference increases at greater speed conditions for the greater loads.

For the tyre offset conditions, the difference between impact temperature for the three-speed conditions considered varies as tyre loading is increased. As tyre speed increases, the data differs from 1.85°C for 20km/h to 0.4°C at 40km/h and 3.6°C at 60km/h.

The data shows that the two measuring devices adopted generated different temperature results. This was a conflict in the method due to the two different measurement principles. It is considered that airflow around the tyre at higher speeds had a greater effect on temperature measurement by increasing airflow around the tyre, therefore, dispersing the air, creating lower impact temperature for the Texsense INF measurement device. This is likely a weakness in the method. In reality, the temperature difference is likely to be greater due to wind conditions and, therefore, greater airflow disturbing the temperature reading. In this context, the Micro-Epilson thermoIMAGER likely generates sound data.

10.5.2 Load Vs Impact Temperature

A range of tyre loading conditions is considered from 0.19kN to 1.55kN. The recommended tyre loading for a standard ASTM friction measuring tyre is 0.19kN. The influence of tyre loading is considered for three-speed conditions.

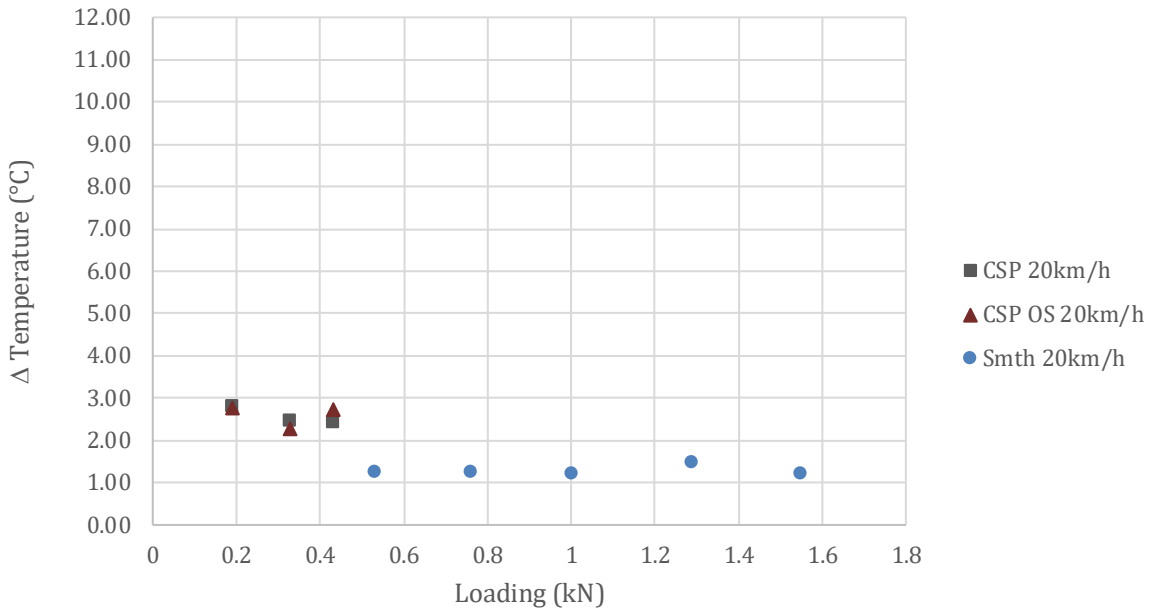

Figure 10.18. Influence of Load on Tyre Impact Temperature based on Texsense INF (V/T) method of measurement for a smooth surface coarse sand paper surface texture and a 4 degree tyre offset at speed 20 km/h..

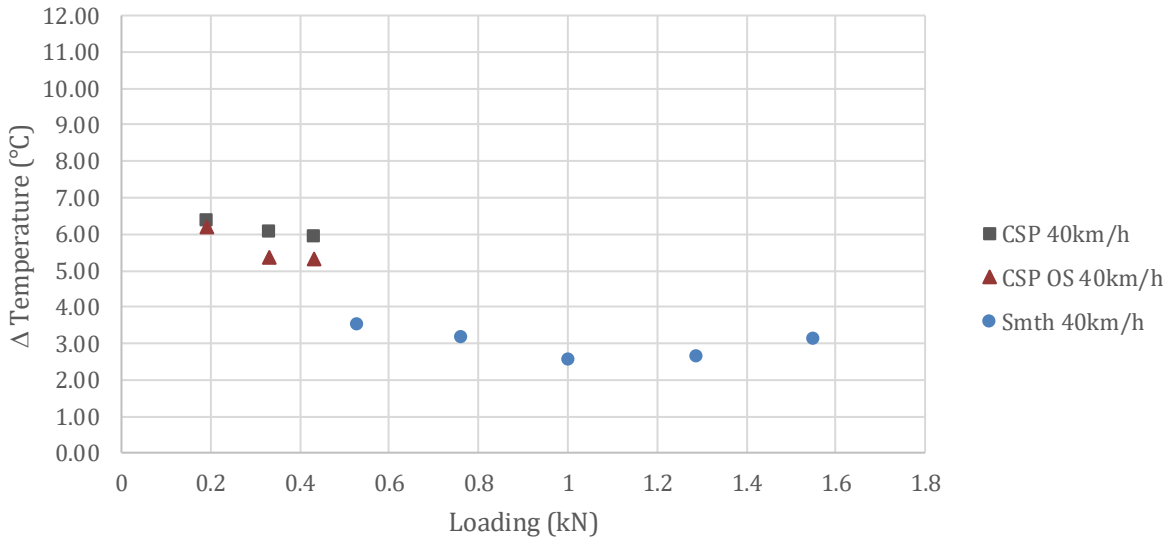

Figure 10.19. Influence of Load on Tyre Impact Temperature based on Texsense INF (V/T) method of measurement for a smooth surface coarse sand paper surface texture and a 4 degree tyre offset at speed 40 km/h..

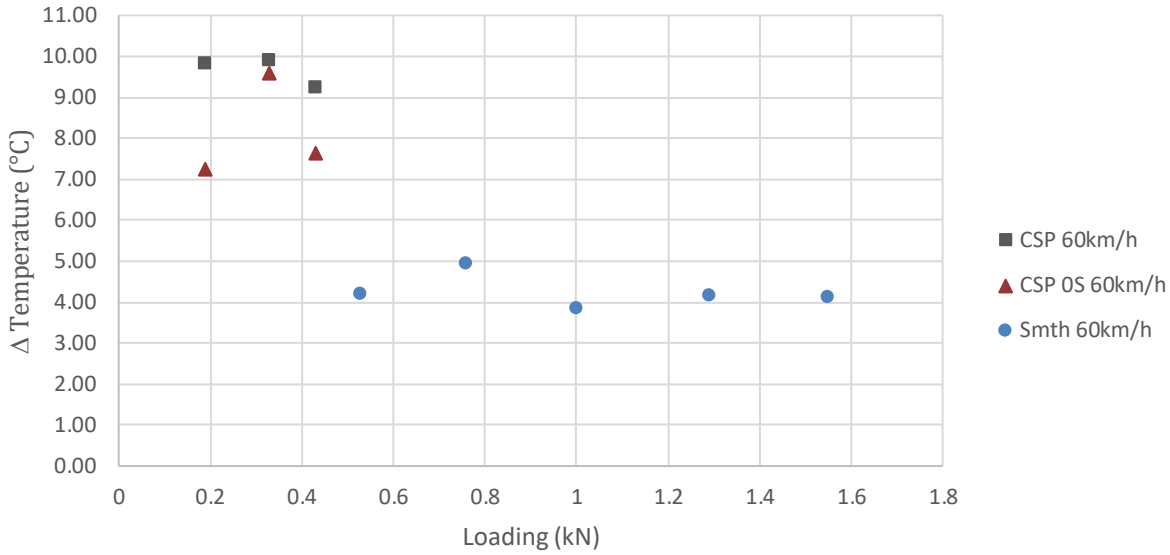

Figure 10.20. Influence of Load on Tyre Impact Temperature based on Texsense INF (V/T) method of measurement for a smooth surface coarse sand paper surface texture and a 4 degree tyre offset at speed 60 km/h..

Figures 10.18 to 10.20 illustrates the influence of load on tyre impact temperature. The temperature considered is the change in temperature (Δ) for the Texsense measurement device. For the smooth ULTRA surface, the incremental addition of load has no notable effect on impact temperature. The impact temperature remains stable within a margin of 0.25°C for the speed condition of 20km/h, within a margin of 0.93°C for 40km/h and 1.09°C for 60km/h. This slight increase suggests that impact temperature may fluctuate within a greater margin as speed conditions increase.

The introduction of texture in the form of coarse sandpaper results in a greater impact temperature. For 20km/h, this averages at 2.56°C with a range of plus-minus 0.37°C amongst the loading conditions to an average of 6.11°C plus-minus 0.46°C amongst the loading conditions and an average of 9.65°C plus-minus 0.67 for the loading conditions considered. For the three-speed conditions 20km/h, 40km/h, and 60km/h, the general relationship identified for the CSP data shows that impact temperature decreases with increasing load; however, for 60km/h, it is notable that impact temperature fluctuates at 0.33kN.

Tyre offset of 4° shows no consistent relationship with the variables considered. The initial impact temperature for a CSP surface was 2.8°C at 0.19kN and decreased to 2.3°C at 0.33kN,

and then increased to 2.7°C at 0.43kN for 20km/h. The deviation of the data occurs within a margin of 0.5°C with no notable relationship amongst the variables. For 40km/h, impact temperature for tyre offset decreases with increasing load from 6.2°C at 0.19kN to 5.3kN at 0.43kN. For 60km/h, the opposite occurs from 20km/h where impact temperatures initially at 7.3°C for 0.19kN increases to 9.6°C at 0.33kN and decreases to 7.6°C.

The difference in impact temperature between the smooth and coarse sandpaper is much greater for the greater speed conditions.

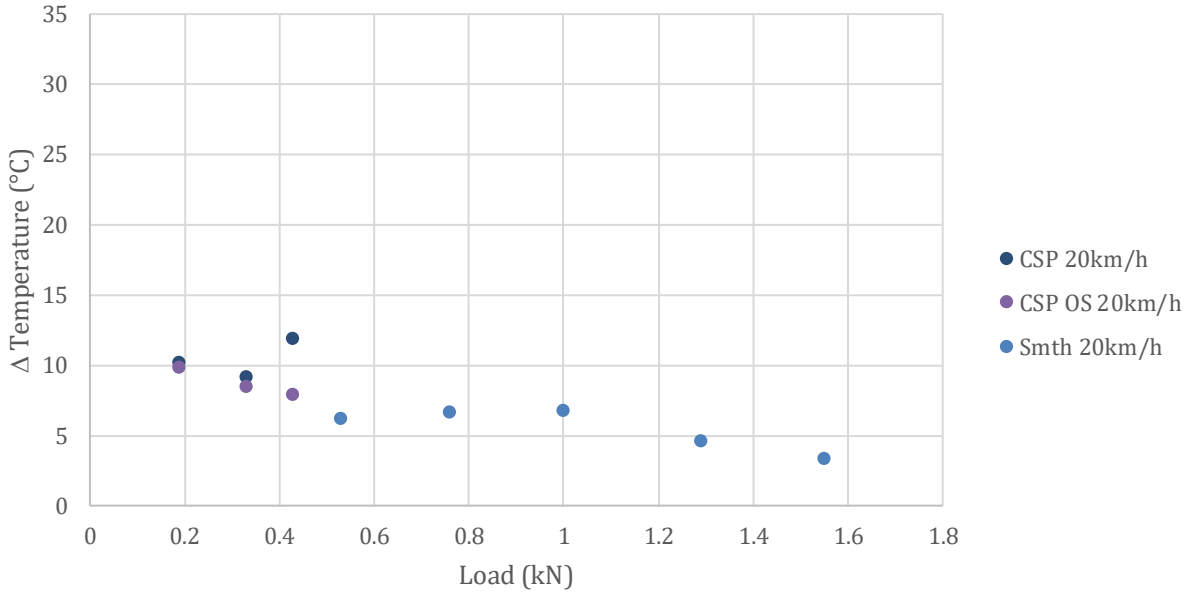

Figure 10.21. Influence of Load on Tyre Impact Temperature based on Micro-Epilson thermoIMAGER 400 method of measurement for a smooth surface coarse sand paper surface texture and a 4 degree tyre offset at speed 20 km/h..

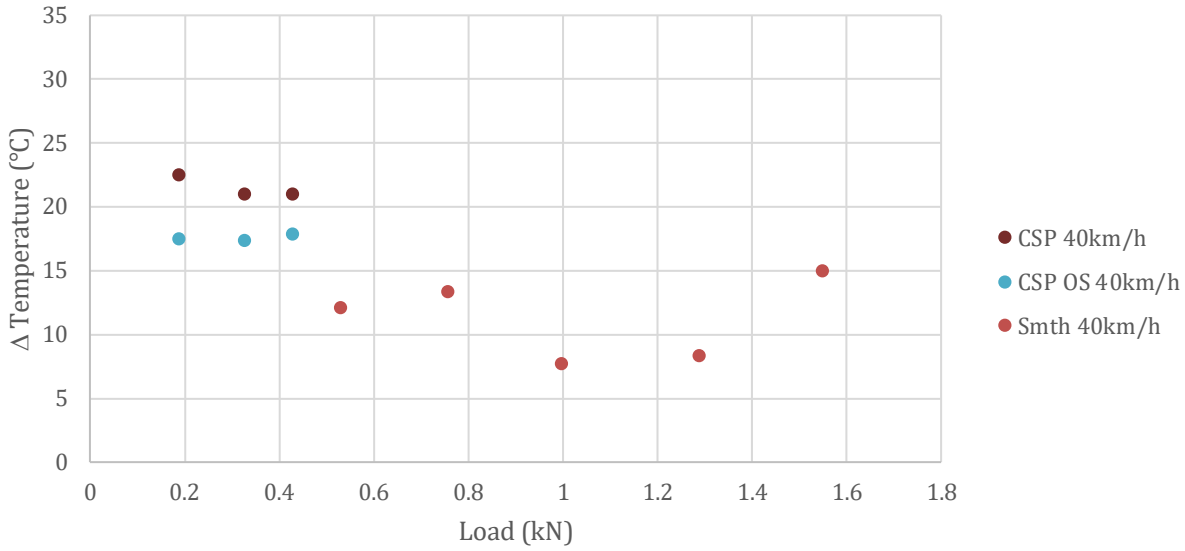

Figure 10.22. Influence of Load on Tyre Impact Temperature based on Micro-Epilson thermoIMAGER 400 method of measurement for a smooth surface coarse sand paper surface texture and a 4 degree tyre offset at 40 km/h.

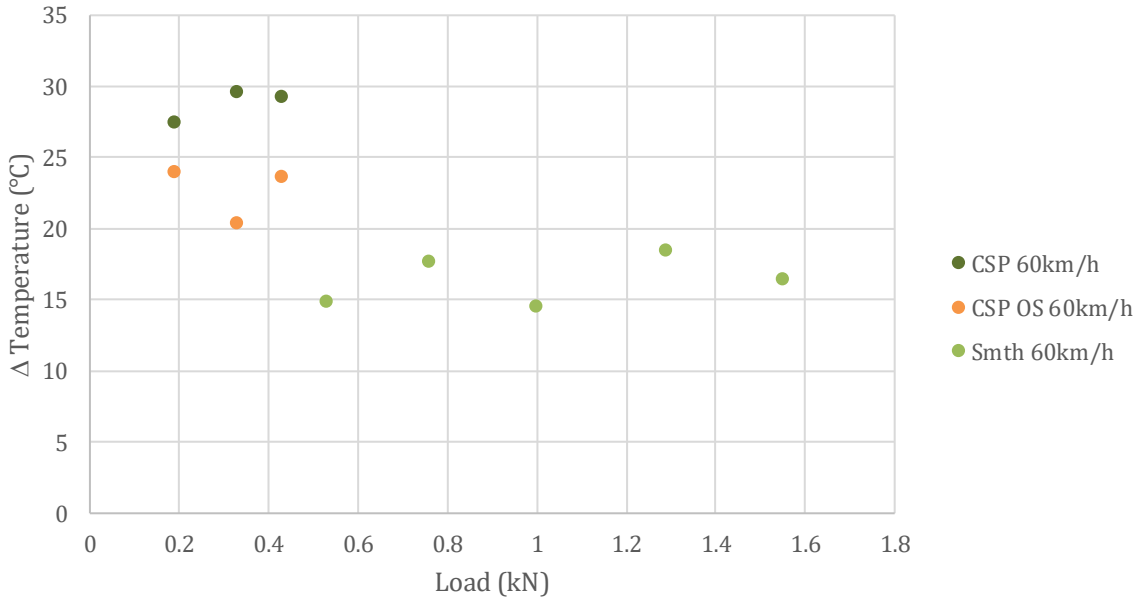

Figure 10.23. Influence of Load on Tyre Impact Temperature based on Micro-Epilson thermoIMAGER 400 method of measurement for a smooth surface coarse sand paper surface texture and a 4 degree tyre offset at 60 km/h.

Figures 10.21 to 10.23 illustrates the influence of load on tyre impact temperature. The temperature considered is the change in temperature (Δ) for the thermoIMAGER measurement device. For the smooth ULTRA surface, the incremental addition of load for 20km/h causes a reduction in impact temperature from 6.13°C to 3.13°C. For the greater speed conditions 40km/h and 60km/h, the addition of load causes a fluctuation in impact temperature with no notable relationship; however, considering the margin within the data fluctuates, it could be argued, similarly to the Texsense measurement data that impact temperature remains stable amongst the loading conditions considered, 40km/h data occurs within a margin on 7.3°C, and 60km/h occurs within a margin of 3.57°C.

The introduction of texture in the form of coarse sand paper results in a greater impact temperature. For 20km/h, this averages at 10.38°C with a range of plus-minus 1.8°C amongst the loading conditions to an average of 21.48°C plus-minus 1.55°C amongst the loading conditions and an average of 28.81°C plus-minus 2.15°C for the loading conditions considered. For the three-speed conditions 20km/h, 40km/h, and 60km/h, the general relationship identified for the CSP data shows that impact temperature decreases with increasing load.

Tyre offset of 4° shows fluctuations in the impact temperature data. For 20km/h, an increase in loading causes impact temperature to decrease from 9.75°C at 0.19kN to 7.9°C at 0.43kN. For 40km/h, an increase in loading causes a marginal increase in impact temperature from 17.4 °C at 0.19kN to 17.75 at 0.43kN; this could be argued almost no increase. For the 60km/h, the data fluctuates between 20.4°C at 0.33kN to 24°C at 0.19kN.

Similarly identified for the Texsense measurement device, the difference in impact temperature between the smooth and coarse sandpaper for the thermoIMAGER is much greater for the greater speed conditions. The scale of temperature measurement between both devices is notably different. The Texsense device generates lower temperature values than that of the thermoIMAGER this is due to the different principles of temperature measurement.

10.6 Surface Texture

A total of four surface textures were considered in this investigation. The smooth metal ULTRA surface and three sandpapers of increasing grit size.

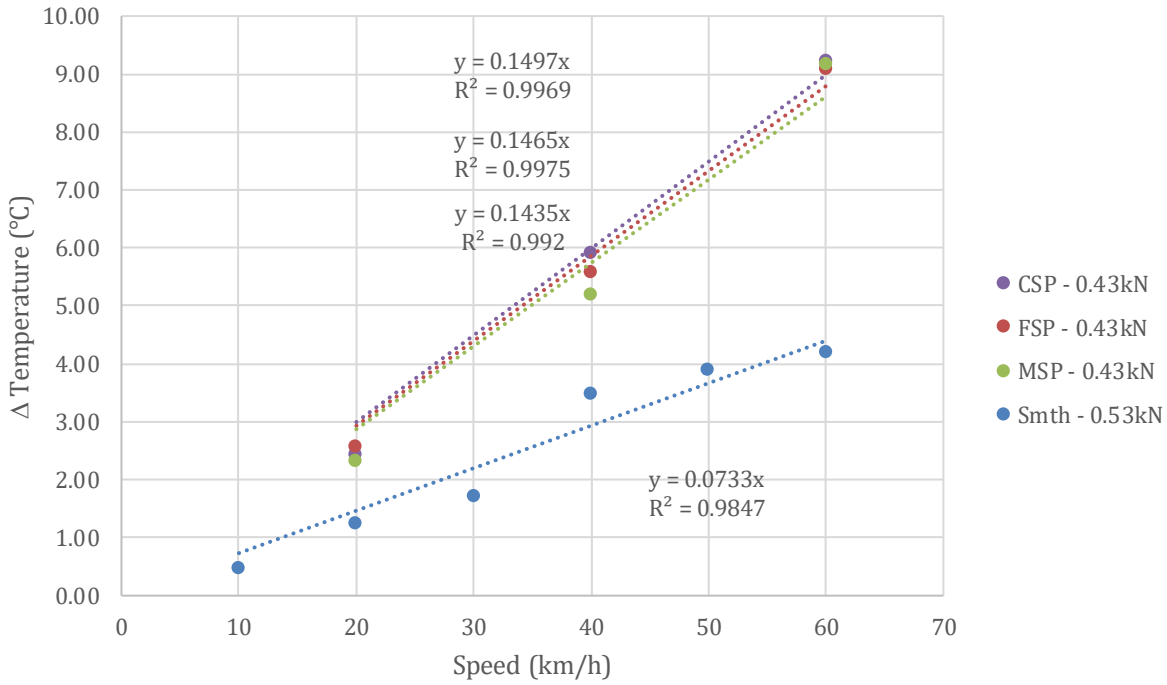

Figure 10.24. Influence of Speed on impact temperature with respect to differing surface texture for the Texsense INF (V/T) method of measurement.

Figure 10.24 represents the influence of Speed on tyre impact temperature with four surface textures considered for the Texsense INF (V/T) measurement method. The sandpaper surfaces have all the same loading conditions, with the smooth surface having a greater loading of 0.10kN. It is fair to suggest that the sandpaper texture significantly increases tyre impact temperature for each speed condition. At each speed condition, impact temperatures amongst the three sandpaper surfaces are similar. Therefore, it is difficult to suggest which amongst the three contributes to the greatest impact temperature. However, it is reasonable to suggest that sandpaper produces a greater impact temperature than a smooth metal surface.

The difference in scale at which impact temperature increases for all three sandpaper surfaces can be considered negligible, further supporting the argument above that sand paper significantly increases impact temperature

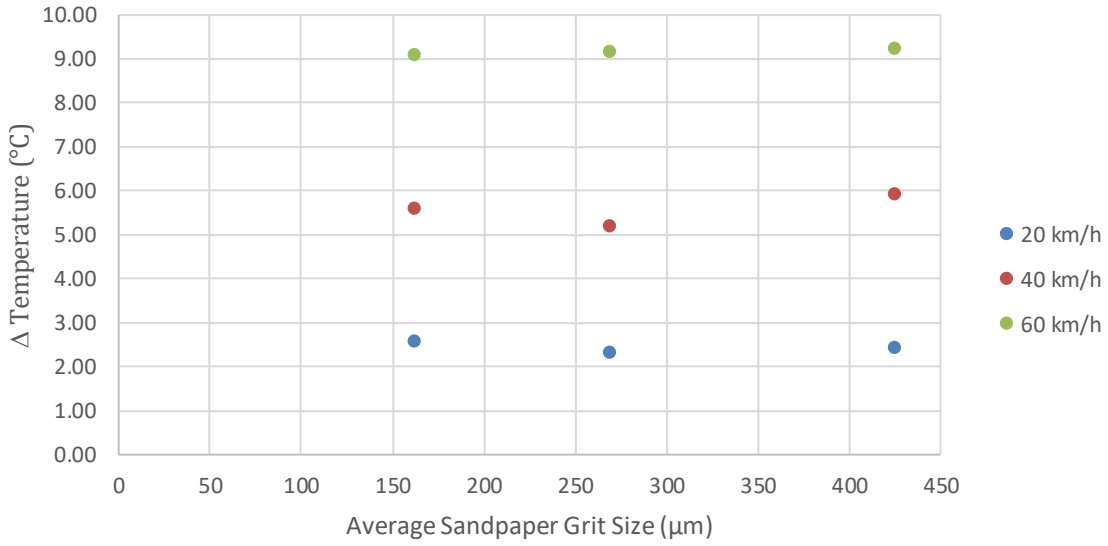

Figure 10.25. Influence of sandpaper grit size on tyre impact temperature based on Texsense INF (V/T) method of measurement.

Figure 10.25 represents the influence of incremental sandpaper grit size on tyre impact temperature. The increase in grit size has no notable effect on tyre impact temperature for the three-speed conditions. All impact temperatures for each speed condition occur within a very small margin; it is, therefore, reasonable to suggest that impact temperature remains stable amongst the grist sizes considered for each speed condition.

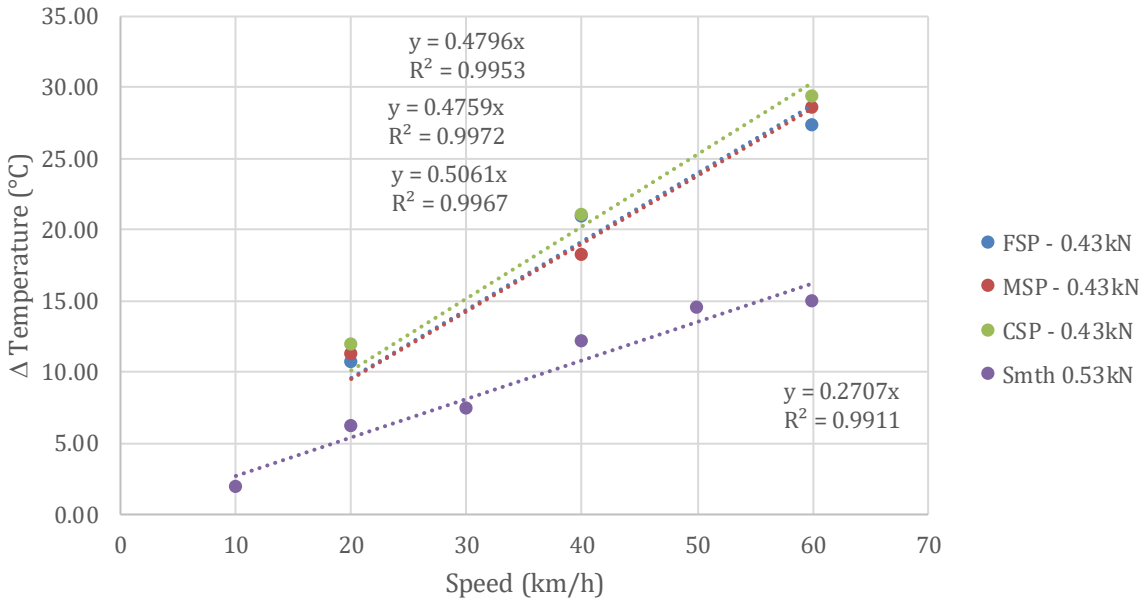

Figure 10.26. Influence of Speed on impact temperature with respect to differing surface texture for the thermoIMAGER 400 method of measurement.

Figure 10.26 represents the influence of Speed on tyre impact temperature with four surface textures considered for the thermoIMAGER 400 methods of measurement. The sandpaper surfaces have all the same loading conditions, with the smooth surface having a greater loading of 0.10kN. Similar to the Texsense data, it is fair to suggest that the sandpaper surface significantly increases tyre impact temperature for each speed condition. Similar to the Texsense device, the impact temperature at each speed condition for the sandpaper surface is similar, and it is difficult to determine which contributes greatest to impact temperature.

The difference in scale at which impact temperature increases for all three sandpaper surfaces is also similar to the Texsense device, and therefore this further supports the argument above.

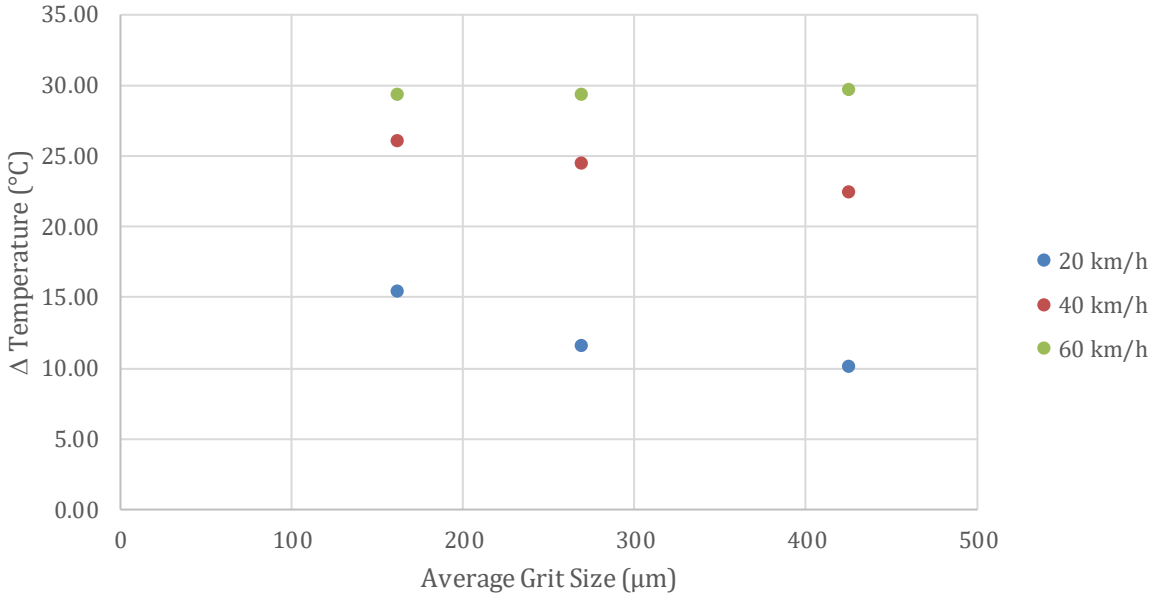

Figure 10.27. Influence of sandpaper grit size on tyre impact temperature based on thermoIMAGER 400 method of measurement.

Figure 10.27 represents the influence of incremental sandpaper grit size on tyre impact temperature. Unlike previously considered, the increase in grit size has a reasonable influence for the smaller speed conditions 20km/h and 40km/h. It is fair to suggest that for the higher speed condition of 60km/h, there is no notable increase in impact temperature and remains stable across the three grit sizes.

10.7 Tyre Off Set

Tyre off set was considered at approximately 4° off set from the regular longitudinal interaction (0°)

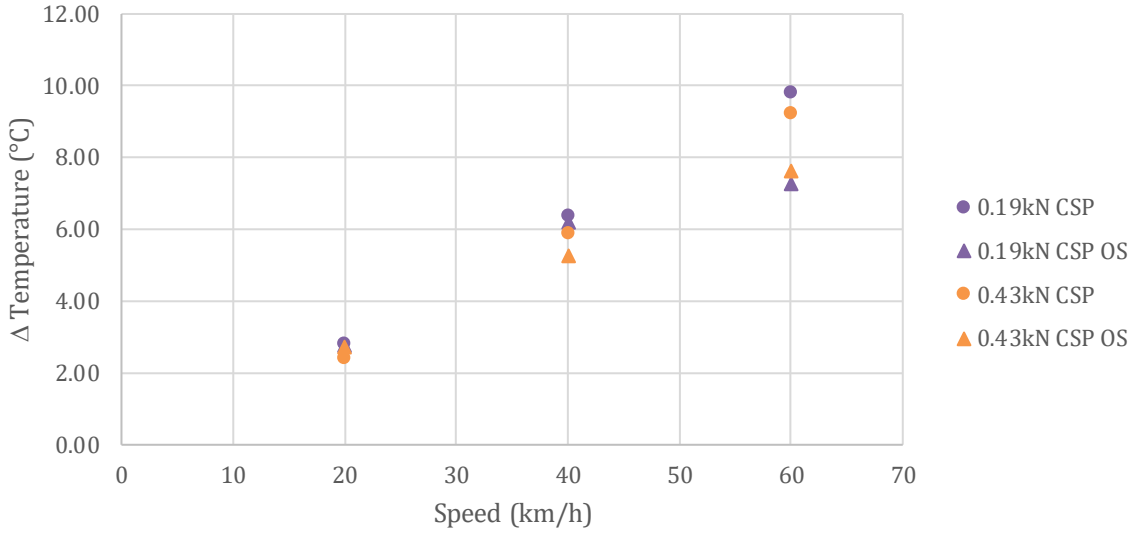

Figure 10.28. Influence of Speed on Tyre Impact Temperature based on Texsense INF (V/T) method of measurement comparing the regular direction of travel of the tyre and a 4 ° offset.

Figure 10.28 details the influence of Speed on Tyre Impact Temperature based on the Texsense device. The data collected details that for the lower loading conditions 0.19 kN, there is next to no difference in impact temperature amongst that standard interacting angle and an offset of 4°. For the lower speed conditions, 20km/h generated an impact temperature in the region of 2.78°C and 40km/h generating an impact temperature of 6.27°C. The data shows a difference at the greater speed of 60km/h, where for the tyre offset, impact temperature decreases from 9.82°C for the standard interacting angle to 7.26°C.

For the greatest load condition considered 0.43 kN for the sandpaper surface, there is a small difference in impact temperature between the standard interacting angle and the 4° offset. This difference becomes greater as the speed conditions increase. Initially, at 20km/h, the tyre offset achieves an impact temperature above that of the standard angle of 2.74°C; as

speed increases, the standard angle dominates impact temperature. The difference in impact temperature between the standard and an offset of 4° increased by 0.61°C at 40km/h and 1.59°C at 60km/h.

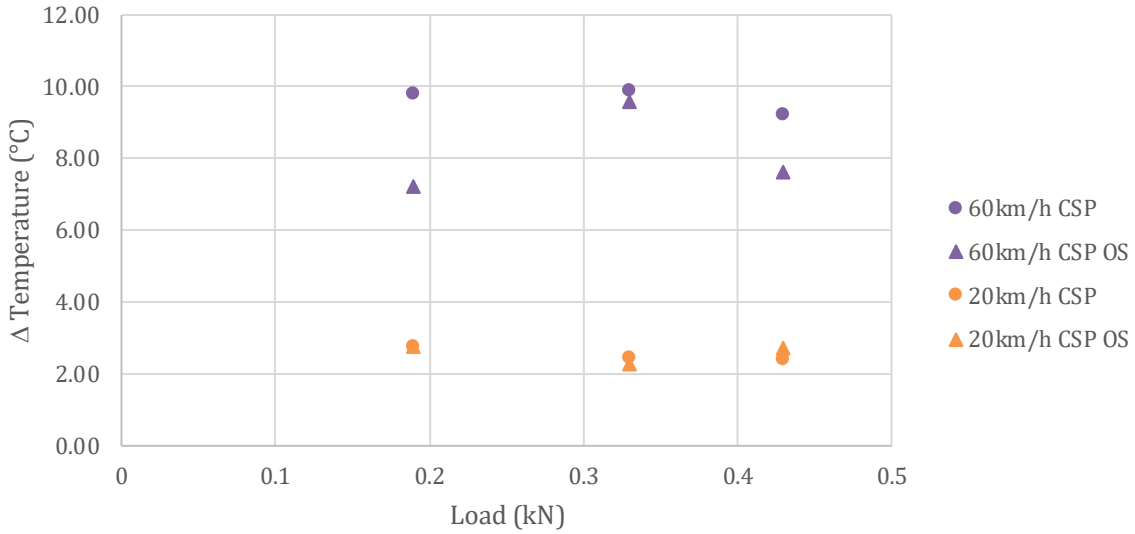

Figure 10.29. Influence of Load on Tyre Impact Temperature based on Texsense INF (V/T) method of measurement comparing the regular direction of travel of the tyre and a 4° offset.

Figure 10.29 details the influence of Load on Tyre Impact Temperature for the Texsense device. The lowest speed condition of 20km/h impact temperature for both standard operating angle and tyre offset of 4° remains stable across the loading conditions considered in the region of 2.28°C and 2.79°C. For the greatest speed condition of 60km/h, the impact temperature for the tyre offset is lower than that of the standard angle for all loading conditions considered. The tyre offset impact temperature fluctuates for loading; however, the standard angle remains relatively stable.

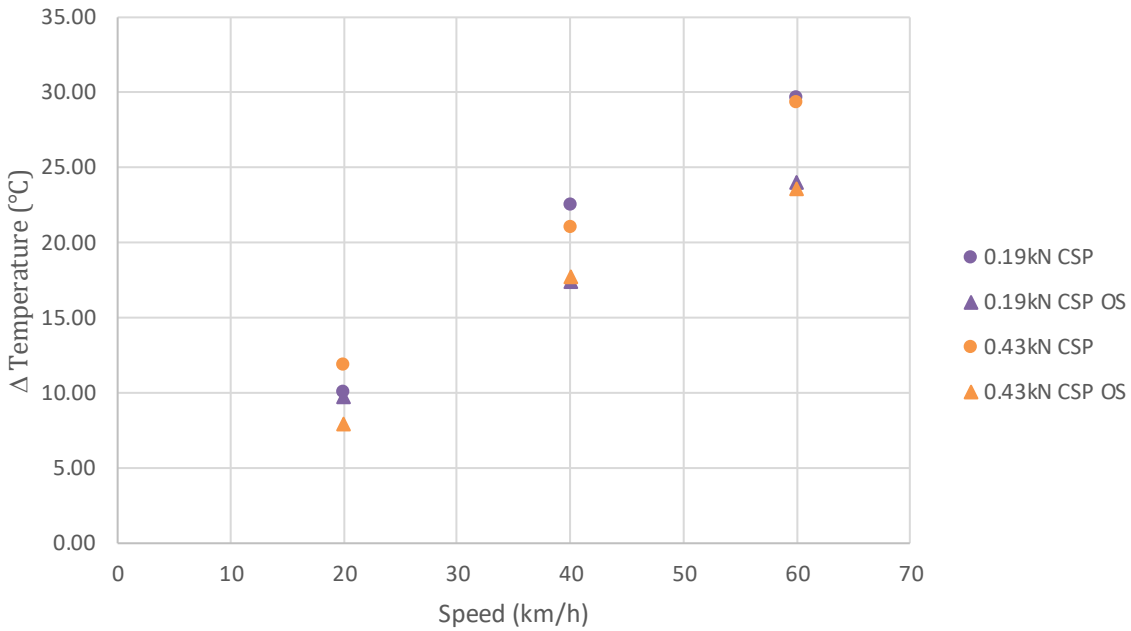

Figure 10.30. Influence of Speed on Tyre Impact Temperature based on Micro-Epilson thermoIMAGER 400 method of measurement comparing the regular direction of travel of the tyre and a 4 ° offset.

Figure 10.30 shows the influence of Speed on Tyre Impact Temperature for the thermoIMAGER device. For the lowest speed condition of 20km/h and lowest loading condition of 0.19kN, both the standard and the offset of 4° is similar in the region of 9.9°C. As speed increases to 40km/h and 60km/h, the difference amongst the loading conditions becomes apparent with the tyre offset achieving an impact temperature of less than the standard this is in the region of a difference of 5.10°C for 40km/h and 5.70 for 60km/h.

For the highest speed conditions of 60km/h, the standard angle achieves the greatest impact temperature across the three-speed conditions considered. The difference in impact between the standard and offset varies from 4°C at 20km/h, 3.25°C at 40km/h and 5.7°C at 60km/h.

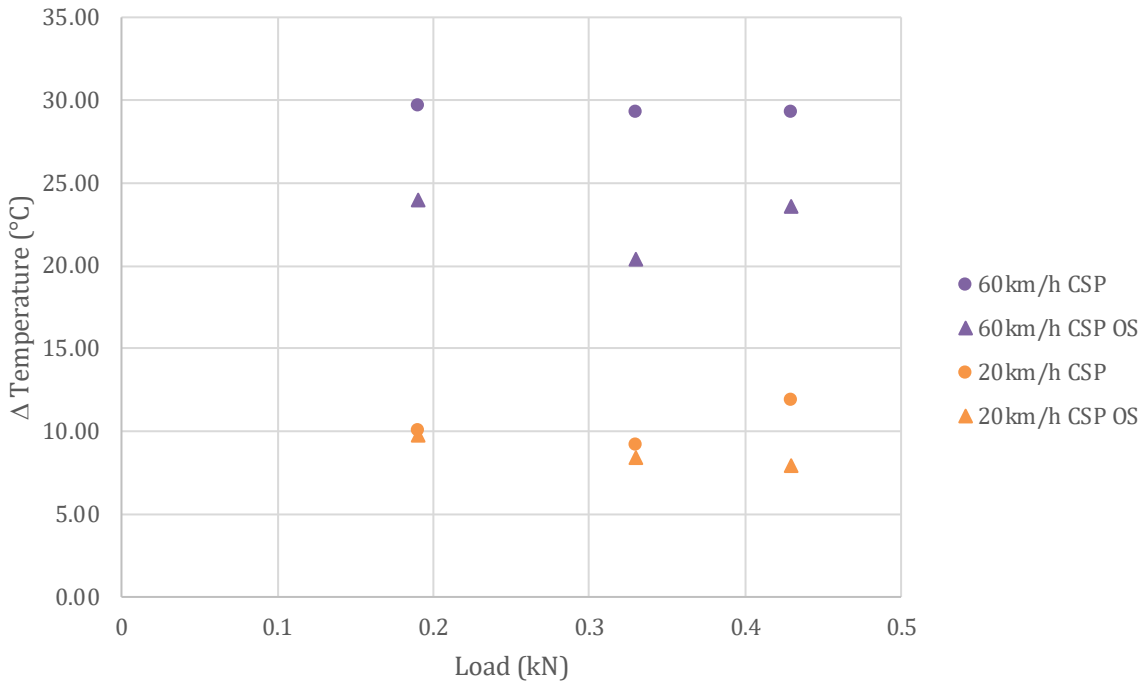

Figure 10.31. Influence of Load on Tyre Impact Temperature based on Micro-Epilson thermoIMAGER 400 method of measurement comparing the regular direction of travel of the tyre and a 4 ° offset.

Figure 10.31 details the influence of load on Tyre Impact temperature for the thermoIMAGER device. For the lower speed conditions of 20km/h, impact temperature for both the standard and tyre offset remains similar for 0.19kN and 0.33kN. As loading continues to increase, the data separates with the tyre offset achieving a lower impact temperature. It could be viewed that as tyre loading increases, the data diverges with the standard operating angle increasing in tyre impact temperature and tyre offset decreasing in tyre impact temperature for increased loading.

The tyre offset data fluctuates across the loading conditions considered for the higher speed condition of 60km/h. The offset data is lower than that of the standard data. The standard interacting angle details a consistent impact temperature across the loading conditions considered achieving a temperature in the region of 29.4°C.

10.8 Tyre Impact Temperature Overview Summary

- Speed conditions have a significant effect on tyre impact temperature; as speed, increases impact temperature increases.
- Surface texture conditions influence impact temperature; transition from smooth ULTRA surface to coarse sandpaper causes an increase in impact temperature.
- For a smooth surface loading conditions cause an initial impact temperature; however, variation in loading has no notable effect on impact temperature; impact temperature remains stable.
- The measurement method influenced the data collected with particular regard to concluding the relationship between load and impact temperature. The influence of load on tyre impact temperature for a textured surface remains inconclusive.
- Tyre offset generates a lower impact temperature for a textured surface than a smooth surface at greater loading conditions.

CHAPTER 11.

DISCUSSION

11.1 Introduction

This thesis aimed to consider the tyre/runway surface. The research focused on a series of laboratory based investigations. This discussion addresses the six objectives listed in Chapter 1.

11.2 Critical review of literature to establish gaps in knowledge

Chapter 2 reviewed literature relating to the tyre/surface interface. This found that an asphalt surface is a complex 3D surface spanning various texture wavelengths, therefore, justifying simplifying the surface texture to an idealised surface to understand the interaction at the tyre/surface interface. The introduction of artificial texture, in the form of grooves, further complicates the surface, therefore utilising an idealised surface will facilitate a better understanding of the interaction at the interface.

Data relating to interface pressure was generally dated and limited to dated technology of strain gauge pins limiting the spatial resolution of the collected data and therefore the quantity and by consequence the quality of data. Pressure mapping utilised by Conville (2010), Millar et al., 2011. Friel (2013), and Woodward et al. (2016) enabled real time collection of pressure interface data utilising pressure mapping technology.

The use of artificial texture in the form of asphalt grooving is widely appreciated to facilitate tyre pavement interaction during wet weather conditions. Grooving provides a path of escape for the bulk removal of surface water. Grooving is considered so effective that it has been claimed that in the presence of water, worn aircraft tyres experience better braking on grooved pavements than newly treaded tyres on non-grooved pavement.

It has been appreciated that trapezoidal-shaped grooving offers improved benefits from the standard square grooving. However, there is limited data to support this. Little research has considered the effect of other groove dimensions on skid resistance. Chu and Fwa, (2019) evaluated the effect of different grooving parameter dimensions. However, their approach is questionable as they drew an analysis by directly comparing three surfaces of different material composition and texture characteristics.

Studies relating to the skid resistance or the frictional value of grooved asphalt draws analysis based on the initial skid resistance before trafficking. Woodward et al. (2016) found after 800 wheel passes, skid resistance of SMA increased up to 8000 wheel passes, albeit for an ungrooved surface; this demonstrates the need to appreciate that initial values may not be representative of the potential frictional values.

A review of the British Pendulum test found that the pendulum exhibits erratic behaviour for course textured surfaces. However, the device is continued to be used. There is no research which has considered the interface between the pendulum and the surface under consideration. It is considered that the pendulum device is continued to be used as there is no other suitable alternative. The adaption to the method stated in BS EN 13036 for the grooved surface is ambiguous. Despite this, published literature suggests the method has not been considered in its entirety as research utilising the British pendulum for grooved surfaces omits reference to the method adaption.

Rubber is deposited on the runway touchdown area when an aircraft tyre makes contact with the pavement surface. The stationary tyre is required to match the horizontal landing speed of the aircraft almost instantly. This result in tyre slippage at the interface, which generates extreme flash temperatures. This is often characterised by a puff of smoke when the tyres make contact with the pavement. The flash temperature of the tyre at the interface and the texture of the surface result in rubber deposition. Studies have focused on removing rubber deposition and, to an extent, have neglected the theory of rubber deposition.

Alroqi et al. (2017) aimed to eliminate the puff of smoke by pre-spinning the tyre of the aircraft, so there was less difference between the horizontal landing speed and the tangential velocity of the tyre radius and therefore reduce the flash temperature. The study did not consider the influence of various parameters which would contribute to this flash temperature.

11.3 Design suitable test methods to address knowledge gaps

The literature review identified there is no method used to determine the durability of Grooved Marshall Asphalt (GMA). A new method for assessing the wear and performance of GMA has been developed and is outlined in Appendix E. The RTM shown in Figure 3.1 simulates low speed high stress conditions has been used to simulate aircraft movements and subject test specimens to wear. Roller compacted slabs have been used to demonstrate how different groove dimensions cut into their surface can resist simulated trafficking. Subjecting test specimens to simulated trafficking enabled the comparison of the performance of the various grooved specimens.

The surface of the grooves were investigated using the British Pendulum, XSENSOR pressure pad and photogrammetry. The surface was investigated at each simulated trafficking interval. The British Pendulum was used to consider how the skid resistance of

the grooves changes with simulated trafficking, the XSENSOR pressure pad was used to consider how the interface pressure between the test tyre and the grooved specimen evolved with simulated trafficking and photogrammetry was used to generate a 3D model for analysis in Digital Surf MountainsMaps analysis software.

The new method developed has demonstrated it can determine the durability of GMA for example, in chapter 7, the British Pendulum has shown that GMA with smaller rib width / groove spacing ratio generates the greatest skid resistance. Similarly, pressure mapping, in chapter 6, has shown that smaller rib width / groove spacing ratio generates the highest interface pressures between the tyre and the rib. Whilst the lower rib width / groove spacing ratio generates favourable skid resistance results the higher interface pressure would draw caution as higher interface pressure would suggest greater stress on the rib. 3D modelling prior trafficking has shown the cross-sectional profile of the groove. The cross sectional profile is shown in Figure 8.3 and Figure 8.7 demonstrates the greatest loss in depth to be that of the lower rib width / groove spacing ratio.

GMA subject to simulated trafficking has shown that lower rib width / groove spacing ratio wears / breakdown the fastest and therefore has a very short life expectancy compared to the other test specimens considered. This is demonstrated in Figure 8.5 and 8.7, the inability to perform pendulum testing due to groove breakdown and the significant interface pressure developed from simulated trafficking. Therefore, the data has shown that smaller rib width / groove spacing ratio are less durable than those larger groove ratios.

The literature review further identified there is no method to consider the deposition of rubber on the touchdown zone of a runway. The literature review identified that the temperature of the tyre upon impact contributed to the deposition of rubber on the touchdown zone. The ULTRA was used to investigate the different parameters which contribute to tyre temperature upon touchdown on the runway. This new method whilst operating within the limitations of a laboratory environment, offers the ability to improve simulated models and or verify data outputs from these.

The new method developed utilising the ULTRA simulated the same scenarios to that of a landing aircraft but within the constraints of a laboratory environment. Speed, load, surface texture and tyre off set angles were considered. The found data demonstrated that speed was the most significant contributor to tyre impact temperature. However, it is noted that different temperature measurement devices whilst agreed with each other in temperature relationship, the scale within the data differed, for example, see Figure 9.12 and 9.15. The

Texsense measurement device shows temperature values much lower than that of the MciroEpsilon device.

This was a conflict in the method due the two different principles of measurement. It was concluded that airflow around the tyre at higher speeds had a greater effect on temperature measurement by increasing airflow around the tyre therefore dispersing the air, creating lower impact temperature.

11.4 Analyse the experimental outputs of test methods in respect of the friction tyre/runway surface interface

The surface interface was evaluated using the XSENSOR Pressure pad shown in Figure 3.0. The method adopted was used to show development from a simple smooth glass surface to an idealised grooved to a complex GMA surface. The method developed has shown that the UTRSI method was able to quantify the friction tyre/surface interface for each of the test surfaces.

The interface between the smooth glass surface has demonstrated that the greatest interface pressure is centralized within the contact patch with interface pressure dissipating / reducing towards the periphery of the contact patch. This is shown in Figure 5.0 and 5.2. This pressure relationship was found to be consistent with both static and dynamic tyre conditions. The average pressure and maximum pressure generated was in the region of 23PSI and 35/36PSI respectively. Comparison of the contact patch had found contact area for the dynamic conditions had decreased by 12%. This was due to the flexing of the tyre.

The interface pressure changed when the idealized grooved surface was introduced. It was found that the tyre envelopes into the grooves of the grooved surface. The greatest interface pressure was concentrated at the leading and trailing edges of the rib when comparing the influence of an increasing rib width of 32 mm, 19 mm and 10 mm using a consistent 6mm groove width, the data in Figure 5.6. The data has shown that this interface pressure dissipates to its lowest in the center of the width. As the rib width decreased, this interface pressure broadly decreased at the leading and trailing edge. However, the interface pressure in the center was greater than that of the larger rib width.

Comparing the influence of an increasing groove width of 3mm, 6mm and 12mm using a consistent rib width of 32mm the data in Figure 5.7 has shown that the greatest interface pressure occurred at the leading and trailing edge of the largest groove width. This

decreased consistently as the groove width decreased. It was also found that whilst the largest groove width had the greatest interface pressure at the edges, it also had the lowest interface pressure in the centre of the rib. This lower interface pressure in the centre of the rib increased as the groove width decreased.

Utilising the above information, the data assists with an understanding of the 'simple' relationships between a friction tyre and idealised surfaces. Introducing Grooved Marshal Asphalt (GMA) and simulated trafficking introduces complexities within the data. However, the relationships found for the idealised surface assisted in analysing the complex surfaces.

It was found there is variation in interface pressure across the length and width of the rib of the GMA surface. For example this is demonstrated in Figure 6.6. It was found there is no two GMA ribs the same and this varies. It was found the same relationship exists as identified for the smooth surface; the leading and trailing edges pertain the greatest interface pressure, however, this pressure relationship changes when subjected to simulated trafficking. It was found when subjected to simulated trafficking, the pressure recedes from the leading and trailing edges towards the centre of the ribs (due to increasing tyre enveloping.) This is demonstrated by comparing Table 6.0 and 6.1.

The cumulative frequency data has shown that when subjected to simulated trafficking the frequency of lower interface pressure increases as well as the frequency of higher interface pressures as shown comparing Figure 6.21 and 6.23. The data collected has identified larger groove ratios' pertaining the narrow rib width were less durable and generated higher interface pressures, similarly the smaller groove ratio's pertaining the narrow groove width was identical to the non-grooved control test specimens. This contribution to knowledge suggests interface pressure are groove dimension specific. To generalise that found relationship within the data would suggest greater enveloping leads to greater interface pressures which results in groove breakdown therefore making the asphalt ribs less durable.

11.5 Evaluate the significance of interface pressure and groove parameters to the tyre/runway surface interface.

The research has demonstrated groove parameters influence how the tyre interacts with the surface. The research has shown that rib width and groove width influence how the tyre interact with the surface. It is noted groove depth would also influence this interaction

however it was not the focus of this research. The research demonstrated groove width influences the depth of enveloping into the groove whilst rib width influences the amount of deflection at the contact patch of the tyre. It has been demonstrated that greater enveloping leads to greater interface pressure on the edges of the rib and therefore greater stress. It has also been demonstrated smaller ribs create a smaller surface area therefore greater deflection at the tyre contact patch generating greater interface pressures. It is appreciated that both groove and rib do not work individually, rather both work simultaneously to influence this interaction as the contact patch spans over various grooves and ribs.

The research has found that smaller groove ratios contribute to higher pressures on the rib. These higher pressures evidently led to premature breakdown of the ribs when subjected to simulated trafficking therefore the performance was short lived. On the other hand, the larger groove ratio generated not as high interface pressure on the ribs. They performed reasonably well when subjected to simulated trafficking. However, it was apparent the largest rib width / groove spacing ratio was identical to that of the non-grooved control test specimen. It is reasonable to conclude that there is balance to be found when considering grooving dependent on long-term purpose of grooving.

11.6 Evaluate the skid resistance performance of different groove dimensions.

The skid resistance of GMA was measured using the British Pendulum. Various grooves of different widths were sawn into Marshall Asphalt test specimens. A rib width / groove spacing ratio was determined for each test specimen was assigned to assign a numerical value to each. The test specimens' references and their determined rib width / groove spacing ratio is shown in Table 4.5.

Test specimens were trafficked using the RTM. A non-grooved specimen acted as a control from which a comparison could be made.

Wet and dry friction were considered. As wet friction is the worst case condition this will be the focus of this discussion. The data demonstrated all grooved test specimens generated superior pendulum values than that of the control as shown in Figure 7.5 and 7.7, apart from MAF /rib width/ groove spacing ratio 0.88 which generated almost identical data to that of the control MAK / groove ratio 1.00. Such similarities suggest that the small groove of 3mm does not contribute to the skid resistance. This is likely due to the inability of the pendulum

slider to interface the wall of the rib whereas in the case of a tyre the narrow groove inhibits the flexibility of the tyre to envelope the groove.

The data demonstrated in Figure 7.8 shows that grooving contributes up to 26 PTV points when measured at 90 degrees and up to 48 PTV points when measured at 80 degrees for wet skid resistance than that of the ungrooved control test specimen - MAK. This significant increase demonstrates there is greater interaction between the pendulum and the grooved surfaces. The data shows the greatest increase to be from the groove dimensions with smallest rib width and largest groove width – MAA. These dimensions facilitate the pendulum slider interfacing the wall of the groove and instantaneously impacting the wall of the rib. Therefore, it is important to consider the data cautiously as this interaction may give rise to mis-leading values.

The data shows those dimensions MAA / rib width / groove spacing ratio 0.55 that contribute to the greatest skid resistance, decline rapidly relative to the other dimensions considered. These same dimensions also could only be pendulum tested up to 6000 wheel passes as the breakdown of the grooved surface prevent the standard swing length being achieved to determine the skid resistance of the surface. The data demonstrates that the lower groove ratio contributes to higher skid resistance and this is consistent up to 75,000 wheel passes. The data up to 75,000 wheel passes shows that as groove ratio increases PTV data across the wheel passes also decreases.

The data collected during this investigation was considered with the information identified in the literature the review that the British Pendulum exhibits erratic and unreliable behavior for grooved surfaces. It is considered that the method has not be read in its entirety i.e., the method is only applied selectively and the ambiguity identified in sub section 2.7.1 has been in place to mitigate the erratic behavior of the pendulum. It can be observed in Figures 9.3 – 9.4 when the pendulum interfaces a groove surface it bounces across the surface and therefore the contact between the pendulum and grooved asphalt is much less than previously thought. It is demonstrated that rotating the grooved test specimen that the bouncing of the pendulum is reduced and there is greater contact as shown by the removal of pink paint. This simple experiment demonstrated the bouncing theory but also led the conclusion that pendulum values for grooved surfaces are being determined from contact area much less than the apparent contact area.

11.7 Evaluate the contribution of 3D modelling to the friction tyre/runway surface interface

3D modelling was used to assess the surface at each simulated trafficking interval. 3D modelling facilitated the collection of point cloud data for importation into the analysis software for consideration. In this case volumetric data was considered as well as height data. 3D modelling enabled quantification of volume of material in the peaks of the surface. These peaks, as identified in the sub section 8.3 were considered to be related to the micro texture of the MA. The parameter was compared against the change on skid resistance of the surface shown in Figures 8.9, 8.11, 8.12, and 8.13. It was found that the use of Vmp is more critical in the earlier stages of trafficking as the surface is generally not extensively influenced by degradation or wear and that the use of Vmp at higher wheel passes may not be appropriate as the loss of aggregate or material may give rise to misleading data. Therefore 3D modelling has highlighted the vulnerability on the reliance of single parameters in isolation.

Step height analysis shown in sub section 8.2 has concluded there is a reduction in height of the asphalt rib when subjected to simulated trafficking. It has demonstrated through the cross sectional profile the width of the asphalt rib remains consistent as shown in Figure 8.4. Figure 8.5 has demonstrated the smaller groove ratio sustained greatest rib depth loss. This is not surprising given the smaller groove ratio generated higher interface pressures between the rib and friction tyre.

The process of 3D modelling demonstrated a weakness within the method. For the grooved surface, light penetration into the groove was a limiting factor when 3D modelling. This was evident in the cross-sectional profiles extracted from the 3D model as they were shown to be V-shaped at the bottom of the grooves when they were a U-shape, as shown in Figure 8.1. This demonstrated difficulty in recovering data at depth within the groove. It was found that the greater the groove depth, the greater difficulty capturing the data at the bottom of the groove due to less light and more phenomena would have occurred.

Draw conclusions and make recommendations for further research.

Groove dimensions significantly influence the interaction between the friction tyre and test surface. A new test method for assessing the wear and performance of GMA has been developed. The research has shown that the performance of grooves is related to the rib / groove ratio. The performance of grooves can be improved by determining the optimum angle at which a tyre interacts with the grooved surface. The research has found that speed

conditions of a landing aircraft significantly contribute to impact temperature and therefore contribute to rubber deposition on the runway surface during landing.

It is recommended the data found in this thesis is validated through field research and the hypothesis of rotation angle is considered for further work.

CHAPTER 12.

CONCLUSIONS

12.1 Introduction

The research presented in this thesis considered the tyre/runway surface interface within the context of laboratory investigation. It has addressed knowledge gaps identified in Chapter 2 and has contributed to knowledge therefore. This chapter presents the conclusions of the research by addressing the Research Questions presented in Chapter 1.5.

12.2 Conclusion

The research highlighted the volume evacuation capability of differing rib width/groove spacing ratio combinations. The research presented a series of 'look up' tables from a rib/groove calculator. The data presented showed that for 1m2 of grooved runway, the number of grooves decreased as the rib width/groove spacing ratio increased. The data demonstrated the relationship between rib width, groove width and groove depth and how they impact the ability of a grooved surface to accommodate water. In practice, the data can be used the determine the appropriate combination of rib width/groove spacing ratio dependent upon the local climatic conditions upon which the groove surface is required.

The research found that, in practice, only a small number of rib/groove dimensions are used at airports around the world. The two considered were the FAA's 32mm x 6mm x 6mm at 38mm centre-to-centre spacing and the CAA's 19mm x 6mm x 6mm at 25mm centre-to-centre spacing. Analysis of the dimensions demonstrated that the CAA had a greater number of grooves per metre, therefore, a greater volume of grooves per square meter. However, the data demonstrated that the FAA dimensions had a greater area of ribs per square meter than the CAA. The ribs are the area the aircraft tyre will be in contact with; therefore, a greater contact area generates greater friction capability. This demonstrates the balance to be struck between water removal capability to improve tyre pavement interaction and the need for maximum contact area at the interface for friction/skid resistance.

The UTRSI method demonstrated the interface between the friction tyre and the idealised surface. The data showed the influence of rib width and groove width on interface pressure. The research found that rib width influences the interface pressure across the width of the rib. It was determined that rib width relates to deflection at the tyre interface due to contact area, smaller contact area, greater deflection, and therefore higher interface pressure. Similarly, it was found that groove width influences interface pressure. A greater groove width resulted in greater enveloping of the tyre into the groove and, therefore, greater stress on the edges of the groove, resulting in greater interface pressures. It was found that a smaller groove width did not affect interface pressures; therefore, there was likely little to no deflection of the tyre into the groove.

Grooving contributes positively to skid resistance. The data has shown that skid resistance decreases when subjected to simulated trafficking. The research found that different groove combinations contribute differently to skid resistance. The data has shown that those groove dimensions of a smaller rib width/groove spacing ratio contribute greater to skid resistance. However, there is a balance to be found as those test specimens also broke down / wore the quickest. The data also demonstrated that measuring the skid resistance of GMA at 80 degrees generated higher skid resistance values than the standard / typical 90 degrees.

3D analysis of the GMA test specimens found that the width of the rib remains stable when subjected to simulated trafficking. However, the height of the rib decreases. It was found that the smaller rib width/groove spacing ratio experienced the greatest height loss. It was found that Vmp can assist in the explanation of the change in pendulum values of the GMA with simulated trafficking. It was determined that Vmp is more critical in the earlier stages of trafficking as the surface is generally not extensively influenced by degradation or wear, whereas at higher wheel passes may not be appropriate as the loss of aggregate or material may give rise to misleading data as the reference line from which Vmp is determined will be affected by the loss of aggregate.

Through the application of pink paint, it was found that the British Pendulum bounces across the groove test specimen when tested at an angle of 0 degrees. This bouncing was mitigated when rotating the grooved surface to 12 degrees. It was found that pendulum values were derived from 57% less contact area when measured at 0 degrees as compared to 12 degrees.

The research considered tyre impact temperature to contribute to rubber deposition on the runway surface. The research has identified that tyre speed conditions have a significant effect / contribution to tyre impact temperature. It was found that greater tyre speed resulted in higher impact temperatures. Similarly, it was found that a greater textured surface contributed to higher impact temperatures. Although it was found that impact temperature conditions remained stable when subjected to differing loading conditions. Finally, the method of measurement influenced the temperature data collected.

Replies to questions raised in sub section 1.4;

12.3 Can the durability of Grooved Marshall Asphalt (GMA) be predicted?

Yes. The research has developed a range of new methods to predict the wear of GMA.

- A new GMA wear test has been developed and is set out in Appendix E.
  - The Road Test Machine (RTM) which simulates low speed high stress conditions has been used to simulate aircraft movements and subject test specimens to wear.
  - Roller compacted asphalt test specimens have been used to demonstrate how different groove configurations can resist simulated trafficking.
  - Groove wear has been evaluated using the standard British Pendulum tester.
- Pressure mapping has been used to better understand the friction tyre / test specimen interface and how it evolves due to simulated trafficking.2D and 3D Areal parameters have been used to quantify how the interface changes with time and 3D modelling.

12.4 Can the friction tyre/runway surface interface be better understood?

Yes. It has been demonstrated that pressure mapping and 3D modelling has contributed to a better understanding of the tyre/runway interface. This evolved from consideration of the interaction between the friction measuring tyre and a smooth surface extending to surfaces with idealised groove patterns and complex GMA surfaces. The process demonstrates development within the research from utilising smooth surface extending to complex surfaces. The research has demonstrated that groove ratio is related to interface contact pressure. Smaller groove ratios contribute to higher interface pressures. This data demonstrated the significance of this to relate to relate to the pre-mature degradation of the grooved surface through groove breakdown.

12.5 Can evolution of the tyre/surface interface be modelled in laboratory experiments in three dimensions?

Yes. The research demonstrated an analysis of 3D models generated at different simulated wheel trafficking intervals.

Analysis of Areal Parameters from 3D models has shown Volume of Material in the Peaks to be related to the British Pendulum Values. It was demonstrated the consideration of Vmp is more critical in the earlier stages of trafficking as the surface is generally not extensively influenced by degradation or wear.

The data from 3D models also support the conclusion that the width of the rib/groove remains relatively stable when subject to simulated trafficking but with significant changes in the height of the ribs and depth of the grooves. The data supports the conclusion that a smaller rib width / groove spacing ratio equates to a greater loss of rib depth and groove depth for selected specimens.

12.6 What is the potential impact of the research presented in this thesis to the design and maintenance of grooved runways?

A new test method for predicting the durability of GMA under laboratory conditions has been developed. This method integrated into the specification of the Marshall Mix Design has the potential to not only strengthen the specification for the material but significantly improve the asphalt material by demonstrating the time at which the asphalt surface degrades. The versatility of the method makes it adaptable to other asphalt surfaces.

The research has highlighted rib width / groove spacing geometry influences the skid resistance of the groove surface therefore when specifying a groove dimension the data has shown there is balance between long term service performance to level of skid resistance desired. The data demonstrated the sensitivity to degradation of a small rib width / groove spacing ratio.

The prediction model generated for grooved surfaces was statistically significant with an R^2 of greater than 0.7. This suggests the model presented in this thesis has potentially significant impact to the design and maintenance of runway surfaces. This includes but is not limited to,

- Identification of the time period when the grooved surface will fall below the desired frictional level. (0.55 for grip tester)
- Frictional characteristic of alternative grooving dimensions
- Frictional performance of alternative configuration of runway grooves

12.7 What are the limitations of the research presented in this thesis and the implications for further work?

The research presented is derived from laboratory experiments. The outputs require validation by in service measurements which is beyond the scope of this thesis.

CHAPTER 13.
FUTURE RECOMMENDATIONS

The research presented in this thesis has investigated the tyre / runway interface. The following recommendations for further work are proposed:

- Ambiguity in the BS EN 13036 method should be considered for revision. The found data should be considered and the method clarified further with use of a diagram.
- The new test method for the Wear of GMA noted in Appendix E should be considered for integration within Specification 13 - Marshall Asphalt for Airfields specification or serve as a stand-alone method to assess wear of Grooved Marshall Asphalt.
- The frictional data generated utilising the British Pendulum Method should be validated / compared with utilising CFME such as the GripTester.
- Alternative grooving configuration should be further explored with CFME.

REFERENCES

Ahmad Sajjad Safi (2016) *Airfield Ground Lighting* , Available at: *https://www.slideshare.net/ahmadsajjadsafi/airfield-ground-lighting-agl* (Accessed: 15/10/2016).

Alroqi, A.A., Wang, W. and Zhao, Y., 2017. Aircraft tire temperature at touchdown with wheel prerotation. *Journal of Aircraft*, *54*(3), pp.926-938.

Anderson, R., 1996. *Tire Test Correlation: Radial Versus Bias-Ply Tires*. Galaxy Scientific Corp Egg Harbour Township NJ.

Asi, I.M., 2007. Evaluating skid resistance of different asphalt concrete mixes. *Building and Environment*, *42*(1), pp.325-329.

Aviation Hunt. (2020). *Aircraft Tyre Design and Construction.* Aviation Hunt. 09/12/2020. < https://www.aviationhunt.com/aircraft-tyre-construction/>

Aviation Pros. 2001. *Understanding the basics of aircraft tire construction and maintenance.* Available at: https://www.aviationpros.com/aircraft/article/10388042/understanding-the-basics-of-aircraft-tire-construction-and-maintenance . (Accessed: 09/12/2020)

Aviation Pros. 2011. *Making the Case for Diamond-Grooved Surfaces.* Available at: https://www.aviationpros.com/airports/airports-municipalities/article/10251434/aoa . (Accessed: 07/12/2020)

Backx, P.W., 2007. Tyre/road contact measurement using pressure sensitive films. Thesis (Bachelor). Technische Universiteit, Eindhoven.

Batterbee, D.C., Sims, N.D., Stanway, R. and Wolejsza, Z., 2007. Magnetorheological landing gear: 1. A design methodology. *Smart Materials and Structures*, *16*(6), p.2429.

BLASTRAC. (2012). *Improving Skid Resistance on Road Surfaces.* Europe. Available At: https://issuu.com/blastraceu/docs/brochure_blastrac_highways (Accessed: 07/11/2020)

BRIDGESTONE (2021) *Functions and performances.* Available from: https://www.bridgestone.com/products/basic_knowledge/function_and_performance/ [Accessed 12/12/2021

British Standards (2000) *BS 7941-2:2000 Methods for measuring the skid resistance of pavement surfaces - Test method for measurement of surface skid resistance using the GripTester braked wheel fixed slip device.* Available online: [Accessed 22/09/2017]

British Standards (2011) *BS EN 13036-4 Road and airfield surface characteristics. Test methods . Method for measurement of slip/skid resistance of a surface: The pendulum test.* Available from: [Accessed 11/10/2017]

British Standards. (2002). BS ISO 13473-2:2002. Characterisation of pavement texture by use of surface profiles. Terminology and basic requirements related to pavement texture profile analysis. London: BSi.

Cambridge Dictionary. (2020). Concise Oxford English Dictionary. 12th ed. Oxford: Oxford University Press.

Chu, L and Fwa, T.F 2019, 'Measuring Skid Resistance of Grooved Pavements', School of Highway, Chang'an University, China

Chu, L. and Fwa, T.F., 2019. Measuring Skid Resistance of Grooved Pavements. In *Bituminous Mixtures and Pavements VII* (pp. 641-645). CRC Press.

Civil Aviation Authority, (2010). *The Assessment of Runway Surface Friction Characteristics.* United Kingdom*, p.23.*

Clark, S.K. and Dodge, R.N., 1979. *A handbook for the rolling resistance of pneumatic tires. Michigan, USA.*

Conant, F.S., Hall, G.L. and Walter, J.D., 1970. *Surface temperature of running tires using infrared scanning* (No. 700475). SAE Technical Paper.

Conville, S., 2010. The measurement of contact phenomena under a GripTester tyre. Thesis (MSc), University of Ulster.

Copetti Callai, S. and Sangiorgi, C., 2021. A review on acoustic and skid resistance solutions for road pavements. *Infrastructures*, *6*(3), p.41.

Daiutolo, H. (2013) *Runway Grooving and Surface Friction.* Society of Research Adminstrators, September 30th – October 4th 2013, Mexico.

De Beer, M. and Fisher C., 1997a. Contact stresses of pneumatic tyres measured with the Vehicle-Road Surface Pressure Transducer Array (VRSPTA) system for the University of California at Berkeley (UCB) and the Nevada Automotive Test Center (NATC) Volume 1. Contract Research CR-97/053, TRANSPORTEK, CSIR.

De Beer, M., 2008. Stress-In-Motion (SIM) - A new tool for road infrastructure protection? Proceedings of the International Conference on Heavy Vehicles (HV Paris 2008 - ICWIM5), WIM Session 7, Paris/ Marne-la-Vallée, France, May 19-22.

De Beer, M., Fisher, C., Jooste, F. J., 1997b. Determination of pneumatic tyre/ pavement interface contact stresses under moving loads and some effects on pavements with thin asphalt surfacing layers. Proceedings of the 8th International Conference on Asphalt Pavements (ICAP '97), Seattle, Washington, August 10-14.

de Solminihac, H., Chamorro, A. and Echaveguren, T., 2008. Procedure to Process, Harmonize and Analyze Grip Tester Measurements. In *7th International Conference on Managing Pavement Assets, TRB Committee AFD10*.

Design Manual for Roads and Bridges (DMRB) (2006). *Surfacing materials for new and maintenance construction. Pavement design and Maintenance.*

Design Manual for Roads and Bridges (DMRB) (2015). *Volume 7 Pavement Design and Maintenance Section 3 Pavement Maintenance Assessment.*

Douglas R.A., Woodward W.D.H. and Rogers R.J., 2003. Contact pressures and energies beneath soft tyres: modelling effects of central tyre inflation-equipped heavy-truck traffic on road surfaces. Transportation Research Record 1819, Washington, DC: Transportation Research Board, 221–227.

Douglas, R.A., 2009 Tyre/road contact stresses measured and modelled in three coordinate directions. NZ Transport Agency Research Report 384, Golder Associates Ltd, Mississauga, Ontario, Canada.

Douglas, R.A., Woodward W.D.H. and Woodside, A.R., 2000. Road contact stresses and forces under tyres with low inflation pressure. Canadian Journal of Civil Engineering, 27:1248–1258.

Dunford, A., 2010. GripTester trial: October 2009: including SCRIM comparison. Crowthorne: TRL.

Dunford, A., 2013. Friction and the texture of aggregate particles used in the road surface course. Thesis (PhD), University of Nottingham.

Edmondson, C., 2011. *Fast Car Physics*. JHU Press.

Ejsmont, J., Taryma, S., Ronowski, G. and Swieczko-Zurek, B., 2018. Influence of temperature on the tyre rolling resistance. *International Journal of Automotive Technology*, *19*(1), pp.45-54.

Ejsmont, J.A., Ronowski, G., Świeczko-Żurek, B. and Sommer, S., 2017. Road texture influence on tyre rolling resistance. *Road Materials and Pavement Design*, *18*(1), pp.181-198.

Federal Aviation Administration (FAA) (1997) Measurement, Construction, and Maintenance of Skid Resistant Airport Pavement Surfaces. from: *https://www.faa.gov/documentlibrary/media/advisory_circular/150-5320-12c/150_5320_12c.pdf* [Accessed 12/09/2018]

Ferguson, J. (2017). 3D Modelling of Surface Parameters of Runway Characteristics. Undergraduate Thesis, School of Built Environment, University of Ulster.

Findlay Irvine. (20220). *GripTester.* Available at: http://www.findlayirvine.com/capabilities/skid/griptester.php (Accessed: 09/12/2020)

Flir. (2020). *Temperature Guns Versus Thermal Imaging Technology.* Flir. 10/12/2020. < https://www.flir.co.uk/discover/rd-science/temperature-guns-versus-thermal-imaging-technology/ >

Friel, S. (2013). Variation of the friction characteristics of road surfacing materials with time. PhD Thesis, School of Built Environment, University of Ulster.

Friel, S. and Woodward, D., 2016. Friction after polishing–initial experiences of new test method to predict skid resistance of Irish road surface materials.

Fwa, T.F., Choo, Y.S. and Liu, Y., 2003. Effect of aggregate spacing on skid resistance of asphalt pavement. *Journal of transportation engineering*, *129*(4), pp.420-426.

Georgia, E.J. and Mayeau, E.F., 1963. Retreading and Repairing of High Performance Aircraft Tires. *SAE Transactions*, pp.302-333.

Ghosh, P., Saha, A. and Mukhopadhyay, R., 2003. Prediction of tyre rolling resistance using FEA. *Constitutive Models for Rubber*, pp.141-146.

Goodyear (2020) *Aircraft Tire Care and Maintenance*. Available from: https://www.goodyearaviation.com/resources/pdf/aviation-tire-care-2020.pdf [Accessed 09/09/2020]

Graul, R.A. and Lenke, L.R., 1985. Runway Rubber Removal Specification Development: Field Evaluation Results and Data Analysis. New Mexico Engineering Research Institute Albuquerque.

Grosch, K.A., 1974. The speed and temperature dependence of rubber friction and its bearing on the skid resistance of tyres. In *The Physics of Tyre Traction* (pp. 264). Springer, Boston, MA.

HAAS Automation (2021). *Mini Mill*. Available at: https://www.haas.co.uk/modular-mini-mill/ (Accessed: 11 May 2020).

Hall, J.W., Smith, K.L., Titus-Glover, L., Wambold, J.C., Yager, T.J. and Rado, Z., 2009. Guide for pavement friction. NCHRP, Contractor's Final Report NCHRP Project 01-43. *Transportation Research Board of the National Academies*.

Hamlet, S., Hammoum, F. and Kerzreho, J.P. 2015. Evaluation of the distribution of local pressures and the real contact area between the tyre and the road surface. International Journal of Pavement Engineering, Vol. 16, Nos 9-10, 832-841

Harsh, D. and Shyrokau, B., 2019. Tire Model with Temperature Effects for Formula SAE Vehicle. *Applied Sciences*, *9*(24), p.5328.

International Civil Aviation Organisation (ICAO). (2017). Physical Characteristics

International Standards Organization (ISO) (2022) *ISO 13473-2:2002(en) Characterization of pavement texture by use of surface profiles — Part 2: Terminology and basic requirements related to pavement texture profile analysis.* Available from: https://www.iso.org/obp/ui/#iso:std:iso:13473:-2:ed-1:v1:en [Accessed 08/03/2018]

Ju, F., Fwa, T.F. and Ong, G.P., 2013. Evaluating wet weather driving benefits of grooved pavements. *International Journal of Pavement Research and Technology*, *6*(4), p.287.

Kellermann-Kinner, Christine, & Golkowski, Gudrun. (2018). Friction after polishing – a new performance orientated test method in situ. Presented at the 7th Transport Research Arena TRA 2018 (TRA 2018) (TRA2018), Vienna: Zenodo.

Kelly, D.P. and Sharp, R.S., 2012. Time-optimal control of the race car: influence of a thermodynamic tyre model. *Vehicle System Dynamics*, *50*(4), pp.641-662.

Kogbara, R.B., Masad, E.A., Woodward, D. and Millar, P., 2018. Relating surface texture parameters from close range photogrammetry to Grip-Tester pavement friction measurements. *Construction and Building Materials*, *166*, pp.227-240.

Kost, F., 2014. Basic principles of vehicle dynamics. In *Fundamentals of Automotive and Engine Technology* (pp. 114-129). Springer Vieweg, Wiesbaden.

Lee, Y.P.K., Fwa, T.F. and Choo, Y.S., 2005. Effect of pavement surface texture on British pendulum test. Journal of the Eastern Asia Society for Transportation Studies, 6, pp.1247-1257.

Lewis, P. (2016) Transportation Failures. In: *Forensic Polymer Engineering (Second Edition):* Woodhead Publishing: Pages 307-346,

Liu, G.X., 1992. The area and stresses of contact between tyres and road surface and their effects on road surface. Thesis (DPhil) University of Ulster.

Liu, Y., Fwa, T.F. and Choo, Y.S., 2004. Effect of surface macrotexture on skid resistance measurements by the British Pendulum Test. *Journal of Testing and Evaluation*, *32*(4), pp.304-309.

Luo, R. and Prozzi, J.A., 2005. Evaluation of the Joint Effect of Wheel Load and Tire Pressure on Pavement Performance. University of Texas, Austin Center for Transportation.

Machemehl, R.B., Wang F. and Prozzi J.A., 2005. Analytical study of effects of truck tyre pressure on pavement with measured tyre-pavement contact stress data. Transportation Research Record 1919. Washington DC: Transportation Research Board, 111–120.

Mataei, B., Zakeri, H., Zahedi, M. and Nejad, F.M., 2016. Pavement friction and skid resistance measurement methods: A literature review. *Open Journal of Civil Engineering*, *6*(04), p.537.

McCarty, J.L. and Tanner, J.A., 1983. *Temperature distribution in an aircraft tire at low ground speeds* (No. NASA-TP-2195).

McQuaid, G. (2015). Development of non-contact 3D measurement of areal pavement texture parameters . PhD Thesis, School of Built Environment, University of Ulster.

Michelin (2015) *What is the difference between Radial and Bias tires?* Youtube. Available from: https://www.youtube.com/watch?v=UJJxSlls-tA [Accessed 17 May 2019].

Michelin. (2001). 'The Tyre – Grip'. [Online]. Available at: *http://www.dimnp.unipi.it/guiggiani-m/Michelin_Tire_Grip.pdf* (Accessed 07/12/20)

Millar, P., Woodward, D., Friel, S. and Woodside, A., 2011. 'An investigation of the variation of contact area with inflation pressure'. *5th International Conference Bituminous Mixtures and Pavements.* Thessaloniki, Greece, 1-3 June 2011.

Miller, T., Swiertz, D., Tashman, L., Tabatabaee, N. and Bahia, H.U., 2012. Characterization of asphalt pavement surface texture. *Transportation Research Record*, *2295*(1), pp.19-26.

Ministry of Defence (MOD) . 2009. *Marshall Asphalt for Airfields.* Specification 13. Defence Estates.

Ministry of Defence 2009, *Hot Rolled Asphalt and Asphalt Concrete (Macadam) for Airfields,* Defence Estates Ministry of Defence, viewed 18/02/2018, https://assets.publishing.service.gov.uk/government/uploads/system/uploads/attachment_data/file/33544/spec_12_2009.pdf

Neves, R.R.V., Micheli, G.B. and Alves, M., 2010. An experimental and numerical investigation on tyre impact. *International Journal of Impact Engineering*, *37*(6), pp.685-693.

Nicholls, J.C., (1999). Laboratory tests on high-friction surfaces for highways. 176, TRL / Thomas Telford, Crowethorne.

O'Hare, N. (2017). A Study on the Fundamental Laws of Friction in relation to Rubber. Post Graduate Thesis, School of Built Environment, University of Ulster.

Otto Alte Teigeler (OAT). 2017. *Surface structure after grinding.* Available at: https://www.oat.de/en/service-areas/texturing-concrete-surfaces/grinding-and-grooving. (Accessed: 07/12/2020)

Pancer, E.B. and Karaca, Z., 2016. Reliability of British pendulum test on macrotextured surfaces. International Journal of Innovation Sciences and Research, 5(1), pp.611-616.

Pasindu, H.R. and Fwa, T.F., 2015. Improving wet-weather runway performance using trapezoidal grooving design. *Transportation in Developing Economies*, *1*(1), pp.1-10.

Patterson Jr, J.W., (2012). Evaluation of trapezoidal-shaped runway grooves. Federal Aviation Administration. Atlantic City, NJ.

Pavement Interactive (2020) Design Parameters – Loads. Available from: https://pavementinteractive.org/reference-desk/design/design-parameters/loads/ [Accessed 17/03/2018]

Quora, (2019) *What is the difference between highway pavements and road pavements?* Available from: https://www.quora.com/What-is-the-difference-between-highway-pavements-and-road-pavements [Accessed 08 March 2019]

Reddit. (2020). 'Radial Vs Bias Ply Tires'. *Reddit*. 01/07/2019. Available at https://www.reddit.com/r/ThingsCutInHalfPorn/comments/c7z19q/radial_left_vs_bias_ply_tires_1466_x_525/ (Accessed 09/12/2020).

Redrouthu, B.M. and Das, S., 2014. *Tyre modelling for rolling resistance* (Master's thesis).

ROADGRIP (2020) *Trapezoidal Runway Grooving Versus Traditional Airfield Grooving Which is Best?* Available from: https://roadgrip.co.uk/blog/trapezoidal-runway-grooving-versus-traditional-airfield-grooving-which-is-best/ [Accessed 04/04/2018]

Sahhaf, S.A. and Rahimi, S., 2014. 'Investigation of Laser Systems Used in Pavement Management Systems (PMS)'. Babol Noshirvani University of Technology. *8th National Congress on Civil Engineering*. Iran. 7-8 May 2014

Serway, R. A. & Vuille, C., 2012. College Physics. 9th ed. Boston: Charles Hartford.

Siegfried, 1998. The study of contact characteristics between tyre and road surface. Thesis (DPhil). University of Ulster.

Simpson, D.W., (1989) Runway Rubber Removal, Air Force Institute of Technology, Virginia. Available at https://apps.dtic.mil/sti/citations/ADA218349 [16th August 2022]

Srirangam, S.K., 2015. 'Numerical simulation of tire-pavement interaction'. Master of Engineering Thesis. Tu Delft University of Technology. Netherlands.

Testo (2022) *Measurement surroundings*. Available from: https://www.testo.com/en-NZ/Measurement+surroundings/services_knowledgebase_thermography_measurement_surroundings [Accessed 10/05/2020]

Usman Hameed, UH. 2022. What is the difference between an airport pavement and a highway pavement?. Blog. 09/01/2019. Available from: https://www.quora.com/What-is-the-difference-between-highway-pavements-and-road-pavements [Accessed 05/05/2020].

Vaiana, R., Capiluppi, G.F., Gallelli, V., Iuele, T. and Minani, V., 2012. Pavement Surface Performance Evolution: an experimental application. *Procedia-Social and Behavioral Sciences*, *53*, pp.1149-1160.

Vieira, T., Sandberg, U. and Erlingsson, S., 2019. Negative texture, positive for the environment: effects of horizontal grinding of asphalt pavements. *Road Materials and Pavement Design*, pp.1-22.

Walley, J. 2019. Email to Jason Ferguson, 19th December.

Wang, W., 2019. Sliding Power in Aircraft Landing. *International Journal of Mechanical Engineering and Robotics Research*. *International Journal of Mechanical Engineering and Robotics Research.* Vol. 8. No 2. Pg 310-315.

WDM Limited (2020) *SCRIM® / SCRIMTEX.* Available from: https://www.wdm.co.uk/equipment/scrim-scrimtex [Accessed 14/05/2020]

Weissman, S.L., 1999. Influence of tyre pavement contact stress distribution on development of distress mechanisms in pavements. Transportation Research Record 1655. Washington DC: Transportation Research Board, 161–167.

White, G. and Rodway, B., 2014. Distress and maintenance of grooved runway surfaces. *Airfield Engineering and Maintenance Summit*. 25-28 March. Singapore.

White, G., 2018. State of the art: Asphalt for airport pavement surfacing. *International Jjournal of Pavement Research and Technology*, *11*(1), pp.77-98.

White, G., 2018. State of the art: Asphalt for airport pavement surfacing. *International journal of pavement research and technology*, *11*(1), pp.77-98.

Woodside, A.R., Woodward, W.D.H., and Siegfried, 1999. The determination of dynamic contact stress. Paper no. CS5-2, Proceedings of the International Conference on Accelerated Pavement Testing, Reno, Nevada, 18–20.

Woodward, D., Mcquaid, G. and Millar, P., 2014. A comparison of techniques to determine surface texture data. *Proc., Civil Engineering Research in Ireland, Queen's University Belfas*t, August 28.

Woodward, D., Millar, P. and McQuaid, G., 2014, May. Use of 3D modelling techniques to better understand road surface textures. *In Proceedings of the 4th International Safer Roads Conference, Cheltenham*., United Kingdom. 18 May. (pp. 18-21).

Woodward, D., Millar, P., Friel, S. and Waddell, C., 2013. Measuring Grip and the Contact Patch. In *Airfield and Highway Pavement 2013: Sustainable and Efficient Pavements* (pp. 841-854).

Woodward, D., Millar, P., Lantieri, C., Sangiorgi, C. and Vignali, V. 2016. The wear of Stone Mastic Asphalt due to slow speed high stress simulated laboratory trafficking. Construction and Building Materials Volume 110, Pages 270-277. http://dx.doi.org/10.1016/j. conbuildmat.2016.02.031.

Woodward, D., Millar, P., Tierney, C. and Waddell, C., (2014), The static contact patch of some friction measuring devices. In *4th International Safer Roads Conference, Cheltenham, United Kingdom*.

Woodward, D., Millar, P., Tierney, C., Ferguson, J. (2020). 'Development of a test method to investigate the tyre road interface'. *Asphalt Professional*. No. 85. Pages 10-20.

WU, S., HAO, P. and HACHIYA, Y., 2002. Laboratory evaluation on durability of grooving for airport runways. Journal of Pavement Engineering, *JSCE*, *7*, pp.30p1-30p7.

Yager, T.J., 1969. 14. NASA. Studies on Effect of Grooved Runway Operation on Aircraft Vibrations and Tire Wear. *Pavement Grooving and Traction Studies*, *5073*, p.189.

Your Data Driven. (2020). *What Should The Temperature Of Your Racing Car Tyres Be?* Your Data Driven. 10/12/2020. < https://www.yourdatadriven.com/what-should-the-temperature-of-your-racing-car-tyres-be/>

Zuzelo, P., 2014. The benefits of runway grooving. *Airfield Engineering and Maintenance Summit, Furama Riverfront, Singapore*, pp.25-28.

APPENDIX A

32mm Rib Width – Raw Data Preparation - Work flow.

The process for preparing interface pressure is demonstrated in this workflow. The raw data from the XSENSOR Pressure Pad is prepared in Microsoft Excel. The data is conditionally formatted with colour thresholding to visually illustrates the pressure difference amongst the data.

5.79	5.32	4.93	4.77	5.38	4.89	5.46	5.92	6.7	6.43	5.95	5.14	4.14	3.86
7.38	7.22	7.56	6.8	7.75	6.75	7.22	6.9	7.34	7.61	8.31	7.39	7.01	6.72
7.71	7.97	8.16	7.7	8.63	8.46	8.66	8.85	8.45	8	7.87	7.21	7.44	8.26
9.34	9.6	9.59	9.52	9.94	9.92	9.96	9.67	9.68	9.96	9.35	8.66	8.89	8.54
9.23	9.55	13.49	9.56	9.87	9.93	10.56	10.24	9.52	9.83	9.63	8.87	9.35	9.05
9.2	11.26	9.98	10	20.58	21.06	11.35	19.2	11.98	15.79	11.6	9.61	9.21	8.73
9.97	22.72	25.41	14.52	20.41	18.41	17.62	22.22	19.36	25.73	22.8	9.57	9.37	8.8
15.23	23.31	21.06	12.2	28	18.58	12.91	26.66	24.79	20.35	27.07	20.05	9.76	9.21
23.55	25.97	31	30.09	32.98	31.07	32.29	33.2	32.51	31.95	37	27.6	18.73	9.32
23.39	23.61	30.31	18.36	31.26	23.64	20.29	29.94	25.32	15.2	25.79	10.95	9.47	9.07
9.16	8.52	8.84	8.6	8.88	7.88	8.83	8.98	9.18	9.16	9.21	9.24	8.92	8.78
9.08	8.59	9.15	9.36	9.47	8.88	9.75	9.58	9.85	9.66	16.22	9.71	9.44	8.89
30.53	35.43	33.14	34.55	32.23	33.55	35.52	32.7	30.56	30.59	35.34	27.78	13.38	9.61
14.11	23.84	23.13	22.48	20	21.23	30.56	21.7	27.13	28.65	28.54	22.45	10.55	9.48
15.89	25.65	12.87	21.3	21.06	21.3	27	25.76	25.41	26.41	20.99	14.61	9.65	9.23
17.29	22.73	14.96	23.79	20.29	10.46	22.18	16.17	18.91	22.92	11.09	12.19	9.79	8.93
9.54	12.38	9.83	20.77	22.6	11.39	24.12	24.47	17.29	17.44	17.59	13.64	9.95	9.18
9.97	24.58	14	22.36	25.76	14.18	20.7	20.7	18.29	23.86	14.18	11.48	9.77	9.02
9.92	22.78	10.61	13.23	18.15	13.23	23.29	21.94	9.71	17.67	15.35	11	13.49	9.37
10	21.13	15.19	11.98	25.56	15.65	18.85	27.75	18.6	15.43	20.17	20.41	17.05	9.84
15.95	20.06	18.63	18.01	21.71	20.23	26.35	20.35	14.15	24.35	13.61	9.64	15.77	9.36
20	21.61	17.25	16.41	23.61	12.29	22.36	29.41	20.12	23.94	24.29	17	16.77	9.89
12.52	28.39	24.26	22.48	30.53	28.82	26.35	30.31	22.12	31.88	24.82	18.46	24.97	9.81
21.01	30.13	31.06	28.46	31.03	31.6	26.74	33.94	23.19	32.32	29.76	24.88	23.35	9.52
25.23	30.06	30.72	25.68	32.85	29.7	30.75	32.32	28.7	21.76	30.91	18.01	24.68	9.62
8.57	8.4	8.97	8.98	8.93	8.99	8.87	9.28	8.52	8.14	8.59	8.48	8.59	7.66
9.06	8.81	9.04	9.2	9.13	8.86	8.98	9.46	8.75	8.57	9.12	8.58	8.7	8.71
28.45	30.34	35.3	37.3	33.7	37.3	34.66	37.26	35.32	39.95	32.66	33.66	29.76	10
20.6	19.4	26.72	30.72	21.01	30.34	27.69	33.26	28.35	32.82	32	22.53	16.21	9.72
25.89	20.66	14.21	20.29	18.27	20.65	23.9	28.58	20.53	23.07	31.63	23.82	14.89	9.92
14.1	13.73	20.65	26.61	20.59	23.15	27.1	28.46	27.47	25.29	29.53	18.11	17.8	9.8
14.18	18.13	27.38	24.22	11.19	26.04	29.11	27.04	26.15	24.2	21.3	15.11	11.73	9.41
11.64	11.7	17.24	20.54	9.85	20.71	22.13	23.43	28.93	21.7	20.7	21.88	10.07	9.6
18.37	21.79	21.48	18.66	18.44	23.07	25.56	20.23	27.75	24.61	23.19	21.77	15.59	9.59
17.93	17.26	20.06	21.48	11.11	17.11	21.66	16.07	23.02	20.83	24.29	14.96	9.82	9.79
15.95	17.93	19.12	21.61	20.12	24.22	23.61	24.97	26.98	23.96	24.5	23.79	10.97	9.82
19.33	23.05	18.09	26.79	19.78	27.38	29.34	27.16	27.1	29.76	25.76	20.59	9.71	9.8
19.26	21.2	22.14	25.83	13.75	25.12	28.04	29.52	25.27	24.44	27.63	23.19	14.59	9.84
21.75	22.81	32.03	34.75	28.81	32.47	30.91	30.31	34.41	33.16	32.91	33	19.41	9.88
32.25	35.51	36.54	40.7	31.81	37.69	35.81	32.97	37.06	37.78	36.38	29.05	20.12	9.91
8.71	8.7	8.86	9.21	8.84	8.86	9.04	9.24	8.79	8.95	8.87	8.91	8.73	8.06
8.98	9.28	8.78	9.41	9.16	9.19	8.81	9.39	9.7	9.18	8.92	9.38	9	8.52
34.32	41.09	38.28	41.97	36.25	37.89	38.48	36.77	37.95	38.27	35.03	34.31	23.29	9.96
18.55	25.8	26.52	26.46	20.95	28.63	30.56	31.06	34.31	30.88	28.11	26.33	20	9.89
14.2	21.45	21.2	26.11	18.84	26.7	23.65	23.69	31.81	26.61	26.48	23.79	15.51	9.68
15.39	16.59	20.12	23.23	9.91	15.87	20.54	17.75	28.21	24.44	17.22	13.94	18.03	9.49
17.41	9.83	20.78	21.55	15.46	15.25	20.71	21.96	31.65	22.44	24.7	19.13	10.36	9.45
14.89	16.36	19.35	22.09	14.96	25.77	23.33	25.71	25.77	27.57	26.39	16.79	9.8	9.63
18.34	15.14	19.86	18.05	9.97	18.63	15.75	25.87	24.58	21.84	27.14	22.8	12.77	9.89
13.57	20.12	24.49	24.01	12.93	21.25	18.13	30.75	31.12	29.46	25.8	28.7	15.58	9.76
17.93	18.36	24.91	22.65	14.6	25.45	18.86	31.25	25	28.45	27.97	23.33	20.89	9.89
19.5	15.18	18.79	24.55	18.79	23.17	19.64	30.93	29.76	25.89	33.96	29.94	21.42	16.69
17.09	21.91	26.52	26.11	25.24	28.14	23.41	30	32.83	31.12	31	31.87	27.57	10.65
25	22.77	30.75	29.46	21.55	27.42	24.31	27.8	31.78	34.62	33.93	26.92	28.39	13.67
34.28	38.91	36.3	37.55	38.02	39.58	34.62	44.07	43.45	36.77	41.73	39.77	31	24.52
8.73	9.38	9.1	9.19	9.14	9.18	9.18	9.57	9.63	9.36	9.53	9.14	8.72	8.07
9.03	9.32	9.11	8.8	8.96	9.51	9.23	9.49	9.29	8.88	9	8.99	9.09	8.25
30.09	35.69	41.57	41.7	34.46	42.51	37.77	42.82	44.54	45.25	40.54	39.61	36.58	28.82
20.06	30.22	28.98	32.88	25.98	32.4	29.64	32.71	32.43	32.9	31.87	20.95	25.44	11.16
17.52	23.11	20.78	26.7	19.79	22.02	19.5	24.61	27.44	28.27	31.5	30.09	20.95	23.61
17.29	27.05	21.43	19.21	25.45	25.57	20.36	27.62	29.82	28.09	26.25	22.43	21.59	15.14
13	25.66	26.77	20.96	20.12	22.5	27.97	29.29	27.8	25.44	26.33	17.27	19.5	9.82
9.92	14.64	25.09	16.86	10.21	18	27.02	31.41	33.88	31.44	28.82	20.41	19.35	9.87
15.36	22.71	24.13	22.57	20.24	19.07	28.63	30.43	32.59	32.09	31.56	21.24	20.12	9.83
13.64	17.84	20.42	17.57	18.5	13.88	19.5	31.09	27.38	21.07	30.43	14.85	16.16	9.84
13.81	16	16.29	25.3	26.07	17.48	18.92	31.03	30.28	24.2	31.53	24.44	16.16	14.74
10.07	23.05	23.75	20.77	25.41	21.79	25.03	28.64	29.05	27.1	31.06	19.42	13.26	9.98
13.02	24.85	23.41	19.14	26.19	20.54	21.01	30.16	25.23	23.51	34.21	25.56	21.18	17.61
9.83	28.2	30.28	25.36	32.57	26.79	21.25	36.34	31.94	30.91	36.72	29.05	27.1	13.55
24.91	37.96	39.73	38.07	37.45	37.45	38.92	44.3	39.75	41	43.28	38.31	34.63	21.35
8.77	8.73	8.87	8.87	8.82	8.72	8.8	8.67	8.89	8.82	8.76	8.73	8.92	8.95
9.08	9.3	8.77	8.96	8.85	8.94	9.14	9.05	8.98	8.94	8.95	9	9.04	8.93
30.94	35.58	34.64	38.17	36.26	33.13	33.75	40.83	37.82	40.34	39.38	31.47	34.66	24.41
17.98	30.31	21.31	26.92	30.47	23.79	30.66	32.82	34.72	31.47	34.75	31.66	24.88	14.6
19.85	24.07	24.29	25.12	27.14	22.02	28.04	22.73	29.52	29.17	28.88	21.23	17.44	9.45
20.06	20.59	20.71	20.77	19.93	12.82	22.66	23.49	22.01	27.34	29.82	19.63	22.48	9.97
9.99	14.56	21.84	20	25.56	16.74	18.91	24.08	27.1	25.5	30.03	16.86	18.17	9.84
10.72	20.24	22.26	24.22	29.16	24.34	20.29	25.44	28.41	23	23.7	20.41	16.35	9.83
15.14	20.77	20.47	20.89	18.04	12.84	15.33	21.77	22.07	29.64	28.52	20.7	18.46	9.72
22.5	19.56	23.31	23.37	23.9	16.64	19.85	26.21	26.92	23.07	28.4	18.45	19.63	9.71
12.41	24.94	23.04	23.63	20.18	11.97	16.13	16.2	18.23	22.23	25.12	17.06	14.48	9.45
10.73	21.13	20.77	21.79	18.98	25.21	25.21	27	26.59	26	26.53	23.35	20	10.29
16.64	22.8	25.91	25.68	21.83	22.01	20.95	25.09	30.28	24.26	31.16	23.53	17.06	9.73
19.93	22.19	29.11	25.03	22.13	30.72	26.8	31.5	31.32	23.76	29.29	26.41	25.94	10.81
24.7	32.07	35.37	35.02	35.77	36.03	35.8	40.47	41.06	41.5	47.68	39.14	35.45	29.41
8.76	8.77	9.29	9.38	9.28	9.3	9.27	9.74	9.61	9.34	9.32	9.16	8.53	8.33
8.57	8.46	8.6	9.19	9.22	9.26	9.21	9.1	9.43	9.41	9.24	9.02	9.13	8.09
24.38	32.17	36.09	31.04	34.68	33.23	35.4	41.22	40.22	39.25	40.23	33.35	33.22	26.08
26.09	32.17	35.25	26.21	30.19	30	27.75	30.81	32.1	28.94	33.73	24.23	18.97	15.66
17.28	25.62	26.21	17.72	27.34	30.19	25.91	30.56	32.07	34.21	30.91	22.57	27.66	12
12.81	21.71	28.16	23.18	27.23	25.41	23.12	27.59	28.94	27.47	30.84	21.58	19.78	15.41
11.54	21.06	19.56	20	18.45	23.7	20.18	21.94	26.7	22.23	18.82	12.79	23.94	31.25
9.81	18.23	14.56	16.62	21.54	23.19	28.28	21.41	25.23	28.53	22.98	18.14	9.85	8.88
15.7	23.19	28.06	21.41	24.82	20.88	22.06	27.06	28.06	26.61	24.38	12.96	14.07	9.41
12.22	24.26	13.38	21.12	23	12.59	12.22	21.64	24.76	25.29	28.7	16.44	16.44	9.66
9.86	23.73	18.81	25.23	24.06	21.94	18.44	24.18	24.35	27.06	22.47	21.59	16.07	9.7
18.22	20.65	18.59	25.35	24.7	15.48	19.63	22.29	18.81	23.68	15.7	16.74	17.41	9.29
17.04	24.2	22.07	19.41	22.53	21.18	21.53	30.16	34.36	31.94	28.24	29.53	16.52	9.7
22.94	31.26	25.47	24.94	24.94	27.48	32.36	30.72	36.25	33.26	33.63	30.34	22.1	9.39
33	39.27	33.87	41.37	35.38	32.83	39.46	38.9	38.3	39.54	38.6	34.67	36.61	22.38
9.02	9.25	8.91	8.98	8.63	8.51	8.5	8.38	8.01	8.54	7.94	8.23	8.2	8.08
9.25	9.16	8	9.46	8.63	8.76	8.56	7.21	9.28	7.83	8.17	7.3	7.2	6.32
14.25	25.18	24.64	30.47	23.94	25.64	26.08	28.24	34.46	31.66	36.31	28.49	15.3	9.83
10	27.06	31.1	31.23	31.13	30.44	28.82	30.41	36	30.59	32.92	28.54	9.96	9.55
9.77	10.75	9.97	23.88	18.13	19.92	25.26	23.57	21.94	14.03	16.49	10	9.3	8.43
8.86	9.29	9.74	9.94	9.84	14.48	11.57	21.17	15.3	10.15	13.95	9.49	8.88	8.19
6.96	8.65	9.07	9.28	9.39	9.65	9.15	9.65	9.95	9.6	9.27	9.07	7.9	7.99
6.16	7.8	8.37	8.52	8.47	8.36	8.33	8.56	8.97	8.71	7.98	7.68	7.29	6.09
4.97	5.39	5.95	6.63	6.06	6.02	6.74	7.84	7.61	7.06	7.14	4.61	3.94	3.44
2.94	3.63	4.5	4.52	4.54	5.57	6.47	6.04	5.28	4.43	3.66	3.36	3.18	2.93
2.89	3.7	5.35	6.3	5.98	5.46	4.7	3.82	3.73	3.94	4.61	5.18	5.11	4.69
3.96	5.75	7.39	6.99	6.06	5.13	4.71	4.03	4.98	6.52	6.55	7.2	7.08	7.82
4.85	6.44	6.9	7.35	7.62	7.31	6.38	6.55	7.06	7.44	6.56	6.38	5.59	5.48

The interface data of interest i.e, that of the ribs is highlighted by a boarder around the data cells. Each rib is assigned a number. The remaining interface pressure outside the ribs is discarded. The average interface pressure across the width of the rib is calculated.

															AVG
RIB 1	30.53	35.43	33.14	34.55	32.23	33.55	35.52	32.7	30.56	30.59	35.34	27.78	13.38	9.61	29.64
	14.11	23.84	23.13	22.48	20	21.23	30.56	21.7	27.13	28.65	28.54	22.45	10.55	9.48	21.70
	15.89	25.65	12.87	21.3	21.06	21.3	27	25.76	25.41	26.41	20.99	14.61	9.65	9.23	19.80
	17.29	22.73	14.96	23.79	20.29	10.46	22.18	16.17	18.91	22.92	11.09	12.19	9.79	8.93	16.55
	9.54	12.38	9.83	20.77	22.6	11.39	24.12	24.47	17.29	17.44	17.59	13.64	9.95	9.18	15.73
	9.97	24.58	14	22.36	25.76	14.18	20.7	20.7	18.29	23.86	14.18	11.48	9.77	9.02	17.06
	9.92	22.78	10.61	13.23	18.15	13.23	23.29	21.94	9.71	17.67	15.35	11	13.49	9.37	14.98
	10	21.13	15.19	11.98	25.56	15.65	18.85	27.75	18.6	15.43	20.17	20.41	17.05	9.84	17.69
	15.95	20.06	18.63	18.01	21.71	20.23	26.35	20.35	14.15	24.35	13.61	9.64	15.77	9.36	17.73
	20	21.61	17.25	16.41	23.61	12.29	22.36	29.41	20.12	23.94	24.29	17	16.77	9.89	19.64
	12.52	28.39	24.26	22.48	30.53	28.82	26.35	30.31	22.12	31.88	24.82	18.46	24.97	9.81	23.98
	21.01	30.13	31.06	28.46	31.03	31.6	26.74	33.94	23.19	32.32	29.76	24.88	23.35	9.52	26.93
	25.23	30.06	30.72	25.68	32.85	29.7	30.75	32.32	28.7	21.76	30.91	18.01	24.68	9.62	26.50
RIB 2	28.45	30.34	35.3	37.3	33.7	37.3	34.66	37.26	35.32	39.95	32.66	33.66	29.76	10	32.55
	20.6	19.4	26.72	30.72	21.01	30.34	27.69	33.26	28.35	32.82	32	22.53	16.21	9.72	25.10
	25.89	20.66	14.21	20.29	18.27	20.65	23.9	28.58	20.53	23.07	31.63	23.82	14.89	9.92	21.17
	14.1	13.73	20.65	26.61	20.59	23.15	27.1	28.46	27.47	25.29	29.53	18.11	17.8	9.8	21.60
	14.18	18.13	27.38	24.22	11.19	26.04	29.11	27.04	26.15	24.2	21.3	15.11	11.73	9.41	20.37
	11.64	11.7	17.24	20.54	9.85	20.71	22.13	23.43	28.93	21.7	20.7	21.88	10.07	9.6	17.87
	18.37	21.79	21.48	18.66	18.44	23.07	25.56	20.23	27.75	24.61	23.19	21.77	15.59	9.59	20.72
	17.93	17.26	20.06	21.48	11.11	17.11	21.66	16.07	23.02	20.83	24.29	14.96	9.82	9.79	17.53
	15.95	17.93	19.12	21.61	20.12	24.22	23.61	24.97	26.98	23.96	24.5	23.79	10.97	9.82	20.54
	19.33	23.05	18.09	26.79	19.78	27.38	29.34	27.16	27.1	29.76	25.76	20.59	9.71	9.8	22.40
	19.26	21.2	22.14	25.83	13.75	25.12	28.04	29.52	25.27	24.44	27.63	23.19	14.59	9.84	22.13
	21.75	22.81	32.03	34.75	28.81	32.47	30.91	30.31	34.41	33.16	32.91	33	19.41	9.88	28.33
	32.25	35.51	36.54	40.7	31.81	37.69	35.81	32.97	37.06	37.78	36.38	29.05	20.12	9.91	32.40
RIB 3	34.32	41.09	38.28	41.97	36.25	37.89	38.48	36.77	37.95	38.27	35.03	34.31	23.29	9.96	34.56
	18.55	25.8	26.52	26.46	20.95	28.63	30.56	31.06	34.31	30.88	28.11	26.33	20	9.89	25.58
	14.2	21.45	21.2	26.11	18.84	26.7	23.65	23.69	31.81	26.61	26.48	23.79	15.51	9.68	22.12
	15.39	16.59	20.12	23.23	9.91	15.87	20.54	17.75	28.21	24.44	17.22	13.94	18.03	9.49	17.91
	17.41	9.83	20.78	21.55	15.46	15.25	20.71	21.96	31.65	22.44	24.7	19.13	10.36	9.45	18.62
	14.89	16.36	19.35	22.09	14.96	25.77	23.33	25.71	25.77	27.57	26.39	16.79	9.8	9.63	19.89
	18.34	15.14	19.86	18.05	9.97	18.63	15.75	25.87	24.58	21.84	27.14	22.8	12.77	9.89	18.62
	13.57	20.12	24.49	24.01	12.93	21.25	18.13	30.75	31.12	29.46	25.8	28.7	15.58	9.76	21.83
	17.93	18.36	24.91	22.65	14.6	25.45	18.86	31.25	25	28.45	27.97	23.33	20.89	9.89	22.11
	19.5	15.18	18.79	24.55	18.79	23.17	19.64	30.93	29.76	25.89	33.96	29.94	21.42	16.69	23.44
	17.09	21.91	26.52	26.11	25.24	28.14	23.41	30	32.83	31.12	31	31.87	27.57	10.65	25.96
	25	22.77	30.75	29.46	21.55	27.42	24.31	27.8	31.78	34.62	33.93	26.92	28.39	13.67	27.03
	34.28	38.91	36.3	37.55	38.02	39.58	34.62	44.07	43.45	36.77	41.73	39.77	31	24.52	37.18
RIB 4	30.09	35.69	41.57	41.7	34.46	42.51	37.77	42.82	44.54	45.25	40.54	39.61	36.58	28.82	38.71
	20.06	30.22	28.98	32.88	25.98	32.4	29.64	32.71	32.43	32.9	31.87	20.95	25.44	11.16	27.69
	17.52	23.11	20.78	26.7	19.79	22.02	19.5	24.61	27.44	28.27	31.5	30.09	20.95	23.61	23.99
	17.29	27.05	21.43	19.21	25.45	25.57	20.36	27.62	29.82	28.09	26.25	22.43	21.59	15.14	23.38
	13	25.66	26.77	20.96	20.12	22.5	27.97	29.29	27.8	25.44	26.33	17.27	19.5	9.82	22.32
	9.92	14.64	25.09	16.86	10.21	18	27.02	31.41	33.88	31.44	28.82	20.41	19.35	9.87	21.21
	15.36	22.71	24.13	22.57	20.24	19.07	28.63	30.43	32.59	32.09	31.56	21.24	20.12	9.83	23.61
	13.64	17.84	20.42	17.57	18.5	13.88	19.5	31.09	27.38	21.07	30.43	14.85	16.16	9.84	19.44
	13.81	16	16.29	25.3	26.07	17.48	18.92	31.03	30.28	24.2	31.53	24.44	16.16	14.74	21.88
	10.07	23.05	23.75	20.77	25.41	21.79	25.03	28.64	29.05	27.1	31.06	19.42	13.26	9.98	22.03
	13.02	24.85	23.41	19.14	26.19	20.54	21.01	30.16	25.23	23.51	34.21	25.56	21.18	17.61	23.26
	9.83	28.2	30.28	25.36	32.57	26.79	21.25	36.34	31.94	30.91	36.72	29.05	27.1	13.55	27.14
	24.91	37.96	39.73	38.07	37.45	37.45	38.92	44.3	39.75	41	43.28	38.31	34.63	21.35	36.94
RIB 5	30.94	35.58	34.64	38.17	36.26	33.13	33.75	40.83	37.82	40.34	39.38	31.47	34.66	24.41	35.10
	17.98	30.31	21.31	26.92	30.47	23.79	30.66	32.82	34.72	31.47	34.75	31.66	24.88	14.6	27.60
	19.85	24.07	24.29	25.12	27.14	22.02	28.04	22.73	29.52	29.17	28.88	21.23	17.44	9.45	23.50
	20.06	20.59	20.71	20.77	19.93	12.82	22.66	23.49	22.01	27.34	29.82	19.63	22.48	9.97	20.88
	9.99	14.56	21.84	20	25.56	16.74	18.91	24.08	27.1	25.5	30.03	16.86	18.17	9.84	19.94
	10.72	20.24	22.26	24.22	29.16	24.34	20.29	25.44	28.41	23	23.7	20.41	16.35	9.83	21.31
	15.14	20.77	20.47	20.89	18.04	12.84	15.33	21.77	22.07	29.64	28.52	20.7	18.46	9.72	19.60
	22.5	19.56	23.31	23.37	23.9	16.64	19.85	26.21	26.92	23.07	28.4	18.45	19.63	9.71	21.54
	12.41	24.94	23.04	23.63	20.18	11.97	16.13	16.2	18.23	22.23	25.12	17.06	14.48	9.45	18.22
	10.73	21.13	20.77	21.79	18.98	25.21	25.21	27	26.59	26	26.53	23.35	20	10.29	21.68
	16.64	22.8	25.91	25.68	21.83	22.01	20.95	25.09	30.28	24.26	31.16	23.53	17.06	9.73	22.64
	19.93	22.19	29.11	25.03	22.13	30.72	26.8	31.5	31.32	23.76	29.29	26.41	25.94	10.81	25.35
	24.7	32.07	35.37	35.02	35.77	36.03	35.8	40.47	41.06	41.5	47.68	39.14	35.45	29.41	36.39
RIB 6	24.38	32.17	36.09	31.04	34.68	33.23	35.4	41.22	40.22	39.25	40.23	33.35	33.22	26.08	34.33
	26.09	32.17	35.25	26.21	30.19	30	27.75	30.81	32.1	28.94	33.73	24.23	18.97	15.66	28.01
	17.28	25.62	26.21	17.72	27.34	30.19	25.91	30.56	32.07	34.21	30.91	22.57	27.66	12	25.73
	12.81	21.71	28.16	23.18	27.23	25.41	23.12	27.59	28.94	27.47	30.84	21.58	19.78	15.41	23.80
	11.54	21.06	19.56	20	18.45	23.7	20.18	21.94	26.7	22.23	18.82	12.79	23.94	31.25	20.87
	9.81	18.23	14.56	16.62	21.54	23.19	28.28	21.41	25.23	28.53	22.98	18.14	9.85	8.88	19.09
	15.7	23.19	28.06	21.41	24.82	20.88	22.06	27.06	28.06	26.61	24.38	12.96	14.07	9.41	21.33
	12.22	24.26	13.38	21.12	23	12.59	12.22	21.64	24.76	25.29	28.7	16.44	16.44	9.66	18.69
	9.86	23.73	18.81	25.23	24.06	21.94	18.44	24.18	24.35	27.06	22.47	21.59	16.07	9.7	20.54
	18.22	20.65	18.59	25.35	24.7	15.48	19.63	22.29	18.81	23.68	15.7	16.74	17.41	9.29	19.04
	17.04	24.2	22.07	19.41	22.53	21.18	21.53	30.16	34.36	31.94	28.24	29.53	16.52	9.7	23.46
	22.94	31.26	25.47	24.94	24.94	27.48	32.36	30.72	36.25	33.26	33.63	30.34	22.1	9.39	27.51

The average interface pressure across the width of each rib is grouped together and the total average of the averages is calculated.

Pressure Data						Average
Rib 1	Rib 2	Rib 3	Rib 4	Rib 5	Rib 6	pressure
29.64	32.55	34.56	38.71	35.10	34.33	34.15
21.70	25.10	25.58	27.69	27.60	28.01	25.94
19.80	21.17	22.12	23.99	23.50	25.73	22.72
16.55	21.60	17.91	23.38	20.88	23.80	20.69
15.73	20.37	18.62	22.32	19.94	20.87	19.64
17.06	17.87	19.89	21.21	21.31	19.09	19.40
14.98	20.72	18.62	23.61	19.60	21.33	19.81
17.69	17.53	21.83	19.44	21.54	18.69	19.45
17.73	20.54	22.11	21.88	18.22	20.54	20.17
19.64	22.40	23.44	22.03	21.68	19.04	21.37
23.98	22.13	25.96	23.26	22.64	23.46	23.57
26.93	28.33	27.03	27.14	25.35	27.51	27.05
26.50	32.40	37.18	36.94	36.39	36.01	34.24

The same process demonstrated above is repeated for that of the 19mm rib width and 10mm rib width.

APPENDIX B

PTV Data for 4 Test Conditions

	Simultated Trafficking - **Testing condition 1 – PTV 90° Angle – Dry Conditions** (Fig.7.0)													
	0	10	100	200	400	800	1500	3000	6000	10000	20000	30000	50000	75000
MAA	107.6	111.1	105.8	114.4	98.7	102.7	96.4	101.6	104.6	-	-	-	-	-
MAB	105.8	98.4	91.7	96.8	89.0	90.4	94.2	88.4	94.4	-	-	-	-	-
MAC	101.5	98.6	93.8	98.2	94.8	91.3	98.0	81.7	92.2	93.8	89.0	88.2	93.8	102.0
MAD	100.0	93.3	97.3	93.2	91.4	84.8	92.0	82.4	88.6	94.6	93.6	93.2	95.4	104.6
MAE	104.5	102.3	91.4	87.6	85.6	88.6	89.7	94.4	93.6	94.2	90.8	91.8	92.8	95.8
MAF	100.0	89.1	93.7	86.0	92.3	78.0	87.0	82.8	85.4	79.4	88.8	77.7	90.0	82.8
MAH	99.0	94.9	95.5	85.2	85.2	77.2	85.8	81.2	78.6	81.6	90.8	93.2	94.0	95.2
MAK	103.4	96.0	78.0	87.8	85.7	79.4	84.6	78.6	85.0	81.9	97.0	81.3	96.8	92.6

	Simultated Trafficking - **Testing condition 2 – PTV 80° Angle – Dry Conditions** (Fig.7.2)													
	0	10	100	200	400	800	1500	3000	6000	10000	20000	30000	50000	75000
MAA	130.3	136.3	121.8	114.3	117.5	116.8	100.8	97.8	88.8	-	-	-	-	-
MAB	114.5	132.3	117.7	119.6	112.6	102.2	110.8	97.8	105.2	-	-	-	-	-
MAC	100.3	110.1	90.3	101.4	92.5	95.6	97.2	92.5	103.8	103.0	105.4	98.6	99.2	102.8
MAD	98.8	92.6	95.4	91.8	94.0	92.4	91.2	85.8	93.8	93.2	99.8	95.2	102.4	107.6
MAE	106.0	102.0	93.5	87.2	98.6	95.2	93.0	94.2	94.2	94.6	97.8	91.7	97.2	96.2
MAF	99.8	91.8	94.7	84.6	87.2	78.0	92.8	81.8	84.0	82.2	83.6	79.8	95.4	86.0
MAH	106.8	99.0	102.6	86.0	101.0	94.2	77.4	92.6	90.2	87.6	91.2	92.8	89.8	94.4
MAK	102.8	95.8	92.2	87.2	86.0	85.6	78.2	81.4	85.6	89.6	95.4	88.0	91.2	89.4

	Simulated Trafficking - **Testing condition 3 – PTV 90° Angle – Wet Conditions** (Fig.7.4)													
	0	10	100	200	400	800	1500	3000	6000	10000	20000	30000	50000	75000
MAA	95.4	97.43	79.17	83.2	75	81.4	92.4	84	76.6	-	-	-	-	-
MAB	97.2	96.86	87.4	89.2	77	82.4	79.4	74.6	72.2	-	-	-	-	-
MAC	96.6	86.00	85.8	85	73.8	74	74.4	73.4	72.2	71.4	64.8	66.4	66.8	76.2
MAD	82.2	81.00	72.8	80.6	64.4	64.2	65.2	65.2	62.8	62.8	81.4	68.6	67.6	84.4
MAE	91.2	88.71	73.2	65.2	64.8	69.6	69	70.8	65.6	67.8	62.4	64.4	63.6	68.4
MAF	72.4	72.00	58.67	60.4	60.6	55.6	59.2	58.8	55.4	55.8	59.8	59.4	60.4	56.8
MAH	85	82.14	64.8	63.2	64	61	62.4	60.4	55.8	57.4	74	81	61	62
MAK	71	73.83	57.8	58.8	60	56.4	58.6	54.6	55.6	56	58.4	59.8	60.4	60.2

	Simualted Trafficking - **Testing condition 4 – PTV 80° Angle – Wet Conditions** (Fig.7.6)													
	0	10	100	200	400	800	1500	3000	6000	10000	20000	30000	50000	75000
MAA	125.00	126.40	115.6	116	112	111	108	109	97	-	-	-	-	-
MAB	112.25	127.86	98.67	94.8	97.2	82.2	94.8	78.8	85.4	-	-	-	-	-
MAC	89.75	97.17	71.5	90.7	80.2	81	85.6	87.4	84.2	90.6	85.6	79.2	83.2	81
MAD	82.00	77.25	70.4	67.8	70.8	68.4	67.8	68.4	66	65.6	74.6	73.8	75.6	82
MAE	84.20	80.29	71.4	63.6	69.2	70	66.8	65	61.2	65.8	71	68.6	71	70
MAF	75.60	74.57	60	60.4	61.8	59.4	59.4	60.2	57.2	58.8	61	61.2	61.8	58.6
MAH	84.20	79.50	72.8	69	78.6	72	72	73.2	68.2	66.2	70.6	71	69	68.8

PTV Data for the difference between un-grooved control and grooved test specimens for wet and dry conditions.

Difference between un-grooved control and grooved test specimens for wet conditions (Figure 7.8)				
	Original Data		Difference	
	90 Wet	80 Wet	90 Wet	80 Wet
MAF	72.4	75.6	1.4	-1
MAD	82.2	82	11.2	5.4
MAH	85	84.2	14	7.6
MAE	91.2	84.2	20.2	7.6
MAC	96.6	89.75	25.6	13.15
MAA	95.4	125	24.4	48.4
MAB	97.2	112.25	26.2	35.65
MAK	71	76.6		
EXAMPLE 72.4 (MAF) - 71 (MAK) = 1.4				

Difference between un-grooved control and grooved test specimens for dry conditions (Figure 7.9)				
	Original Data		Difference	
	80 Dry	90 Dry	80 Dry	90 Dry
MAF	99.75	100	-3.05	-3.4
MAD	98.75	100	-4.05	-3.4
MAH	106.75	99	3.95	-4.4
MAE	106.00	104.5	3.20	1.1
MAC	100.25	101.5	-2.55	-1.9
MAA	130.25	107.6	27.45	4.2
MAB	114.50	105.75	11.70	2.35
MAK	102.80	103.4		
EXAMPLE 71 (MAF) - 99.75 (MAK) = -3.05				

PTV Data for the difference between 80 and 90 degree PTV dry and wet.

	Difference between 80 and 90 degree PTV, dry. (Fig.7.10)													
	Simulated Trafficking													
	0	10	100	200	400	800	1500	3000	6000	10000	20000	30000	50000	75000
MAA	22.7	25.1	16.0	-0.2	18.8	14.0	4.3	-3.8	-15.9	-	-	-	-	-
MAB	8.8	33.9	26.0	22.8	23.6	11.8	16.6	9.4	10.8	-	-	-	-	-
MAC	-1.3	11.6	-3.5	3.2	-2.3	4.3	-0.8	10.8	11.6	9.2	16.4	10.4	5.4	0.8
MAD	-1.3	-0.7	-1.9	-1.4	2.6	7.6	-0.8	3.4	5.2	-1.4	6.2	2.0	7.0	3.0
MAE	1.5	-0.3	2.1	-0.4	13.0	6.6	3.3	-0.2	0.6	0.4	7.0	-0.2	4.4	0.4
MAF	-0.3	2.7	1.0	-1.4	-5.1	0.0	5.8	-1.0	-1.4	2.8	-5.2	2.2	5.4	3.2
MAH	7.8	4.1	7.1	0.8	15.8	17.0	-8.4	11.4	11.6	6.0	0.4	-0.4	-4.2	-0.8
MAK	-0.6	-0.2	14.2	-0.6	0.3	6.2	-6.4	2.8	0.6	7.7	-1.6	6.7	-5.6	-3.2

	Difference between 80 and 90 degree PTV, wet. (Fig.7.12)													
	Simualted Trafficking													
	0	10	100	200	400	800	1500	3000	6000	10000	20000	30000	50000	75000
MAA	29.6	29.0	36.4	32.8	37.2	29.8	15.8	25.4	20.4	-	-	-	-	-
MAB	15.1	31.0	11.3	5.6	20.2	-0.2	15.4	4.2	13.2	-	-	-	-	-
MAC	-6.8	11.2	-14.3	5.7	6.4	7.0	11.2	14.0	12.0	19.2	20.8	12.8	16.4	4.8
MAD	-0.2	-3.8	-2.4	-12.8	6.4	4.2	2.6	3.2	3.2	2.8	-6.8	5.2	8.0	-2.4
MAE	-7.0	-8.4	-1.8	-1.6	4.4	0.4	-2.2	-5.8	-4.4	-2.0	8.6	4.2	7.4	1.6
MAF	3.2	2.6	1.3	0.0	1.2	3.8	0.2	1.4	1.8	3.0	1.2	1.8	1.4	1.8
MAH	-0.8	-2.6	8.0	5.8	14.6	11.0	9.6	12.8	12.4	8.8	-3.4	-10.0	8.0	6.8
MAK	5.6	1.2	2.7	1.6	2.4	2.0	2.2	0.6	0.4	1.2	1.0	1.8	0.6	-0.2

APPENDIX C

Change in contact area for all idealised groove test specimens when rotated from 0 degrees up to 12 degrees.

Change in contact area for all idealised groove test specimens. (Fig.9.7)		
Rib Width / Groove Spacing Ratio	Rotation Angle (Degrees)	Contact Area (mm^2)
0.77	0	4591
	3	5263
	6	5556
	9	6642
	12	7359
0.63	0	3559
	3	2626
	6	3005
	9	6642
	12	5608
0.45	0	1153
	3	1048
	6	838
	9	735
	12	523
0.91	0	8114
0.84	0	3927
	3	6049
	6	5901
	9	5133
	12	8043
0.73	0	1388
	3	1356
	6	3117
	9	2872
	12	4076
0.76	0	2995
	3	3853
	6	3540
	9	4937
	12	7610
1.00	0	9100
	10	9051

PTV data for all Rib / width / Groove spacing ratio for rotation angle between 0 and 12 degrees.

Plot of Pendulum Test Value (PTV) and rotation angle. (Fig.9.12)					
Rid Width / Groove spacing ratio	Rotation Angle (Degrees)				
	0	3	6	9	12
0.77	64	55.6	57.4	43	35.6
0.63	74.4	85.8	97	91.6	46.8
0.45	72.2	88.2	93.2	114.4	115.4
0.91	43	-	-	-	-
0.84	49	39.6	39.4	34.8	24.6
0.73	96.2	90	76.4	79.2	70.6
0.76	66.8	55.8	67	46.2	28.4
1	14.2	15	14.4	14.2	14

PTV Data of Idealised grooves Vs rib width / groove spacing ratio

PTV of idealised grooves Vs rib width / groove spacing ratio. (Fig.9.13)		
Rib Width / Groove Spacing Ratio	Rotation Angle (Degrees)	Contact Area (mm^2)
0.77	0	64.0
	3	55.6
	6	57.4
	9	43.0
	12	35.6
0.63	0	74.0
	3	85.8
	6	97.0
	9	91.6
	12	46.8
0.45	0	72.0
	3	88.2
	6	93.2
	9	93.2
	12	115.4
0.91	0	43.0
0.84	0	49.0
	3	39.6
	6	39.4
	9	34.8
	12	24.6
0.73	0	96.0
	3	90.0
	6	76.4
	9	79.2
	12	70.6
0.76	0	67.0
	3	55.8
	6	67.0
	9	46.2
	12	28.4

Measured contact area Vs measured pendulum value for all rib width / groove spacing ratios

Measured Contact Area Vs Measured Pendulum Value for all Rib width / Groove spacing ratios. (Fig.9.14)		
Contact Area (mm2)	Rib Width / Groove Spacing Ratio	PTV
4591	0.77	64
5263	0.77	55.6
5556	0.77	57.4
6642	0.77	43
7359	0.77	35.6
3559	0.63	74.4
2626	0.63	85.8
3005	0.63	97
6642	0.63	91.6
5608	0.63	46.8
1153	0.45	72.2
1048	0.45	88.2
838	0.45	93.2
735	0.45	114.4
523	0.45	115.4
8114	0.91	43
3927	0.84	49
6049	0.84	39.6
5901	0.84	39.4
5133	0.84	34.8
8043	0.84	24.6
1388	0.73	96.2
1356	0.73	90
3117	0.73	76.4
2872	0.73	79.2
4076	0.73	70.6
2995	0.76	66.8
3853	0.76	55.8
3540	0.76	67
4937	0.76	46.2
7610	0.76	28.4

Multiple Linear Regression – Statistical outputs

Regression Statistics	
Multiple R	0.86
R Square	**0.74**
Adjusted R Square	0.73
Standard Error	**15.53**
Observations	35

ANOVA					
	df	*SS*	*MS*	*F*	*Significance F*
Regression	2	22198.21	11099.11	46.00	0.00
Residual	32	7720.52	241.27		
Total	34	29918.73			

	Coefficients	*Standard Error*	*t Stat*	*P-value*	*Lower 95%*	*Upper 95%*	*Lower 95.0%*	*Upper 95.0%*
Intercept	181.26	13.10	13.84	0.00	154.59	207.94	154.59	207.94
Ratio	-156.92	16.60	-9.46	0.00	-190.73	-123.12	-190.73	-123.12
Angle	-1.00	0.62	-1.61	0.12	-2.26	0.26	-2.26	0.26

PTV Data for Angled GMA subjected to 75,000 simulated wheel passes

Angle (degrees)	Simulated Trafficking - Angled GMA subjected to 75,000 simulated wheel passes. (Fig 9.19)												
	0	100	200	400	800	1500	3000	6000	10000	20000	30000	50000	75000
6	88.2	77.4	69.8	73.4	70.0	69.0	70.7	67.2	64.0	61.8	65.2	63.8	62.5
9	86.8	75.0	69.2	69.2	66.6	66.6	69.0	64.6	64.2	66.2	67.0	66.6	66.6
12	86.6	67.4	62.8	64.8	61.0	62.6	62.0	63.6	63.0	63.0	60.2	56.6	57.4

APPENDIX D

The Red Lion load cell Calibration data is detailed below

Red Lion Calibration		
Applied Load (kg)	Red Lion Value	
	Load	Unload
0	-0.04	-0.04
10	0.05	0.05
20	0.14	0.14
30	0.24	0.24
40	0.33	0.33
50	0.43	0.43
60	0.53	0.53
70	0.63	0.63
80	0.73	0.73
90	0.83	0.83
100	0.93	0.93

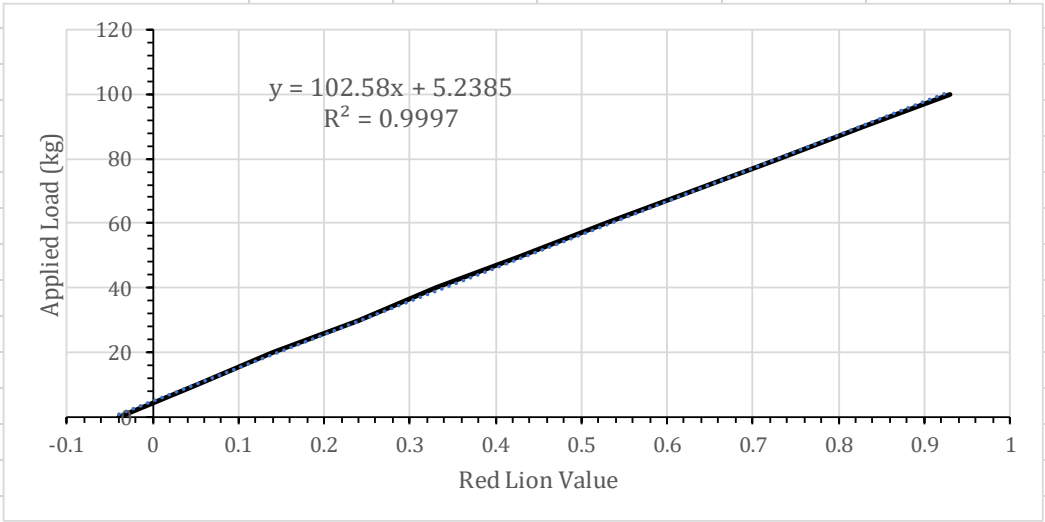

Determination of the resultant force acting through the friction tyre

		Red Lion Value		Force on Tyre			Resultant force acting through friction tyre (kN)
	Applied Load	Load	Unload	Load	Unload	Newtons	
Zero Load	-	0	-	0	-	-	-
Loading Carriage Self Weight	0	0.28	0.34	33.96	40.12	333.16	0.33
	10	0.38	0.45	44.22	51.40	433.79	0.43
	20	0.48	0.56	54.48	62.68	534.42	0.53
	30	0.59	0.67	65.76	73.97	645.11	0.65
	40	0.7	0.81	77.04	88.33	755.81	0.76
	50	0.83	0.93	90.38	100.64	886.63	0.89
	60	0.94	1.1	101.66	118.08	997.32	1.00
	70	1.07	1.23	115.00	131.41	1128.14	1.13
	80	1.23	1.37	131.41	145.77	1289.15	1.29
	90	1.35	1.44	143.72	152.95	1409.91	1.41
	100	1.49	1.49	158.08	158.08	1550.79	1.55

APPENDIX E

DRAFT - Grooved Marshall Asphalt Wear Test

1. Pre-pare Marshall Asphalt Test Specimens using mould sizes of 305mm x 305mm x 50mm.
2. Assess the surface of the Marshall Asphalt before trafficking.
    a. Testing should include determination of initial pendulum values utilising the BS EN 13036 - Road and airfield surface characteristics – Part 4 - The Pendulum Test and photogrammetry to generate 3D models of the test surface to analyse in Digital Surf MountainsMap Software.
    b. Additional testing should be adopted dependent on purpose of data collection.
3. Groove Marshall Asphalt to recommended / desired groove dimensions.
4. Assess the surface of the Grooved Marshall Asphalt before trafficking.
    a. Testing should include determination of initial pendulum values utilising the British Pendulum Tester, photogrammetry to generate 3D models of the test surface.
    b. Additional testing should be adopted dependent on purpose of data collection.
5. Subject Grooved Marshall Asphalt to simulated trafficking using the Road Testing Machine. Visual observation should be carried out regularly to visually assess the change of the grooves / rib.
6. At each trafficking interval assessment of the surface should be made and testing as per **3.a** should be carried out. Assessment of the surface should be carried out at regular trafficking intervals to be able to identify the time where critical changes in the surface may occur.

The method above serves as a draft which and it is recommend this method be integrated into the Ministry of Defence (United Kingdom) - Specification 13 - Marshall Asphalt for Airfields specification or serve as a stand-alone method to assess wear of Grooved Marshall Asphalt.

APPENDIX F

3D Modelling and Digital Surf MountainsMap process flow diagram.

Zephyr 3DF Aerial was used to create a 3D Model. A series of images of the test surface were imported in Zephyr 3DF.

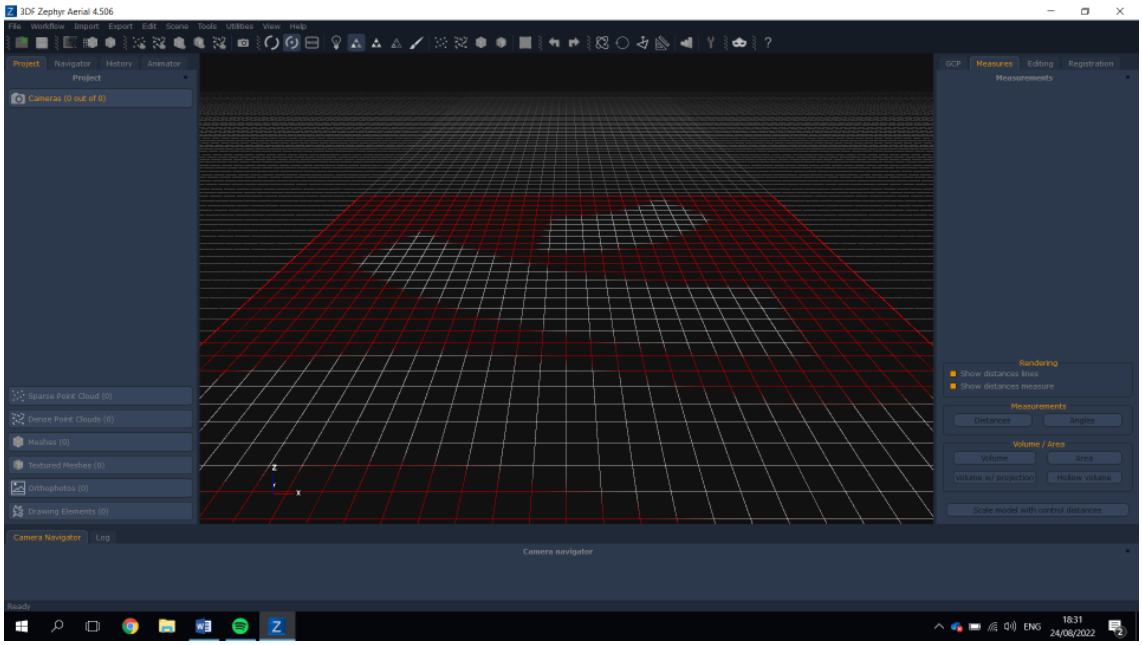

The home screen of Zephyr is shown above.

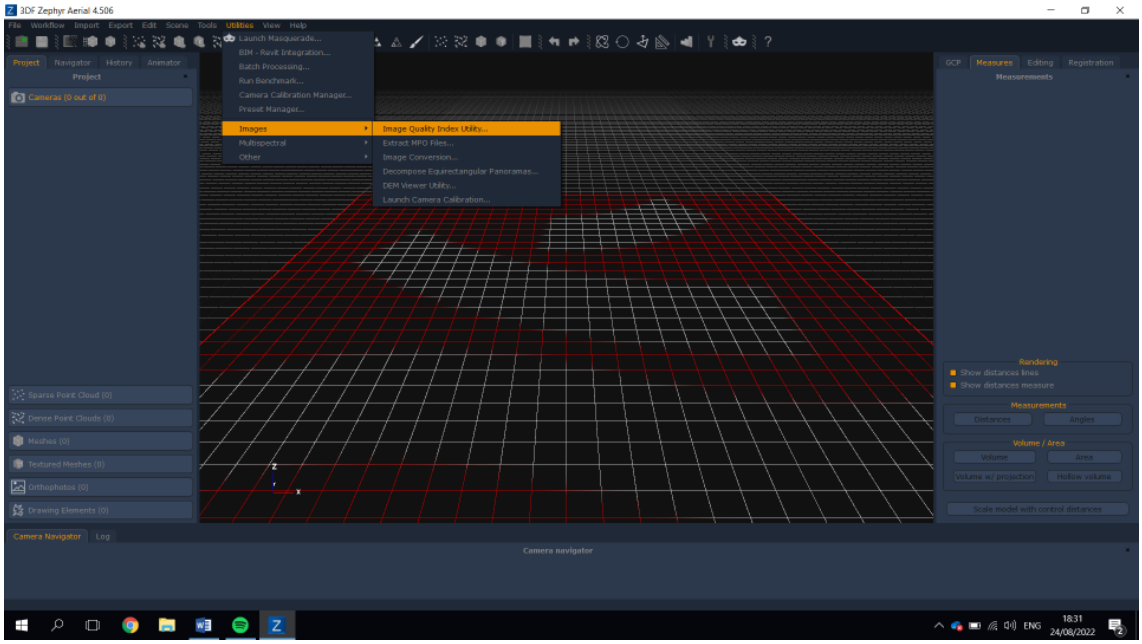

Before 3D modelling, the series of images were graded based on quality of image using the 'Image Quality Index Utility'.

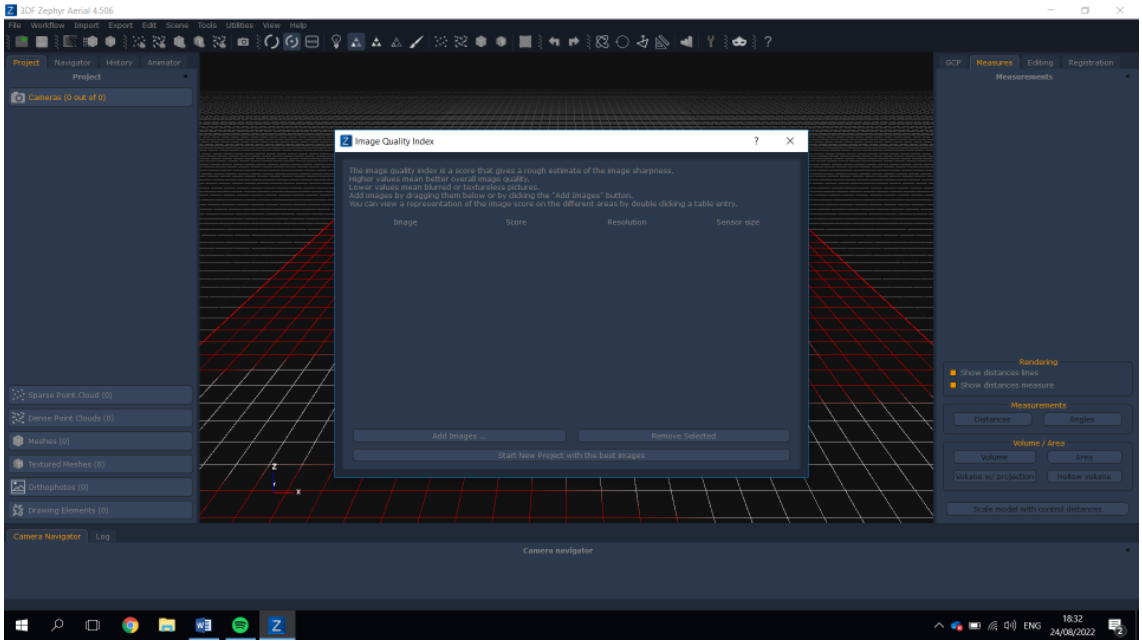

Images were imported into the ‘Image Quality Index Utility’ shown above.

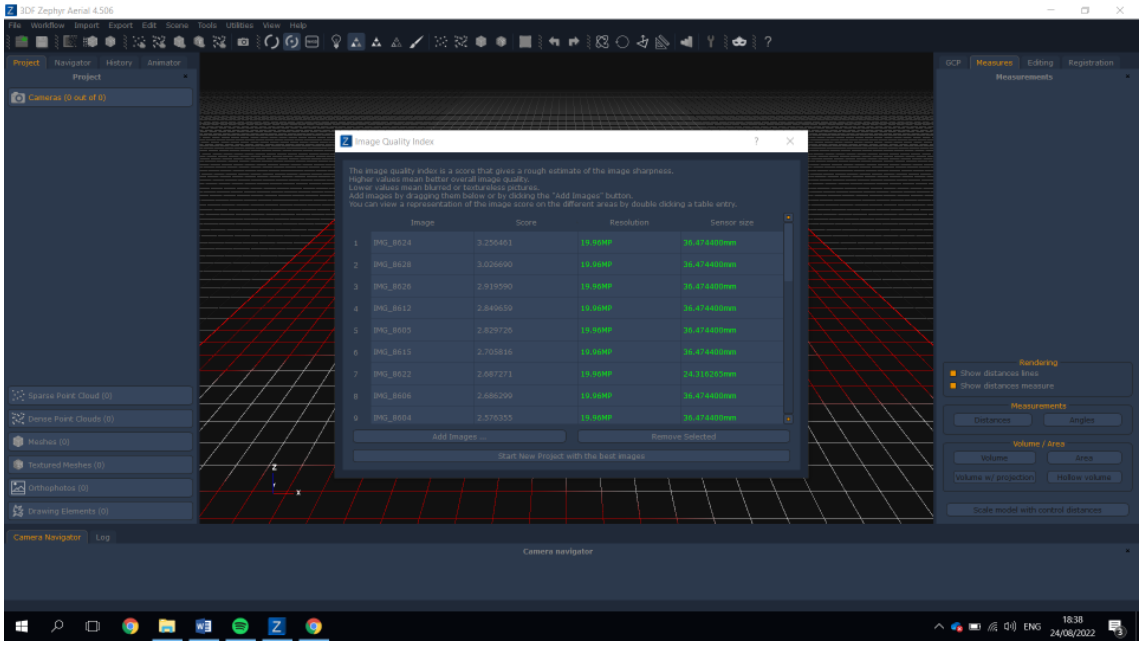

The ‘Image Quality Index Utility’ graded the images as shown above.

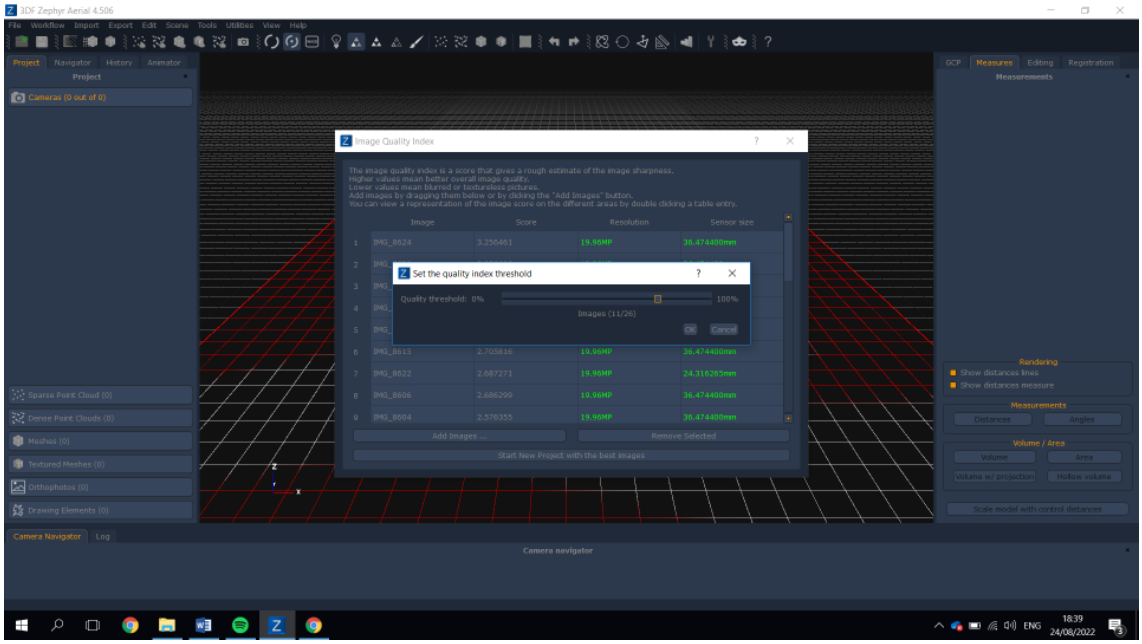

Zephyr recommends the number of images to used based on the 'Image Quality Index Utility'.

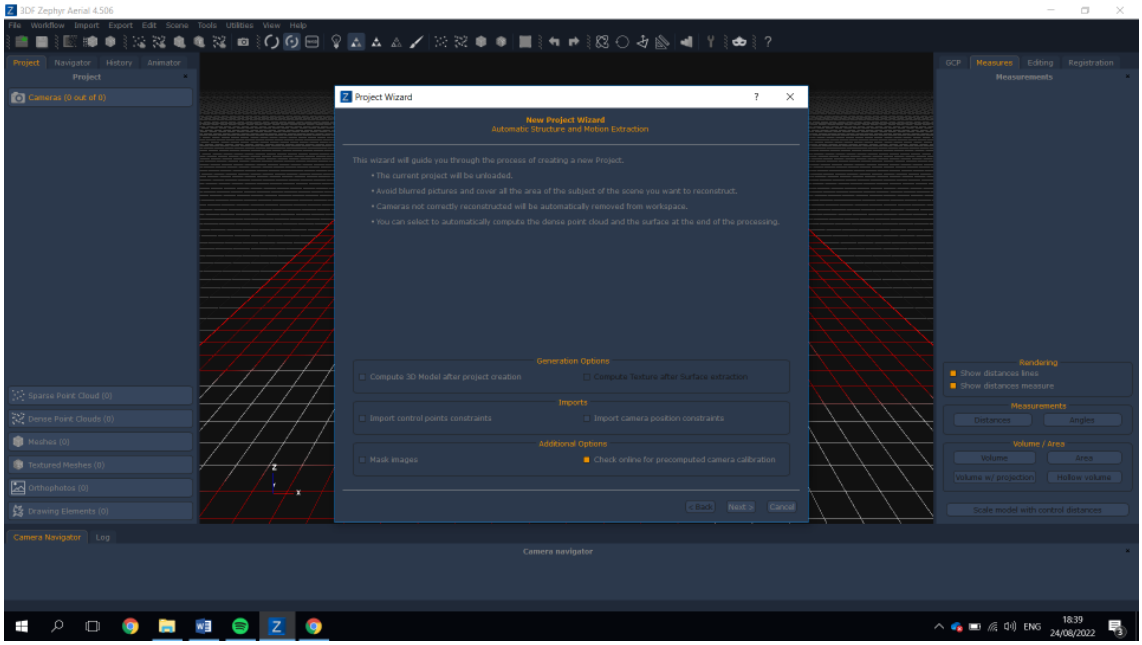

Based on Zephyrs recommended images, the software will recommend images to proceed with 3D modelling.

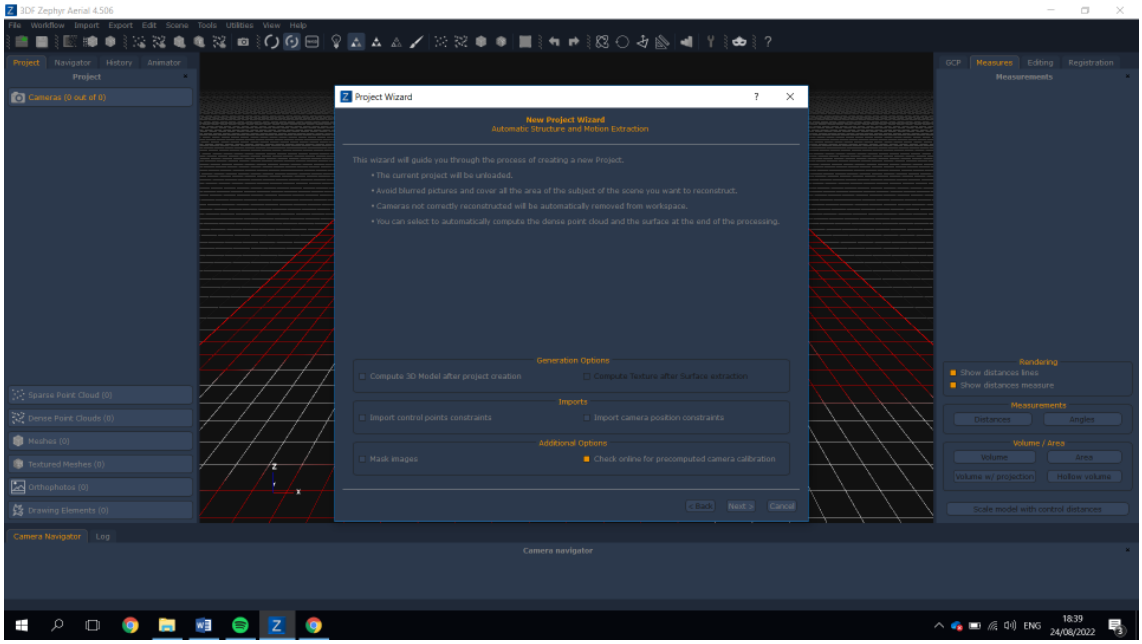

A new project wizard will appear. This is the beginning of the 3D modelling process.

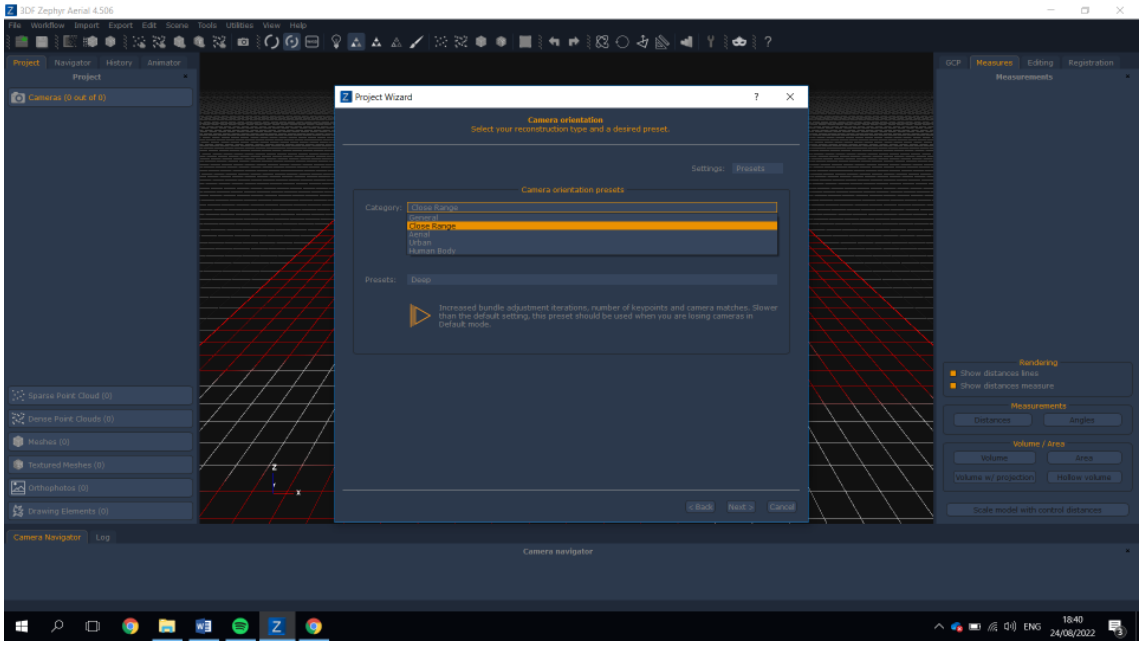

Two number settings require in put. ‘Category’ and ‘Presets’. ‘Category’ refers to how the images were captured. In this case ‘Close Range’ was selected.

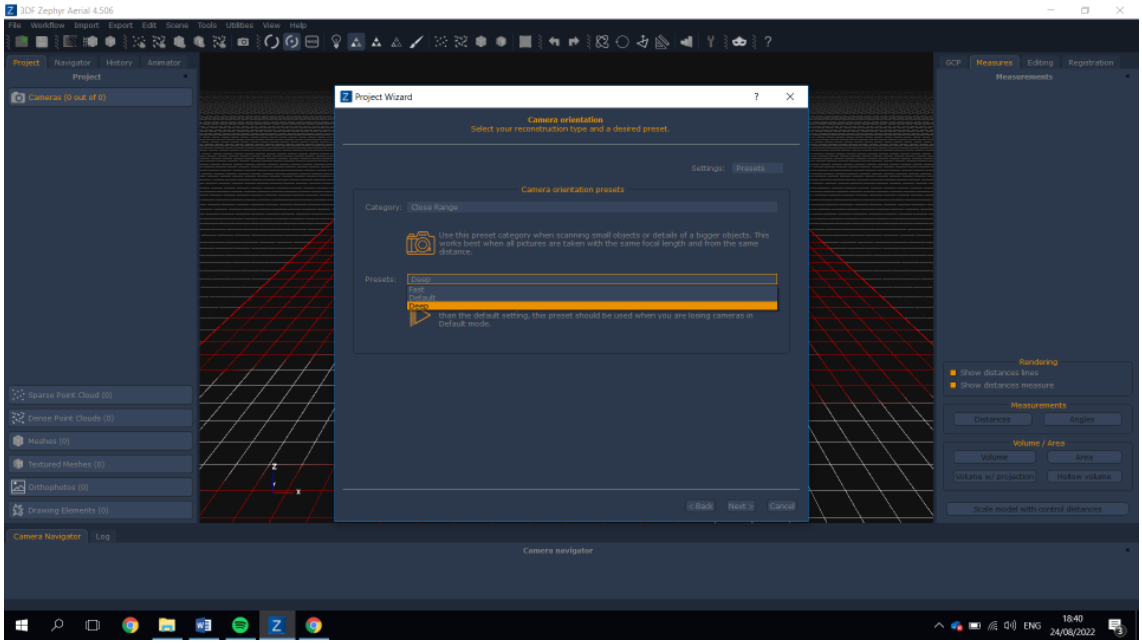

'Presets' refers to the processing detail and subsequently the speed at which the software generates point data.

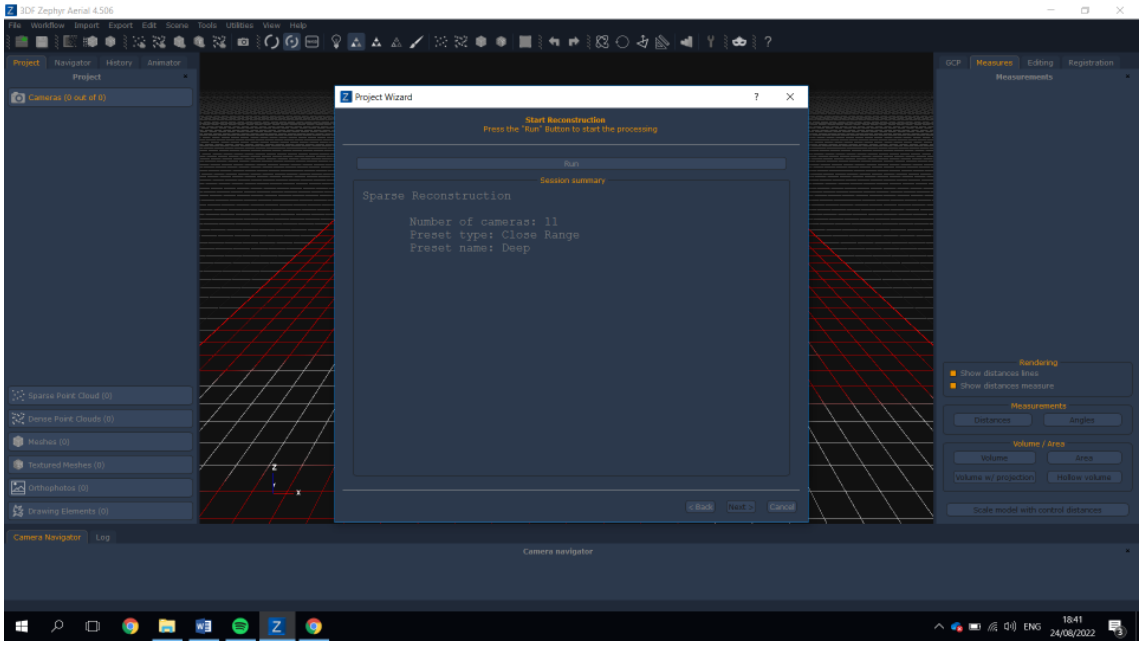

Once 'Category' and 'Presets' have been selected. The software illustrates the selected settings - Stating the number of images the model will be based on, the category and the preset.

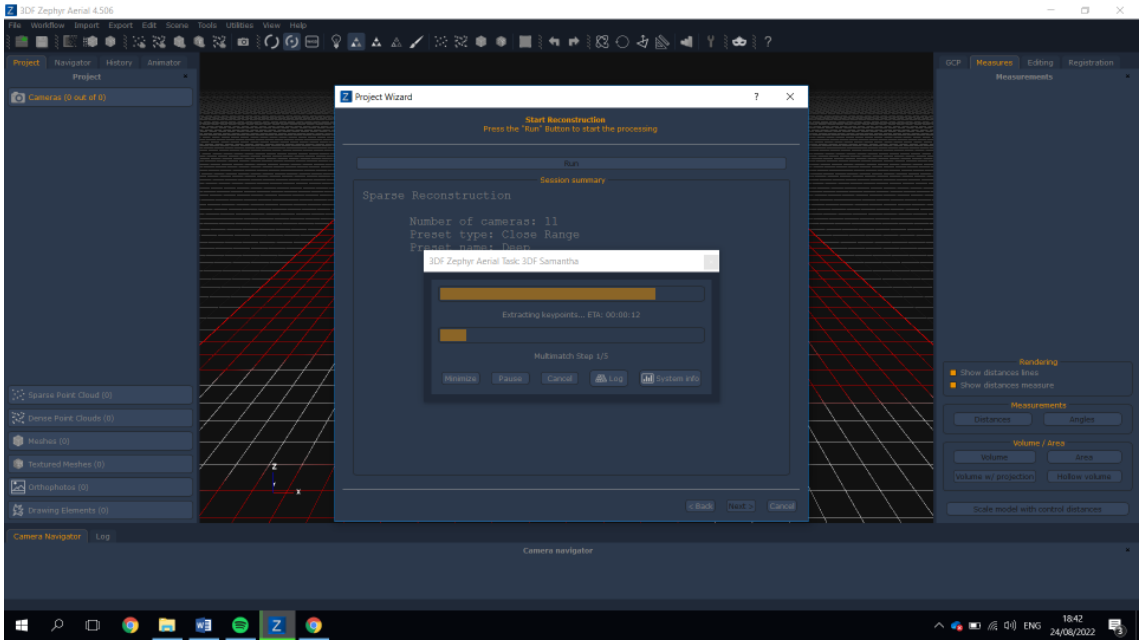

The software processed the selected images to generate a 'Sparse Point Cloud'.

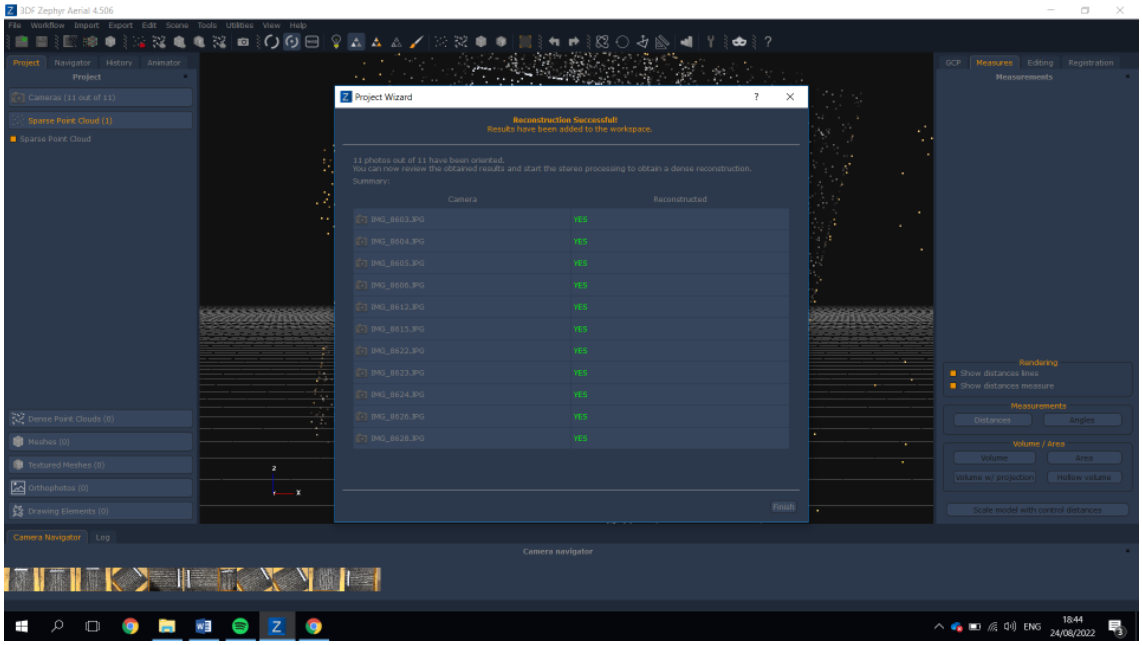

After the software processed the images it will display a project wizard that states if reconstruction of the surface could be generated from the images selected.

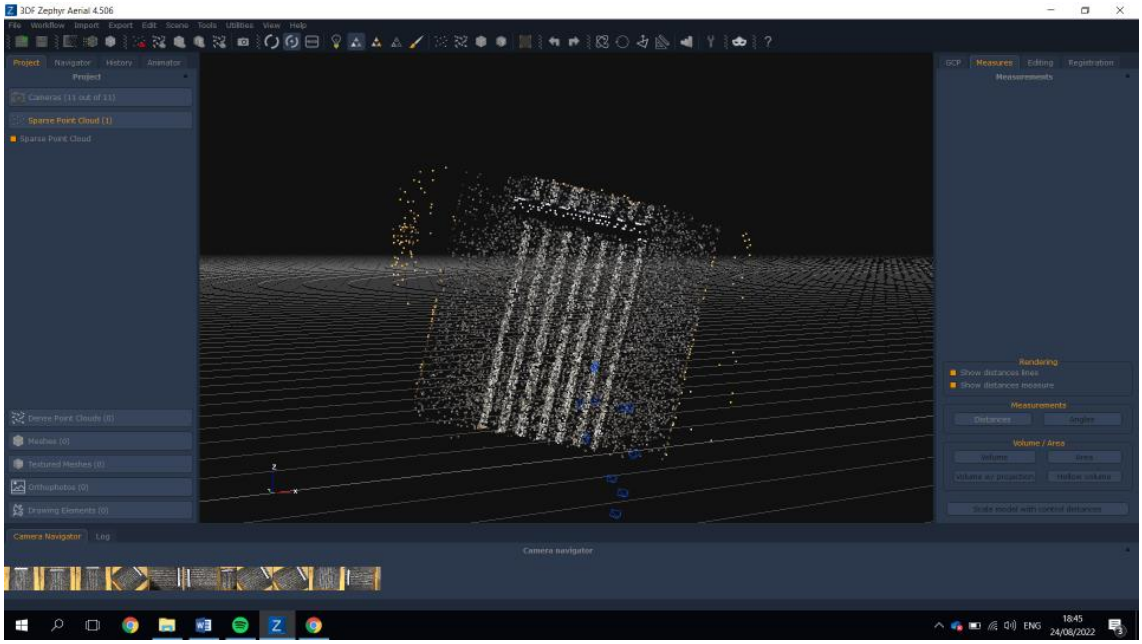

The software will generate a ‘Sparse Point Cloud’.

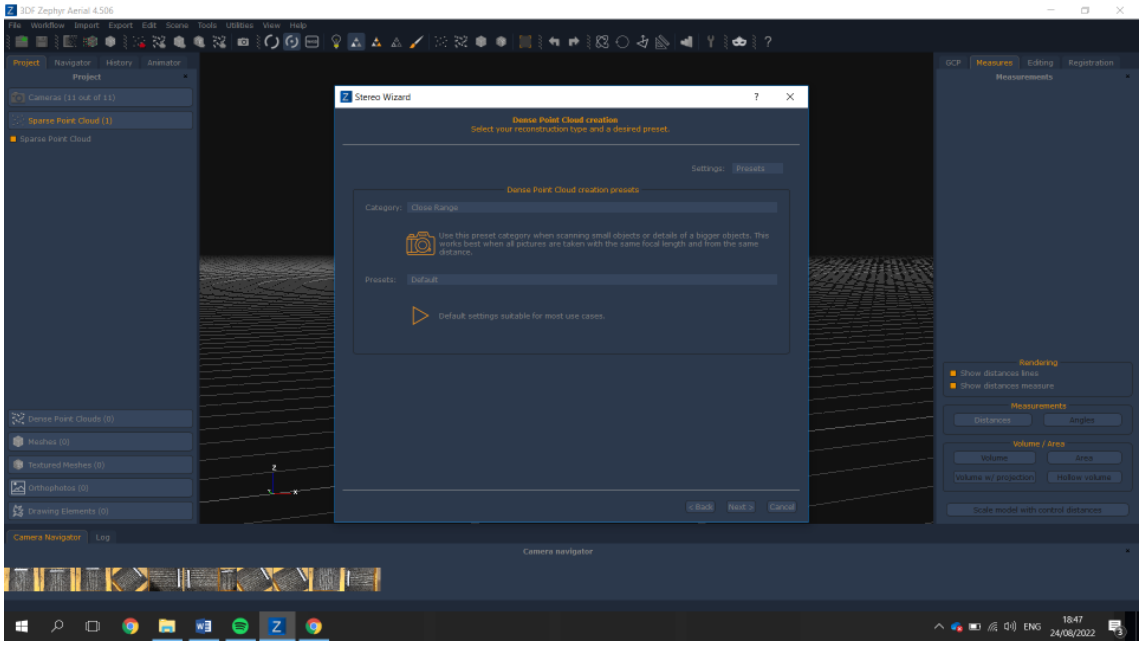

The ‘Sparse Point Cloud’ is then further re-constructed to develop a ‘Dense Point Cloud’. Similar to before, the ‘Category’ and ‘Presets’ were selected.

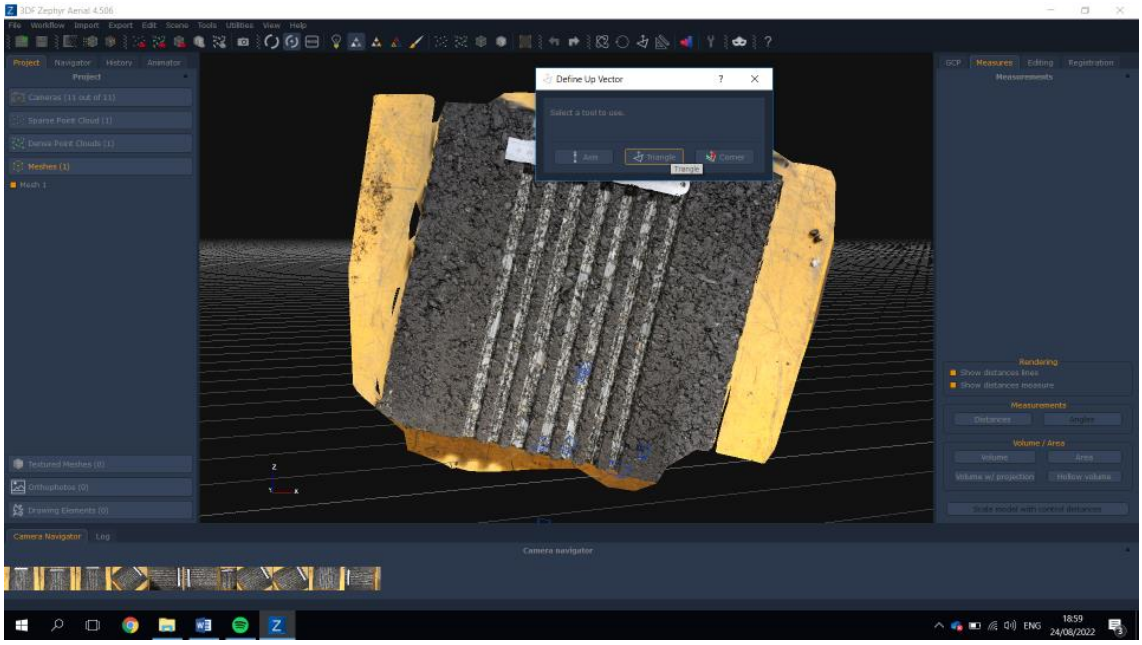

Once the 'Dense Point Cloud' is generated. The surface required re-orientation to determine the Z – Axis. This was done through the 'Triangle' method within the software.

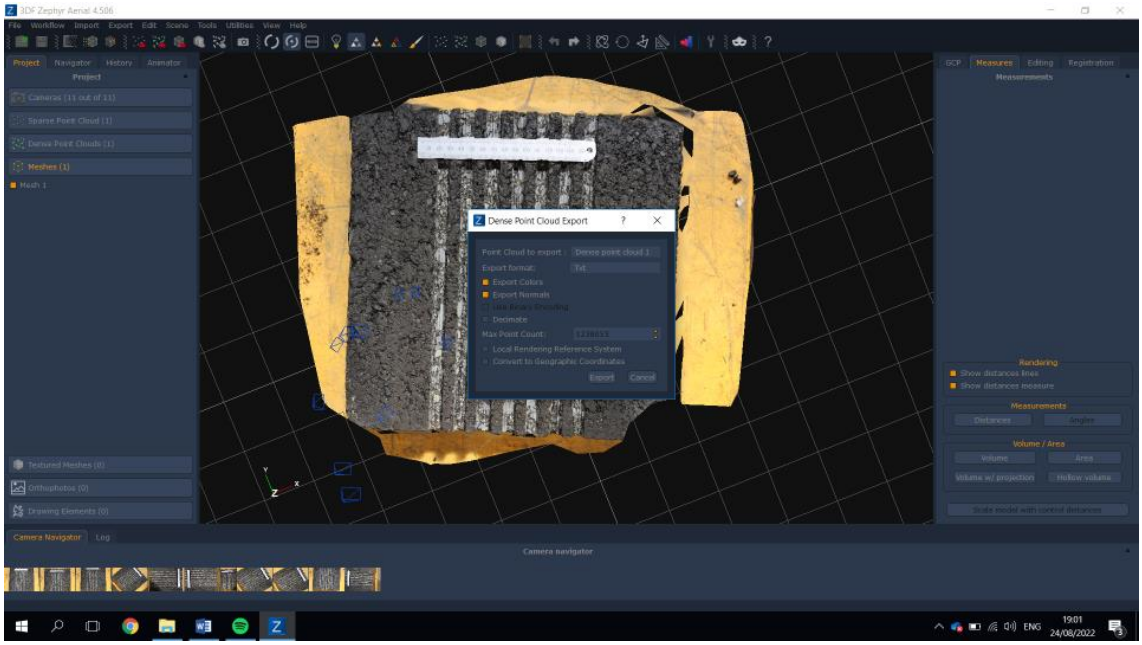

The 3D g surface is now created and the Z – axis determined. The 3D model was exported as a txt file to use in Digital SurfMountains Map.

Digital Surf MountainsMap was used to analyse the 3D models generated.

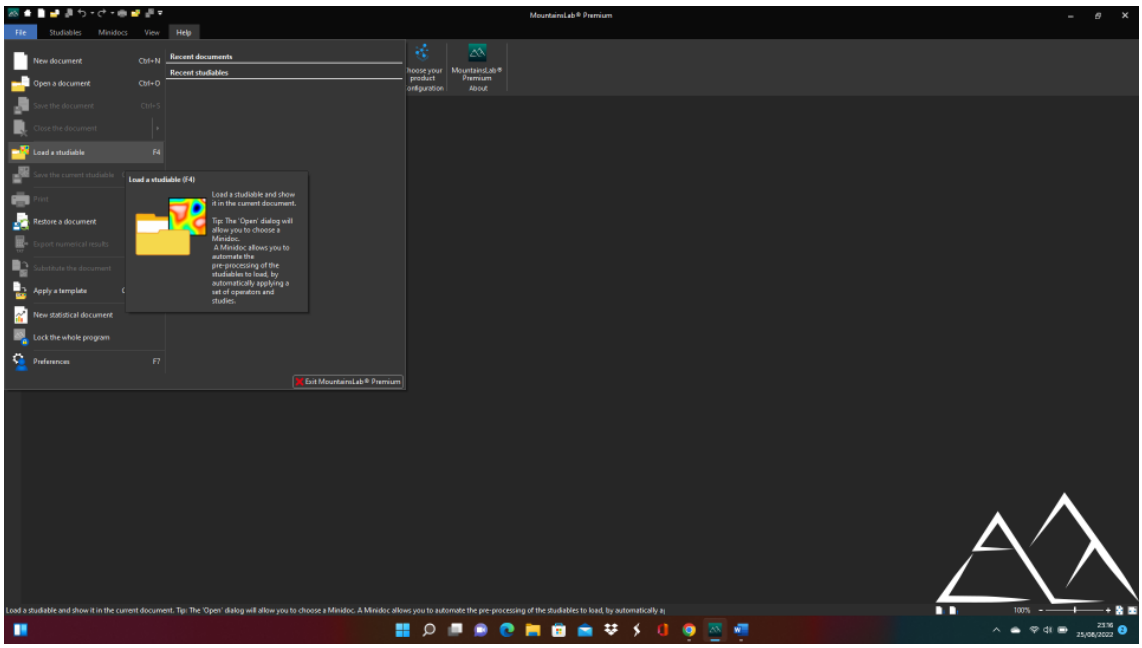

The txt file exported from Zephyr 3DF was loaded as a ‘Studiable’.

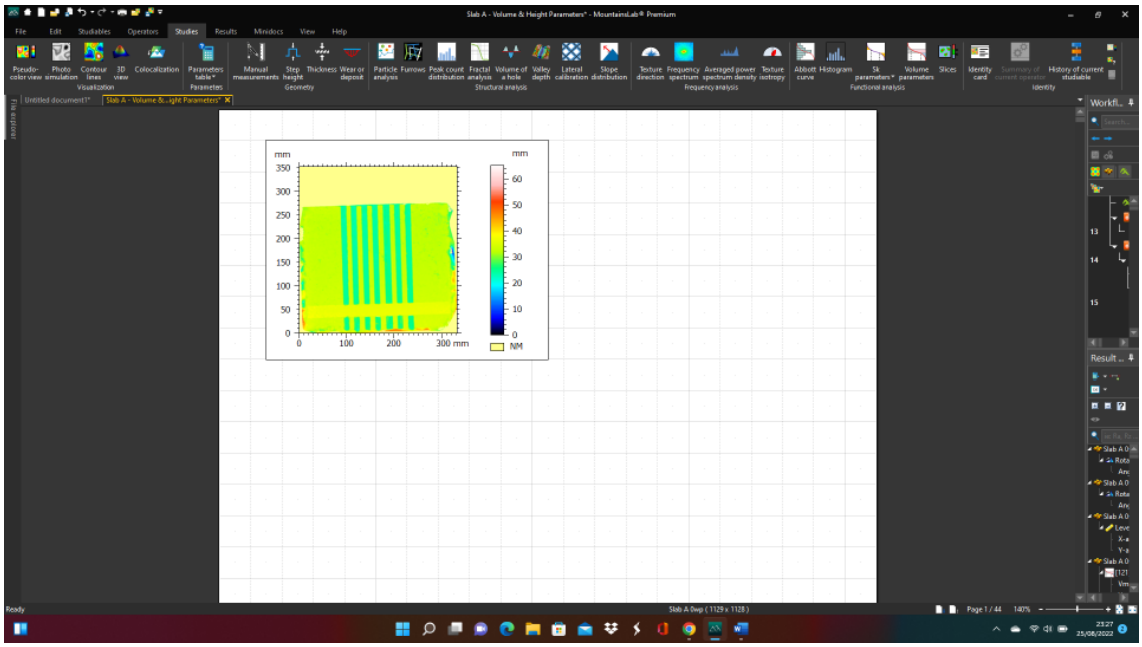

The txt file is loaded into a MountainsMap document to be analysed.

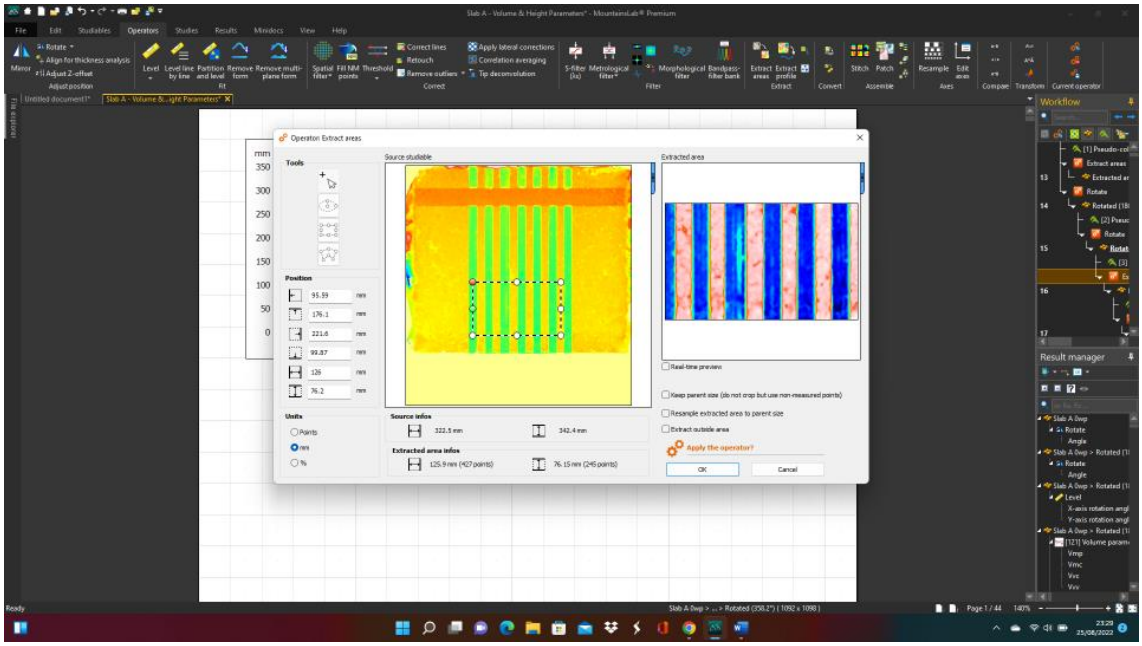

The Area of Interest (the pendulum contact area) was extracted from the approximate area the pendulum would interface when pendulum testing the test specimen.

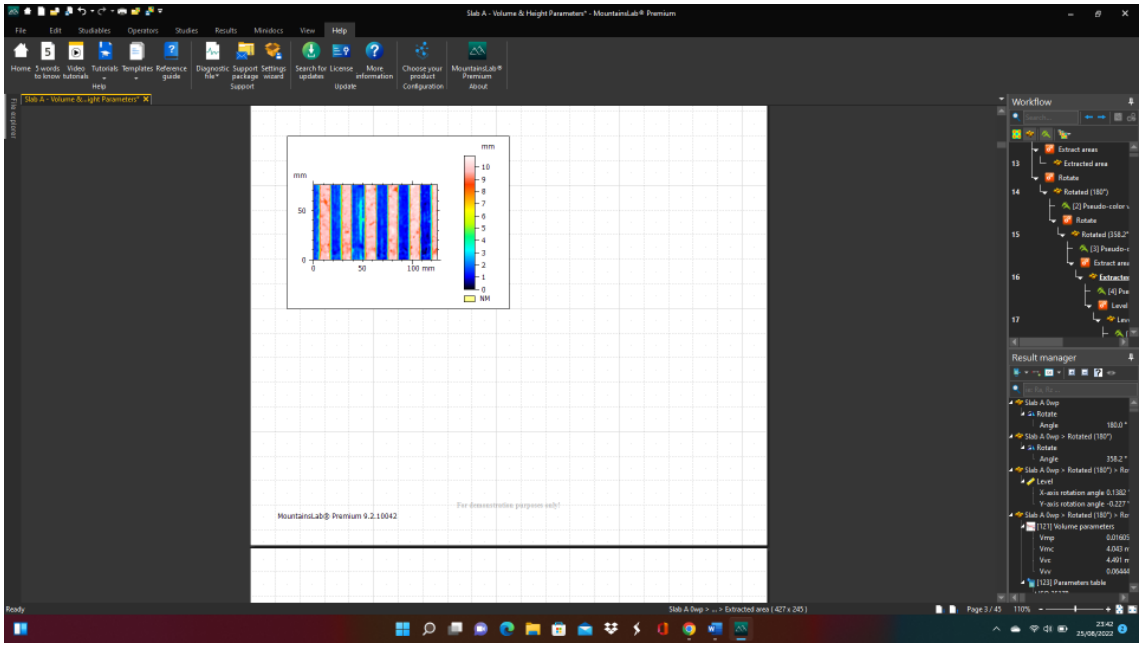

The Area of Interest was then extracted from the original model.

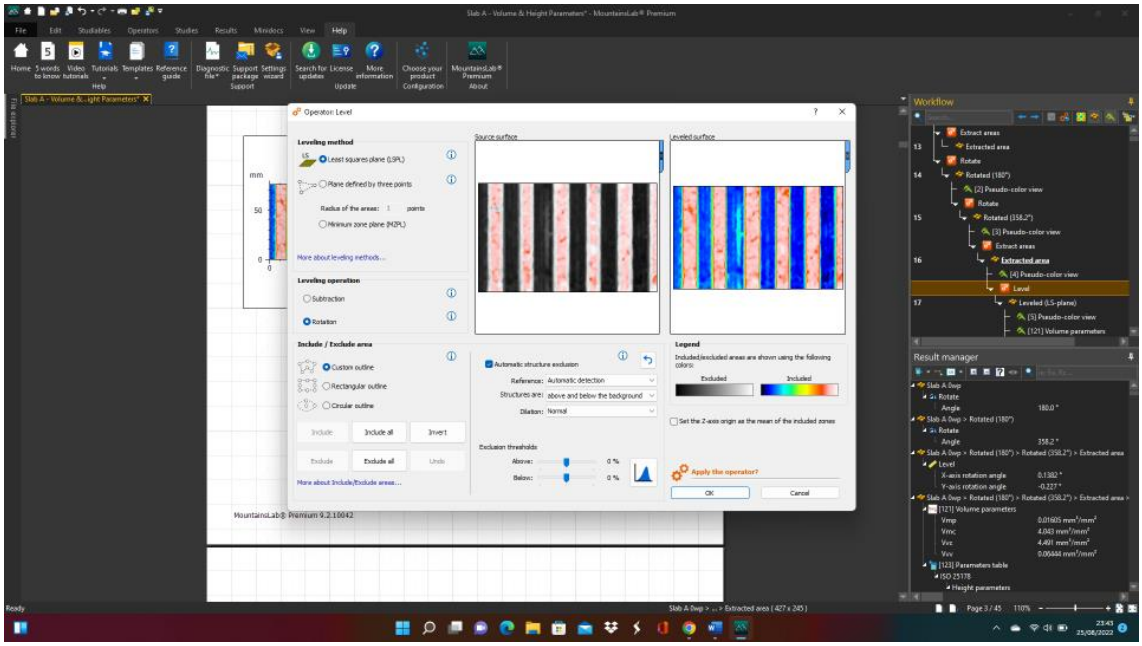

The Area of Interest was Levelled by the ‘Least Squares Plane’ method.

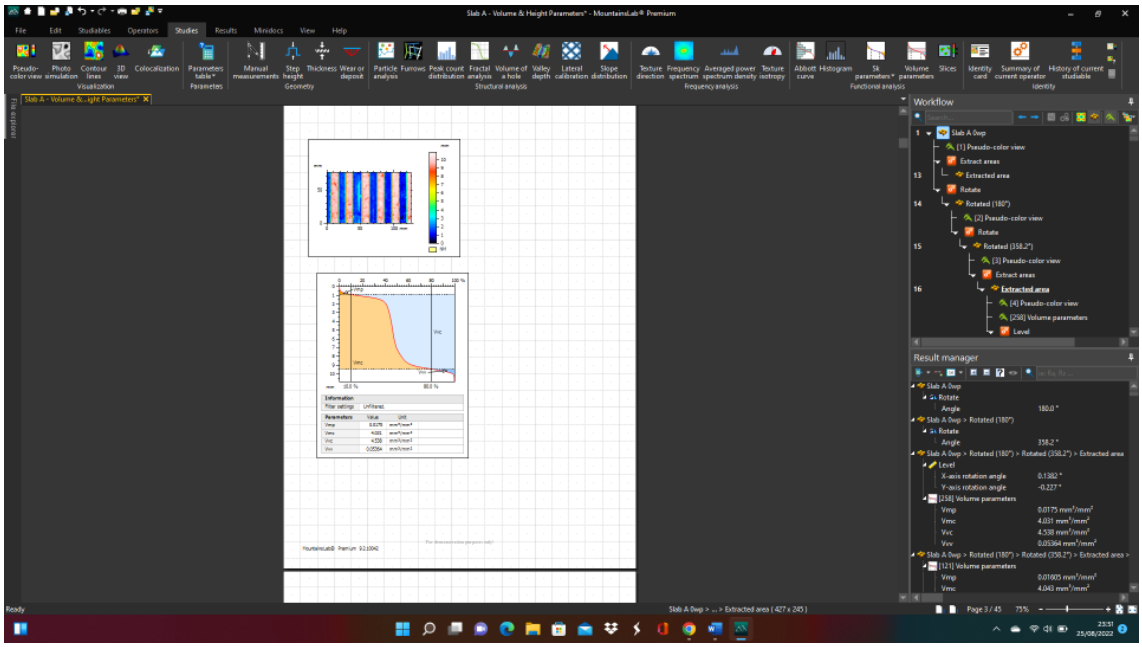

The ‘Volume Parameters’ was then generated from the Area of interest. This data was collected and analysed.

APPENDIX G

Publications by J.D. Ferguson

Ferguson, Jason, D. Woodward, and Phillip Millar. "Laboratory investigation of the landing aircraft tire contact patch." In *7th international conference bituminous mixtures and pavements*. CRC Press, 2019.

Ferguson, J., Woodward, D., Millar, P. (2022). 'Laboratory prediction of grooved Marshall Asphalt skid resistance performance'. *The Institute of Asphalt Technology 2022 Yearbook*. Pages 63 - 67.

Woodward, D., Millar, P., Tierney, C., Ferguson, J. (2020). 'Development of a test method to investigate the tyre road interface'. *Asphalt Professional*. No. 85. Pages 10-20.